UNIVERSITY COLLEGE LONDON

Faculty of Mathematics and Physical Sciences

Department of Physics & Astronomy

EFFECTS OF FIELD-ALIGNED CURRENTS IN THE IONOSPHERE-THERMOSPHERE SYSTEM

Thesis submitted for the Degree of Doctor of Philosophy of University College London

by

Rosie K. E. Hood

Supervisors:
Dr. Anasuya Aruliah
Prof. Alan Aylward

Examiners:
Dr. Adrian Grocott
Dr. Robert Wicks

December 13, 2018

In Loving Memory of Elizabeth F. Hood

1916 – 2017

I, Rosie Hood, confirm that the work presented in this thesis is my own. Where information has been derived from other sources, I confirm that this has been indicated in the thesis.

Abstract

Space weather is one of the most significant natural hazards to modern day civilisation, posing a risk to both space and ground infrastructure. It describes the near-Earth and terrestrial environment as affected by the Sun, namely as a result of radiation, interactions with the interplanetary magnetic field and plasma outflow, the latter termed the solar wind.

Field-aligned currents (FACs), that is, solar wind-driven currents aligned with the Earth's geomagnetic field and closed in its ionosphere, play an essential role in the transfer of energy and circulation between the solar wind and the ionosphere-thermosphere system. We study two main consequences of FACs in this system: the induced ground geomagnetic disturbances (GMDs), which arise as FACs close in the ionosphere, and the resultant Joule heating and perturbed thermospheric neutral winds as the energy transferred by FACs dissipates via their closure currents.

We find, within data restrictions, no strong linear correlation between FAC and GMD magnitudes, instead suggesting solar wind parameters as a better indication of the location and strength of harmful ground GMDs. We probe the effect a neutral wind disparity between ground-based instrument and satellite measurements will have on the distribution and magnitude of wind-derived Joule heating, after using a model to show the winds should be equivalent. We suggest the cause of the disparity is due to uncertainties in the satellite wind derivation. Finally, we investigate small-scale FAC-driven Joule heating and electron precipitation as the causes of a satellite-measured cusp density enhancement and FPI-measured cusp and nightside auroral oval upwellings. We model an empirical heating source representative of soft and hard precipitation in these regions. Our simulations support a mechanism of soft precipitation and Joule heating in the cusp but are unable to reproduce the nightside upwelling. We suggest this is a storm-related anomaly, requiring an adjusted mechanism.

Impact

Space weather refers to the conditions in the solar system and on the Sun that can interfere with technology in space and on the ground, affecting many aspects of life from the health of astronauts to GPS to the electric grid delivering electricity to your home. It can describe ambient solar wind conditions, which persistently degrade space infrastructure, or severe events, such as solar flares and coronal mass ejections, two of the greatest threats to modern day civilisation. It is therefore of interest to the general public, but also many industries, who can be injured by its costly and disruptive effects. It is vital that we understand the mechanisms driving space weather in order to monitor, forecast and, eventually, mitigate or prevent.

This thesis focuses on the main facilitator of energy transfer from the solar wind, the plasma outflow of the Sun, into the ionosphere-thermosphere system on Earth: field-aligned currents. These currents close in the ionosphere, and can induce geomagnetic disturbances on the ground, obstructing the electric grid and gas industries, which rely on susceptible long manmade frameworks of cables and pipelines able to conduct induced ground currents during geomagnetic storms. At its worse, this can lead to gas pipelines cracking and transformer breakdown, disconnecting power. Field-aligned currents also distribute their electromagnetic energy locally in the ionosphere leading to Joule heating. This modulates the composition and density of the upper atmosphere, altering the drag satellites experience, and therefore their orbit determination.

Space weather is extremely complex, and a coordinated effort between industry, research and government agencies is required for its various mechanisms to be fully resolved. This thesis contributes to on-going research, and provides insight into one of the most significant aspects of the labyrinthine field of space weather. Crucially, this thesis is able to study several effects individually and their combined result. A thorough discussion of research and proposals of future work are presented, providing repeatable methods and

suggestions of data sources. This research has also been disseminated in the U.K. and international communities, and is also in part due to a collaboration with the U.S..

Several space weather datasets are amalgamated, containing both satellite and ground-based instruments, their strengths and differences assessed and comparisons to a physics-based general circulation model provided. Several commonly adopted assumptions in the ionosphere-thermosphere system are also questioned in this thesis, providing clarity and in-depth analysis where it had previously not been. The findings of this thesis have immediate implications for drag models, particularly work on data dissimilarities and cusp modelling. The national grid network industry will also benefit from our ground geomagnetic disturbance study, as well as the broader scientific community. To fully realise the implications of this research more work is needed (for example, with statistical studies), however, we have provided the groundwork and have shown that common assumptions are not always correct. Indeed, space weather research is often said to be where weather research was 50 years ago.

Acknowledgements

This thesis would not have been possible without the kind and nurturing supervision of Anasuya Aruliah, whose guidance over the last few years has been invaluable. I would like to thank Steve Morley and Jesse Woodroffe, two of the kindest and most insightful academics in the space weather community, for their stateside supervision, particularly when it was no longer their responsibility. Many thanks also to Alan Aylward for his advice and time during his retirement, and to the APL and Astrophysics groups and broader space weather community for their help throughout my PhD. During my PhD I was fortunate to overlap with the APL-ers Amy Ronksley, David Johnson and David Barnes - thank you all for your constant supply of helpful advice.

Most of all I would like to thank my family for their continuing support, if I have achieved anything it is because of you. To my friends, thank you for your unabated encouragement and comic relief; 55A, that means you. And to Neal, for your support, patience and generosity - I will be forever grateful.

The eastern sky appeared of a blood red colour. It seemed brightest exactly in the East, as though the full moon, or rather the Sun, was about to rise. It extended almost to the zenith. The whole island was illuminated. The sea reflected the phenomenon, and no one could look at it without thinking of the passage in the Bible, which says, 'the sea was turned to blood.' The shells on the beach, reflecting light, resembled coals of fire.

Eyewitness account on Sullivan's Island reported in the Charleston Mercury, 1859.

Contents

List of Figures

List of Tables

Chapter 1

Introduction

Space weather is one of the most significant natural hazards of the 21st century (Cabinet Office 2015; Krausmann & Bothmer 2012; DHS Office of Risk Management and Analysis 2011; Jonas & McCarron 2016), posing a risk to both space and ground infrastructure and modern day civilisation as we know it (see for example: National Research Council (2008); Royal Academy of Engineering (2013); Zanetti (2013); Schrijver et al. (2015) and references therein). The term space weather describes the near-Earth and terrestrial environment as affected by solar activity; this can include nominal activity as well as severe events such as solar flares, coronal mass ejections (CME) and solar energetic particle events (SEP). The radiation produced during a solar flare, the magnetised plasma of an ejection released into the solar wind, and the high energies of a particle event can all impact both space and ground systems by affecting, for example, GPS, the national grid and gas industries, as well as satellite function and orbit (Reay et al. 2005; National Research Council 2008; Royal Academy of Engineering 2013; Zanetti 2013; Viljanen et al. 2014; Schrijver et al. 2015).

Field-aligned currents, that is solar wind-driven currents aligned with the Earth's geomagnetic field and closed in its ionosphere, play a vital role in the transfer of energy and circulation between the solar wind and magnetosphere-ionosphere-thermosphere system (Iijima 2013). The two main consequences of field-aligned currents investigated in this thesis are the induced ground disturbances which arise as field-aligned currents close in the ionosphere, and the effect of the energy transferred by field-aligned currents and dissipated

by these closure currents.

Firstly, the closure currents formed generate ground fluctuations in the magnetic field, inducing ground geomagnetic disturbances (Nishida 1964). A key part of this vulnerability are ground effects, where long man-made frameworks such as gas pipelines and cabling used in the electrical grid system can conduct induced ground currents during geomagnetic storms, causing pipelines to crack and transformers to overload and melt (Lloyds 2013; Viljanen et al. 2014). The impact of such ground disturbances can be fatal and financially damaging; an example of the latter is the Quebec power grid failure in 1989 resulting in a 9-hour blackout and $2 billion of estimated losses (National Research Council 2008).

Secondly, the electromagnetic energy that field-aligned currents bring into the ionosphere is significant locally, dissipating in the ionosphere as Joule heating and transferring momentum to the neutrals via ion-neutral collisions (see for example: St.-Maurice & Hanson (1982); Thayer (2000); Iijima (2013); Cowley (2000) and references therein). Joule heating is a significant energy dissipation mechanism in the magnetosphere-ionosphere-thermosphere system (Akasofu 1981; Cierpka et al. 2000) and product of space weather, affecting, amongst other mechanisms, the density profile and composition of the upper atmosphere, a major component of general circulation models (Deng & Ridley 2007; Huang et al. 2012) and drag models (Jacchia 1970; Storz et al. 2005; Bruinsma et al. 2014; Bruinsma 2015). Another localised but noticeable example affecting drag models is the neutral density enhancement in the cusp region, which introduces a systematic model error (Lühr et al. 2004). This in turn has significant impacts on understanding atmospheric physical processes used in, for example, satellite orbit determination and prediction (see for example: Vallado (2001); Lühr et al. (2004); Storz et al. (2005)), a notable failure being satellite collision (National Research Council 2008; Royal Academy of Engineering 2013). It is therefore vital that the effects of field-aligned currents and their role in space weather are well-understood.

In this introduction we provide a brief overview of the the solar-terrestrial system, and specifically the ionosphere-thermosphere system. We discuss how energy is transferred into the system via the magnetosphere, including how field-aligned currents are formed and their resultant role in these systems to build an understanding of their effects. With this background, we then discuss the theory behind the three subject areas discussed in the following chapters of this thesis where field-aligned currents play a significant role: Joule heating, polar neutral winds and ground geomagnetic disturbances.

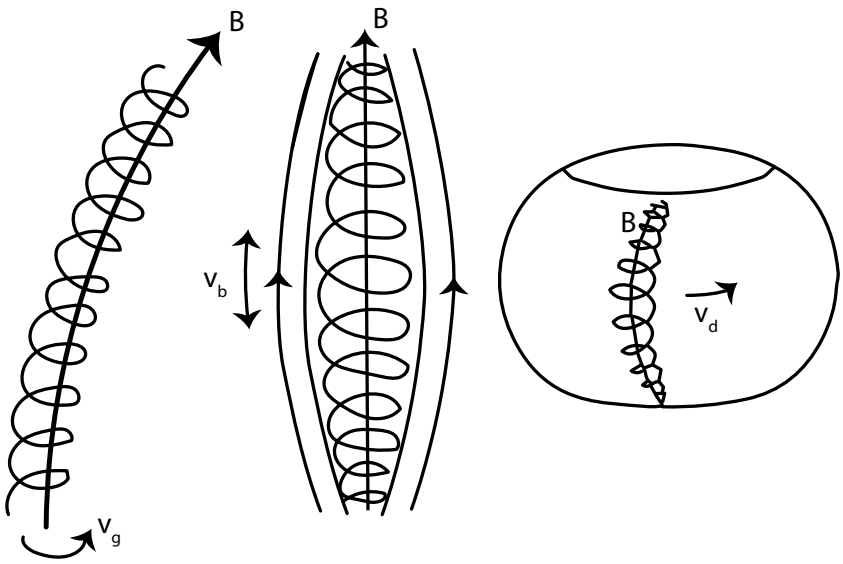

Figure 1.1. Illustration of three types of charged particle motion: gyromotion v_g, bounce motion v_b, and drift motion v_d.

1.1 Introduction to Plasma

The fundamental physics behind field-aligned currents, their effects and the ionosphere-thermosphere system as a whole lies in magnetohydrodynamics. We begin this thesis with a recap of charged particle motion and magnetohydrodynamics (as it relates to this thesis) to provide clarity when applying these concepts to our complex system. We base this section on the description provided by Grant & Phillips (2013).

1.1.1 Single Particle Motion

Magnetohydrodynamics is rooted in the Lorentz force law, which describes the electromagnetic force due to a charged particle q travelling through an electric field $\mathbf{E}$ and/or magnetic field $\mathbf{B}$ at velocity $\mathbf{v}$:

$$F_{Lorentz} = m\frac{d\mathbf{v}}{dt} = q(\mathbf{E} + \mathbf{v} \times \mathbf{B}) \tag{1.1}$$

and Maxwell's equations, comprising Gauss' law, Gauss' law for magnetism, Faraday's law of induction and Ampère's circuital law; respectively:

$$\begin{aligned} \nabla \cdot \mathbf{E} &= \frac{\rho}{\epsilon_0} \\ \nabla \cdot \mathbf{B} &= 0 \\ \nabla \times \mathbf{E} &= -\frac{\partial \mathbf{B}}{\partial t} \\ \nabla \times \mathbf{B} &= \mu_0 \mathbf{j} + \mu_0 \epsilon_0 \frac{\partial \mathbf{E}}{\partial t} \end{aligned} \tag{1.2}$$

where μ_0 is the permeability of free space, ϵ_0 is the permittivity of free space, $\mathbf{j}$ is the current density, ρ is the charge density, and t is time. The corresponding current density, $\mathbf{j}$, can be found using Ohm's law:

$$\mathbf{j} = \sigma \cdot \mathbf{E} \tag{1.3}$$

where σ is the conductivity tensor.

There are several scenarios of charged particle motion we can consider. We focus on the three types of charged particle motion, demonstrated in Figure 1.1. The simplest is the motion of a charged particle in a parallel uniform magnetic field with no electric field. Referencing Equation 1.1, the Lorentz force acts perpendicular to the magnetic field and motion direction of the charged particle. This causes the particle to curve (see Figure 1.1 for a schematic), following a circular motion termed 'gyromotion' (v_g or $v_\perp$), with a given gyroradius r_g. When equating the centripetal force of the circular motion to the Lorentz force, the gyroradius can be calculated:

$$r_g = \frac{m v_g}{|q| B} \tag{1.4}$$

with gyrofrequency equal to:

$$\Omega_g = \frac{qB}{m} \tag{1.5}$$

If the magnetic field converges, however, a process known as magnetic mirroring occurs (where two magnetic mirrors form a magnetic bottle). Here the charged particle motion is in the direction of the convergence or increased field strength and 'bounces' backwards (see Figure 1.1). The perpendicular velocity increases in the stronger magnetic field (see Equation 1.6), whilst the parallel motion decreases, conserving energy. As the Lorentz force is perpendicular to the magnetic field, this leads to a force against the direction of

motion and therefore an acceleration backward. We can calculate the perpendicular velocity by considering the first adiabatic variant or magnetic moment, μ, which is conserved during the motion of a charged particle (provided the magnetic field changes slowly) and defined as the kinetic energy over the magnetic field strength:

$$\mu = \frac{mv_{\perp}^2}{2B} \tag{1.6}$$

Defining a pitch angle as the angle between the motion vector and the magnetic field, where $v_{\perp}$ is equivalent to:

$$v_{\perp} = v \sin \alpha \tag{1.7}$$

Inserting Equation 1.7 into Equation 1.6 we obtain:

$$\mu = \frac{mv^2 \sin^2 \alpha}{2B} \tag{1.8}$$

where the velocity and bouncing point B_m can be calculated, the latter by considering the ratio of B and B_m:

$$\begin{aligned} \frac{\sin^2 \alpha_0}{\sin^2 \alpha_m} &= \frac{B_0}{B_m} \\ \sin \alpha_0 &= \sqrt{\frac{B_0}{B_m}} \end{aligned} \tag{1.9}$$

where $\alpha_m = 90°$ at B_m. This is the second type of motion, bounce motion. The shape generated by Equation 1.9 is a cone; this is known as the loss cone. If $\alpha < \alpha_0$ particles can enter the loss cone and precipitate into the denser atmosphere.

If there is a parallel electric field component, the velocity has a non-constant parallel component $v_{\parallel}$, where:

$$\frac{dv_{\parallel}}{dt} = \frac{qE_{\parallel}}{m} \tag{1.10}$$

giving rise to a constant acceleration along the magnetic field lines. Equation 1.10 shows that the presence of the electric field causes positively (negatively) charged particles to move in (away from) the direction of the electric field. This produces an electric field anti-parallel to the original electric field, eventually producing a net parallel field of 0. However, it should be noted that collisions can disturb the net flow, such as with field-aligned currents, which means that the electric field can be non-zero (see Section 1.4.4 for further detail).

Conversely if there is a perpendicular electric field, a drift velocity acts on the charged particle (see Figure 1.1). If we move to the frame of gyromotion, setting Equation 1.1 to 0, we obtain:

$$\mathbf{E} = -\mathbf{v} \times \mathbf{B} \tag{1.11}$$

and by crossing with $\mathbf{B}$ we can solve for this drift, v_d:

$$v_d = \frac{\mathbf{E} \times \mathbf{B}}{B^2} \tag{1.12}$$

This is the third type of motion, drift motion.

1.1.2 Magnetohydrodynamics

A further magnetohydrodynamical concept underlying solar-terrestrial physics is Alfvén's Theorem, or the frozen-in flow approximation. This states that magnetised plasma field lines in the plasma are 'frozen-in' and move with the motion of the plasma, with the charged particles gyrating around a specific field line. This also implies that two separated magnetised plasmas cannot mix, as in a collision-less plasma the magnetic field lines cannot cross. We can derive this approximation assuming an an infinitely conducting plasma and using Faraday's law of induction (see Equation 1.2), Ampère's law (see Equation 1.2) and Ohm's law (see Equation 1.3). In the presence of a magnetic field and with moving plasma, Ohm's law requires an extra term due to the current induced by the Lorentz force, such that:

$$\mathbf{j} = \sigma(\mathbf{E} + \mathbf{v} \times \mathbf{B}) \tag{1.13}$$

Rearranging for $\mathbf{E}$ where $\mathbf{j}$ is given by Ampère's law, we can substitute this into Faraday's law to obtain:

$$\frac{\partial \mathbf{B}}{\partial t} = \nabla \times (\mathbf{v} \times \mathbf{B}) + \frac{1}{\sigma_o \mu_o} \nabla^2 \mathbf{B} \tag{1.14}$$

where the first term describes frozen-in flux and the second term is a diffusion relationship. The magnetic Reynolds number, R_m, is the respective ratio of these two terms, and is typically high in space plasmas.

The frozen-in approximation breaks down when there are collisions (as Equation 1.14 assumes a collision-less plasma), when the $\mathbf{E} \times \mathbf{B}$ drift in Equation 1.12 is not the dominant drift and when spatial scales reach the order of the charged particle's gyroradius, allowing the particle to separate from its magnetic field line ($\mathrm{R}_m < 1$). There are two types of drifts

where this can occur, both can be calculated using the general drift term, itself derived from Equation 1.12 and $F = qE$:

$$v_F = \frac{\mathbf{F} \times \mathbf{B}}{qB^2} \tag{1.15}$$

Firstly, we examine gradient drift v_∇, where a charged particle experiences an increased magnetic field during its gyromotion. Here the force experienced by the particle is $F_\nabla = -\mu\nabla\mathbf{B}$; substituting this and Equation 1.6 into Equation 1.15 gives:

$$v_\nabla = \frac{mv_\perp^2}{2qB^3}\mathbf{B} \times \nabla\mathbf{B} \tag{1.16}$$

Secondly, curvature drift v_R is due to a charged particle moving along a curved field line, where $F = mv_\parallel^2\mathbf{R_c}/R_c^2$ and $\mathbf{R_c}$ is the local radius of curvature. Again, substituting this and Equation 1.6 into Equation 1.15 gives:

$$v_R = \frac{mv_\parallel^2}{qR_c^2B^2}\mathbf{R_c} \times \mathbf{B} \tag{1.17}$$

Finally, considering two magnetised plasmas, and referring to Ampère's law (see Equation 1.2), we see that a current sheet is induced between the plasmas. The current sheet is of the order of a gyroradius and therefore breaks down the frozen-in flow approximation.

1.2 The Solar-Terrestrial System

The solar-terrestrial system comprises the Sun, solar wind, magnetosphere, ionosphere and neutral atmosphere of the Earth. Though divided into these subject areas, and sub-divided still further, the system is very coupled. This section is devoted to the sources of energy in the ionosphere-thermosphere system, namely the Sun's emitted radiation and plasma, the latter in the form of the solar wind.

1.2.1 The Sun as the Initial Driver

The Sun is the initial driver of processes on the Earth through its radiation and emitted plasma. Solar ultraviolet (UV) and X-ray radiation are dominant heat sources of the atmosphere, and ionise the upper atmosphere to create the Earth's ionosphere. Plasma from the Sun, or solar wind (see Section 1.2.2), can also precipitate into the system causing increased flux and heating via collisions, in turn changing the composition of the

atmosphere.

The variability of the Sun greatly influences the ionosphere-thermosphere system. The Sun has a quasi-periodic variation with an average period of 11 years, when it reverses its magnetic field. Solar minimum and maximum occur when the sunspot number is at its lowest and highest respectively during this period. During solar maximum, the presence of sunspots on the solar surface increases solar activity by producing harmful solar flares, CMEs and SEP events; the total solar irradiance seen at Earth is also greater due to the presence of hotter regions on the Sun's surface (for example, faculae). To measure solar irradiance a proxy wavelength of 10.7 cm is commonly used, known as the F10.7 index (Tapping 2013). The F10.7 index is often used in models as an input to calculate radiative heating in the atmosphere (see Section 2.4.4, and for example: Richmond et al. (1992); Harris et al. (2002)).

1.2.2 Solar Wind and the Near-Earth Environment

The solar wind describes the plasma outflow from the Sun due to the extreme temperature difference between the Sun's corona and the interstellar medium outside the solar system. Due to the rotation of the Sun, the plasma emission is not purely radial. However, the faster the solar wind stream, the more radial the flow is. Though continuous, the solar wind is not constant, with variations in density, temperature and speed. Typically the solar wind consists of primarily electrons and protons, and has a density of 7 cm^{-3} at Earth, with a speed of 440 km s^{-1} (Russell 2000). The solar wind is frozen into the Sun's magnetic field lines (due to Alfvén's Theorem), with one footprint anchored to the rotating Sun, causing the field to be drawn into a spiral, which is viewed at Earth as the Interplanetary Magnetic Field (IMF). This spiral-like field is termed the Parker spiral, demonstrated in Figure 1.2 (Parker 1963). Due to the hemispheric asymmetry of the field a neutral current sheet in the solar magnetic equatorial plane is induced between opposing field lines. The offset of the Sun's equator introduces a wave-like quality to the current sheet, taking the form of a 'ballerina's skirt'. The IMF is described by three components in Geocentric Solar Magnetospheric (GSM) coordinates, B_x, B_y and B_z, each of the order ∼1-10s nT. Here, x is towards the Sun from the centre of the Earth, y is perpendicular to the Earth's dipole and x (positive duskwards) and z completes the system (also described in Chapter 2). The IMF components' strength and direction each affect the Earth's magnetic field, allowing the solar wind to couple to the ionosphere-thermosphere system. Indeed Akasofu (1979)

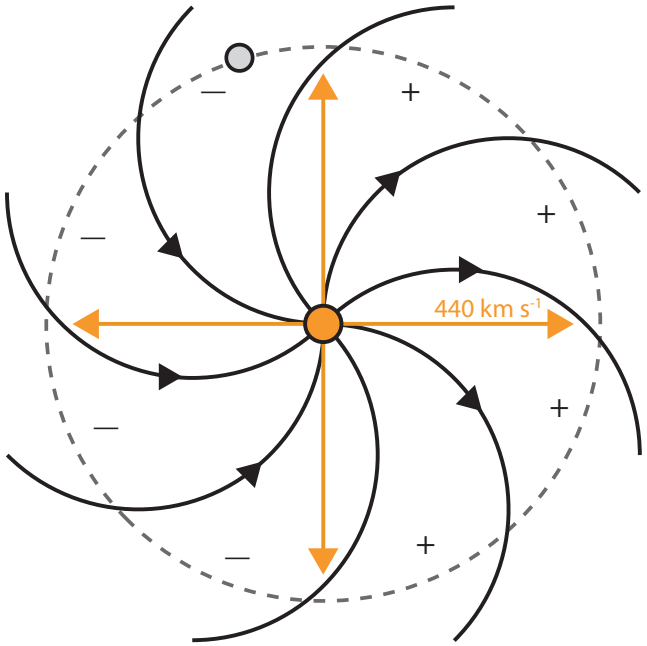

Figure 1.2. Illustration of the Parker spiral in the ecliptic plane, adapted from Parker (1963). The straight orange lines from the Sun represent the trajectory of the solar wind. The arrows detail the magnetic field polarity at the Sun, with positive signs representing outward field and negative inward. The Earth's orbit is overlaid in a dashed line.

showed that the energy input into the magnetosphere could be estimated by considering the orientation of B_y and B_z.

As well as nominal solar wind conditions, a CME can be emitted from the Sun during a solar flare, releasing vast amounts of plasma of the order of $\sim 10^{12}$ kg and frozen-in IMF into the solar system at speeds which can reach 2,000-3,000 km s^{-1} (Gopalswamy 2004). This fast stream of plasma reaches slower moving solar wind plasma and causes a compression, which in turn increases the density of the solar wind and the magnetic field strength of the frozen-in IMF. The interplanetary CME (ICME) reaches the Earth within days and is primarily deflected by the Earth's magnetic field. However, depending on the direction and strength of the IMF components, magnetic reconnection can occur, transferring energy and plasma from the solar wind into the poles. The orientation of both B_y and B_z are important in this process; though B_z drives magnetic reconnection on the dayside, the dawn-dusk B_y can introduce an asymmetry to the field, demonstrated in Figure 1.3 for the cases of positive and negative B_y (Hughes 1995). This causes magnetic

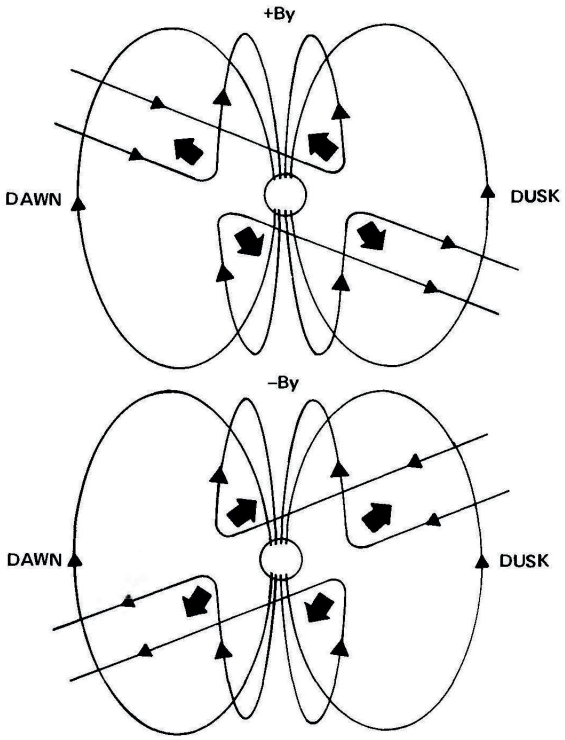

Figure 1.3. Illustration from Hughes (1995) showing effect of positive (top) and negative (bottom) B_y on the newly reconnected magnetic field lines at Earth. The arrows indicate the direction of the field lines due to magnetic tension.

tension in the dawn-dusk line, which affects the convection in the ionosphere (discussed in Section 1.4.4). When B_z is northward, reconnection at the lobes can also occur at high latitudes with tailward magnetic field lines. Magnetic reconnection is discussed in further detail in the following section.

1.3 Solar-Terrestrial Energy Transfer

The solar wind couples to the ionosphere-thermosphere system at Earth through its magnetosphere, the region of space where the Earth's magnetic field is separate from the IMF but can magnetically reconnect with the IMF in a process known as the *Dungey cycle* (Dungey 1961). In this section we describe this process as well as the basic structure of the magnetosphere and its various current systems. We then focus on field-aligned currents as a main facilitator of energy transfer in the solar-terrestrial system.

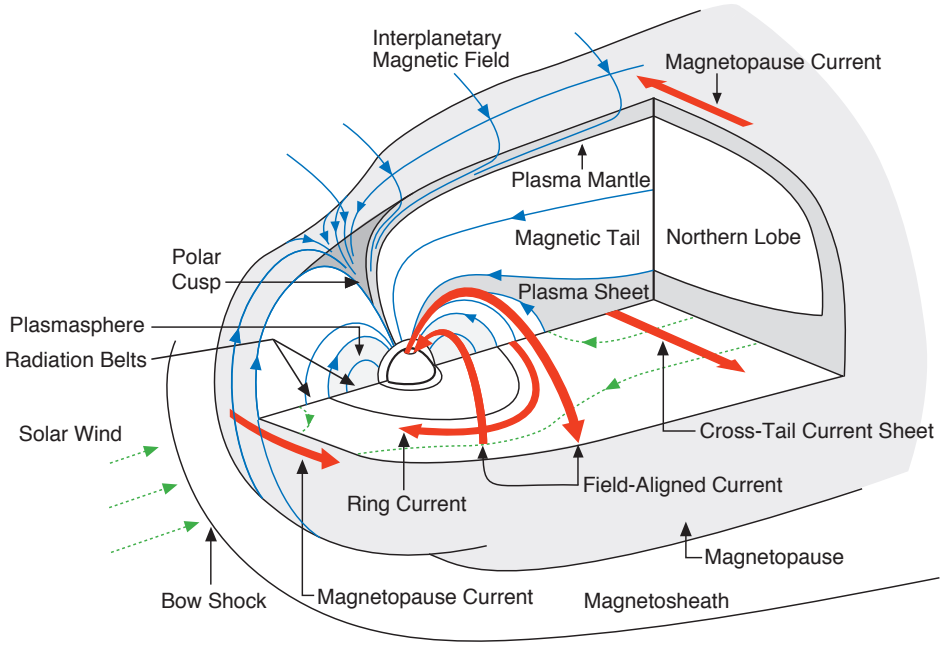

Figure 1.4. Schematic of the magnetosphere adapted from Russell (2000), including the respective magnetospheric currents (red) and magnetic fields (blue).

1.3.1 The Earth's Magnetosphere

Figure 1.4 shows a schematic of the magnetosphere with its respective currents (in red) and magnetic fields (in blue). The Earth's magnetic field is dipolar in nature, and offset by ∼11° from the geographic poles. The field has two cusp regions at the geomagnetic poles, which are characterised by open geomagnetic field lines and are fixed with respect to the Sun. The magnetosphere is compressed on the dayside to ∼10-15 Earth radii[1] and is dragged on the nightside by the fast solar wind to several 10s Earth radii forming a magnetic tail (or magnetotail) (Kivelson & Russell 1995). Both the compression and elongation can be more extreme depending on the solar wind dynamic pressure (Cowley 2000). This boundary between the magnetosphere and IMF is defined as the magnetopause, where the solar wind pressure is in equilibrium with the magnetic pressure. Between the magnetopause and Sun lies the bow shock, ∼3 Earth radii sunward of the magnetopause, where the solar wind meets the magnetosphere and is slowed to sub-sonic speeds, creating a shock wave. This plasma is deflected around the magnetopause due to the frozen-in condition, preventing the two magnetised plasmas mixing. This region of shocked solar wind plasma is known as the magnetosheath.

[1]Radius of Earth = 6,371 km

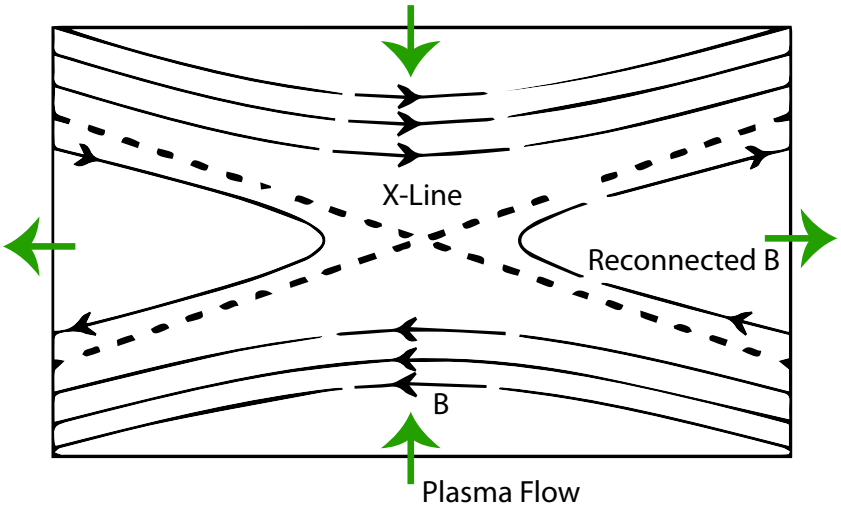

Figure 1.5. Schematic of magnetic reconnection between field lines. The black lines are magnetic field lines, with arrows signifying their orientation. The dashed lines indicate two magnetic field lines in the process of reconnecting. The green arrows show plasma flow.

However, the solar wind is not always deflected around the magnetosphere. If the IMF is southward ($B_z < 0$), and therefore anti-parallel to the Earth's northward field ($B_z > 0$), a process called magnetic reconnection can occur, injecting solar wind plasma into the magnetosphere-ionosphere-thermosphere system along recently opened geomagnetic field lines in the polar cusps. In detail, as the IMF and Earth's magnetic field plasma regions, with their respective frozen-in opposing fields, collide, a current sheet forms between them. The current sheet is of the order of the gyroradius, breaking down the frozen-in assumption of the field. As the plasmas accelerate towards the sheet, the separate magnetic fields can reconnect forming an 'X-shaped' region with two plasma outflows towards and away from Earth due to magnetic tension, and a 'separatrix' region separating the inflow of plasma from these outflows. This is demonstrated in Figure 1.5. Several magnetic field lines can reconnect at the same location.

Figure 1.6 shows a diagram of magnetic reconnection at Earth's magnetosphere in numbered stages, with an insert showing the locations of the geomagnetic field line footprints and corresponding convection in the polar region (Kivelson & Russell 1995). The Dungey cycle is driven by IMF orientation and solar wind speed, density and pressure (see for example, Cowley et al. (2003)) and strengthens ionospheric convection (Morley & Lockwood 2006). Referring to Figure 1.6, southward IMF B_z at [1'] interacts with the

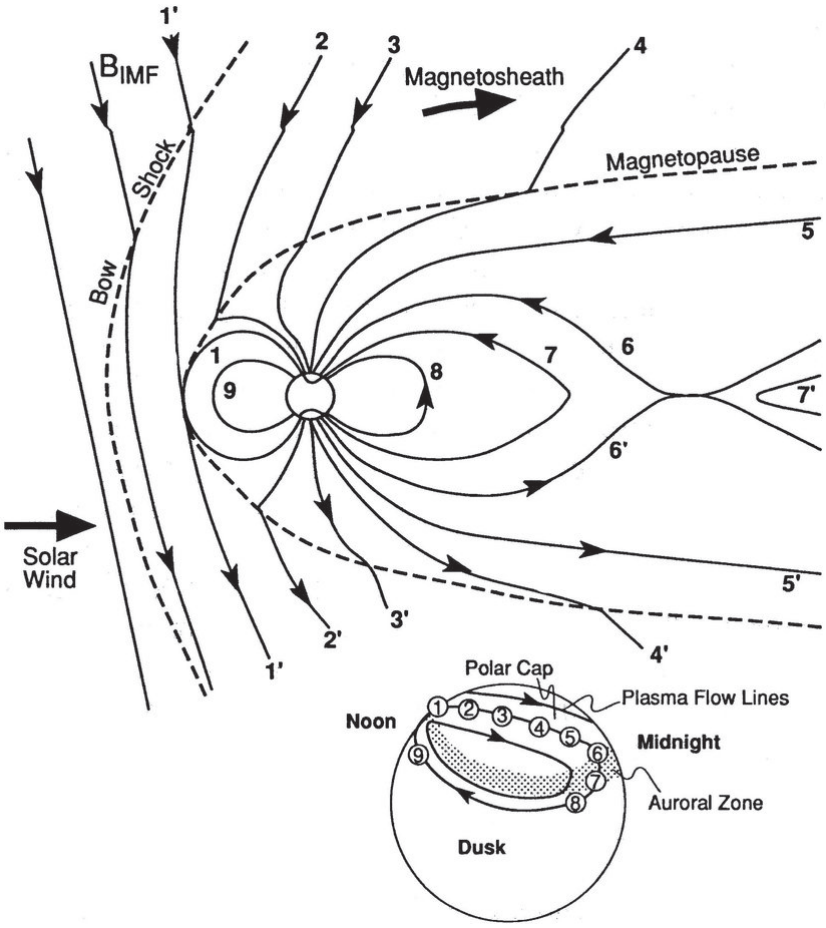

Figure 1.6. Schematic of magnetic reconnection at Earth for southward IMF B_z, from Kivelson & Russell (1995). The insert details the magnetic footprints of the numbered field lines in the polar region.

northward dayside magnetic field of Earth at [1], which due to the opposite polarity reconnect, 'opening' the Earth's magnetic field and allowing the solar wind via the IMF to couple to the magnetosphere and upper atmosphere (Dungey 1961; Vasyliunas et al. 1982; Cowley et al. 2003). This open field line is then pulled back across the polar cap to the nightside due to magnetic contraction, with the IMF component following due to the solar wind forcing the field lines inward, shown by [2-5] in the northern hemisphere and [2'-5'] in the southern hemisphere. On the nightside, magnetic reconnection occurs at the tail [6, 6'], closing the field lines [7] and leading to an ejection of plasma (or 'plasmoid') away from the Earth [7'] and inward release of energy stored in the tail into the magnetosphere, the latter initiating substorms (Milan et al. 2003, 2007; Angelopoulos et al. 2008). The nightside field lines then reach lower latitudes [8], a result of the newly closed field lines moving from the poleward boundary of the auroral oval (where they have reconnected)

through the auroral oval towards the equatorward boundary. The auroral oval itself expands equatorward if dayside reconnection is ongoing at a rate that is larger than the nightside rate (Burch 1973, 1979). The field lines then finally return to the dayside [9] as the magnetosphere redistributes the magnetic flux to balance the solar wind pressure and magnetic pressure of the magnetosphere. These closed field lines [1, 7, 8, 9] have their magnetic footprints in the auroral oval, whilst the open field lines [2-5, 2'-5'] have their magnetic footprints in the polar cap region. This entire process is the Dungey cycle. This causes an 'active' (as opposed to 'quiet') ionosphere-thermosphere system. In extreme conditions, such as a CME forcing prolonged southward IMF B_z, this can lead to a geomagnetic storm and substorm (see Section 1.4.7), two of the most significant space weather events at Earth.

There are several plasma populations in the magnetosphere, as detailed in Figure 1.4, including the plasma mantle, plasmasphere, plasma sheet, magnetotail lobes (northern and southern) and radiation or Van Allen belts. When the IMF reconnects to the Earth's magnetic field, plasma travels towards the Earth and down the field lines. If this plasma does not enter the loss cone, the charged particles bounce backward due to magnetic mirroring, returning along the field lines. These field lines have since moved across the polar cap, thus the plasma is convected to the nightside to a confined region known as the plasma mantle, until tail reconnection forces the plasma towards Earth, which then undergoes an $\mathbf{E} \times \mathbf{B}$ drift. This drift leads to collisions, heating the plasma and causing a hot plasma sheet to form in the equatorial magnetotail. This plasma sheet flows sunward, and also separates the northern and southern magnetotail lobes.

The magnetotail lobes are connected to the polar caps, and are comprised of upflowing plasma from the Earth's upper atmosphere; the plasma density is therefore very low, typically 10^{-2} cm^{-3}. The plasmasphere is confined to 5 Earth radii (Kivelson & Russell 1995), and consists of any higher energy populations upflowing from the Earth's upper atmosphere. This plasma follows the co-rotation of the Earth, driving the plasma eastward. The final plasma population in the magnetosphere lies in two toroidal radiation belts: an inner belt 0.2-2 Earth radii and an outer belt between ∼3-10 Earth radii (Kivelson & Russell 1995). These belts consist of ions and electrons confined by the Earth's magnetic field, with the inner belt primarily made up of high energy (∼50 MeV) protons and the outer belt mostly consisting of high energy (∼10 MeV) electrons. The density of the belts is very changeable due to interactions with the upper atmosphere at the mirroring sites

as well as the influence of the solar wind (for example, when compressed).

1.3.2 Magnetospheric Currents

In Figure 1.4, we saw several current systems in the magnetosphere (shown in red), namely, the magnetopause currents, cross-tail current sheet, ring current and field-aligned currents. These current systems are due to particle motions and are therefore dynamic, connecting various parts of the magnetosphere. We briefly outline the first three current systems in this section, with field-aligned currents discussed in the following section.

Magnetopause Currents

The magnetopause defines the magnetosphere boundary. Magnetopause currents (also known as Chapman-Ferraro currents (Kivelson & Russell 1995)) arise in a closed magnetosphere. We can infer their existence by considering the incoming solar wind particles and their interaction with the Earth's magnetic field. As the particles approach the magnetic field, assuming a perpendicular flow, the resultant Lorentz force (see Equation 1.1) moves a proton (electron) eastwards (westwards) and then backwards away from the field. This difference in direction for protons and electrons when at the magnetic field produces a net flow giving rise to the magnetopause current. The resultant force when integrating the magnetopause currents over their area balances the solar wind pressure.

Cross-Tail Current Sheet

The cross-tail current sheet is a dawn-dusk current in the equatorial tail (Hughes 1995) and lies between the northern and southern magnetotail lobes. It is induced by the opposing magnetic field directions in the lobes, poleward and tailward respectively. The tail current can be calculated from the curl of the magnetic field and Ampère's law (see Equation 1.2).

Ring Current

In the inner magnetosphere, charged particles trapped in the Earth's magnetic field in the radiation belts can both gyrate and bounce along the magnetic field, but they can also experience a curvature drift (see Equation 1.12) perpendicular to the magnetic field, where positively charged particles move westwards and negatively charged particles drift eastwards, and a gradient drift (see Equation 1.16) due to a charged particle experiencing an increased magnetic field during its gyromotion. This net motion establishes a ring

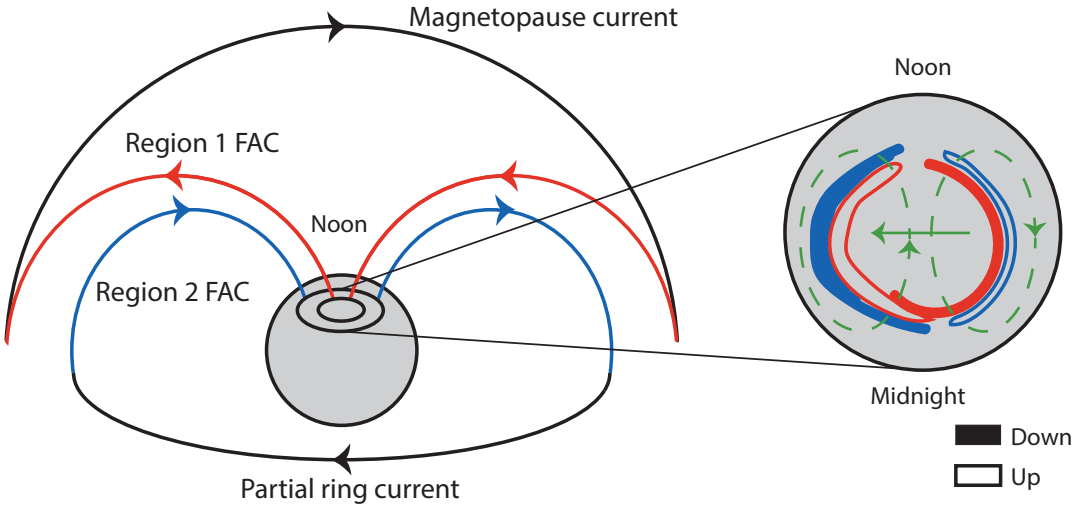

Figure 1.7. Illustration of Region 1 (red) and 2 (blue) FACs adapted from Cowley (2000) and Iijima & Potemra (1976) viewed from the tail for the northern hemisphere. The insert details a topside view of Region 1 (red) and 2 (blue) FACs and ionospheric Pedersen and Hall currents (in green), which are discussed in Section 1.4.4.

current around the Earth at 3-5 Earth radii (Kivelson & Russell 1995). It arises from the large gradient of the magnetic field nearer to Earth. Increasing the particle population in the inner magnetosphere, such as during a geomagnetic storm (see Section 1.4.7), increases the magnitude of the current and expands the magnetosphere.

A partial ring current can also form on the nightside. Here, the cross-tail current sheet flowing duskwards on the nightside produces an $\mathbf{E}\times\mathbf{B}$ drift forcing the ring current plasma sunward. This plasma build up leads to a further drift, with positively charged particles drawn to dusk and negatively charged particles drawn to dawn. This requires a closure current, known as a Region 2 field-aligned current (described in the next section), which establishes an electric field opposite to the convection.

1.3.3 Field-Aligned Currents

Field-aligned currents or Birkeland currents (FACs) allow the closure of ionospheric currents (see for example: Iijima (2013); Cowley (2000) and references therein). They are categorised into two types: Region 1 FACs that close in the tail current and Region 2 FACs that close in the ring current (as shown in Figure 1.4). Initially the system is driven by magnetopause currents induced by the IMF or solar wind, as explained previously, which then close via the magnetotail and return as magnetopause currents or flow along

geomagnetic field lines as poleward Region 1 FAC sheets. These Region 1 FACs flow into the ionosphere in the dawn sector, induce a Pedersen current (see Section 1.4.4), and flow outward in the dusk sector. Region 1 FACs can be explained by considering their location near the open/closed field line boundary (OCB) where, due to Alfvén's Theorem and Ampère's law, the shear between the dipolarised open field lines and closed field lines leads to a current sheet. Equatorward Region 2 FACs then arise from the formation of a partial ring current, flowing into the dusk sector and out of the dawn sector (see for example, Cowley (2000)). Figure 1.7 shows an illustration of Region 1 and 2 FACs.

FACs that flow upwards are tied to electron motion down the field line (and vice versa); this is a strong current due to the electron populations in the tail current (see for example, Ohtani et al. (2009) and references therein). Naturally if electron populations reduce so too does the FAC magnitude. FACs have widths of ∼1,000s km, which depend on geomagnetic activity (Iijima & Potemra 1976), and amplitudes of at least 0.1 μA m^{-2} (Peria et al. 2013), which can increase by two orders of magnitude during a geomagnetic storm (Adhikari et al. 2017). FACs carry Poynting flux, that is, electromagnetic energy, into the ionosphere where the Poynting flux vector, $\mathbf{S}$, is equal to:

$$\mathbf{S} = \frac{\mathbf{E} \times \mathbf{B}}{\mu_0} \tag{1.18}$$

allowing electromagnetic energy to dissipate via ionospheric electric fields (see Section 1.4.4). Poynting's theorem is the associated conservation of energy for the electromagnetic field, such that:

$$\frac{\partial W}{\partial t} + \nabla \cdot \mathbf{S} + \mathbf{j} \cdot \mathbf{E} = 0 \tag{1.19}$$

where the first term is the rate of change of the electromagnetic energy density where $W = (B^2/2\mu_0) + (\epsilon_0 E^2/2)$, the second term is the divergence of the Poynting flux vector and the third term describes the conversion of electromagnetic energy (Thayer & Semeter 2004), for example, into Joule heating (see Section 1.4.5).

1.4 The Ionosphere-Thermosphere System

The Earth's atmosphere is comprised of several layers, each defined by temperature gradients through the region caused by different energy sources. These are, from the ground upwards: the troposphere (ground-12 km), stratosphere (12-45 km), mesosphere (∼45-85

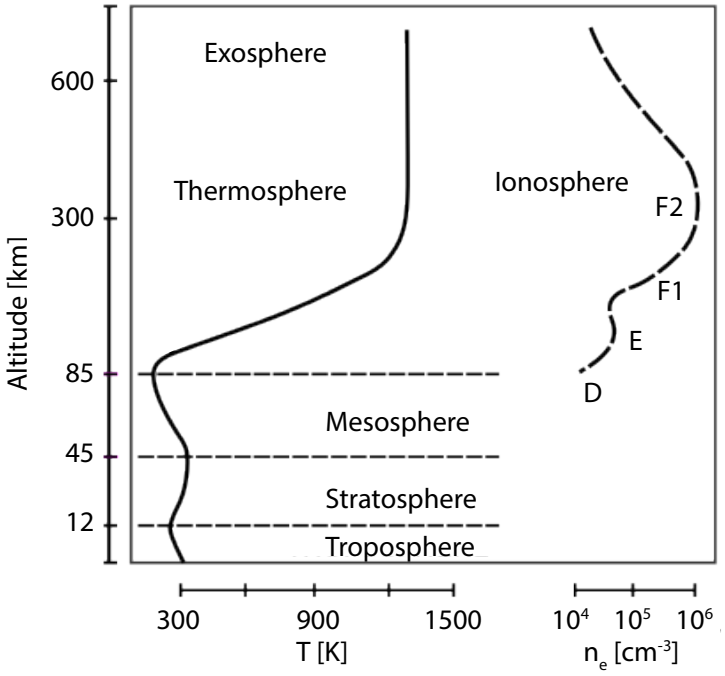

Figure 1.8. Temperature and electron density with altitude. The layers of the atmosphere and ionosphere are also labelled. Adapted from Rishbeth & Garriott (1969).

km), thermosphere (85-∼500 km) and exosphere (500 km +) (Rishbeth & Garriott 1969). Between these layers are their 'pauses', the boundaries defining constant temperature. From the mesosphere upwards, a region of ionised plasma between ∼50km to exospheric heights defines the ionosphere. The ionosphere is categorised into D, E and F (sub-divided into F1 and F2) regions, also defined by their energy sources and peaks in electron density. Figure 1.8 shows these respective neutral layers and their temperature with altitude (Rishbeth & Garriott 1969), as well as the various ionospheric layers and their electron density with altitude.

In this section we begin by discussing each layer and introducing the main equations that govern the neutral atmosphere. We then focus on the ionosphere and its respective currents. Finally we detail the three subject areas discussed in this thesis where FACs play a significant role: Joule heating, polar neutral winds, and ground geomagnetic disturbances. We describe an ionosphere-thermosphere system due to the coupled nature of the regions, where ions influence neutral motion, composition and density and vice versa (see for example, Thayer et al. (1995)). The fundamental physics included in this section is based on Rishbeth & Garriott (1969).

1.4.1 The Neutral Atmosphere

As mentioned above, the layers of the neutral atmosphere are divided by their temperature gradients, shown in Figure 1.8. The troposphere absorbs infrared (IR) radiation (via water vapour, CO_2 etc) and is characterised by temperature decreasing with height due to its reliance on radiative transfer from the ground. The stratosphere comprises a temperature increase due to the presence of ozone-absorbing UV radiation. The mesosphere encompasses a temperature decrease, dropping to the coldest temperature ($\sim$180 K) in the atmosphere, where heat conducted downwards from the thermosphere is convected to lower altitudes or radiated by IR and visible airglow. The thermosphere, a focus of this thesis, absorbs extreme UV (EUV) and is therefore the hottest region of the atmosphere. In the lower thermosphere heat is conducted downward, however in the upper thermosphere the heat conductivity is sufficient to produce an isotherm between 1,000-2,000 K depending on solar activity, to which it is strongly dependent. Above this is the exosphere, where the lack of collisions leads to ballistic trajectories dominated by gravity.

In the thermosphere there is a heat balance between production, loss and transport. Main heat sources include the absorption of EUV and X-rays, which ionise the atmosphere and therefore heat it, the absorption of precipitating charged particles, the dissipation of atmospheric waves and tides and the dissipation of Poynting flux via ionospheric currents (see Section 1.4.5). Heat is lost in the system due to radiation in non-opaque wavelengths such as visible and IR 630 nm atomic oxygen emission. Heat is further transported by conduction, eddies (<100 km), neutral winds (see Section 1.4.6) and ionised and dissociated gas transport.

Adiabatic temperature changes are due to variations in pressure; as pressure decreases with increasing altitude, so too does temperature. The dry adiabatic lapse rate, Γ, describes this relationship:

$$\Gamma = -\frac{dT}{dz} = \frac{g}{c_p} \tag{1.20}$$

which can be calculated using Equations 1.23 and 1.26. When Γ is non-zero the density of the atmosphere approximately decreases exponentially with increasing altitude, which describes the non-isotherm region of the atmosphere. This leads to >90% of the atmospheric mass confined to the troposphere. In the upper thermosphere, atomic oxygen dominates (see Figure 1.10) thus density is influenced by the amount of EUV radiation, with a minimum occurring in summer due to the increased ionisation. Below the turbopause ($\sim$100

km) the composition is dominated by N_2 (∼80%) and O_2 (∼20%), and is well-mixed by a process known as turbulent mixing. Above the turbopause molecular mixing occurs, with transport between molecules, this leads to diffusive separation where molecular weight controls the altitude of the constituent.

Fundamental Equations of the Neutral Atmosphere

Atmospheric gases are assumed to be ideal, where an ideal gas comprises many molecules moving randomly, whose volumes are negligible compared to the total volume of the gas, with no forces acting on the molecules except during elastic collisions. An ideal gas should therefore obey Newton's laws of motion, and follows the ideal gas law:

$$P = \frac{RT}{M}\rho = gH\rho \tag{1.21}$$

where P is the pressure, T is the gas temperature, ρ is the density of air, M is the mean molecular mass of the gas, R is the universal gas constant, g is the acceleration due to gravity and H is the scale height, where:

$$H = \frac{RT}{Mg} \tag{1.22}$$

Their distribution with height is governed by hydrostatic equilibrium, where the gravity acting on air is balanced by the pressure gradient it experiences:

$$\frac{dP}{dz} = -g\rho \tag{1.23}$$

where z is the height at pressure P and ρ is the density of air. Inserting Equation 1.21 into Equation 1.23 and integrating, where $dz = dh/H$, shows pressure decreasing exponentially with altitude:

$$P = P_0 \exp^{-\frac{z-z_0}{H}} \tag{1.24}$$

Atmospheric gases are also assumed to follow three fundamental conservation laws: continuity, momentum and energy. The continuity equation arises from conservation of mass:

$$\frac{\partial\rho}{\partial t} = -\nabla \cdot \mathbf{V} \tag{1.25}$$

The momentum equation describes the motion of neutral air; see Equation 1.27 in Section

1.4.2. The energy equation is based on the first law of thermodynamics, where a change in the internal energy of a system equals the energy crossing the boundary of the system such that:

$$C_p \frac{dT}{dt} = \frac{1}{\rho} \frac{dP}{dt} + Q \tag{1.26}$$

where C_p is the specific heat capacity at constant pressure and Q is the net heat change. This is applied to the atmosphere by summing the kinetic, internal and geopotential energies.

1.4.2 Dynamics of the Neutral Atmosphere

In this section we discuss the main neutral dynamics in the ionosphere-thermosphere system; these are tides due to the Sun and Moon, turbulence (discussed previously), gravity waves and neutral winds driven by pressure gradients, the latter due to temperature differences from, for example, solar radiation.

Global tidal oscillations are a result of solar and lunar tidal forces due to solar heating and the gravitational pull of the Moon respectively, both with periods of ∼24 hours. The Moon primarily causes ocean tides, whilst the Sun is predominantly responsible for atmospheric tides. Tides give rise to periodic fluctuations in neutral wind, density, temperature and pressure. They lead to a solar diurnal (24 hours) and semi-diurnal (12 hours) variations, and a lunar semi-diurnal variation (∼12 hours). Solar heating of the lower atmosphere can also lead to propagating tides in the upper atmosphere, a form of gravity wave.

Gravity waves have smaller periods than tides, on the scale of minutes to hours, with wavelengths reaching 1,000s km horizontally and <10 km vertically. They are generated when gravity acts as a restoring force in a fluid or at an interface to enforce equilibrium. They can be created by the dissipation of tides in the upper atmosphere and by winds (for example, wind shears or surface interaction such as when a wind flows over a mountain) in the lower atmosphere; the latter is more common. As their amplitude varies exponentially with altitude, they become unstable and dissipate their energy and momentum. They often break at the turbopause where molecular diffusion begins to dominate over turbulent diffusion, and viscosity is greater, particularly if they are small-scale waves. Above this altitude gravity waves break due to ion drag, that is, the drag between colliding ions and neutrals.

Neutral thermospheric winds are predominantly driven by solar heating induced pressure gradients. As the Earth rotates the flow experiences a Coriolis force, producing a clockwise motion in the northern hemisphere and an anti-clockwise motion in the southern hemisphere. The winds are further modulated by tides, the large viscosity of the upper atmosphere and ion drag. Based on this understanding we can write an approximate equation for the motion of neutral air (Rishbeth & Garriott 1969):

$$\frac{dV_n}{dt} + 2\boldsymbol{\Omega} \times \mathbf{V_n} = \mathbf{g} - \frac{1}{\rho}\nabla P - \nabla\Psi + \frac{\mu_m}{\rho}\nabla^2\mathbf{V_n} - \nu_{ni}(\mathbf{V_n} - \mathbf{V_i}) \tag{1.27}$$

where $2\boldsymbol{\Omega}\times\mathbf{V_n}$ is the effect from Coriolis acceleration and $\boldsymbol{\Omega}$ is the Earth's angular velocity, $\mathbf{g}$ is gravitational acceleration, ∇P is the solar heating induced pressure gradient and $\nabla\Psi$ represents the tidal forces, with Ψ equal to a scalar potential. The penultimate term describes viscous effects removing wind shears, where μ_m is the molecular viscosity, and the final term is the effect from ion drag, where $\mathbf{V_i}$ is the ion drift and ν_{ni} is the frequency of ion collisions with the neutrals. In the mesosphere, the pressure gradient force balances the Coriolis force and so motion is dominated by the pressure gradient from UV heating; this is known as geostrophic balance. This leads to zonal mesospheric jets. In winter a northern hemisphere westward jet and a southern hemisphere eastward jet are formed, with the direction reversing in summer. Mesospheric winds are on average $\sim$100 m s^{-1}.

In the thermosphere these forces do not balance, with winds reaching several 100s m s^{-1}. The solar heating experienced during the day leads to a post-noon diurnal bulge at low latitudes, which drives a large pressure gradient away from the maximum heating around 14 UT[2], known as the diurnal tide. At high latitudes this is realised as an anti-sunward flow (see Section 1.4.6). The viscosity of the upper atmosphere also plays a greater role in modulating the wind compared to the lower atmosphere due to its dependence on density. We devote a separate section (Section 1.4.6) to thermospheric neutral winds in the polar region.

1.4.3 The Ionosphere

The ionosphere is the region of the atmosphere where X-rays and EUV radiation (and cosmic rays to a lesser extent) ionise and heat the neutral atmosphere, forming a charged layer comprised of ions and electrons as well as neutrals. Figure 1.9 shows the day and night

[2]Universal Time

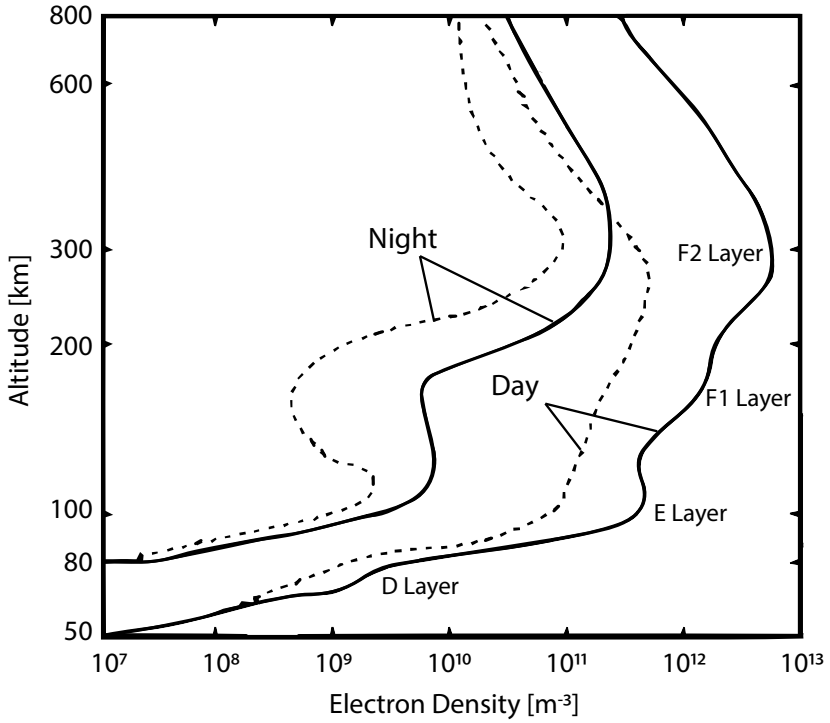

Figure 1.9. Electron density with altitude for day and night (labelled) during solar maximum (solid line) and solar minimum (dashed line). The layers of the ionosphere are also labelled. Adapted from Rishbeth & Garriott (1969).

electron density profiles during solar minimum and maximum, with labelled ionospheric regions. Both the heights and the amount of ionisation vary strongly with solar activity, as well as seasonally, daily and latitudinally. Figure 1.10 shows the ion number density and neutral air density of the atmospheric constituents in the upper D, E and F regions with respect to altitude.

The D region (∼60-90 km) is the lowest part of the ionosphere. During quiet activity it is only present during the daytime due to photoionisation by solar radiation. However, it can be populated by energetic particles from the radiation belts and solar wind, which can precipitate into the polar regions at any time. Its main source of ionisation is Lyman α radiation emitted from the Sun and absorbed by NO, and solar hard X-rays absorbed by O_2. Typical electron densities in the region range from 10^9-10^{10} m^{-3} in the day. Figure 1.9 shows the region is mostly independent of solar cycle.

The E region (∼90-140 km) is primarily ionised by soft X-rays, with EUV also contributing, producing O_2^+, N_2^+ and NO^+ ions (Johnson 1969). This has a strong dependence on solar activity. The E region is substantially less dense than the D region, therefore the

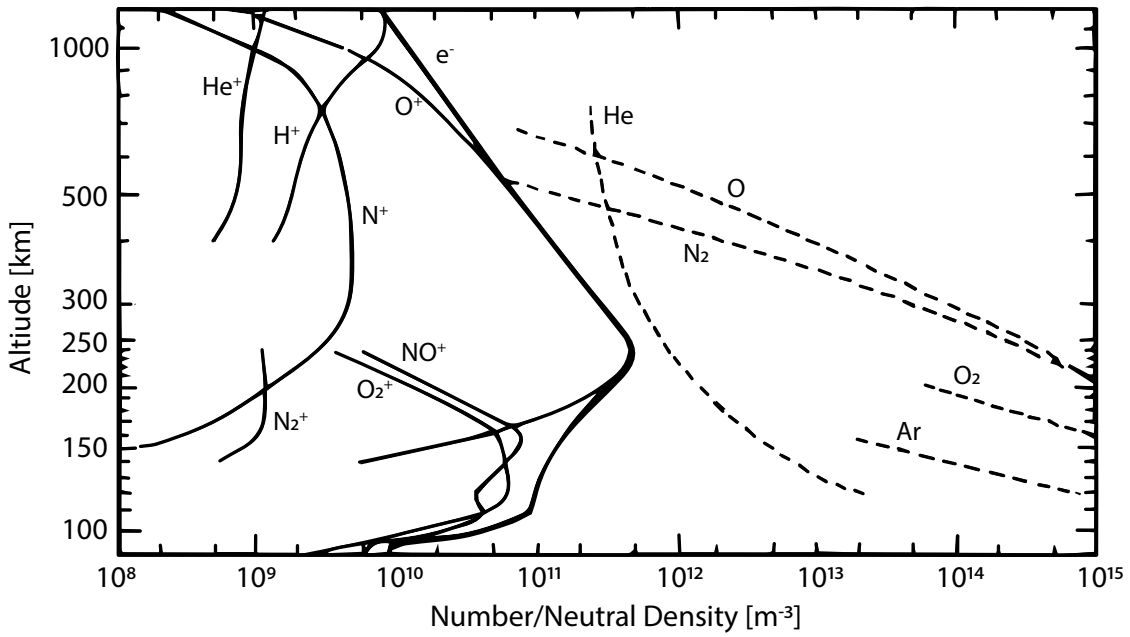

Figure 1.10. Ion number density and neutral air density of the atmospheric constituents in the upper D, E and F regions with respect to altitude. Adapted from Johnson (1969).

collisional recombination of ions and electrons is a slow process. Electron densities in the region peak between 10^9-10^{12} m^{-3} at ∼120 km, depending on the time of day and solar activity (see Figure 1.9). It is utilised in radio communications as it reflects medium-frequency radio waves due to its high electron density.

The F region (∼140-800+ km) is ionised by UV and EUV radiation and encompasses most of the ionosphere, peaking in electron density between $\sim 10^{11}$-10^{13} m^{-3} at 250-300 km (see Figure 1.9). It is significantly influenced by solar activity as the highest part of the ionosphere. At night a significant amount of ionisation remains due to the even more sparse atmosphere, with recombination approximately a quarter to that of the E region. Typically in summer daytime conditions (and more noticeably in solar maximum) it can be divided into two layers by its constituents, the lower F1 (∼150-220 km) region due to a combination of O_2^+, NO^+ and O^+, and the higher F2 (∼220-800 km) region due to the dominance of atomic oxygen and therefore O^+ ions (Johnson 1969), the location of both labelled in Figure 1.9. It is responsible for the red line atomic oxygen aurora, and is used in high-frequency radio communications. However, when the E region is most enhanced, due to strong absorption, resultant reflections can cause a high-frequency radio blackout.

1.4.4 Ionospheric Convection and Currents

Plasma circulation within the ionosphere is governed by the Lorentz force (see Equation 1.1), and modulated by collisions between charged particles and neutrals, collisions between ions and electrons, pressure gradient forces and gravity. Due to the presence of an electric field, the bulk of the drifts can be described by the Lorentz force and collisions with neutrals:

$$\begin{aligned} m_i \frac{\mathrm{d}\mathbf{V_i}}{\mathrm{d}t} &= e\mathbf{E} + e\mathbf{V_i} \times \mathbf{B} + m_i \nu_{in}(\mathbf{V_n} - \mathbf{V_i}) \\ m_e \frac{\mathrm{d}\mathbf{V_e}}{\mathrm{d}t} &= -e\mathbf{E} - e\mathbf{V_e} \times \mathbf{B} + m_e \nu_{en}(\mathbf{V_n} - \mathbf{V_e}) \end{aligned} \tag{1.28}$$

where ν_{in} and ν_{en} are the respective ion and electron to neutral collision frequencies and m_i and m_e are the ion and electron single particle masses. If $\mathbf{E}$ is parallel to $\mathbf{B}$, the magnetic field does not influence the charged particle drift, as demonstrated by Equation 1.10. However, if $\mathbf{E}$ is perpendicular to $\mathbf{B}$ and we assume constant electric and magnetic fields, an $\mathbf{E} \times \mathbf{B}$ drift forms as shown in Equation 1.12. Figure 1.11 provides a schematic of the Figure 1.7 Region 1 (red) and 2 (blue) FACs in a polar projection of the northern hemisphere. Figure 1.11 is fixed with respect to the Sun and is shown in magnetic local time (MLT, as described in Chapter 2), with the magnetic field pointing into the figure. We can see that electric fields (shown by orange arrows) are induced by these FACs in the ionosphere. The $\mathbf{E} \times \mathbf{B}$ drift results in twin cell convection of the plasma (shown by the black arrows), with anti-sunward flow across the polar cap and sunward flow at lower latitudes (Cowley & Lockwood 1992; Lockwood & Cowley 1999; Lockwood & Morley 2004).

The drift is irrespective of charge, however due to collisions with neutrals and the collision frequency (and therefore deceleration) of ions being larger than electrons (see Equation 1.28) currents are induced. The current density, $\mathbf{j}$ is equal to:

$$\mathbf{j} = Ne(\mathbf{V_i} - \mathbf{V_e}) \tag{1.29}$$

where N is the electron and ion concentration and e is the charge of an electron. In the F region $\mathbf{j} \approx 0$, as collisions are few and the drifts experienced by ions and electrons are equivalent. In the denser E region, $\mathbf{j} > 0$. Here, a transverse current is induced due to the Lorentz force (Equation 1.1) acting on collided charged particles, which follows the

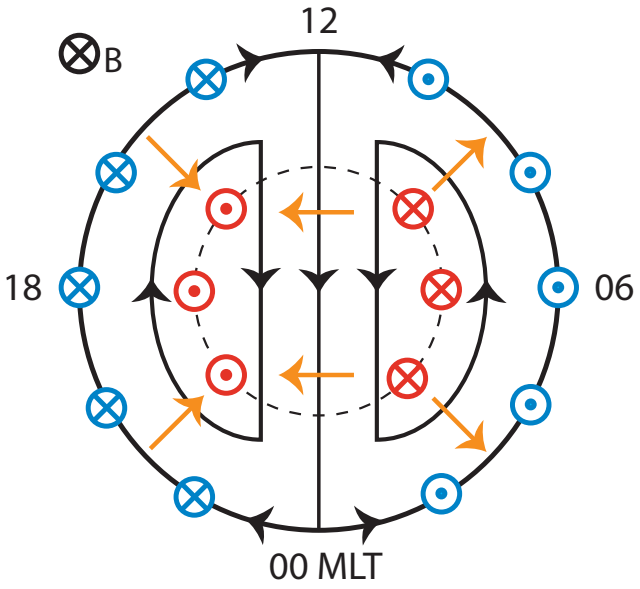

Figure 1.11. Schematic detailing the northern hemisphere Region 1 (red) and Region 2 (blue) FACs with overlaid electric fields (orange) in the ionosphere, adapted from Cowley (2000). Plasma circulation is shown by the black arrows. The dashed line represents the OCB. The time is in MLT (as described in Chapter 2), where 12 MLT is sunward. The magnetic field direction is into the page in the northern hemisphere.

direction of the electric field (orange in Figure 1.11). This is termed the Pedersen current. As the currents are dependent on collisions with neutrals, they are also tied to the neutral density of the atmosphere. The collision frequency is greater than the gyrofrequency below 125 km, so that ions move with the neutral motion. A second ionospheric current therefore arises in the lower E region where electrons $\mathbf{E}\times\mathbf{B}$ drift but ions become immobile (Cowley 2000), forming a loop circuit around the FACs. This is known as the Hall current, and flows in the opposite direction to the plasma circulation in Figure 1.11. The lower latitude dawn and dusk anti-sunward Hall currents are also known as the westward and eastward auroral electrojets respectively. Where these electrojets meet in the evening sector is termed the Harang Discontinuity, due to a region of sharp flow reversal. The total ionospheric current can be found using Equation 1.3:

$$\mathbf{j} = \sigma_P \mathbf{E} + \sigma_H \frac{\mathbf{E}\times\mathbf{B}}{B} \tag{1.30}$$

where σ_P and σ_H are the Pedersen and Hall conductivities. Their distribution with height is dependent on Equation 1.29, and is shown in Figure 1.12, where the Hall conductivity

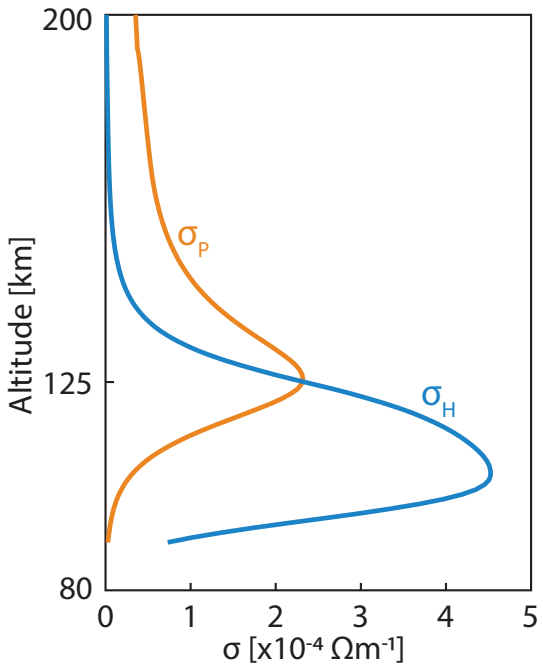

Figure 1.12. Illustration of Pedersen and Hall conductivities with altitude; adapted from Rishbeth & Garriott (1969).

dominates below 125 km and the Pedersen conductivity dominates above 125 km.

As discussed in Section 1.2.2 the dawn-dusk IMF B_y can introduce an asymmetry to the Earth's magnetic field (see Figure 1.3). The resultant magnetic tension in the dawn-dusk line distorts the typical convection pattern of Figure 1.11 about the noon-midnight meridian to produce Figure 1.13 for the cases of positive and negative B_y. Plasma circulation is shown by the solid lines, the OCB is a dashed line and FACs are flowing into and out of the page. When IMF B_y is positive, the dusk cell is larger than the dawn cell and vice versa for negative B_y.

1.4.5 Joule Heating

FACs closing in the ionosphere via Pedersen currents do so where the Pedersen conductivity is greatest, ∼125 km in Figure 1.12. Poynting flux is dissipated in the ionosphere via ion-neutral collisions in a process known as Joule heating (Iijima 2013), the second largest dissipation mechanism of magnetospheric energy after the ring current, and considerably greater than that of particle precipitation (Akasofu 1981; Cierpka et al. 2000). Joule heating is an important process in the ionosphere-thermosphere system, due to its ability to affect temperature, neutral density, electron density and atmospheric composition, all

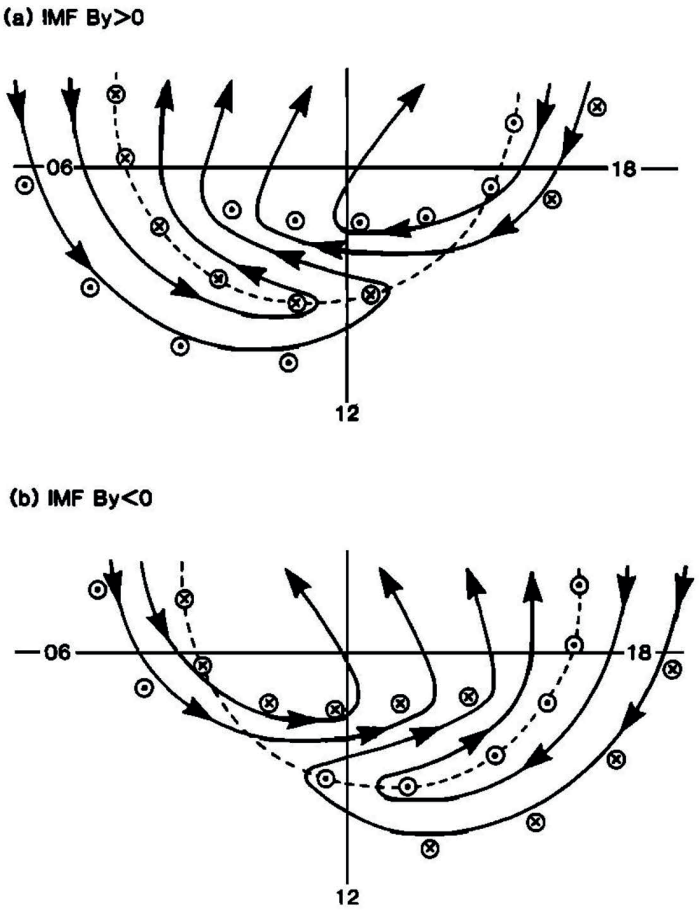

Figure 1.13. Illustration by Cowley et al. (1991) showing the effect of positive (top, a) and negative (bottom, b) B_y on the newly reconnected magnetic field lines at Earth when B_z is negative. Plasma circulation is shown by the solid lines, the OCB is a dashed line and FACs are flowing into and out of the page.

of which can affect satellite drag (Vallado 2001; Storz et al. 2005; Deng & Ridley 2007) (see Chapters 2 and 5 for further detail). Joule heating is also often underestimated in models due to their poor resolution compared to its high spatial and temporal variability (Codrescu et al. 2000; Deng & Ridley 2007).

Joule heating is the local heating rate and occurs when the current is in the direction of the electric field. Using Equation 1.30 to calculate the current density, Joule heating is equal to (in the Earth's frame[3]):

$$\frac{\partial Q_j}{\partial t} = \mathbf{j} \cdot \mathbf{E} = \sigma_P |\mathbf{E}|^2 \tag{1.31}$$

[3]In the plasma frame: $\mathbf{E}' = \mathbf{E} + \mathbf{V}_n \times \mathbf{B}$

Hall currents do not contribute to Joule heating as the current flow is perpendicular to the electric field (see Equation 1.31), thus they cannot dissipate energy. Joule heating can also be described in terms of collisions (i.e. frictional heating), with reference to Equation 1.27 (Thayer & Semeter 2004):

$$\frac{\partial Q_j}{\partial t} = \sum_i n_i m_i \nu_{in} (\mathbf{V}_i - \mathbf{V}_n)^2 \tag{1.32}$$

where the energy transfer between ions and neutrals, from kinetic to thermal, is equal to (Thayer & Semeter 2004):

$$\frac{\delta E_i}{\delta t} = \sum_n \frac{n_i m_i \nu_{ni}}{m_i + m_n} \left\{ 3k_B(T_n - T_i) + m_n(V_i - V_n)^2 \right\} \tag{1.33}$$

This is known as the ion-energy equation (for the neutral-energy equation interchange the subscripts), where the first term is the heat exchange between ions and neutrals and the second term is the frictional heating due to their different velocities. This can be simplified further by assuming the two terms equate, which has been shown to be a good approximation in the F region (St.-Maurice & Hanson 1982) and is discussed in Chapter 4. Joule heating can also be affected by precipitation that reaches the upper atmosphere. This causes ionisation, which in turn changes the conductivity of the ionosphere (see Figure 1.12) and therefore the altitudinal distribution of Joule heating. This is discussed in detail in Chapter 5.

1.4.6 Polar Thermospheric Winds

Polar thermospheric winds describe the neutral winds in the high-latitude region, typically between 60-90° magnetic latitude. These winds facilitate energy re-distribution in the ionosphere-thermosphere system (see for example, Dhadly et al. (2017*b*) and references therein). They are therefore greatly influenced by solar activity, IMF orientation and geomagnetic activity (see for example, Morley & Lockwood (2006); Dhadly et al. (2017*b*) and references therein). In this section we discuss the distinguishing features of polar thermospheric winds (see for example: Killeen et al. (1982); Lühr et al. (2007); Förster et al. (2008); Emmert et al. (2006*b*); Dhadly et al. (2017*a*,*b*) and references therein), which are also described in further detail in Chapter 4.

Solar heating induced pressure gradients dominate the neutral circulation, producing

an anti-sunward flow across the polar cap (discussed in Section 1.4.2). There are two convection cells on the dawnside (6 MLT, anti-clockwise) and duskside (18 MLT, clockwise) respectively located in the auroral oval region between 60-80° magnetic latitude as demonstrated in Figure 1.14. These cells arise due to the rotation of the Earth, where the Coriolis force acts perpendicular to the spin axis and the anti-sunward flow (see Equation 1.27). This rotation also causes a centrifugal force to act radially outward from the spin axis. On the duskside the Coriolis force and centrifugal force act in the same direction to reinforce the flow, whereas on the dawnside the forces act in opposing directions to reduce the flow (Fuller-Rowell & Rees 1984).

Polar thermospheric winds can be modulated by the $\mathbf{E} \times \mathbf{B}$ ion drift due to ion-neutral collisions and particle precipitation (see for example: Cierpka et al. (2000); Morley & Lockwood (2006); Kwak & Richmond (2007) and references therein). At low geomagnetic activity, solar heating induced pressure gradients dominate over the ion-neutral coupling. During higher geomagnetic activity the increased momentum that ions transfer to neutrals via collisions can divert the winds (Aruliah & Griffin 2001). This evidence of coupling can remain long after the increased activity due to the inertia of the neutral atmosphere, known as the flywheel effect (Lyons et al. 1985; Odom et al. 1997).

Figure 1.14 shows northern hemisphere modelled horizontal neutral winds for quiet conditions (top), from Dhadly et al. (2017*a*), and active conditions (bottom), from Dhadly et al. (2017*b*), during equinox and the June and December solstices. Referring to the quiet conditions in Figure 1.14 (top), we can see a weaker dawn cell and stronger dusk cell during all seasons. During the summer solstice the winds are strongest, driven by solar heating, with the duskside cell most apparent. Referring to the active conditions in Figure 1.14 (bottom), we can see the increased ion population has reinforced the anti-cyclonic dusk cell due to increased ion drag. The cross-cap winds are also magnified as the anti-sunward winds are in the same direction as the ion drifts.

A final feature of note is the stagnation at the cusp (located between 72-76° and centred on 12 MLT (Newell et al. 1989)), observable in Figure 1.14 during quiet and active conditions (also seen in, for example, Förster et al. (2008)). This is discussed further in Chapter 4, and explained by vertical winds in Chapter 5. Due to hydrostatic equilibrium (see Equation 1.23), vertical winds are comparatively weaker than horizontal winds, typically $<$10 m s^{-1}. However, they are vital in distributing energy between the layers of the atmosphere, and can affect the horizontal wind pattern by causing divergent

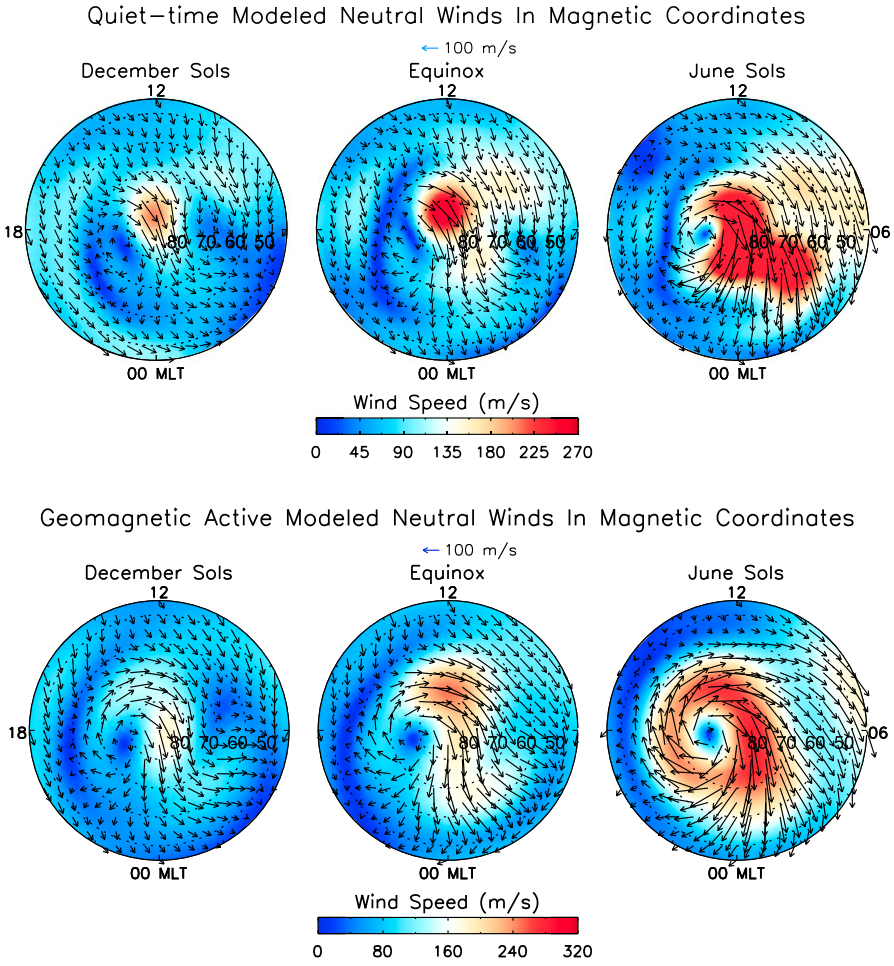

Figure 1.14. Northern hemisphere modelled horizontal neutral winds for quiet conditions, from Dhadly et al. (2017*a*), and active conditions, from Dhadly et al. (2017*b*), during equinox and the June and December solstices. These plots are in MLT, where the Sun is located at 12 MLT (see Chapter 2 for more detail).

flow. They are predominantly caused by the expansion of the atmosphere when heated.

1.4.7 Geomagnetic Disturbances

In this section we describe three effects of active geomagnetic conditions as described in Section 1.3.1; these are geomagnetic storms, substorms and ground geomagnetic disturbances (as studied in Chapter 3). These three effects arise from extreme conditions in the ionosphere-thermosphere system, and are the most destructive examples of space weather. However, it should also be noted that quiet-time conditions (seen in Chapters 4 and 5) still affect and degrade space-borne infrastructure.

Geomagnetic Storms and Substorms

As discussed previously in Section 1.3.1, reconnection at the tail completes the Dungey cycle. However, if the rate of dayside reconnection is greater than the nightside, open flux loading can lead to a huge release of energy, known as a substorm, when the nightside finally reconnects (McPherron et al. 1973; Cowley et al. 2003; Milan et al. 2003, 2007). Here, dayside loading gives rise to the 'growth' phase of the substorm, whilst unbalanced nightside loading is tied to its 'expansion' phase, the latter referring to an expansion of the poleward edge of the auroral oval. It should be noted that their exact cause is still unknown (see for example, Sergeev et al. (2012)). During a substorm the cross-tail current is disturbed and effectively short-circuited by FACs and the westward electrojet, forming a substorm current wedge (SCW) (see for example, McPherron et al. (1973)). Substorms can continue for several hours, mainly affecting high latitudes. They occur relatively close to the Earth, beginning on closed field lines in the inner magnetosphere.

When their duration is prolonged (over several hours), enough energy can dissipate into the ionosphere-thermosphere system to cause a geomagnetic storm, resulting in a global geomagnetic disturbance. A geomagnetic storm can be likened to a very large substorm growth phase, where an initial injection of plasma into the ring current (due to, for example, the interaction between a CME and the magnetosphere) causes an enhancement of the ring current, stabilising the magnetotail to reconnection, which in turn leads to a prolonged interval of unbalanced dayside reconnection and subsequent polar cap equatorward expansion (see for example, Milan et al. (2009)). When these substorms ultimately do release this stored energy they are intense events, and occur at lower (more populated) latitudes.

The Disturbance Storm Time (Dst) index is a proxy for the magnitude of a geomagnetic storm as it relates to the size of the ring current established, which increases with increased activity. The index is calculated using several low latitude ground magnetometers to measure the resulting deviation to the horizontal component of Earth's geomagnetic field, and has a 1-hour resolution. A geomagnetic storm can be described as having three phases: growth, main and recovery. The growth phase describes the reconnection event, the main phase comprises the prolonged decrease in the Dst index and the recovery phase spans the restoration of the geomagnetic field to quiet conditions (this is described in further detail in Chapter 3). The most extreme geomagnetic storms are due to CMEs (see for example,

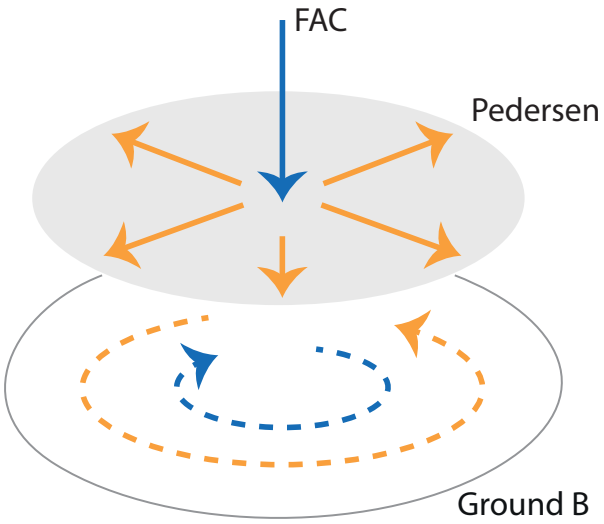

Figure 1.15. Illustration demonstrating Fukushima's theorem. Currents are in solid lines, with both FACs (blue) and Pedersen (orange) currents shown. Dashed lines represent the induced ground magnetic field from each of the currents.

Benacquista et al. (2017)).

Ground Geomagnetic Disturbances

Ground geomagnetic disturbances (GMDs) result from a complex global and magnetospheric current system, and can be driven by several sources such as the ring current, electrojets and Chapman-Ferraro currents on the magnetopause. In this thesis we focus on their generation via FACs. Region 1 and 2 FACs are known to drive ionospheric currents during geomagnetic storms and are believed to be responsible for GMDs (see for example: Kamide (1982); Tamao (1986); Wu & Stening (1991); Laundal et al. (2015); Adhikari et al. (2017)). As the FACs are fed into the ionosphere they close via a Pedersen current and generate a Hall current, which in turn generates ground fluctuations in the magnetic field (see Equation 1.2), inducing what is known as a GMD (Nishida 1964). There are three types of GMDs that are most harmful to infrastructure: magnetic perturbations due to changes in the total magnitude of the geomagnetic field horizontal component, magnetic time variations due to the rate of change of the same component and geoelectric fields due to both spatial and temporal changes and the ground conductivity (Woodroffe et al. 2016). These ground GMDs can affect the national electric grid as well as susceptible infrastructure used in the military, gas, airline and drilling industries (Reay et al. 2005; Vallée et al. 2007; Lloyds 2013; Viljanen et al. 2014).

As FACs flow into the ionosphere a clockwise magnetic field is induced around the field line (demonstrated in Figure 1.15). Conversely as the transverse Pedersen currents flow from the FACs, they induce an anti-clockwise magnetic field. For uniform conductivity and vertical FACs, these induced magnetic fields cancel. This is known as Fukushima's theorem (Fukushima 1976), and is illustrated in Figure 1.15. This is discussed in further detail in Chapter 3.

1.5 Summary

This chapter has described the many mechanisms of the ionosphere-thermosphere system discussed in the latter parts of this thesis. We have provided an overview of this system, and where FACs sit within it as a major facilitator of energy transfer. This thesis focuses on three main effects of FACs, namely, Joule heating, the modulation of polar neutral winds and density and ground geomagnetic disturbances. As FACs enter the ionosphere they induce ionospheric currents and dissipate their energy. This leads to two primary effects: the induction of ground GMDs and, more locally, ionospheric Joule heating. In the cusp region, this latter mechanism causes enough heating at an altitude where extreme upwellings and density enhancements can occur as a result.

In Chapter 2 we focus on the instrumentation, modelling and coordinate systems used in this thesis. In Chapter 3 we study the first of the mentioned effects, ground GMDs, and how they are related to the drivers of FACs and to FACs themselves. In Chapter 4 we move our attention to Joule heating in the northern hemisphere polar region, comparing ground-based instrument, satellite and model data to probe the effect a neutral wind disparity between datasets has on the distribution of wind-derived Joule heating. We then conclude in Chapter 5 by applying the latter mechanism of FAC-driven Joule heating to investigate and model the cause of upwellings and neutral density enhancements in the cusp and nightside auroral oval regions. In Chapter 6 we outline the main conclusions of this thesis.

Chapter 2

Instrumentation, Modelling and Coordinate Transforms

In this chapter we discuss the data sources used in this thesis, namely the Challenging Minisatellite Payload, the UCL Fabry-Pérot Interferometer network and the UCL Coupled Middle Atmosphere and Thermosphere model. We also briefly discuss other secondary data sources used in this thesis. Finally, we summarise the various coordinate frames and transforms needed in the following chapters.

2.1 The CHAllenging Minisatellite Payload

The CHAllenging Minisatellite Payload (CHAMP) was a low Earth orbiting (LEO) German mini-satellite managed by Deutsches GeoForschungsZentrum (GFZ) in Potsdam, Germany, and was operational between 2000-2010. CHAMP was developed to provide high-precision global atmospheric and geophysical data using several instruments, including two fluxgate magnetometers (FGMs) with star sensors, an Overhauser magnetometer (OVM), a digital ion driftmeter and Langmuir probe, an onboard triaxial accelerometer, a laser retro-reflector array and a GPS Precise Orbit Determination (POD) antenna (Reigber et al. 2001). CHAMP's main objectives were to sample the Earth's gravitational field and geomagnetic field for applications in solid Earth, geodesy, oceanography, weather forecasting, climate change and solar-terrestrial science. Figure 2.1 shows a schematic of

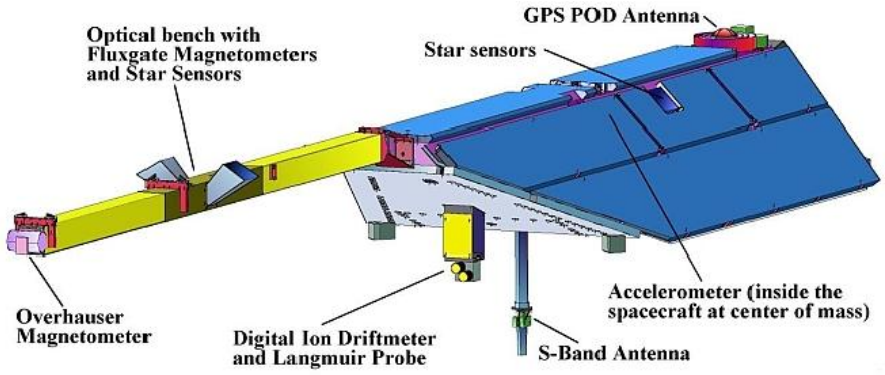

Figure 2.1. Illustration of CHAMP payload adapted from Reigber et al. (2001).

the CHAMP payload.

CHAMP was in a near-polar circular orbit (inclination = 87.3°, mean eccentricity = 0.003) initially at ∼450 km altitude, decaying to ∼320 km in early 2009, and re-entering naturally in 2010. Figure 2.2 outlines several orbits of CHAMP on a global map with underlaid ground magnetometers (in green) included to demonstrate CHAMP's spatial and temporal resolution. In the following sections we first describe the FGMs (Reigber et al. 2002), part of the Magnetometer Instrument Assembly System (MIAS), measuring the Earth's geomagnetic field vector as used in Chapter 3. We then describe the Space Three-axis Accelerometer for Research mission (STAR) monitoring acceleration (Bruinsma et al. 2004) from which the neutral wind and mass density can be inferred (Doornbos et al. 2010), used in Chapters 4 and 5 respectively.

2.1.1 FGM: The Geomagnetic Field

Each MIAS FGM consists of a three-axis orthogonal coil system mounted onto a sphere to measure the 3-D magnetic flux vector (Reigber et al. 2001). In brief, a three-axis FGM consists of a permeable ring core, a drive coil with alternating current to magnetise the core and three orthogonal sensor coils for each vector component. Due to the shape of the core, it has some magnetic field component in and against the direction of any external magnetic field being measured. As the current alternates the parallel magnetic field component of the coil field has a lag compared to the anti-parallel component, and this temporary difference in fields is linked to a feedback loop which cancels the measured field, and whose voltage is directly linked to the magnitude and direction (negative or positive) of the measured field. The two FGMS are separated on a boom to allow for concurrent

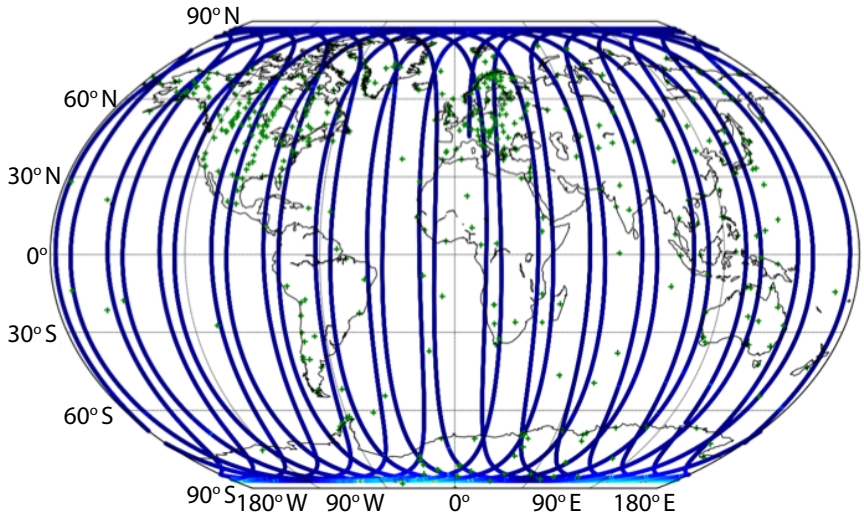

Figure 2.2. Illustration of CHAMP orbit (blue) and SuperMAG stations (green) on a global geographic projection map.

sampling. Star sensors as part of the Advanced Stellar Compass (ASC) are also mounted onto the boom (ASC L1) and body (ASC L2), each consisting of two Camera Head Units (CHU). This aids in the accuracy of the measured vector by providing quaternion attitude measurements to within 2" (Bruinsma et al. 2004). The OVM allows in-flight calibration of the FGMs (see Reigber et al. (2001) for further information on the operation of the FGMs and OVM).

Magnetic field data have a 0.1 nT resolution, a ±65,000 nT measuring range and a sampling rate of 50 Hz (∼150 m resolution) (Reigber et al. 2001), and are available as the processed 1 Hz (averaged to 1 sample per second) calibrated Level 2 data product CH-ME-2-FGM-NEC from the GFZ Information System and Data Center (ISDC)[1]. The data have a ±100 pT deviation from linearity and a <50 pT RMS noise level. We filter the magnetic field data using Quality and Flag metadata to ensure higher accuracy. In the Quality metadata we check the attitude information is accurate by using the following criteria: the first bit of byte 0 of the quality flag indicates magnetic torquer data was available for use in the OVM processing; the ASC L1 (mounted to the boom) CHU1 and CHU2 star sensors of the first two bits of byte 1 show when both star sensor cameras were available; and the third bit of byte 1 confirms the quaternion norm was not flagged. In the Flag metadata we check the ASC L1 star sensor flag bit is below 1, where 0 is the best quality and 6 the poorest; this is the 5th bit. These recommendations were suggested by

[1]Available from: `isdc.gfz-potsdam.de/champ`

GFZ (private communication, Jan Rauberg) and are similar to the Level 3 data description available online[2].

Magnetic field data were provided in Earth-fixed local North-East-Centred (NEC) geographic coordinates, where x is northward, y is eastward and z is pointing towards the Earth's centre of gravity (Lühr et al. 2002). This is analogous to the more commonly known North-East-Down (NED) satellite coordinate system, as described in Cai et al. (2011), and similar to the East-North-Up (ENU) system by a simple re-ordering as shown in Figure 2.8. The NEC coordinate system itself is achieved by first transforming the sensor system to the optical bench system, which is then transformed into the spacecraft frame using Euler angles specified in Lühr et al. (2002); ASC attitude data of the optical bench, as described in Lühr et al. (2002), are then used for the final rotation.

2.1.2 STAR: Neutral Wind and Mass Density

The STAR accelerometer sensor unit consists of a proof mass, with its centre of mass fixed to the centre of mass of CHAMP by six-degree-of-freedom servo-controlled electrostatic suspension, in turn connected to capacitive detectors measuring any movement (Bruinsma et al. 2004). All gravitational forces act on both the sensor and satellite, whilst any non-gravitational forces only affect the satellite, causing the suspended proof mass to move. The resultant capacitance change measured by the detectors is then used to assess the required voltage needed by the servo-rotor to reset the proof mass position, and this voltage is directly related to the acceleration measured and therefore drag (Bruinsma et al. 2004). The accelerometer reference frame is instrument-fixed and aligned with the spacecraft body frame, with any error in alignment corrected with a small rotation as described in Lühr et al. (2002). Figure 2.3 illustrates the spacecraft (top) and acceleration (bottom) reference frames, where *orbit* is the orbit frame, SBF is the spacecraft body frame, $STAR$ is the accelerometer frame and *model* is the drag model frame.

Neutral density is directly proportional to satellite drag and can be found by subtracting the other acceleration contributions due to radiation pressure from the acceleration acting on the satellite, and scaling with density predicted by a model, ρ^{model}, as demonstrated in Bruinsma et al. (2004):

$$\rho^{STAR} = \frac{a_{total}^{STAR} - a_{solar}^{model} - a_{albedo}^{model} - a_{IR}^{model}}{a_{drag}^{model}} \rho^{model} \tag{2.1}$$

[2]See: `ftp://magftp.gfz-potsdam.de/CHAMP/L3_DATA/README-CHAMP-L3_20140818.txt`

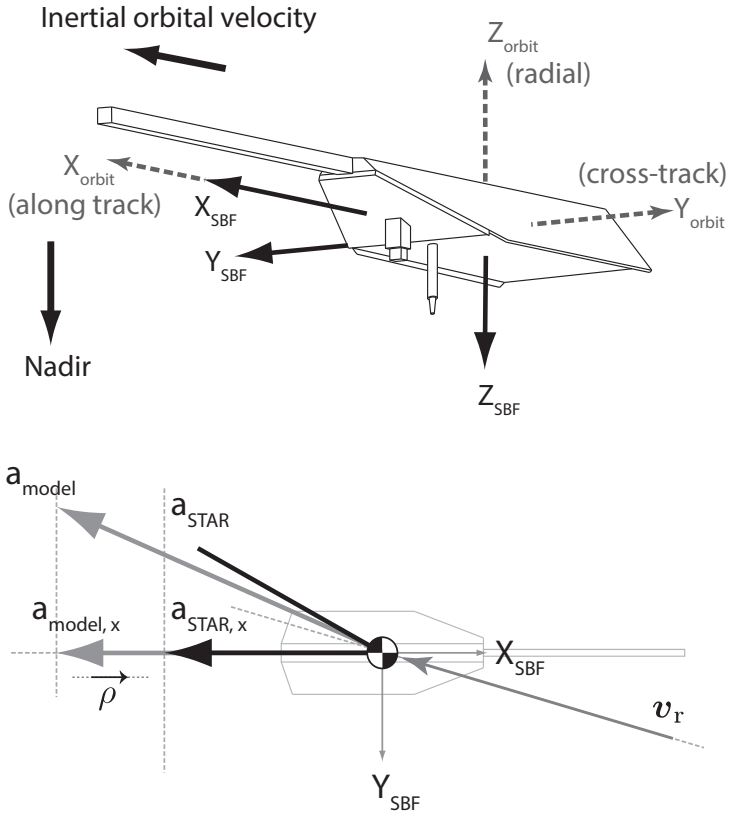

Figure 2.3. Illustration of CHAMP orbit (top) and acceleration (bottom) reference frames, adapted from Doornbos et al. (2010). The following subscripts are used: *orbit* is the orbit frame, SBF is the spacecraft body frame, $STAR$ is the accelerometer frame and *model* is the drag model frame. ρ is the density the satellite samples and v_r is the relative velocity of the atmosphere with respect to the satellite.

where a_{solar}^{model}, a_{albedo}^{model} and a_{IR}^{model} are modelled accelerations due to solar radiation pressure, the Earth's albedo and infrared radiation respectively. Equation 2.1 ignores the lesser contributions of lift and minor forces perpendicular to drag. We can also apply this reasoning to a_{drag}^{model} to obtain the simplified drag equation (Doornbos et al. 2010):

$$\mathbf{a}_{drag}^{model} = C_d \frac{A_{ref}}{m} \frac{1}{2} \rho v_r^2 \hat{\mathbf{v}}_r \tag{2.2}$$

where ρ is the neutral mass density, A_{ref} is the effective cross-sectional satellite area in the ram direction (normally a fixed reference value), C_d is the drag coefficient and v_r is the relative velocity of the atmosphere with respect to the satellite; the latter is a sum of the inertial orbital velocity of the satellite, the velocity due to the co-rotation of the

atmosphere and the wind velocity (Doornbos et al. 2010). This shows a linear relationship between deceleration and neutral density. Typically for CHAMP A_{ref} is 0.74 m^2, C_d is 2.2, m is 520 kg and v_r is 7.6 km s^{-1} (Lühr et al. 2004).

By inserting Equation 2.2 into Equation 2.1 we are able to calculate ρ^{STAR}; this is the general principle behind accelerometer-derived density. The x component of Equation 2.2 is in the along-track direction (x_{orbit} in Figure 2.3, top) of the satellite and is most aligned with the spacecraft body (x_{SBF} in Figure 2.3), thus a direct determination of density uses this axis alone. This alignment is also demonstrated by the acceleration frame in Figure 2.3 (bottom).

Cross-track neutral winds can be derived from the x and y components of v_r in the spacecraft frame (see Figure 2.3), which are aligned with the acceleration vector such that (Lühr et al. 2007):

$$\frac{v_y}{v_x} = -\frac{\mathbf{a}_y^{STAR}}{\mathbf{a}_x^{STAR}} \tag{2.3}$$

where $\mathbf{a}_x^{STAR}$ and $\mathbf{a}_y^{STAR}$ are the x and y components, that is the respective along-track and cross-track directions, of the relative acceleration in the spacecraft frame found in Equation 2.1. We denote this as a^{STAR}, where:

$$a^{STAR} = a_{total}^{STAR} - a_{solar}^{model} - a_{albedo}^{model} - a_{IR}^{model} \tag{2.4}$$

Correcting for the co-rotation of the atmosphere, v_c, and using model wind values, this gives (Lühr et al. 2007):

$$U_{cross} = -\frac{\mathbf{a}_y^{STAR}}{\mathbf{a}_x^{STAR}} v_x - v_c \tag{2.5}$$

Due to the polar nature of the orbit, cross-track winds are analogous to East-West zonal winds, measuring on a global scale as the satellite precesses (Liu et al. 2006), with 220×230 km spatial resolution (Lühr et al. 2007).

An obvious complication of using Equation 2.1 to derive neutral density (and therefore wind) is its dependence on an accurate model of density, ρ^{model}, and drag, a_{drag}^{model}, the latter also dependent on density (see Equation 2.2). The largest noise error comes from this modelling, 1%, whilst the largest systematic error is due to the drag coefficient in Equation 2.2, between 5–10% (Bruinsma et al. 2004). The drag coefficient relation was determined experimentally, and found to depend on the surface temperature of the satellite. As orbit conditions are not replicable on the ground this is a substantial source of error (Bruinsma

et al. 2004). This is discussed further in Chapter 5.

Doornbos et al. (2010) advances the derivation of ρ and U_{cross} by using a modified Equation 2.2, where the lift and other small forces are included to reduce the error from their exclusion. Doornbos et al. (2010) also uses an iterative algorithm to reduce the error from misalignment with a_{drag}^{model} and a^{STAR}, as shown schematically in Figure 2.3 (where a_{drag}^{model} is simplified to a^{model}). This involves changing the relative velocity vector, $\mathbf{v}_r$, in Figure 2.3 whilst conserving magnitude until a_{drag}^{model} is aligned with a^{STAR}, and then respectively changing ρ until the accelerations equate (Doornbos et al. 2010). A further correction involves normalising measurements to the same altitude using a scale height of 60 km, calculated using a density model (Lühr et al. 2004).

Both neutral wind and density data are available from the DEOS Thermosphere web server for satellite drag observations[3]. We use the Wind_Local_Iterative data, which provide zonal, meridional and vertical winds in the geographic ENU frame, as detailed in Figure 2.8. The wind speeds are expressed with respect to a co-rotating atmosphere, not with respect to inertial space, taking into account the orientation of the satellite and additional aerodynamic lift generated by strong winds. Other data available on the server (and used in Chapters 3, 4 and 5) include CHAMP geodetic (or geographic) coordinates, magnetic coordinates and satellite speed data. All data have a 10-second resolution, equivalent to ∼76 km along-track.

Doornbos et al. (2010) estimates an error in neutral density cross-track wind due to the instrumentation and modelled parameters in Equation 2.1 by propagating an approximated error of 10 nm s^{-2} in acceleration for all data in 2004. This is realised as a 3.2% RMS error in density and 140 m s^{-1} RMS error in cross-track wind. The precision and systematic instrumental error, discussed previously, translate to ∼15 m s^{-1} and ∼20 m s^{-1} respectively (Liu et al. 2006). The wind error is improved most by using high solar activity data (and thus earlier years), and as much data as possible to improve the statistics if averaging (private communication, Eelco Doornbos). It should be noted that not including the along-track winds, due to their much smaller magnitude with respect to the satellite speed (Liu et al. 2006), introduces a ∼10% error at polar latitudes as meridional winds increase in magnitude (Aruliah et al. 2018).

[3]See: `http://thermosphere.tudelft.nl/acceldrag/data.php`

2.2 The UCL Coupled Middle Atmosphere and Thermosphere model

The UCL Coupled Middle Atmosphere and Thermosphere (CMAT2) general circulation model (GCM) is a 3-D time-dependent model based on atmospheric physical processes (Harris 2001; Harris et al. 2002), and the successor of UCL's CMAT, first developed by Fuller-Rowell (1981)[4]. It extends from 15-300+ km globally depending on solar activity, with a resolution grid in this thesis (CMAT2 has variable resolution, we use the standard) of 2° latitude and 18° longitude steps and 63 pressure levels corresponding to various altitudes (see Equation 1.24). The pressure range has levels 1-59 set to 1/3 of the scale height (see Equation 1.22 for a definition of scale height as described in Chapter 1) and 60-63 to 1.0 of the scale height, due to exponentially decreasing density with increasing altitude. The time step of the model can be specified (down to a resolution of a minute), but is typically 1-hour.

CMAT2 then solves the momentum, energy and continuity equations in Chapter 1 over these grid points, using a finite difference method to discretise the differential equations (as detailed in Harris (2001)). To simplify this further CMAT2 also uses several assumptions, including hydrostatic equilibrium and the ideal gas law (as described in Chapter 1), both common assumptions within GCMs (see for example: Richmond et al. (1992); Roble & Ridley (1994)). The model uses a daily solar activity proxy, the F10.7 index (Tapping 2013), to calculate the solar EUV input, and a three-hourly averaged geomagnetic activity proxy, the Kp index (Menvielle & Berthelier 1991), to determine particle precipitation (see Section 2.4.4 for more information on these proxies). The time-dependent nature of the model allows real-time data to be used, unless forced to be constant. CMAT2 then calculates mesospheric heating, thermospheric heating, photodissociation and photoionisation due to X-ray, EUV and UV radiation using solar fluxes and absorption and ionisation cross-sections, with radiative cooling calculated from NO, O, CO_2 and O_3 radiative emission (Harris 2001).

[4]CMAT2 can be run on a local machine; see the CMAT2 User Guide at `http://astroweb.projects.phys.ucl.ac.uk/cmat2/www/html/httpd/shared_docs/cmat2_UserGuide.pdf` for further information on installation.

2.2.1 Electrodynamics of the Upper Atmosphere

With the date specified the magnetic field is particular to the period of time chosen, correcting for the magnetic poles drifting. The magnetic field in CMAT2 is simplified to a dipole field where the magnitude is equal to (Harris 2001):

$$|B| = \frac{B_0}{R^3}\sqrt{1 + 3\sin^2\lambda} \tag{2.6}$$

where λ is the geomagnetic latitude. This is then described by a series of 300 flux tubes, each suspended from two base points at 130 km (Barnes 2017) and extended to high-latitudes by an open flux tube model (AIAA Standards 1999). These flux-tubes follow the $\mathbf{E} \times \mathbf{B}$ drift discussed in Chapter 1.

The standard CMAT2 version uses high-latitude Foster electric fields (Foster et al. 1986) to calculate $\mathbf{E}$ and the electric field strength to determine the thermospheric electric field and particle precipitation. Foster et al. (1986) used the Millstone Hill radar with satellite ion drift measurements to create an index (0-7) for the intensity and coverage of the resultant electrostatic potential. Foster et al. (1986) related this to the Kp index and a precipitation index based on measurements of particle influx by the TIROS and NOAA satellites (Fuller-Rowell & Evans 1987). CMAT2 uses this relation to calculate the Foster fields and high-latitude precipitation energy input. This high-latitude auroral energy input is significant for Kp>5+ where it reaches >96 GW; it is not utilised in this thesis due to the quiet periods chosen throughout all modelling studies.

The polar cap potential associated with each Foster field index value is used to construct a convection pattern based on the $\mathbf{E} \times \mathbf{B}$ drift. A new development in CMAT2 is to use the Super Dual Auroral Radar Network (SuperDARN, see Section 2.4.2) (Greenwald et al. 1995; Chisham et al. 2007) to simulate the energy input from the solar wind by providing more realistic electric fields, as described in Barnes (2017), which in turn provide more realistic ion drifts. This is discussed further in Chapter 4. We use both Foster and SuperDARN electric fields in this thesis.

2.2.2 Ionospheric Models

CMAT2 can be used in parallel with three ionospheric models. The most basic is a parametrisation of the ionosphere using the empirical Chiu (1975) model. This uses fewer than 50 coefficients (using empirically-fitted constants with independent variables such as

time) but is a good first order approximation, particularly at mid-latitudes. An improvement on this is the Parameterised Ionospheric Model (PIM), developed by Daniell et al. (1995), providing a more realistic theoretical climatology above mid-latitudes. This uses GCM outputs to obtain functions using several million coefficients. The most-advanced, the Global Ionosphere Plasmasphere model (GIP) (Millward et al. 2007), is an extension of the Coupled Thermosphere Ionosphere Plasmasphere model (CTIP) (see for example, Millward et al. (1996)). GIP uses an improved approximation of the Earth's dipole field, including a tilt and offset from the Earth's centre, and solves for more ion constituents. Popular outputs include the ion density profiles, including H^+, O^+, N_2^+, O_2^+, NO^+ and N^+, based on chemical equilibrium, and ion temperatures, calculated from the thermal balance between ion-neutral frictional heating, electrons and the neutral atmosphere (AIAA Standards 1999).

As well as the simplified description empirical ionospheric models provide, a further disadvantage is their inability to model dynamic conditions (Millward et al. 1996), affecting electron and ion density profiles, temperatures and $\mathbf{E}\times\mathbf{B}$ plasma drifts. For example, PIM has a diurnal variation with 30-minute resolution, whilst GIP has a temporal variation of 1-15 minutes (AIAA Standards 1999). We use GIP in this thesis unless there is no ionospheric requirement, as in probing viscous drag effects in Chapter 4, in which case we use the less computationally expensive PIM.

2.2.3 The CMAT2 Neutral Atmosphere

As a physics-based model, the CMAT2 neutral atmosphere is governed by the concepts and equations discussed in Section 1.4.1 in Chapter 1. Harris (2001) provides a full breakdown of the neutral component of CMAT2, including specific model inputs and planetary parameters; here we summarise the inputs used in the CMAT2 simulations of this thesis.

Climatologies provided the composition of the atmosphere using several data sources in accordance with a standard CMAT2 simulation, namely Mass Spectrometer Incoherent Scatter (MSISE-90) (Hedin 1991) data for O, O_2, and N_2, the UK Universities Global Atmospheric Modelling Programme (UGAMP) ozone climatology data for O_3 and SNOE and UARS satellite data for NO and NO_2, with the CO_2 composition taken as a global mean below the turbopause. The model has four compositions switches: (1) use climatologies; (2) use equation rates; (3) use equation rates for major constituents and climatologies for minor constituents; (4) adopt mode (3) but calculate O_3 from climatologies.

Several boundary conditions are applied in the model. In this thesis the neutral component of the CMAT2 model used was quite basic as complex lower boundary analysis, for example, was not necessary in any of the studies. We adopted a constant lower boundary of 15 km using the MSISE-90 global mean. The upper boundary is defined to have no external energy sources or vertical velocity, so that the temperature and horizontal velocity gradients tend to zero and the vertical velocity is set to 0 m s^{-1}. The Alexander & Dunkerton (1999) gravity wave scheme was used in all simulations, as the latest gravity wave model to be included in CMAT2. The standard gravity wave model, Rayleigh friction, is somewhat outdated and is noted by the UCL group as overestimating the mesosphere zonal wind speed magnitudes compared to other models, and can also dampen diurnal tides (Roble & Ridley 1994).

A 30-day 'spinup' simulation was performed for all runs; this puts the model into perpetual mode, producing a standard CMAT2 atmosphere by repeating the same day until an equilibrium state is reached and the atmosphere parameters have converged. CMAT2 builds up from empirical models, such as the semi-empirical Horizontal Wind Model (HWM) (Drob et al. 2008), and therefore the spinup is essential to include the physical processes of the model. The length of spinup is important to reach an equilibrium state, for example, GIP is integrated after 7 days and can vary non-negligibly. These data are then used as an input for day-step runs or used to simulate an individual day.

Model outputs used in this thesis include neutral temperature, ion temperature, height (as the model grid is given in pressure levels), neutral density and the three components of the neutral wind vector. CMAT2 winds are defined as South-East-Down, where x is the meridional wind, y is the zonal wind and z is the vertical wind.

2.3 The UCL Fabry-Pérot Interferometer Network

The UCL Fabry-Pérot Interferometer (FPI) network is comprised of four narrow field-of-view (FOV) FPIs (Aruliah & Rees 1995; Aruliah et al. 2005), and an all-sky wide angle Scanning Doppler Imager (SCANDI) (Aruliah et al. 2010) in Arctic Scandinavia. They provide simultaneous measurements of neutral winds and neutral temperatures of the polar thermosphere using line-of-sight Doppler shifts and Doppler broadening, measuring Arctic aurorae airglow at the 630.0 nm atomic oxygen red emission line, with peak emission typically located at 240-250 km altitude, and the 557.7 nm atomic oxygen green emission

line, peaking at the lower altitude of ∼110 km, though the emission height is more difficult to determine than the former (Link & Cogger 1988; Vlasov et al. 2005).

2.3.1 Fabry-Pérot Interferometers

Two FPIs are located at the Kiruna ESRANGE Optical Platform Site (KEOPS) in Sweden (geographic 67.93°N, 21.07°E), another at the Sodankylä Geophysical Observatory in Finland (geographic 67.37°N, 26.63°E) and a final at the Kjell Henriksen Observatory (KHO) in Longyearbyen, Svalbard (geographic 78.15°N, 16.04°E). They have a narrow 1° FOV and a high temporal resolution from using exposure times between 10-60 seconds (Aruliah & Rees 1995; Aruliah et al. 2005). Figure 2.4 shows the locations of each FPI with their emission line and FOV. It should be noted that the FOV of the auroral oval FPIs at Sodankylä and Kiruna overlap. The FPIs are situated in close proximity with the European Incoherent Scatter Scientific Association (EISCAT) (Rishbeth & Williams 1985) incoherent scatter radars (see Figure 2.4 and Section 2.4.3), allowing sampling of spatially similar regions in the ionosphere and thermosphere.

FPIs consist of a rotatable mirror at an elevation angle of 30-45° (depending on the site) which can be adjusted to various 'look' directions corresponding to different wind components, an etalon made up of two semi-reflecting glass plates on an optical bench in which concentric interference fringes are created, a telescope to focus the interference pattern, a bandpass filter to remove optical contamination and a sensitive electron multiplying charge coupled device (EMCCD) detector. As an atomic transition occurs in the thermosphere light is emitted, which can be Doppler shifted if its source is moving. This light is reflected multiple times between the etalon plates causing different rays to follow separate paths, shifting their respective phases. When recombined, these rays interfere to make a concentric ring interference pattern, where the fringes are related to the incident wavelength, from which the spectra can be fitted. Intensities are determined using the integrated area of the spectral profile, with a Ne lamp of known emission allowing for calibration of the zero Doppler shift baseline. Line of sight velocities, that is, neutral winds are calculated using the measured Doppler shifts, whilst neutral temperatures are calculated from the Doppler broadening of the emission, itself due to the many small resultant Doppler shifts from the thermal motion of the species. A stabilised He-Ne laser emission is used to provide an instrument function to calibrate the neutral temperatures. A full description of the instrumental design of the UCL FPIs can be found in Ronksley (2016).

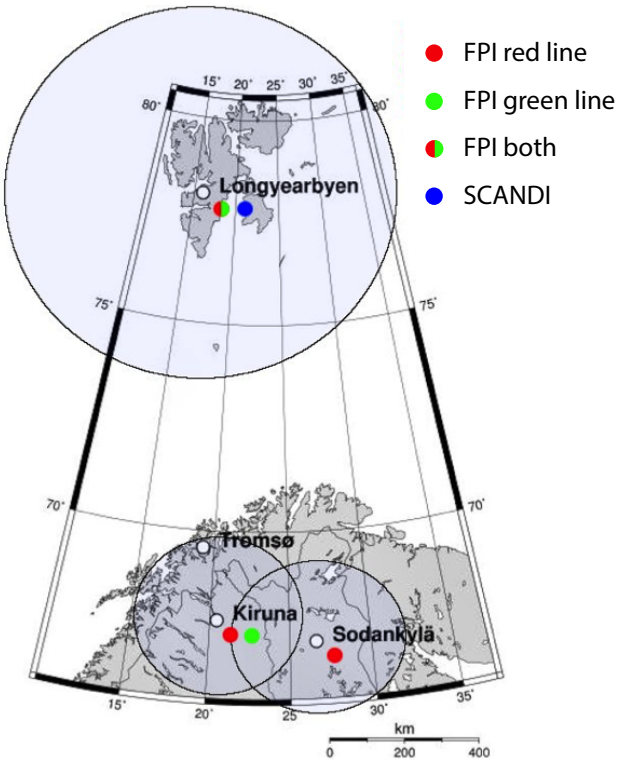

Figure 2.4. A geographic projection detailing the locations of the Kiruna, Sodankylä and Svalbard FPIs in Scandinavia, with their respective fields of view; adapted from Ronksley (2016). The legend indicates red (red marker) or green (green marker) line emission and SCANDI (blue marker). White markers show the location of EISCAT radars (see Section 2.4.3).

FPIs have several look directions, for example, North, East, South, West and Zenith (vertical upwards); these are observed in a sequence typically over a period of 10-15 minutes interspersed with calibration lamp measurements, each with a 30 or 60-second integration. The meridional winds can be calculated using the North and South directions, separated by 500 km in Kiruna and 800 km in Svalbard. As each look direction corresponds to a different volume of neutral air separated by large distances, accuracy is improved by not averaging. Zonal winds can be measured using the East and West directions. Vertical winds are measured using the zenith direction. The nighttime ionospheric electron density also correlates with the intensities due to dissociative recombination of O_2 with electrons (Pant et al. 2011; Yiu 2014).

As the airglow emission is extremely weak, FPIs can only measure accurately during total darkness. Svalbard at 78°N is located in the polar cap region, whilst Kiruna and Sodankylä at ∼68°N are located in the auroral oval region. This means Svalbard is

under ∼24-hour darkness during November-January with observations from late October to March, whilst Kiruna and Sodankylä have up to 18-hour darkness during November-December with observations from late August to April. Clear skies are also required to avoid contamination due to cloud scatter, which can be checked with an all-sky camera, and more recently, with a cloud sensor monitor that compares ground and sky temperatures to eliminate cloud cover. Scatter can also arise due to light (i.e. twilight) and aerosols. This is harder to correct for, but an all-sky camera can be used to a large extent, as with cloud contamination.

FPI limitations include an uncertain emission height, their reliance on height integration and inability to measure in sunlit periods or under cloudy conditions (see Aruliah et al. (2010) for further detail). In the case of the former the peak emission height has been modelled as between 220-250 km (Link & Cogger 1988; Vlasov et al. 2005) and is typically located between 240-250 km (Aruliah et al. 2005, 2010). Recent studies such as auroral arc studies (Gillies et al. 2017) which show the peak lowering, or E-region precipitation studies (Sica et al. 1986) which show the peak at higher altitudes, are applicable over very small periods of time during active geomagnetic conditions. The wind and temperature errors are proportional to the 630 nm intensities measured by the FPI. The average neutral temperature error of the UCL FPIs is ±90 K and ±10 m s^{-1} for the neutral wind (Ronksley 2016). Further detail on the UCL FPIs can be found in Aruliah & Rees (1995); Aruliah et al. (2005); Ronksley (2016).

2.3.2 SCANDI

SCANDI is an all-sky FPI located in Longyearbyen, Svalbard (Aruliah et al. 2010), sharing its location with a narrow FOV FPI. SCANDI has been operating since 2007 to the present day, with a 7-minute resolution. SCANDI has a FOV of 150°, covering a 1,000 km diameter circle ranging from 70-80° magnetic latitude. During 2007-2012 this was divided into 25 zones including a central zenith zone at 75° magnetic latitude, after which it was increased to 51 zones and then finally to 91 zones (Ronksley 2016). Figure 2.5 outlines the 25-zone FOV, used in this thesis. Figure 2.4 shows the location of SCANDI, with its larger FOV compared to the narrow FOV FPIs. To calculate both horizontal wind components from line-of-sight measurements a polynomial is fitted in several rings centred on the zenith zone. This assumes the vertical wind is constant in the FOV and greatly reduced in magnitude compared to the zonal and meridional winds. The wind vectors in each ring

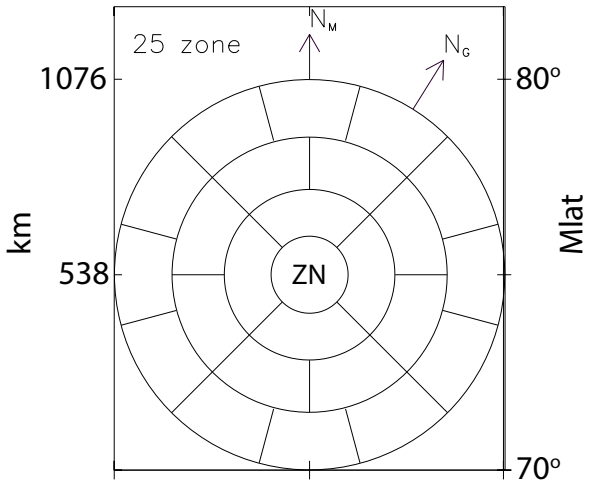

Figure 2.5. SCANDI FOV and zone configuration adapted from Ronksley (2016), where ZN indicates the zenith zone at the centre of the SCANDI FOV. Note N_M and N_G denote geomagnetic and geographic north respectively.

are consistent with each other, however, the wind vectors are not necessarily consistent with the other rings when there is disturbed flow. This fitting technique is described in detail by Ronksley (2016).

2.4 Other Data Sources

In this section we discuss other secondary data sources used in the following chapters of this thesis. These include the SuperMAG Consortium ground magnetometer, Sym-H index and OMNI solar wind data used in Chapter 3, the SuperDARN and EISCAT radar data used in Chapter 4 and the Kp and F10.7 indices referenced throughout.

2.4.1 SuperMAG

The SuperMAG Consortium (Gjerloev 2012) provides a collection of data from a global network of over 300 ground-based magnetometers[5]. Figure 2.2 shows the location of SuperMAG ground stations (green markers) on a global projection map with several CHAMP orbits overlaid. Ground magnetic field perturbations are provided in geomagnetic NEZ (local magnetic North, local magnetic East, vertical down) coordinates, with 1-minute resolution and an optional baseline subtracted. The baseline is calculated using one year

[5]Available from: `http://supermag.jhuapl.edu`. A list giving station names, abbreviations and locations can also be found here.

of measurements, in which the daily variations, yearly trend and any residual offsets are subtracted from the data (Gjerloev 2012).

The NEZ frame is a local coordinate system, which uses a time-dependent declination angle to transform magnetometer data in, for example, magnetic and geographic coordinates (see Section 2.5). The angle is time-dependent as it is affected by periodic changes in the Earth's geomagnetic field and seasonally-varying temperature (Gjerloev 2012). This transformation is reversible using the International Geomagnetic Reference Field (IGRF, see Section 2.5.1) (Thébault et al. 2015).

The focus of ground GMD component in this thesis is the peak magnetic perturbation, typically responsible for incidents relating to navigation such as industrial drilling (Reay et al. 2005), and car, rail and aircraft GPS guiding systems (Royal Academy of Engineering 2013) (see Woodroffe et al. (2016) for further discussion on GMD components). This is a disturbance in the horizontal component of the Earth's magnetic field and is calculated using the North and East components:

$$\Delta B = \sqrt{B_N^2 + B_E^2} \tag{2.7}$$

2.4.2 SuperDARN

SuperDARN[6] (Greenwald et al. 1995; Chisham et al. 2007) is an international network of ground-based high-frequency coherent scatter radars measuring F region (∼250 km) ionospheric plasma convection in the northern and southern polar regions. The main northern hemisphere array, used in this thesis, is made up of nine radars covering most of the 60-75°N magnetic latitude ring, with a further two PolarDARN radars used for better coverage at higher latitudes from 2007 onwards. Due to the expanse of SuperDARN over the northern hemisphere SCANDI's FOV overlaps with SuperDARN, as demonstrated in Figure 2.6.

Each radar measures line-of-sight plasma drifts, which are combined to produce a plasma convection pattern. The drifts themselves are calculated by transmitting radio waves into the F region, which are then back-scattered due to electron density variations affecting the refractive index. Plasma convection Doppler shifts these back-scattered waves, which are then measured as line-of-sight velocities. Combining line-of-sight radar

[6]SuperDARN is funded by the national scientific funding agencies of Australia, Canada, China, France, Italy, Japan, Norway, South Africa, United Kingdom and the United States of America.

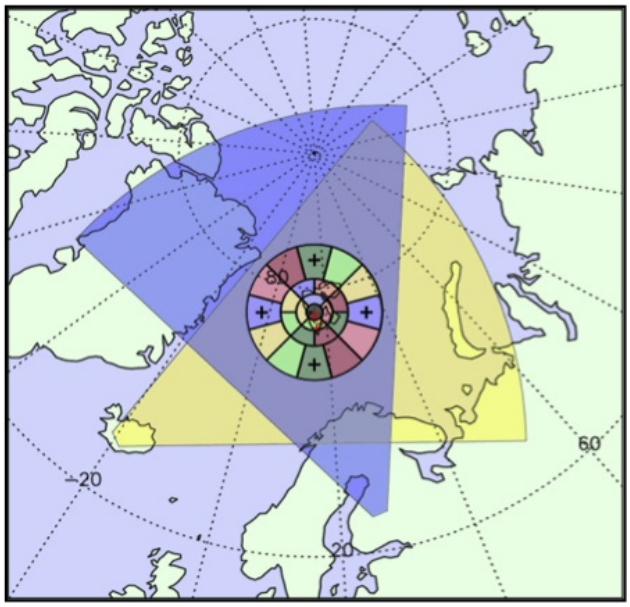

Figure 2.6. A polar stereographic projection detailing the SCANDI FOV in Svalbard, with overlapping SuperDARN fan FOVs (purple and yellow) (image courtesy of Eoghan Griffin).

measurements with those from an empirical model dependent on IMF and fitting to an expansion of the ionospheric electric potential in spherical harmonics allows the horizontal drift components to be determined (Ruohoniemi & Baker 1998). If there is an absence of back-scatter, the empirical model alone can be used. Ion convection data where over 200 vectors are included in the map potential technique provide the most accurate data (as detailed in Ruohoniemi & Baker (1998)).

ECLAT level 3 data used in this thesis[7] are in the form of a 40×40 grid of electrostatic potential in solar magnetic coordinates (see Section 2.5) centred on the geomagnetic north pole and extending to $\pm 50°$. 0° is defined at 0 MLT, with -180°/180° at 12 MLT (it should be noted that ECLAT SuperDARN data uses the opposite convention to other magnetic coordinate systems; see for example, Laundal & Richmond (2017)). The gradient of the potential is computed from the electric field ($\mathbf{E} = -\nabla\Phi$) and is used to calculate the ion drift (see Equation 1.12 in Chapter 1) where the IGRF (see Section 2.5.1) is used to calculate the magnetic field. This method is described in full in Milan et al. (2013). Data have a 2-minute resolution.

[7]Data from 2000-2010 courtesy of the University of Leicester; data from 2010 onwards courtesy of the University of Lancaster.

2.4.3 EISCAT Radars

EISCAT[8] (Rishbeth & Williams 1985) operates three types of incoherent scatter radars systems: ultra high frequency (UHF), very high frequency (VHF) and the EISCAT Svalbard radar (ESR). The UHF radar has a 32 m antenna located in Tromsø, the VHF radar has a 30 × 40 m rectangular antenna transmitter and receiver in Tromsø and two passive 32 m antenna receivers in Kiruna and Sodankylä respectively making a tristatic system and the ESR has both 32 m and 42 m dishes that transmit and receive at Svalbard. The ESR 32 m dish is moveable, whilst the ESR 42 m dish measures at the zenith, which lies in the centre of the SCANDI FOV and is equivalent to 75°N geomagnetic latitude with a 5° FOV (see Figure 2.5). Figure 2.4 shows the locations of these antennae (in white markers), and where they overlap with the UCL FPI network.

Using EISCAT incoherent scatter radars allows us to measure the profiles of electron density, electron temperature, ion temperature and ion drift velocity along the line-of-sight. Radars detect the Doppler shift from scattering due to single electrons, which creates a double peaked spectrum. From this we can calculate number density from integrating the spectrum, the ion temperature from its width, the ratio of T_e to T_i from its peaks and the mean ion drift from the Doppler shift. Processed archived data are available from EISCAT[9].

Figure 2.7 details the specifications of the EISCAT radars and modes used in this thesis, including the ESR 42 m radar in 'ipy' mode, used for lower thermosphere studies, and the UHF and VHF radars in 'beata' mode, used for lower and upper thermosphere studies as the mode allows measurements of the E and F regions simultaneously. Figure 2.7 includes the code length, baud length, sampling rate, range span, time resolution, transmitter frequency and efficiency with altitude. Using these specifications approximate values of the range resolution, spectral resolution and spectral range can be calculated from the baud length, inverse of the product of code length and baud length and inverse of the sampling rate respectively (Tjulin 2017).

[8]EISCAT is an international association supported by research organisations in China (CRIRP), Finland (SA), Japan (NIPR and STEL), Norway (NFR), Sweden (VR), and the United Kingdom (NERC).

[9]Available from: `http://eiscat.com/schedule/schedule.cgi`

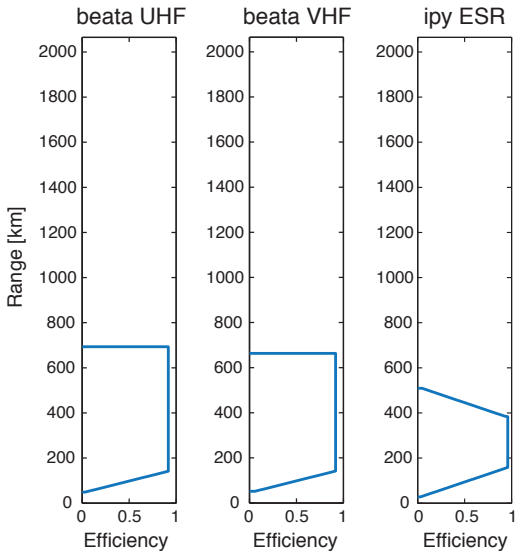

	beata UHF	beata VHF	ipy ESR	taro ESR
Code length [bit]	32	32	30	16
Baud length [μs]	20	20	30	50
Sampling rate [μs]	10	20	15	25
Range span [km]	49–693	52–663	28–509	47–830
Time resolution [s]	5.0	5.0	6.0	6.4
Trans. Freq. [MHz]	929.9	223.2	499.85	499.5+

Figure 2.7. EISCAT UHF and VHF radar specifications, including efficiency profiles, adapted from Tjulin (2017).

2.4.4 Geomagnetic and Solar Wind Indices

This section details four geomagnetic and solar wind indices and their data sources. These include three activity proxies, that is, the Kp, F10.7 (both commonly used to define activity conditions in GCMs) and Sym-H indices, and one solar wind index, namely the OMNI-provided IMF components described in Chapter 1.

The Kp Index

The Kp index (Menvielle & Berthelier 1991) is a three-hourly averaged geomagnetic activity proxy available from the World Data Center (WDC) for Geomagnetism[10]. It uses thirteen mid-latitude ground magnetometers to measure the maximum deviation in the horizontal component of the geomagnetic field over three-hour periods, and quantifies them into a representative integer, ranging from 0 to 9 in equal steps of '−', '○' and '+'. Here, 0-3 represents quiet geomagnetic activity conditions, 3-4 shows moderate conditions and 5-9 signifies a geomagnetic storm from minor (Kp = 5) to extreme (Kp = 9).

The F10.7 index

The F10.7 index (Tapping 2013) is a daily solar activity proxy, also available from the WDC. It is the solar radio flux per unit wavelength at the 10.7 cm radio wavelength

[10] Available from: `http://wdc.kugi.kyoto-u.ac.jp`

emission, which is emitted from the upper chromosphere and lower corona of the Sun. The index correlates well with sunspot number, solar UV and EUV emission and visible solar irradiance. It is observed from the ground using radio telescopes, and is measured in solar flux units (sfu), typically ranging between ∼10s-100s sfu over an entire solar cycle.

The Sym-H Index

The Sym-H index (Wanliss & Showalter 2006) is a 1-minute resolution geomagnetic activity proxy similar to the Dst index discussed in Chapter 1. It is also available from the WDC. It is measured by 10 magnetometer stations at mid-latitudes, different to those measuring the Dst index. For storms with intensities >-300 nT, the index can essentially be treated as a high-resolution Dst index (Wanliss & Showalter 2006). Like the Dst index, it is indicative of the ring current formation (Li et al. 2011) and geomagnetic storm activity, and designed to measure the intensity of the ring current.

IMF components

IMF B_x, B_y and B_z data are provided in GSM coordinates (see Section 2.5) by the High Resolution OMNI dataset (King & Papitashvili 2005)[11]. OMNI combines measurements from the Wind, ACE, IMP 8 and GEOTAIL satellites propagated to the bow shock nose, where Wind and ACE are in heliocentric orbits at L1 and IMP 8 and GEOTAIL are in eccentric Earth orbits. This propagation assumes that the IMF is confined to a phase front that moves with the solar wind, where the phase front normal determines the direction (see for example, Weimer et al. (2003)). Data are averaged to provide 1-minute resolution.

2.5 Coordinate Transforms

In this section we describe the various coordinate transforms and frames used in this thesis. This includes two main coordinate transforms: the derivation of the field-aligned coordinate system used in Chapter 3, and the transformation of geographic coordinates to solar magnetic coordinates used in Chapter 4. Coordinate frames which are referenced throughout this thesis are also defined in this section.

[11] Obtained from NASA/GSFC's Space Physics Data Facility's OMNIWeb service; available from: `http://omniweb.gsfc.nasa.gov/ow_min.html`

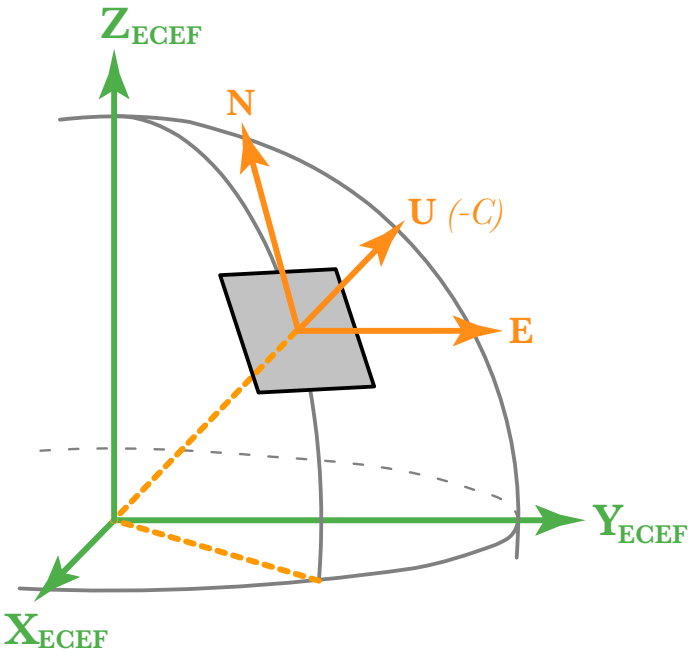

Figure 2.8. Illustration demonstrating the ECEF (green), ENU (orange) and NEC (orange and italics) coordinate systems.

2.5.1 Field-Aligned Coordinates

When using the magnetic field measurements to infer FACs, the data are best viewed in a field-aligned (FA) coordinate system using the location- and time-dependent IGRF model (Thébault et al. 2015) to extract the field direction. IGRF uses a spherical harmonic expansion to represent the Earth's field, where each Gauss coefficient introduces an added complexity to the field; the first three coefficients (where l=1) being the dipole itself. The IGRF is calculated from the magnetic scalar potential, V:

$$\begin{aligned} \boldsymbol{B}(r,\phi,\theta,t) &= -\nabla V(r,\phi,\theta,t) \\ V(r,\phi,\theta,t) &= a\sum_{l=1}^{L}\sum_{m=0}^{l}\left(\frac{\alpha}{r}\right)^{l+1}\left(g_l^m(t)\cos m\phi + h_l^m(t)\sin m\phi\right)P_l^m(\cos\theta) \end{aligned} \tag{2.8}$$

where r is the distance from the Earth's centre, L, is the degree of truncation, ϕ is the eastward longitude, θ is the geocentric colatitude, α is the Earth's radius, g_l^m and h_l^m are the Gauss coefficients and $P_l^m(\cos\theta)$ is the Schmidt quasi-normalised associated Legendre functions (where n is the degree and m the order) (Thébault et al. 2015).

Though the eastward component in the NEC frame is largely similar to the eastward

component in the FA frame, they can differ nearer to the poles. We define the FA frame using the IGRF, where the z-direction is defined as the unit vector of the magnetic field at the input position and time. The y-direction is defined as the cross product of the magnetic field unit vector with the locally radial unit vector. The x-direction completes the frame ($y \times z$). The IGRF is obtained in spherical Earth-Centred-Earth-Fixed (ECEF) geographic coordinates using the International Radiation Belt Environment Modelling library (IRBEM-LIB) package (Boscher et al. 2004-2008), which allows the computation of the magnetic field at all locations using various models adopted and created by the radiation belt physics community. We use the IRBEM-LIB wrapper in SpacePy (Morley et al. 2010)[12]. IGRF is converted from ECEF to the local NEC frame, for use with the CHAMP magnetic field data, using the $\underset{ecef \to enu}{\mathbf{R}}$ rotation described in (Laundal & Richmond 2017):

$$[\mathbf{r}]_{enu} = \underset{ecef \to enu}{\mathbf{R}} [\mathbf{r}]_{ecef} = \begin{pmatrix} -\sin\phi & \cos\phi & 0 \\ -\cos\theta\ \cos\phi & -\cos\theta\ \sin\phi & \sin\theta \\ \sin\theta\ \cos\phi & \sin\theta\ \sin\phi & \cos\theta \end{pmatrix} [\mathbf{r}]_{ecef} \tag{2.9}$$

and re-ordering for NEC as illustrated in Figure 2.8; where each row is $\hat{\mathbf{e}}$, $\hat{\mathbf{n}}$, and $\hat{\mathbf{u}}$ respectively and θ and ϕ are the latitude and longitude in radians in the ECEF frame. This is shown graphically in Figure 2.8. We can then output this as a West-Radial-North (WRN) system with some simple re-ordering as a pre-cursor to the FA frame. We take the normalisation in the z-direction to get the $\hat{z}$ unit vector of the FA system in the WRN frame. Then, with the radial unit vector in the y-direction we can obtain the eastward and northward components of the FA system:

$$\begin{aligned} \hat{\mathbf{z}}_{fa} &= \frac{\mathbf{B}_{wrn}}{|\mathbf{B}_{wrn}|} \\ \hat{\mathbf{y}}_{fa} &= \frac{\hat{\mathbf{z}}_{fa} \times \hat{\mathbf{r}}_{wrn}}{|\hat{\mathbf{z}}_{fa} \times \hat{\mathbf{r}}_{wrn}|} \\ \hat{\mathbf{x}}_{fa} &= \frac{\hat{\mathbf{y}}_{fa} \times \hat{\mathbf{z}}_{fa}}{|\hat{\mathbf{y}}_{fa} \times \hat{\mathbf{z}}_{fa}|} \end{aligned} \tag{2.10}$$

where $\hat{r}$ is a unit vector in the y-direction. This gives the unit vectors of the FA system. When dotted with the magnetic field CHAMP measures this gives the magnetic field in the FA frame so that the z-direction is along the IGRF vector, the y-direction is geomagnetic

[12]See: `https://pythonhosted.org/SpacePy/irbempy.html`

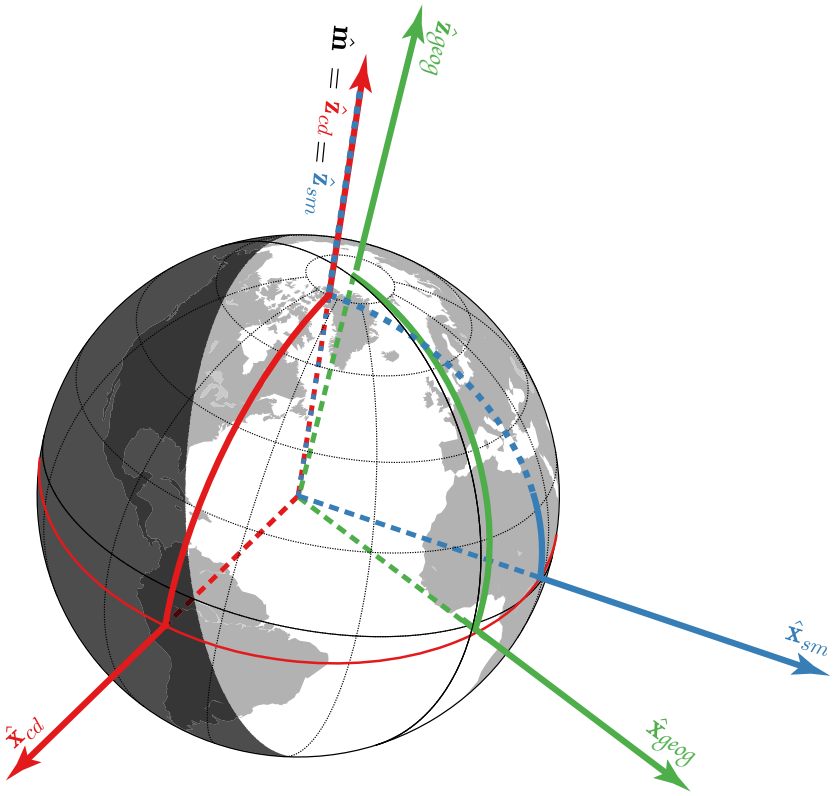

Figure 2.9. Illustration detailing the global projection of the geographic (green), centred-dipole (red) and solar magnetic (blue) coordinate systems, adapted from Laundal & Richmond (2017). $\hat{\mathbf{m}}$ signifies the dipole axis.

East and the x-direction is geomagnetic North.

2.5.2 Geographic to Magnetic Coordinates

Both CMAT2 and CHAMP neutral wind data are in geographic coordinates. It can be argued that due to the geographic-based Coriolis, centrifugal and solar heating forces that act on the neutral atmosphere (Lühr et al. 2007; Förster et al. 2008), winds should be viewed in the geographic frame. However, as ions are organised by the geomagnetic field, and ion drag modulates the neutral motion, both populations are best viewed in the more informative magnetic coordinate system (see for example, Emmert et al. (2002, 2010*b*); Laundal & Richmond (2017)). In this section we describe the geographic to magnetic coordinate transform. We use the method detailed in Laundal & Richmond (2017).

First, we define the geographic, centred-dipole (CD) and solar magnetic (SM) coordinate systems. The geographic coordinate system has its z-axis aligned with the rotation

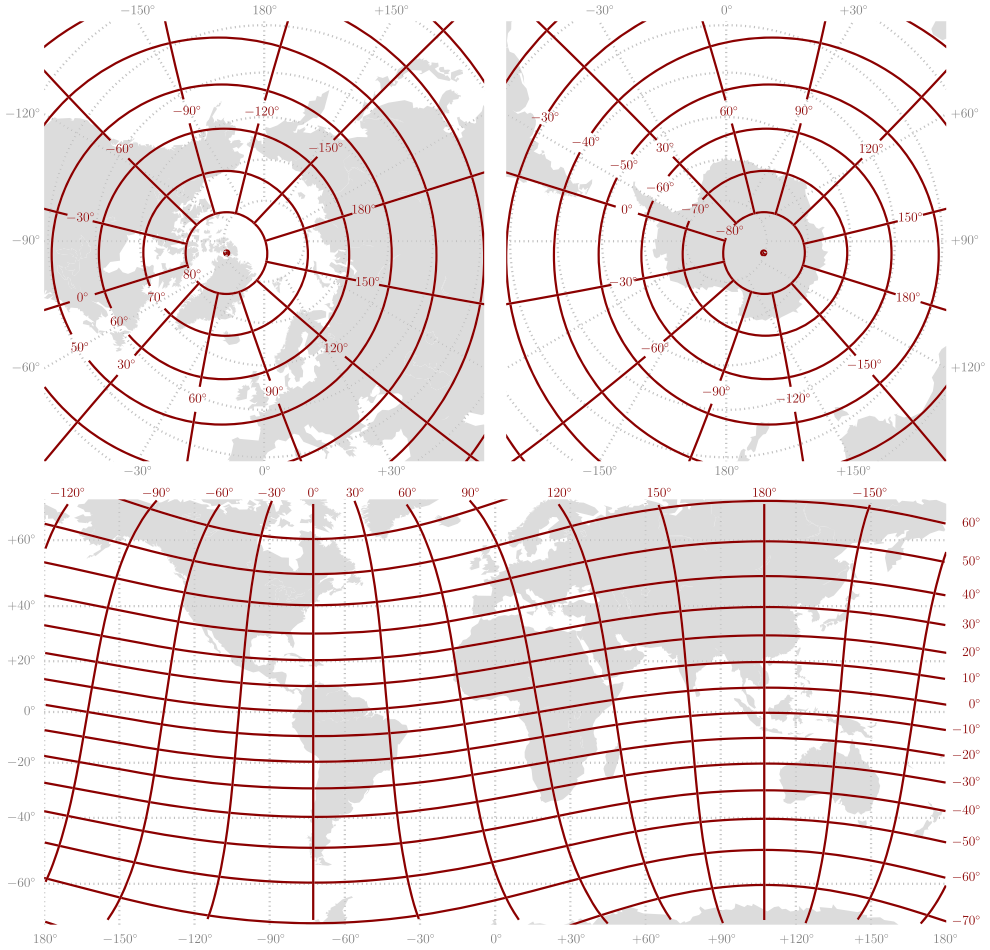

Figure 2.10. Illustration from Laundal & Richmond (2017) detailing the meridians and parallels of the geographic (grey) and centred-dipole (red) coordinate systems.

axis of the Earth, $\hat{\mathbf{z}}_{geog}$, and is defined in terms of either geocentric coordinates, ECEF, or local geodetic coordinates, ENU. The former is more commonly known as geographic latitude and longitude, where 0° is defined at Greenwich meridian and increases eastwards to 360° and latitude extends from -90° at the south geographic pole to 90° at the north geographic pole. The CD coordinate system (also known as magnetic or 'MAG') is an Earth-fixed magnetic coordinate system where the z-axis aligns with the dipole axis, $\hat{\mathbf{m}}$, and the y-axis is perpendicular to both the dipole axis and the geographic rotation axis, $\hat{\mathbf{z}}_{geog}$. Here the dipole axis is derived from the first three coefficients of the IGRF for a given time. SM coordinates share their z-axis with the dipole axis and therefore CD coordinate system. However, there is a rotation about the z-axis such that the Sun-Earth line

lies within the x-z plane, though typically not directly at the Sun. Then, from the magnetic midnight meridian, MLT is defined as 1 hour per 15° eastward, from 0 to 24 MLT. Figure 2.9 shows the global representation of these three coordinate systems. Figure 2.10 details a projected map of the globe, with the meridians and parallels of the geographic and CD coordinate systems.

A breakdown of the geographic to CD transform is as follows:

$$V_{enu}^{cd} = R_{ecef \to enu} \cdot R_{geo \to cd} \cdot R_{ecef \to enu}^{T} \cdot V_{enu}^{geographic} \tag{2.11}$$

where $R_{ecef \to enu}$ is the rotation matrix transforming ECEF to the local ENU frame as detailed in Equation 2.9, $V_{enu}^{geographic}$ is the zonal, meridional and vertical winds in geographic coordinates (the given frame of both CMAT2 and CHAMP), V_{enu}^{cd} is our desired wind in CD coordinates, and $R_{geo \to cd}$ is the rotation matrix transforming geocentric geographic (GEO) coordinates (an ECEF frame) to CD such that:

$$[\mathbf{r}]_{cd} = \underset{geo \to cd}{\mathbf{R}} [\mathbf{r}]_{geo} = \begin{pmatrix} [\hat{\mathbf{x}}_{cd}^{T}]_{geo} \\ [\hat{\mathbf{y}}_{cd}^{T}]_{geo} \\ [\hat{\mathbf{z}}_{cd}^{T}]_{geo} \end{pmatrix} [\mathbf{r}]_{geo} \tag{2.12}$$

where:

$$\begin{aligned} \hat{\mathbf{z}}_{cd} &= \hat{\mathbf{m}} \\ \hat{\mathbf{y}}_{cd} &= \frac{\hat{\mathbf{z}}_{geo} \times \hat{\mathbf{z}}_{cd}}{|\hat{\mathbf{z}}_{geo} \times \hat{\mathbf{z}}_{cd}|} \\ \hat{\mathbf{x}}_{cd} &= \hat{\mathbf{y}}_{cd} \times \hat{\mathbf{z}}_{cd} \end{aligned} \tag{2.13}$$

Here, $\hat{\mathbf{m}}$ is the CD dipole axis, positive outwards in the northern hemisphere, and found using the GEO colatitude, Θ_N, and longitude, Φ_N, of the geomagnetic pole:

$$\hat{\boldsymbol{m}} = \begin{pmatrix} \sin\Theta_n \ \cos\Phi_N \\ \sin\Theta_n \ \sin\Phi_N \\ \cos\Theta_N \end{pmatrix} \tag{2.14}$$

where $\Theta_N = 9.91°$ and $\Phi_N = -72.21°$ in 2010. $\hat{\mathbf{z}}_{geo}$ is the unit vector in GEO coordinates. CMAT2 and CHAMP winds are in the local ENU geographic frame, however the transform from geographic to CD requires the geographic coordinates to be in the non-local GEO

frame, which necessitates wrapping the transform with a rotation from ECEF to ENU. This transform is described in Equation 2.9. To extract θ and ϕ in ECEF coordinates we can resolve the following, where the geocentric Cartesian coordinates (x, y, z) at a point are defined using geodetic latitude, longitude and height above the Earth's surface (λ_{gd}, ϕ, h):

$$\begin{aligned} x &= (\rho + h)\cos\lambda_{gd}\cos\phi \\ y &= (\rho + h)\cos\lambda_{gd}\sin\phi \\ z &= (\rho + h - e^2\rho)\sin\lambda_{gd} \end{aligned} \tag{2.15}$$

where:

$$\rho = R_{eq}(1 - e^2\sin^2\lambda_{gd})^{-1/2} \tag{2.16}$$

and the eccentricity, e, is dependent on the flattening, f, due to the oblateness of the Earth:

$$e^2 = 2f - f^2 \tag{2.17}$$

where R_{eq} is the Earth's radius at the equator equal to 6,378 km and $f = 1/298.25$, both defined by the World Geodetic System 1984 (WGS84)[13]. θ and ϕ are the polar form of the Cartesian coordinates in Equation 2.15:

$$\begin{aligned} r &= \sqrt{x^2 + y^2 + z^2} \\ \theta &= \cos^{-1}\left(\frac{z}{\sqrt{x^2 + y^2 + z^2}}\right) \\ \phi &= \arctan 2(y, x) \end{aligned} \tag{2.18}$$

The magnetic coordinates can be found using either the IRBEM-LIB wrapper in SpacePy (Morley et al. 2010) or Altitude-Adjusted Corrected Geomagnetic coordinates (AACGM) (Shepherd 2014); the latter is based on field line tracing using the IGRF and maps to a given height (Laundal & Richmond 2017). Finally, to convert between CD and SM to obtain the MLT, a rotation in the z-axis is required as illustrated in Figure 2.9. By using the magnetic longitude of when the Sun is in zenith as a reference point, we can

[13]See: `http://earth-info.nga.mil/GandG/wgs84/index.html`

calculate MLT as (Laundal & Richmond 2017):

$$\mathrm{MLT} = \frac{(\phi_{\mathrm{cd}} - \phi_{\mathrm{cd},\hat{\mathrm{s}}})}{15} + 12 \tag{2.19}$$

where $\phi_{cd,\hat{s}}$ is the subsolar point, dependent on time and date. The derivation of the subsolar point is detailed in Laundal & Richmond (2017).

Geocentric Solar Magnetospheric

Geocentric Solar Magnetospheric (GSM) coordinates are often used when describing the solar wind interacting with the magnetosphere, such as in the case of IMF. Here, x is towards the Sun from the centre of the Earth, y is perpendicular to the Earth's dipole and x (positive duskwards) and z completes the system and contains the Earth-Sun line and Earth's dipole (see Laundal & Richmond (2017) for a detailed description). It has the following basis vectors:

$$\begin{aligned}
\hat{\mathbf{x}}_{gsm} &= \hat{\mathbf{s}} \\
\hat{\mathbf{y}}_{gsm} &= \frac{\hat{\mathbf{m}} \times \hat{\mathbf{x}}_{gsm}}{|\hat{\mathbf{m}} \times \hat{\mathbf{x}}_{gsm}|} \\
\hat{\mathbf{z}}_{gsm} &= \hat{\mathbf{x}}_{gsm} \times \hat{\mathbf{y}}_{gsm}
\end{aligned} \tag{2.20}$$

2.6 Summary

In this chapter we have discussed the three main data sources used in this thesis: CHAMP, the UCL CMAT2 model and the UCL FPI network. We have described the collection of raw data and processing applied to CHAMP to extract the geomagnetic field, used in Chapter 3 to infer FACs, the neutral winds, used in Chapter 4 and the neutral density, used in Chapter 5. We have outlined the general principles behind the generation of a CMAT2 atmosphere, providing model atmospheric conditions used in Chapters 4 and 5. We have also detailed the instruments and structure of the UCL FPI network, including the wide-angle SCANDI and narrow-field FPIs used in Chapters 4 and 5 respectively.

We have also included brief summaries of other data sources used in this thesis, such as SuperMAG measuring ground magnetic perturbations in Chapter 3, SuperDARN providing ionospheric plasma drifts in Chapter 4, EISCAT radars sampling the ionosphere in Chapters 4 and 5 and the geomagnetic and solar wind indices, which are employed throughout this thesis. Finally, we have summarised the various coordinate frames and

transforms referenced and utilised in the following chapters.

Chapter 3

Behaviour and Correlation of Storm Time FACs and Ground GMDs

A key part of the ground-based vulnerability of space weather stems from the generation of ground GMDs. These ground GMDs can affect national electric grid and gas systems as well as infrastructure used in the military, airline and drilling industries (Reay et al. 2005; Vallée et al. 2007; Lloyds 2013; Viljanen et al. 2014), to which they are both disruptive and financially damaging (Riswadkar & Dobbins 2010; Lloyds 2013; Oughton et al. 2017). To combat this it is vital to understand what drives their equatorward motion (to populated regions) and strength to disrupt.

Region 1 and 2 FACs, driven by the magnetopause and partial ring currents respectively, are known to drive ionospheric currents during geomagnetic storms and are believed to be responsible for GMDs (see Chapter 1, and for example: Kamide (1982); Tamao (1986); Wu & Stening (1991); Laundal et al. (2015); Adhikari et al. (2017)). Using the CHAMP fluxgate magnetometer to calculate FAC current densities and magnetic latitudes, with SuperMAG ground magnetometers analogously providing GMD magnetic perturbations and latitudes, we probe FAC locations and strengths as predictors of GMD locations and strengths. We also study the relationships between solar wind drivers and

global magnetospheric activity, and both FACs and GMDs using IMF B_z and the Sym-H index.

We present three case studies from the 22-29 July 2004 storm time interval, which had particularly large GMDs given its respective storm intensities. We find no correlation between FAC and GMD magnitudes, perhaps due to CHAMP orbit limitations or ground magnetometer coverage, but acknowledge a statistical analysis of many storms is needed to verify this. We find IMF B_z is correlated with dayside FAC and GMD magnetic latitudes during the first and second less intense storms, indicating solar wind as an initial driver. The ring current influence increases during the final most intense storm, with improved correlations between the Sym-H index and FAC magnetic latitudes. There are also strong correlations between both IMF B_z and the Sym-H index and nightside GMD magnitudes throughout, supportive of their generation via tail reconnection.

This chapter is based on work carried out in collaboration with the Los Alamos Space Weather Summer School under the supervision of Jesse Woodroffe and Steve Morley (see Hood et al. (2016) and Hood et al. (2018)). We thank the Los Alamos Space Weather Summer School, funded by the Center for Space and Earth Sciences (CSES) at the Los Alamos National Laboratory, for making this study and collaboration possible.

3.1 Introduction

GMDs result from a complex global and magnetospheric current system, and can be driven by several sources such as the ring current, electrojets and Chapman-Ferraro currents on the magnetopause. Here we outline their association with FACs, which play a vital role in the transfer of energy and circulation between the solar wind and magnetosphere-ionosphere system (Iijima 2013). As discussed in Chapter 1, initially the system is driven by currents in the magnetosphere induced by the IMF or solar wind, for example, which then flow along geomagnetic field lines as poleward Region 1 FAC sheets into the ionosphere in the dawn sector and outward in the dusk sector. Equatorward Region 2 FACs then arise from the formation of a partial ring current, flowing into the dusk sector and out of the dawn sector (see for example, Cowley (2000)). As the FACs are fed into the ionosphere they close via a Pedersen current and generate a Hall current (see for example, Cowley (2000)), which in turn generates ground fluctuations in the magnetic field, inducing ground GMDs (Nishida 1964).

Adopting this reasoning, it follows that the strength of the FAC should influence the GMD magnitude – strong FACs should drive strong ionospheric currents, and in turn strong GMDs. However, the location of the FAC is also significant. At higher latitudes Pedersen currents screen the radial component of FACs resulting in a GMD perturbation solely due to Hall currents (known as Fukushima's Theorem, see Chapter 1 and Fukushima (1976)); at lower latitudes this component is less radial (Tamao 1986), thus the more equatorward the latitude the more likely FACs are to contribute directly to severe GMDs. The FAC location is also associated with the auroral oval belt (Iijima 2013), thus a more equatorward FAC is also an indication of the auroral oval expanding (Wang et al. 2005), in turn tied to storm intensity (see for example, Xiong et al. (2014) and references therein).

Previous focus on the relationship between FACs and GMDs has often investigated the two phenomena separately and assumed or inferred certain correlations (see for example, Kamide (1982) and references therein), with focus on GMDs driven by ionospheric currents and their corresponding ground effects (see for example, Woodroffe et al. (2016)) or FACs and their role in magnetosphere-ionosphere coupling (as in Wang et al. (2005, 2006) and references therein). Focusing on the latter study, Wang et al. (2006) probed the relationships between FAC magnetic latitudes and magnitudes and several magnetospheric indices during two intense 2003 geomagnetic storm events. They found the dayside FAC magnetic latitudes and strengths correlated with IMF B_z and solar wind pressure respectively, whilst nightside FAC magnetic latitudes were better tied to the Dst index.

In this chapter we are able to verify the relationships found in Wang et al. (2006) and crucially extend the Wang et al. (2006) FAC study to include GMDs, probing the correlations between the magnetic latitude and magnitude of FACs, derived from CHAMP (Reigber et al. 2002) high-precision magnetometer data (see Chapter 2 and Section 3.3.2), and the magnetic latitude and magnitude of peak GMD perturbations, using the network of SuperMAG ground magnetometers (again see Chapter 2 and Section 3.3.3). It is also valuable to understand whether FACs, as demonstrated by Wang et al. (2006), and GMDs are responding similarly or differently to solar wind or ring current variations, as these are main drivers of Region 1 and 2 FACs respectively. IMF B_z and the Sym-H index (see Section 3.3 and Section 2.4.4 in Chapter 2), indicative of the magnetosphere configuration (see for example: Dungey (1961); Cowley et al. (2003)), and the ring current formation (Li et al. 2011) and geomagnetic storm activity, are therefore also compared to FAC and GMD magnetic latitudes and magnitudes.

We present an event study of the 22-29 July 2004 storm time interval, a series of three storms with smaller magnitudes than those studied by Wang et al. (2006) but which produced markedly large GMDs (reaching >4,000 nT) given their Sym-H index minimum of -208 nT; ∼1,000 nT GMD magnitudes are more typical for this storm intensity (see for example, Woodroffe et al. (2016)). The three storms within this interval allow for a comparison when treated separately, providing a means to assess the significance of their sequence, particularly interesting due to their successive deepening Sym-H index minima, which may be contributing to the larger magnitudes of the GMDs. As the GMDs magnitudes are sizeable given the storm intensity of the period, this may also aid in assessing the relationship between FACs and GMDs as effects should be more pronounced. It should be noted that though observable (Zanetti et al. 1994; Kamide 1982; Tamao 1986; Wu & Stening 1991; Laundal et al. 2015; Adhikari et al. 2017), the direct relationship between FACs and GMDs is difficult to obtain. In the ionosphere currents tend to flow across extended regions of space in complex distributions (see for example, Ebihara et al. (2005)) and on the ground the conductivity influences the electric field associated with geomagnetically induced currents, thus the overhead FACs may not be directly responsible for the final measured ground GMD. However, GMDs near regions where strong FACs are observed should still be enhanced, and processes can still be inferred using satellite-based magnetometry and magnetospheric indices, such as IMF B_z and the Sym-H index, to identify specific FAC systems.

3.2 Overview of the 22-29 July 2004 storm time interval

In the period 22-29 July 2004, three sequential ICMEs reached the Earth (Zhang et al. 2007) resulting in three severe geomagnetic storms of increasingly negative peak Sym-H index on the 23rd (-123 nT at 02:40 UT), 25th (-168 nT at 18:32 UT) and 27th (-208 nT at 13:38 UT). During each storm the Kp increased, indicating active conditions, peaking at 9- soon after midday during the final storm. Figure 3.1 outlines the magnetospheric and geomagnetic conditions during this interval (from the top panel): IMF B_z, solar wind speed, solar wind pressure, Akasofu parameter (an estimate of the energy input into the magnetosphere (Akasofu 1979)), Auroral Electrojet (AE) index (Davis & Sugiura 1966), and the Sym-H (black line) and Kp indices (coloured bars, where red indicates active conditions). The solar wind data are 1-minute averaged OMNI data presented in GSM

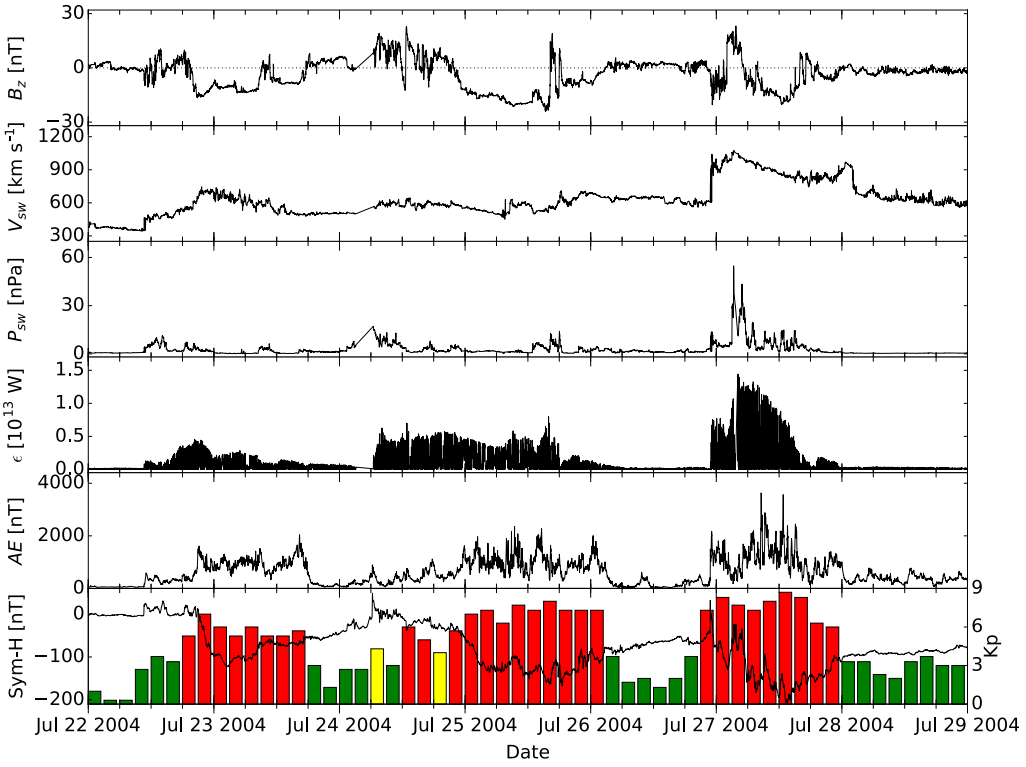

Figure 3.1. Ground and magnetospheric indices during the 22-29 July 2004 storm time interval. From top: IMF B_z, solar wind speed, solar wind pressure, Akasofu parameter, AE index, and the Sym-H (black line) and Kp indices (coloured bars, where red indicates active conditions). The x-axis details the date and time (from 0 UT) during the storm time interval. The three storms can be identified by their Sym-H index minima on the 23rd (-123 nT at 02:40 UT), 25th (-168 nT at 18:32 UT) and 27th (-208 nT at 13:38 UT).

coordinates (King & Papitashvili 2005) (see Section 2.4.4). The AE, Sym-H and Kp indices are 1-minute averaged (excluding the Kp which is a 3-hour range index (Menvielle & Berthelier 1991); see Section 2.4.4 for a full description of these indices).

The initial, main and recovery phases of the storms are described in detail in Pedatella et al. (2008); we give a brief overview here. The first of these storms coincided with a ∼13-hour period of southward IMF B_z, beginning its main phase around 19:00 UT on the 22nd, where a southward IMF B_z drives the energy input from the solar wind into the magnetosphere (Dungey 1961; Vasyliunas et al. 1982). The Sym-H index is then seen to arguably fully recover after reaching its minimum in the early hours of the 23rd. The second storm begins its main phase on the following day at 21:30 UT soon after the

alignment of IMF B_z shifts strongly southward for an extended period of ∼16 hours. The final storm has some overlap with its predecessor but enters its main phase on the 27th at 05:00 UT with intermittent southward IMF B_z for ∼11 hours, and has a prolonged recovery phase with a continued negative Sym-H index up to the 31st (Pedatella et al. 2008). The shock at the start of the final storm is very large, with solar wind speeds reaching ∼1,100 km s^{-1}, also evident in the sudden peak in solar wind pressure, which then spikes twice later on the 27th.

The AE index suggests a strong enhancement of ionospheric currents in the auroral oval, and in turn, energy deposition and Joule heating. An integration of the Akasofu parameter with respect to time is also an indication of the total energy input into the magnetosphere, consecutively for each storm this equates to 1.4, 3.9, 3.2 × 10^{16} J. During the final storm, there are two spikes in the AE index on the 27th (3,632 nT at 08:34 UT and 3,568 nT at 12:47 UT) indicating the occurrence of two significant substorms, which have been identified as some of the most extreme substorms in the period 1996-2012 (Nakamura et al. 2015). These two AE peaks also correspond to intensifications in total electron content (TEC) data (Ngwira et al. 2012).

Figure 3.2 details the ground response during this time period; this shows the SuperMAG-measured ΔB by ground stations above 50° magnetic latitude[1], with the colour wheel indicating the local time sector. The three encompassed storms are seen in the data, with the largest ground GMDs occurring in the nightside (blue) or near where night meets evening and morning (red and green respectively).

3.3 Data and Methodology

In this section we present a description of the data used in this study, including: OMNI high-resolution IMF B_z data, WDC Sym-H index data, CHAMP magnetometer data used to derive the FAC magnetic latitudes and current density magnitudes and SuperMAG Consortium data which provided the GMD magnetic latitudes and perturbation measurements.

[1]Code software to parse SuperMAG magnetometer data was provided by Jesse Woodroffe.

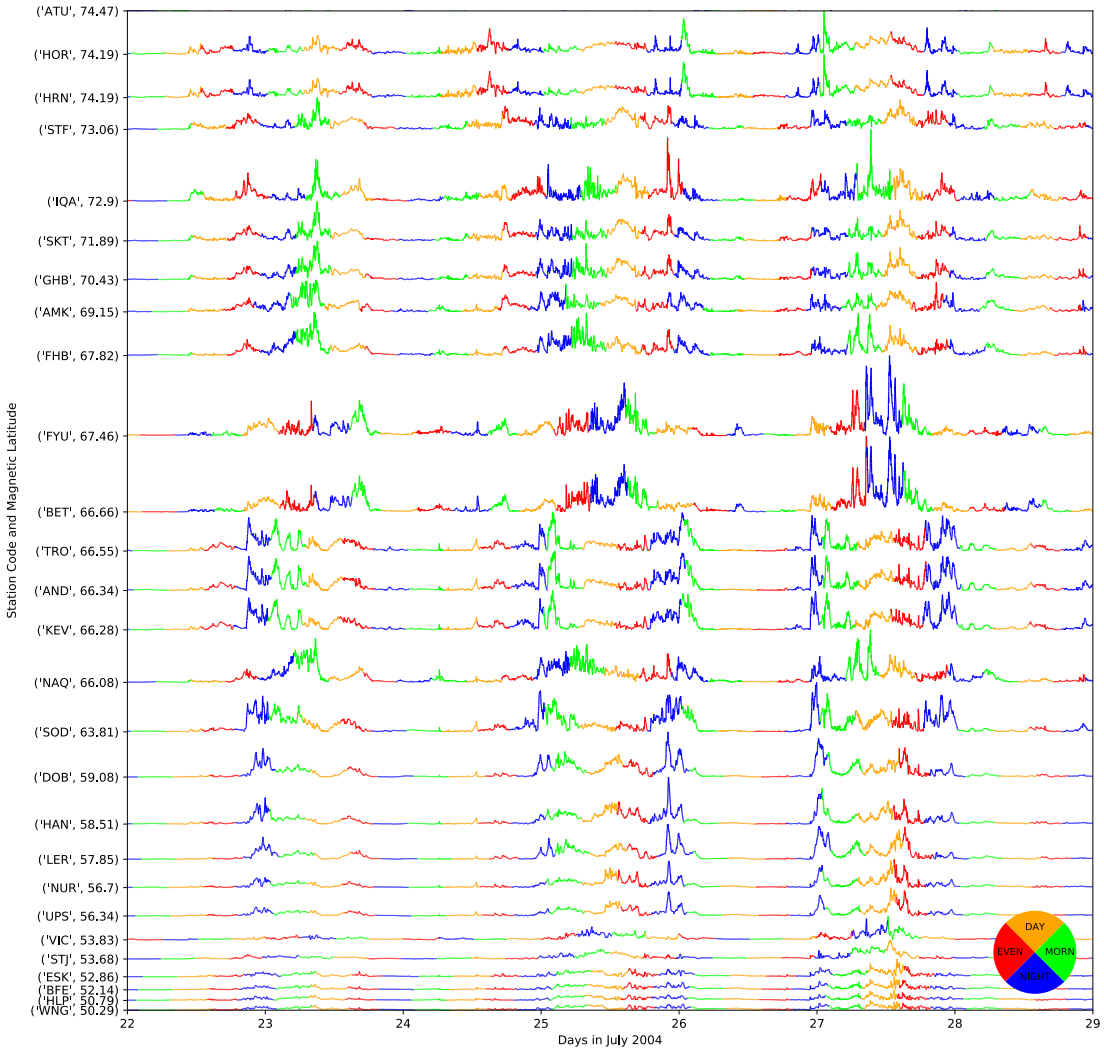

Figure 3.2. Ground SuperMAG magnetometer data outlining the geomagnetic disturbances measured by ground stations above 50° magnetic latitude for the storm period 22-29 July 2004. The perturbations are offset so that they are ordered by latitude, and all use the same scaling, with the largest value of any of the series reaching >4,000 nT. The colour wheel indicates the local time sector. The 3-letter acronyms define the SuperMAG station codes.

3.3.1 IMF B_z and the Sym-H Index

IMF B_z and Sym-H index data have been previously described in Chapter 2; here we discuss how they relate to this study. The IMF B_z component was obtained from 1-minute averaged OMNI data, which during 22-29 July 2004 used data predominantly provided by the ACE and Wind satellites propagated to the bow shock nose in the magnetosphere. Data were lagged by 15 minutes to represent the response time from the bow shock to the FAC system. This period is suggested by Vennerstrøm et al. (2002), and was also found experimentally in this study when correlating the FAC magnetic latitudes to IMF B_z with respect to time, that is, the best correlation occurred when adding a lag of $\sim$15 minutes to the IMF B_z data (see Section 3.4). This is also similar to the reconfiguration timescale for ionospheric convection (Cowley & Lockwood 1992; Lockwood & Morley 2004), due to the evolution of Region 1 FACs as the open-closed field line boundary evolves towards an equilibrium configuration (see for example, Freeman (2003)). It should be noted that there was a secondary peak around $\sim$45 minutes, which is thought to be related to the propagation time to reach the nightside (see for example: Bargatze et al. (1985); Freeman & Morley (2009)). Figure 3.3 shows the degree of correlation between the IMF B_z and FAC magnetic latitudes for lagging the IMF B_z, using the coefficient of determination, R^2, as described in Section 3.4. Peaks in correlation near 15 and 45 minutes can be seen in each storm.

For the storm intensities seen in this study the Sym-H index can essentially be treated as a high-resolution Dst index (Wanliss & Showalter 2006), providing 1-minute resolution measurements. The Sym-H index was also used to separate the storms into three events, with a condition of 0 nT adopted to define the beginning and end of each storm (note this is conservative, Gonzalez et al. (1994) use -30 nT).

3.3.2 Calculating FACs with CHAMP

Filtered 1 Hz magnetic field data are obtained using CHAMP's fluxgate magnetometer (Reigber et al. 2002) as detailed in Chapter 2. The data were provided in Earth-fixed local NEC geographic coordinates, where x is northward, y is eastward and z is pointing towards the Earth's centre of gravity (see Section 2.5 in Chapter 2 for a description of this coordinate system). During July 2004 the mean altitude of CHAMP was 387 km.

A similar method to that adopted by Wang et al. (2005) (and many other studies,

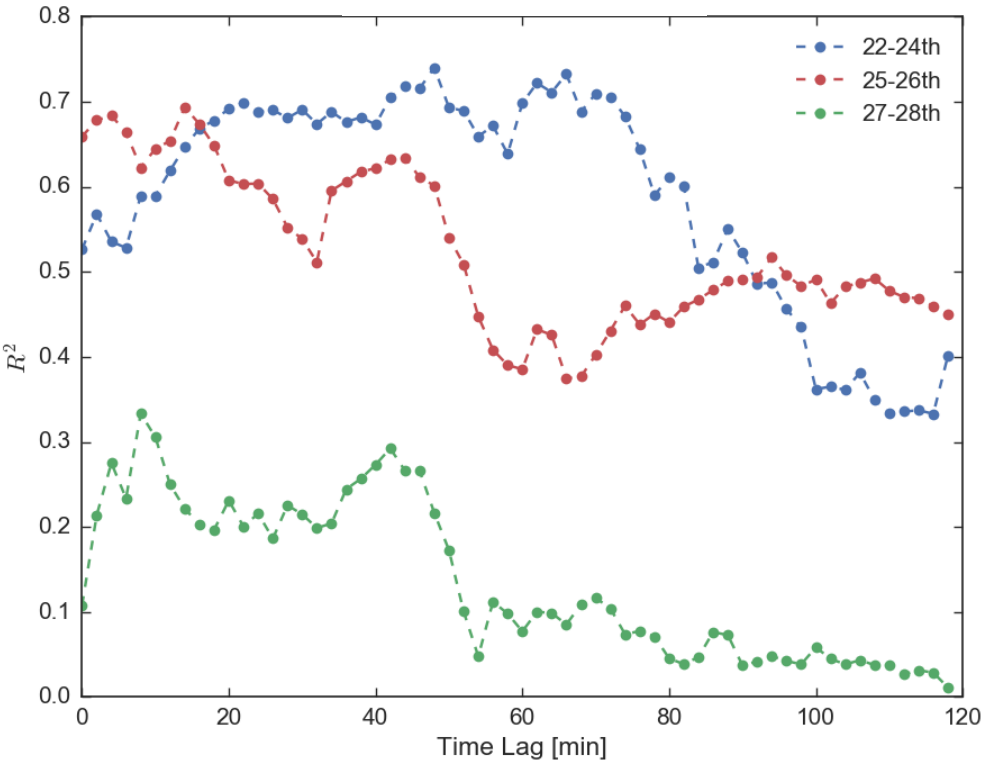

Figure 3.3. The coefficient of determination, R^2, between IMF B_z and FAC magnetic latitudes for shifting the IMF B_z with respect to time for no lag up to a 2-hour lag. The storm period has been separated into its respective three storms, encompassing the 22-24th (blue), 25-26th (red) and 27-28th (green). The data are not binned by magnetic latitude.

see Iijima (2013) and references therein) was applied to derive the FAC densities from CHAMP magnetic field data. Here, the magnetic field vector components in the NEC frame are typically transformed into the Mean Field-Aligned (MFA) frame, where z lies along the magnetic field line pointing from the southern to the northern hemisphere, y is perpendicular to the magnetic meridian and is primarily eastward, and x points outwards completing the coordinate system (Ritter et al. 2013). Then, by computing the curl of the magnetic field using Ampère's law (see Equation 1.2 in Chapter 1) in this new coordinate frame, the current density of the FAC becomes dependent on two field components:

$$j_z = \frac{1}{\mu_o}\left(\frac{\partial B_y}{\partial x} - \frac{\partial B_x}{\partial y}\right) \tag{3.1}$$

where j_z is the field-aligned current density, B_x and B_y are the transverse magnetic field

vector components generated by the currents and μ_o is the permeability of free space.

Although CHAMP is a single satellite system, by assuming the current sheet as non-moving during the intersection of the satellite and FAC sheet due to the high velocity of the former, the perpendicular component to the current sheet is cancelled out and current density dependencies reduce to a discrete temporal relation (Lühr et al. 1996):

$$j_z = \frac{1}{\mu_o v_x} \frac{\Delta B_y}{\Delta t} \tag{3.2}$$

where B_y is the eastward component of the magnetic field and v_x is the northward component of the satellite velocity. Due to the high inclination of the CHAMP orbit its speed is interchangeable with v_x, and as over the storm time interval this varies little we use the average, 7.68 km s^{-1}. We use the B_y component of the FA frame (see Section 2.5), which is an approximation of the MFA coordinate system calculated with the IGRF field to extract the main field direction. Here, z points downwards along the main field, x is positive towards geomagnetic North and y is positive in the direction of geomagnetic East. This is described in full in Section 2.5.1 in Chapter 2.

To obtain the magnetic deflection of this component, ΔB_y, a Savitzky-Golay filter (Press et al. 1992) was used in this study to subtract a running background representative of the Earth's magnetic field. A Savitzky-Golay filter fits a low-degree polynomial using least squares over sequential samples of data, specified by a window size; we iteratively chose a window size of 31 minutes with a polynomial order of 6. Any missing data were interpolated to 1-second intervals, and a low-pass Butterworth filter (similar to a low-pass filter but with a flatter response in the passband frequency range) was applied with the 20-second (150 km wavelength) cutoff period proposed by Wang et al. (2005) to remove contamination in the magnetic field deflections from Alfvén waves (Lühr et al. 1994; Wang et al. 2005) and ensure the FAC measured is stationary (Ritter et al. 2013). The absolute FAC densities were used, with a lower limit of 0.1 μA m^{-2} imposed to remove quiet-time FACs (Peria et al. 2013). It should be noted that filtering and thresholding ensure we are measuring distributed, spatially-integrated FACs, as the processes change the response and spacing of the FACs as well as removing short-scale artefacts (see Wang et al. (2005) for a full description of the method).

The magnetic latitude of the FAC was obtained from the location of CHAMP at the time of the measurement, and was calculated using the Apex and Quasi-Dipole magnetic

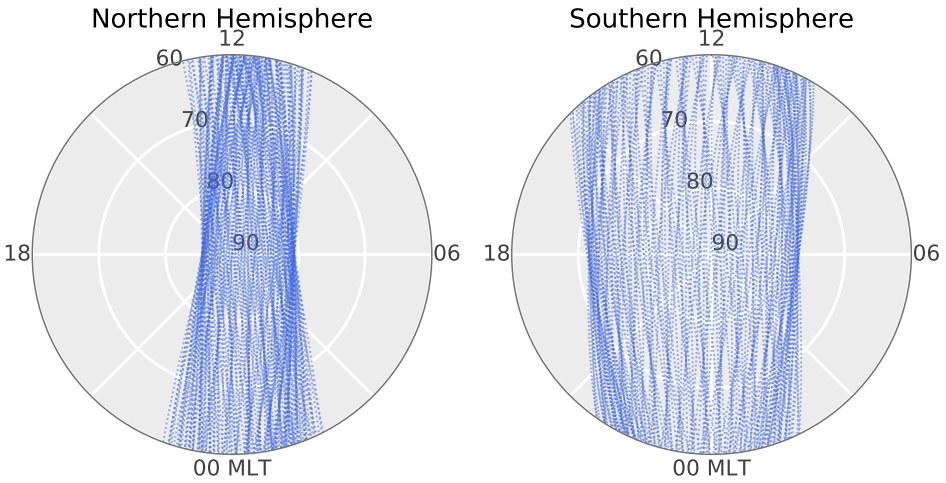

Figure 3.4. CHAMP's orbit in solar magnetic coordinates during the 22-29 July 2004 storm time interval (see Section 2.5 in Chapter 2 for a description of this coordinate system).

field model described by Emmert et al. (2010*b*)[2]. Data were separated by dayside and nightside sectors using their MLT. Northern and southern hemisphere data were superimposed, due to the similarity in magnetic latitudes with respect to time when splitting by time sector. However, it should be noted that without a visual inspection of the data it is not advisable to combine hemispheric data given the large asymmetries that can be introduced due to, for example, IMF B_y.

We also note that CHAMP as a single satellite system has obvious sampling limitations, measuring a restricted range of longitudes at a certain time, however, the key characteristics of the FAC system can still be inferred from what we do sample. The orbit is near-polar with a 1-hour precession in local time per 11 days, translating to a limited local time range (1-1.5 hours on the dayside and nightside sectors) for the sequence of storms in this study. However, during this storm time interval CHAMP's orbit is approximately noon-midnight aligned, which allows determination of the currents in locations meaningful to the study. This is demonstrated in Figure 3.4, which shows CHAMP's orbit during the 22-29 July 2004 storm time interval in a solar magnetic coordinate frame with respect to MLT.

[2]Available from the DEOS Thermosphere web server for satellite drag observations, see Chapter 2.

3.3.3 Measuring GMD perturbations with the SuperMAG Consortium

The SuperMAG Consortium (Gjerloev 2012) ground-based magnetometer data have been previously discussed in Chapter 2. Ground magnetic field perturbations were provided in geomagnetic NEZ (North, East, Vertical down) coordinates, with 1-minute resolution and a baseline subtracted (Gjerloev 2012). The focus of GMD component in this study is the peak magnetic perturbation, ΔB, as defined in Chapter 2.

At the time of the CHAMP FAC measurement, the ground fluctuation resulting from that FAC should be nearly simultaneous, at least within the resolution of SuperMAG data, thus the SuperMAG data are interpolated to the CHAMP FAC measurement times. When comparing GMDs to the indices we assume the GMD occurs in the same time sector as the FAC (dayside or nightside), as we are interested in global mechanisms and are applying the method of Wang et al. (2006) to GMDs. When comparing the FACs to GMDs, however, we are testing whether there is a local association between FACs and GMDs. We expect the nightside FACs and GMDs to be substorm-related, where the primary current system is the SCW (see Section 1.4.7 in Chapter 1). We assume the SCW to be a large-scale current system closing through a westward current sheet in the auroral zone, as described by McPherron et al. (1973) (see also Chu et al. (2014)). Previous studies have shown that the typical local time extent of the SCW is of order 2 hours (Lester et al. 1984; Vagina & Sergeev 1996; Liu et al. 2013*a*). Though this large-scale model has been successful in explaining many ground-based observations (see for example, Kepko et al. (2015) and references therein), it should be noted that other recent work has confirmed that the SCW can have sub-structure that may not be predominantly East-West aligned (see for example, Forsyth et al. (2014)). However, assuming the idealised model described above, we consider only the SuperMAG stations used at any given time that lie within a 2-hour local time window centred on the CHAMP spacecraft ($\pm 15^\circ$ magnetic longitude).

All stations in both hemispheres above 50° magnetic latitude are considered, which translated to 105 working stations during the 22-29 July 2004 storm time interval. Northern and southern hemisphere data were also superimposed due to the similarity in magnetic latitudes with respect to time, which also increased the latitudinal coverage (a limitation of the dataset). The peak ΔB at the time of each FAC measurement was recorded out of these stations, along with the magnetic latitude of that station to create a dataset of peak ΔB measurements and their corresponding magnetic latitudes.

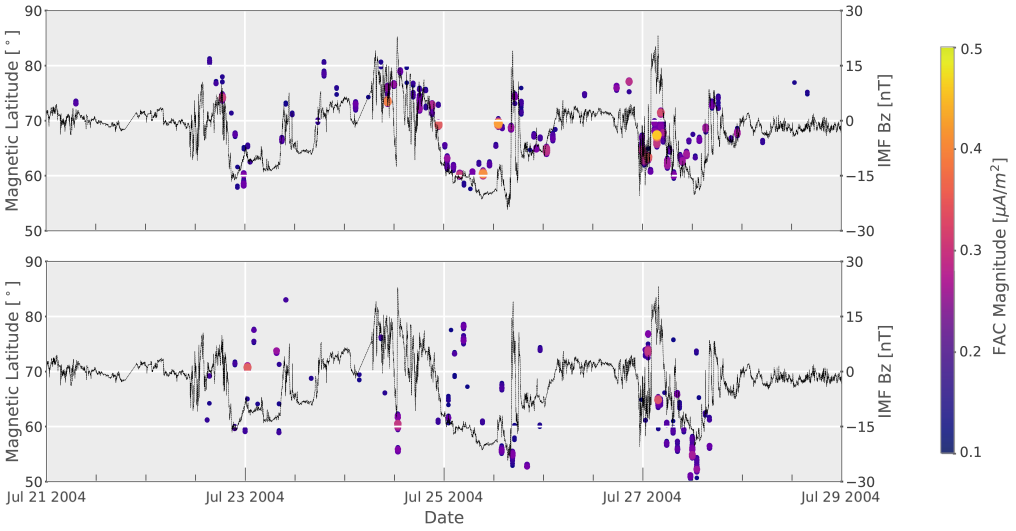

Figure 3.5. IMF B_z (black line, right y-axis) with overlaid FAC magnetic latitudes (left y-axis) for dayside (top) and nightside (bottom) FACs during the 22-29 July 2004 storm time interval from 0 UT (shared x-axis). The colour bar denotes the FAC current density magnitudes, limited to 0.1-0.5 μA m^{-2} to exclude quiet-time FACs and highlight the variation in values.

3.4 Results

Figure 3.5 shows IMF B_z (black line) with overlaid FAC magnetic latitudes (scatter plot) during the 22-29 July 2004 storm time interval, where the colour bar denotes the absolute magnitude of the FAC current density. FACs are separated by dayside (top plot) and nightside (bottom plot) time sectors. Quantitative assessments of the correlations between the dayside and nightside FAC magnetic latitudes and magnitudes with both IMF B_z and the Sym-H index for each storm are obtained using Ordinary Least Squares linear regression and the coefficient of determination, R^2, as outlined in Table 3.1. This is simply the square of the Pearson product-moment correlation coefficient (r), and gives the fraction of the variation explained by the linear model indicating the degree to which the data follow a fitted linear regression line. Data in Table 3.1 are 1°-binned by magnetic latitude and averaged to highlight latitudinal trends, as adopted by Wang et al. (2006). It should be emphasised that R^2 is seen as a 'qualitative' measure of these physical relations, and we are not concerned with quantifying beyond this depth in this study.

Figure 3.5 and Table 3.1 indicate strong correlations between IMF B_z and the magnetic latitudes of dayside FACs for the first and second storms, where greater southward IMF

Table 3.1. The coefficient of determination, R^2, is a measure of the linear correlation between IMF B_z and the Sym-H index and 1°-binned dayside and nightside FAC magnetic latitudes and magnitudes for each of the three storms during the 22-29 July 2004 storm time interval. Values in bold indicate a strong correlation ($r \gtrsim 0.7$).

Index	Time Sector	Storm	R^2 of FAC magnetic latitude	R^2 of FAC magnitude
IMF B_z	Dayside	1	**0.85**	0.05
		2	**0.84**	0.01
		3	0.23	0.00
IMF B_z	Nightside	1	0.17	0.04
		2	0.06	0.11
		3	0.12	0.00
Sym-H Index	Dayside	1	0.42	0.06
		2	**0.66**	0.00
		3	0.14	0.05
Sym-H Index	Nightside	1	0.06	0.11
		2	0.00	0.00
		3	**0.62**	0.02

B_z correlates with more equatorward dayside FACs ($R^2 = 0.85$ and 0.84 respectively). The largest FACs occur on the dayside mostly during periods of large southward IMF B_z, excluding the largest measured FAC, 0.46 μA m^{-2} on the 27th at 03:29 UT (as outlined in Table 3.3), which follows a period of large southward IMF B_z. In the nightside sector there is much spread, suggesting the presence of multiple FAC sheets, and poor correlations with IMF B_z. The nightside FACs descend to lower magnetic latitudes than the dayside, reaching ∼50° in the final storm, and are weaker, peaking at 0.34 μA m^{-2} on the 23rd at 00:31 UT during the first storm. Table 3.1 reveals no correlations between IMF B_z and dayside or nightside FAC magnitudes.

Figure 3.6 uses the same format as Figure 3.5, demonstrating correlations instead with the Sym-H index. Figure 3.6 and Table 3.1 suggest dayside FACs in the first and second storms are better correlated with the Sym-H index ($R^2 = 0.66$ for the second storm) than their nightside counterparts, with Figure 3.6 highlighting a 2-3 hour lag between dayside FACs and the Sym-H index. The last storm, however, has a stronger correlation between nightside FACs and the Sym-H index ($R^2 = 0.62$). The nightside FACs also descend sequentially lower with increasing storm intensity, unlike the dayside FACs. The peak FAC magnitude per storm increases with storm intensity, though Figure 3.6 shows no correlation between FAC magnitude maxima and the Sym-H index minima, and Table 3.1 details poor correlations between FAC magnitude and the Sym-H index.

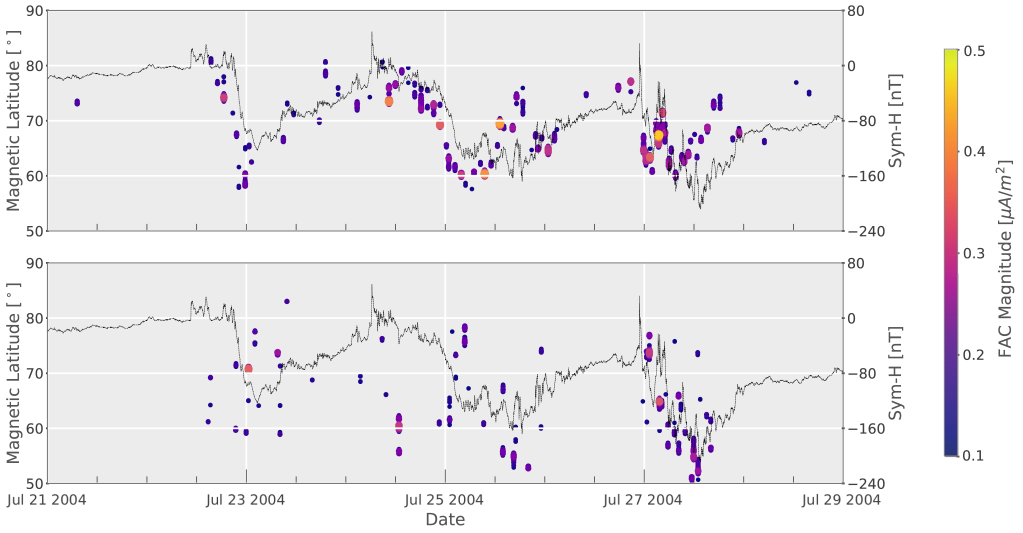

Figure 3.6. Sym-H index (black line, right y-axis) with overlaid FAC magnetic latitudes (left y-axis) for dayside (top) and nightside (bottom) FACs during the 22-29 July 2004 storm time interval from 0 UT (shared x-axis). The colour bar denotes the FAC current density magnitudes, limited to 0.1-0.5 μA m^{-2} to exclude quiet-time FACs and highlight the variation in values.

Figure 3.7 shows IMF B_z (top, black line) and the Sym-H index (bottom, black line) with overlaid GMD magnetic latitudes observed at the time of the FAC CHAMP measurements (scatter plot) during the 22-29 July 2004 storm time interval. The colour bar denotes the magnitude of the GMD and whether it is located in the dayside (red) or nightside (blue) sector. The size of the markers is also scaled to the GMD magnitude, providing an aid when comparing between dayside and nightside GMD magnitudes. Table 3.2, similarly to Table 3.1, outlines the correlations between the indices and both dayside and nightside GMD magnetic latitudes and magnitudes for each storm.

As shown by the red markers in the top plot of Figure 3.7 and quantitatively in Table 3.2, there is a strong correlation between dayside GMD magnetic latitudes and IMF B_z during the first two storms ($R^2 = 0.67$ and 0.71), and no correlation in the nightside. The dayside GMDs are larger than their nightside counterparts during northward IMF B_z, reductions in magnitude of southward IMF B_z and lower geomagnetic activity, although not as large relative to the strongest nightside GMDs during the storm interval. They are on average more poleward and tend to precede nightside GMDs. In contrast, the nightside GMD magnitudes (in blue) are strongly correlated with southward IMF B_z (R^2

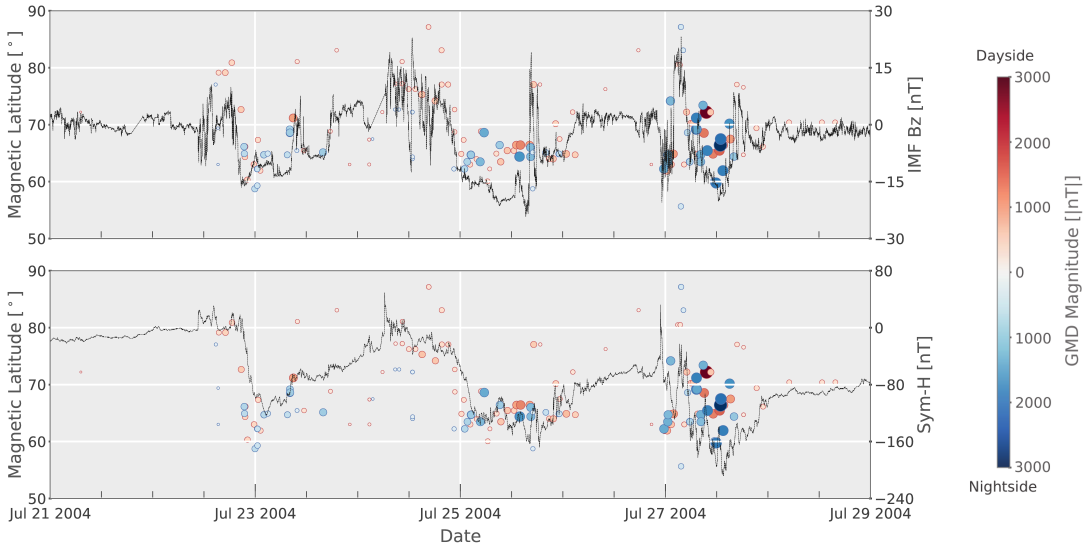

Figure 3.7. IMF B_z (top, right y-axis, black line) and the Sym-H index (bottom, right y-axis, black line) with overlaid GMD magnetic latitudes observed at the time of the FAC CHAMP measurements (left y-axis) during the 22-29 July 2004 storm time interval from 0 UT (shared x-axis). The colour bar (logged scale) denotes the magnitude of the GMD and whether it is located in the dayside (red) or nightside (blue) sector, and is limited between 100 nT and 3,000 nT to depict the variation in values. The size of the markers is scaled to the GMD magnitude.

= 0.71, 0.49, 0.73 for each respective storm). There is again some correlation with the Sym-H index and magnetic latitudes, and Figure 3.7 shows stronger GMDs occurring during periods of greater storm intensity, but no real trends can be drawn from Table 3.2. The correlations between the Sym-H index and dayside GMD magnitudes are very poor, however, the nightside GMDs show a strong correlation for each of the storms (R^2 = 0.49, 0.62 and 0.57 respectively). Nightside GMDs, like their FAC counterparts, reach to lower magnetic latitudes than the dayside GMDs. There is also a noticeable threshold to the equatorward GMDs, the lowest reaching ∼55° on the 27th, higher than the respective lowest FAC magnetic latitude by 5°.

Table 3.3 shows the maximum FAC and peak GMD magnitude for each storm, including the GMDs observed at the time of CHAMP FAC measurements ('this study') and for all GMD data available ('all data'), with their corresponding magnetic latitude, date, time and time sector. The peak FACs and GMDs occur during periods of more strongly negative Sym-H index and predominantly southward IMF B_z. The peak FAC magnitude increases with storm intensity, with the FAC magnetic latitude descending, though there is no relationship seen in its time sector, and it is not always coincidental with the Sym-H

Table 3.2. The coefficient of determination, R^2, is a measure of the linear correlation between IMF B_z and the Sym-H index and 1°-binned dayside and nightside GMD magnetic latitudes and magnitudes for each of the three storms during the 22-29 July 2004 storm time interval. Values in bold highlight a strong correlation ($r \gtrsim 0.7$).

Index	Time Sector	Storm	R^2 of GMD magnetic latitude	R^2 of GMD magnitude
IMF B_z	Dayside	1	**0.67**	0.20
		2	**0.71**	0.07
		3	0.38	0.39
IMF B_z	Nightside	1	0.10	**0.71**
		2	0.18	**0.49**
		3	0.18	**0.73**
Sym-H Index	Dayside	1	0.14	0.00
		2	**0.57**	0.07
		3	0.01	0.09
Sym-H Index	Nightside	1	0.45	**0.49**
		2	0.21	**0.62**
		3	0.20	**0.57**

Table 3.3. The maximum FAC and peak GMD magnitudes per storm, including the GMDs observed at the time of CHAMP FAC measurements ('this study') and for all data available ('all data'), with their corresponding magnetic latitude, date, time and time sector. The SuperMAG station code that measured the GMD is also shown.

Data Type	Storm	Magnitude	Magnetic Latitude [°]	Date and Time [UT]	Time Sector
FAC	1	0.34	70.8	23rd, 00:31:32	Nightside
	2	0.41 μA m^{-2}	69.5	25th, 13:10:35	Dayside
	3	0.46	67.4	27th, 03:28:38	Dayside
GMD	1	1270	71.2 (B19)	23rd, 08:55:18	Dayside
(this study)	2	1829 nT	64.4 (MCQ)	25th, 13:53:35	Nightside
	3	3134	72.2 (B23)	27th, 09:37:36	Dayside
GMD	1	1816	66.1 (DAW)	23rd, 07:59:00	Nightside
(all data)	2	3131 nT	66.1 (DAW)	25th, 14:38:00	Nightside
	3	4392	66.8 (GIM)	27th, 12:49:00	Nightside

index minima of the three storms. The peak GMD also increases with storm intensity, and occurs between 1-8 hours after the peak FACs and near the Sym-H index minima of the storms. There is no relationship seen in the magnetic latitude or time sector. However, this latter GMD result is limited by interpolating the abundant SuperMAG data to the scarce CHAMP FAC measurements, if we instead use all of the SuperMAG data available during the storm time interval (this is represented solely in Table 3.3) we see that the largest GMDs occur in the nightside and at ∼66° magnetic latitude.

3.5 Discussion

3.5.1 Correlations between FAC magnitude, FAC magnetic latitude, IMF B_z and the Sym-H index

IMF B_z is strongly correlated with dayside FAC magnetic latitudes and is known to be closely related to FAC generation (Cheng et al. 2013), due to the process of dayside reconnection where magnetopause currents feed into Region 1 FACs (also seen in Wang et al. (2006) for higher storm intensities). Most of the larger dayside FACs occur during periods of large southward IMF B_z, consistent with reports of northward IMF B_z suppressing FAC magnitudes (Friis-Christensen et al. 1985). However, a notable exception occurs during the final storm, which also produced a poor correlation with FAC magnetic latitude (R^2 = 0.23). Previous statistical studies using CHAMP data have shown FAC total magnitudes increasing with southward IMF B_z (Juusola et al. 2009) and larger IMF amplitudes (Juusola et al. 2014), however there is no apparent magnitude correlation between IMF B_z and FACs in the present study. Figure 3.6 and Table 3.3 instead show the peak FAC magnitude per storm increases with storm intensity, though this does not always coincide with the deepest Sym-H index minima. It is possible that some significant FACs may not have been sampled by CHAMP due to its ∼90-minute orbit and point-measurements along its orbital track, however, this poor correlation with magnitude is also seen by Wang et al. (2006), who instead found a better correlation between dayside FAC strength and solar wind pressure, as strong compressions cause strong FACs. Gjerloev et al. (2011) also found a poor correlation with both IMF B_z and the Sym-H index and dayside FAC magnitudes, and a variable relationship with nightside FACs during storm conditions. The Sym-H index is less correlated with dayside FACs than IMF B_z, indeed there is a 2-3 hour lag between the FACs and the index in Figure 3.6 as the ring current response requires inward

transport of plasma driven by enhanced convection and substorm injections (Daglis et al. 1999).

The nightside FACs are more equatorward than those on the dayside, extending to ∼50° in the final storm, in agreement with the statistical study of Xiong et al. (2014) for a storm of similar intensity. This asymmetry is driven by the auroral oval, to which nightside FACs are tied (Mauk & Zanetti 1987), and further exaggerated by the time of year as nightside FACs are more equatorward in summer, and dayside FACs are more poleward (Ohtani et al. 2005). The nightside FACs descend with decreasing Sym-H index in Figure 3.6, as the auroral oval latitude location depends on storm intensity (see for example, Xiong et al. (2014) and references therein). This is not the case on the dayside, where it is IMF B_z that directly controls the expansion of the auroral oval (Burch 1973, 1979). Intervals of strongly negative IMF B_z also coincide with the most equatorward nightside FACs in the first and second storms in Figure 3.5, which may be suggestive of tail reconnection as a secondary source or driver. Indeed, Tsyganenko & Stern (1996) found that Region 1 currents present in the midnight sector are driven by the magnetotail. There are also multiple substorms throughout the storm time interval (Frey et al. 2004; Frey & Mende 2006; Nakamura et al. 2015; Forsyth et al. 2015), where a substorm indicates nightside reconnection in the magnetotail (Baker et al. 1996; Milan et al. 2007), and nightside FACs are known to map to both the ring and tail current systems (Mauk & Zanetti 1987; Wang et al. 2006). However, the influence of dayside reconnection is still apparent as the nightside FAC magnitudes are weaker than the dayside (Milan 2013), likely due to the higher conductivity of the latter (Wang et al. 2005).

The nightside FAC magnetic latitudes during the last storm in Table 3.1 show a correlation with the Sym-H index ($R^2 = 0.62$), which is of particular interest as it suggests the correlation improving with storm intensity. Indeed, Wang et al. (2006), studying storms of significantly higher intensities, saw magnetic latitudes of nightside FACs follow the Dst index more closely. This improved correlation with the Sym-H index may be in part the result of improved observations as the ring current migrates inwards with increased storm intensity, but also suggests the increasing influence of the partial ring current in the system, as Region 2 FACs may begin to dominate. Region 2 FACs are typically lower in magnitude than Region 1 FACs (Iijima 2013), but they are also more equatorward (FACs descend to ∼50° during the final storm), and so are more likely to contribute directly to severe GMDs (Tamao 1986). Their magnitude may also have been higher during the final

storm due to spikes in solar wind pressure (seen in Figure 3.1), which can drive a sudden storm commencement causing particle precipitation from the ring current, forcing Region 2 FACs equatorward (Xiong et al. 2014) and increasing their intensity (Nakano et al. 2009). Ngwira et al. (2012) also saw an increase in the electron density in the F region ionosphere during the final two storms, and thus an increase in ionospheric conductivity known to also increase the magnitude of Region 2 FACs (Zheng et al. 2008). It should, however, be noted that as the entire system moves equatorward, we may also sample some Region 1 FACs at lower latitudes. A statistical analysis of many storms is needed to verify this, and is left as future work.

3.5.2 Correlations between GMD magnitude, GMD magnetic latitude, IMF B_z and the Sym-H index

Figure 3.7 and Table 3.2 show dayside GMD magnetic latitudes during the first two storms are strongly influenced by solar wind driving like their FAC counterparts, are on average more poleward and occur during intervals of northward turning IMF B_z. Nightside GMDs do not share this correlation with magnetic latitude, are more equatorward and occur during periods of southward IMF B_z. A trend of poleward dayside GMDs preceding equatorward nightside GMDs at the start of each storm is a strong indication of a system driven by reconnection at the lobes. Dayside reconnection reconfigures open magnetic flux in the polar cap, driving twin-cell convection (Cowley & Lockwood 1992; Lockwood & Cowley 1999; Lockwood & Morley 2004), and expanding the auroral oval, demonstrated by the equatorward movement of FACs with increasing storm intensity. This is followed by a delay in which a build up of open magnetic flux in the magnetotail, shown by the expansion of the polar cap, leads to eventual tail reconnection (Milan et al. 2003, 2007) subsequently driving nightside GMDs (Viljanen et al. 2006).

This link between tail reconnection and nightside GMDs is also shown by the strong correlation between the magnitudes of nightside GMDs and IMF B_z for each storm (see Table 3.2), the former strongest during greater southward IMF B_z (Snekvik et al. 2012). This also supports a relationship between substorms and nightside GMDs, as substorm magnitude depends on the strength of the solar wind driver (Tanskanen et al. 2005; Morley & Freeman 2007; Li et al. 2013); though this is further complicated by the dependence of substorm magnitude on the size of the auroral oval (Milan et al. 2009; Milan 2009). However, if intervals of IMF B_z lead to tail reconnection, and the largest GMDs are

indicative of substorms, then this supports a link between tail reconnection and substorms. Indeed, the largest GMDs occur in the nightside, peaking at a markedly large 4,392 nT on the 27th at 12:49 UT (as recorded in Table 3.3), within minutes of a particularly large substorm (see Nakamura et al. (2015), and the AE index in Figure 3.1 spiking at 12:47 UT). Nightside GMD magnitudes during all three storms also show a correlation with the Sym-H index ($R^2 = 0.49$, 0.62 and 0.57 respectively). As well as the influence of tail reconnection, the magnitudes of the nightside GMDs are dependent on the ring current. This supports the common assumption that the intensification of GMD magnitudes is related to storm intensity as measured by the Dst index (see for example: Watermann & Gleisner (2009); Ngwira et al. (2013); Woodroffe et al. (2016)), and IMF B_z (inferred from the relationship between the polar cap index and geomagnetic disturbances, see for example, Stauning (2013)).

The maximum GMD per storm increases with storm intensity and saturates at $\sim$66°, occurring between 1-9 hours after the peak FACs (see Table 3.3) and near the Sym-H index minima of the storms. However, Table 3.2 shows the correlation between nightside GMD magnetic latitudes and the Sym-H index decreasing with storm intensity, with very poor correlations for the second and third storms. This may be due to limiting SuperMAG data to CHAMP FAC measurement times or the coverage itself, or instead suggests (temporal and/or spatial) conjunctions only exist between the largest GMDs and Sym-H index minima.

3.5.3 Correlations between FAC magnitude, FAC magnetic latitude, GMD magnitude and GMD magnetic latitude

Table 3.4 shows the correlations between FACs and GMDs when restricting GMDs by ±15° magnetic longitude from the respective FAC locations. The majority of coefficients in Table 3.4 show no significant or strong correlations. However, though the correlations are weaker ($r < 0.7$), we can still identify a linear relationship when correlating the FAC magnetic latitudes and GMD magnitudes, particularly on the dayside during the first storm ($R^2 = 0.47$), that is, a decreasing FAC magnetic latitude corresponds to a larger GMD magnitude. We expect poorer correlations in Table 3.4 due to the removal of binning by 1° magnetic latitude. To increase the number of data points we combine all three storms, and find the correlation may indicate some linearity ($R^2 = 0.29$). To test for significance we adopt the methodology of Lockwood (2002) and first calculate the autocorrelation, which is the

Table 3.4. The coefficient of determination, R^2, is a measure of the linear correlation between respective dayside and nightside FAC and GMD magnetic latitudes and magnitudes for each of the three storms during the 22-29 July 2004 storm time interval. FAC and GMD data have not been binned for these correlations.

Time Sector	Storm	FAC & GMD magnetic latitudes	FAC magnetic latitude & GMD magnitude	FAC magnitude & GMD magnetic latitude	FAC & GMD magnitudes
Dayside	1	0.04	0.47	0.01	0.03
	2	0.06	0.04	0.00	0.02
	3	0.00	0.22	0.02	0.00
Nightside	1	0.01	0.00	0.07	0.02
	2	0.06	0.39	0.01	0.01
	3	0.06	0.02	0.01	0.00

Table 3.5. The Student's t-statistic is a measure of the significance of the linear correlation between respective dayside and nightside FAC and GMD magnetic latitudes and magnitudes for each of the three storms during the 22-29 July 2004 storm time interval. FAC and GMD data have not been binned for these correlations. If the t-statistic is greater than the critical value of a two-tail test with significance less than 0.05, given the number of degrees of freedom, there is a significant linear correlation. In this table this holds true for two relationships: 3.28 > 1.70 and 3.18 >1.65.

Time Sector	FAC & GMD magnetic latitudes	FAC magnetic latitude & GMD magnitude	FAC magnitude & GMD magnetic latitude	FAC & GMD magnitudes
Dayside	0.02	**3.28**	0.79	**3.18**
Nightside	1.07	0.01	0.74	0.44

correlation coefficient of each series correlated with itself when offset by one data point. Our calculated values are high, thus we correct for the degrees of freedom[3], and use this to calculate the Student's t statistic[4]. This t statistic is compared to a critical value of a two-tail test for the number of data points (see Sheskin (2003) for these critical values) and a significance of 0.05, corresponding to a 95% confidence level. Our R^2 of 0.29 is statistically significant (p value less than 0.05) after accounting for autocorrelation in each series (Lockwood 2002). These statistics are outlined in Table 3.5.

With this in mind, the auroral oval location, strongly influenced by IMF B_z on the dayside (Burch 1973, 1979) and where FACs are typically embedded (Wang et al. 2005),

[3] $n_{eff} = n(1-a)/(1+a)$ where a is the lag-1 autocorrelation and n is the number of data points.
[4] $t = |r|(n_{eff}-2)/(1-r^2)^{0.5}$

is a reasonable indication of the dayside GMD response. This is further supported by the domination of solar wind driving on the location of the FACs and GMDs seen in Tables 3.1 and 3.2, though it should be noted that these relationships were not seen during the final storm. Tables 3.4 and 3.5 also suggest that FAC magnetic latitude can be considered as the only possible predictor or indicator of the system, and its magnitude plays no part in the location or extent of the GMD generated on the dayside or the nightside. This is contrary to a general assumption that stronger FACs generate stronger ionospheric currents, and thus stronger GMDs (see for example: Kamide (1982); Tamao (1986); Wu & Stening (1991); Laundal et al. (2015); Adhikari et al. (2017)).

This implies that the relationship between FACs and GMDs is both non-local and non-linear. A correlation (albeit low in this study) between dayside FAC magnetic latitudes and GMD intensities is expected; the presence of lower magnetic latitude FACs is most likely due to magnetopause erosion, causing a deposition of energy into the magnetosphere, in turn transmitting magnetic stresses leading to GMDs. The correlation may be lower than expected due to a dependence not only on the current magnetospheric state, but also the history, particularly in the case of substorms which drive nightside activity. The dynamics of substorms lead to rapid reconfiguration of magnetotail geometry, which can lead to strong, transient magnetic disturbances that may propagate across field lines, complicating source identification, as well as the production of enhanced ionospheric conductance, which strongly affects the magnitude of resultant GMDs. This may explain the lack of both dayside and nightside correlations in Tables 3.4 and 3.5.

As stated previously, there are also multiple processes involved that may hide any magnitude correlations. One such example is the tendency for FACs to increase in both magnitude and width (Wang et al. 2005), the latter not investigated here but which would certainly mask the contribution of the former. These current systems involved are large, and there may be variable time lags between FACs and GMDs that we cannot account for in this study. A poor magnitude correlation may also be the result of a varying Pedersen/Hall conductance ratio (Watermann et al. 2003), a ratio proportional to the FAC contribution to the ionospheric eddy current (Tamao 1986). Although, the relationship between FACs and GMDs is complicated and dependent on more than the conductance ratio, see for example the model described by Lysak & Yoshikawa (2006). Local effects, such as the time of year, during the event may also play a role. Specifically, the high conductivity from solar-illumination during quiet conditions in summer can influence the

dayside FAC magnetic latitudes and magnitudes, causing them to be more equatorward and stronger when sunlit (Wang et al. 2005). However, the former effect is small (2°), though it may be larger during active conditions. Ohtani et al. (2005) also show dayside Region 1 FACs increasing in intensity during the summer by a factor of 2-3, which may be affecting their correlation with GMD magnitude.

3.5.4 Potential effects of prior activity on response

During the final storm the nightside FAC magnetic latitudes are strongly correlated with the Sym-H index, whilst dayside FAC and GMD magnetic latitudes become poorly correlated with IMF B_z. This suggests these relations are only valid for higher intensity storms (such as those studied in Wang et al. (2006)), or those that follow storms as part of a sequence. In Figure 3.6 the first two storms show a delay between FACs and the Sym-H index, however, this vanishes during the final storm, and the Sym-H index correlates with nightside FAC magnetic latitudes as well as nightside GMD magnitudes. This lack of delay and increase in correlation suggest the current system is established, that is, there is memory of prior activity. There is also further evidence for this in the IMF B_z; the most southward IMF B_z occurs during the second storm, and not the final storm where the Sym-H index is lowest and the FAC and GMD magnitudes are largest. Kozyra et al. (2002) found that in 'multistep' storm processes, such as this study, the plasma sheet population can be preconditioned (see also, Lavraud et al. (2006)), which sources the ring current and controls nightside FAC characteristics (Gjerloev et al. 2011), and can counteract less favourable storm conditions. Multistep storm processes can be driven by sequential ICMEs, preconditioning the magnetosphere-ionosphere system, with later ICMEs driving geomagnetic storms to reach deeper Sym-H index minima than the leading ICME (Benacquista et al. 2017), which in turn increases the GMD response. Similar effects have also been linked to the ionosphere-thermosphere system with higher geomagnetic activity increasing the rate of Joule heating (Aruliah et al. 1999), and strengthening ionospheric convection (Morley & Lockwood 2006), which would also amplify the GMD response.

There is also evidence supporting the dominance of the nightside sector during the final storm, which is likely the cause of such strong GMDs on the nightside. Multiple substorms occur during the storm time interval (Frey et al. 2004; Frey & Mende 2006; Nakamura et al. 2015; Forsyth et al. 2015), with two unusually large substorms on the 27th (Nakamura et al.

2015) when both the largest GMDs and FACs were observed. These substorms are driven by tail reconnection, as detailed by the correlation between nightside GMD magnitudes and IMF B_z in Table 3.2. We also see the nightside FAC magnetic latitudes and GMD magnitudes correlate with the Sym-H index, suggesting the influence of Region 2 FACs and the ring current on nightside GMD magnitude. The GMDs are largest in the nightside sector and are concurrent with the Sym-H index minima of each storm, saturating at $\sim$66°, which suggests the more equatorward Region 2 FACs may be responsible for the largest GMDs. Significantly, there is also a lack of correlation between IMF B_z and the dayside FAC and GMD magnetic latitudes during the final storm in Tables 3.1 and 3.2, again suggestive of the increased influence of the nightside sector as the main driver of FACs (and GMDs) over dayside reconnection. Preconditioning of the ring current would force a shift into a regime where the nightside sector dominates. However, this increased nightside control may be due to the increased storm intensity, implying a transitionary value in the Sym-H index between dayside and nightside mechanisms. The study of additional storms will help to clarify this.

3.6 Conclusions

The GMDs studied here reach latitudes (the lowest recorded at 55°) that could affect infrastructure in many populated regions, including mainland Europe and North America, with particularly large magnitudes given the storm intensity during the interval; the largest GMDs reaching $\sim$66° magnetic latitude and peaking above 4,000 nT in the nightside sector. Significantly, this study has suggested GMD magnitudes may be independent of FAC magnitudes, contrary to a common assumption (see for example: Kamide (1982); Tamao (1986); Wu & Stening (1991); Laundal et al. (2015); Adhikari et al. (2017)). Indeed, there is little to no correlation between the dynamics of FACs and those of nearby GMDs (most R^2 values in Table 3.4 are below 0.10) despite a clear causal chain linking them. Though we note that this may be due in part to CHAMP orbit limitations or ground magnetometer coverage, this suggests that any magnitude relationship is non-local and non-linear. This is the first study of its kind to show evidence that FACs and GMDs may have a non-local and non-linear relationship.

We find that solar wind is a significant dayside driver of FACs, which is expected considering its relation to FAC generation (Cheng et al. 2013), also shown by Wang et al.

(2006), and that this also extends to GMDs. This is likely due to the presence of lower magnetic latitude FACs from magnetopause erosion, causing a deposition of energy into the magnetosphere, in turn transmitting magnetic stresses leading to GMDs. Interestingly, despite the strong dependence of both on IMF B_z there is no correlation between FAC and GMD magnetic latitudes (see Table 3.4), which is likely an effect of their non-local relationship, or is an implication that IMF B_z is an independent driver of both FAC and GMD magnetic latitudes. IMF B_z is strongly correlated with dayside FAC and GMD magnetic latitudes for the less intense first and second storms, which may imply a Sym-H index threshold on the correlations. Indeed, Wang et al. (2006), studying storms of significantly higher intensities, saw magnetic latitudes of nightside FACs follow the Dst index more closely.

Nightside GMD magnitudes (the largest GMDs measured) are strongly controlled by IMF B_z and the Sym-H index, which is supportive of tail reconnection driving nightside GMDs. Substorm magnitude is also known to depend on the strength of the solar wind driver (see Tanskanen et al. (2005); Morley et al. (2007) and references therein), and there are multiple substorms during this period, including an unusually large substorm coinciding with the largest recorded GMD. If intervals of IMF B_z lead to tail reconnection, and the largest GMDs are indicative of substorms, then this supports a link between tail reconnection and substorms, as well as a mechanism where tail reconnection drives substorms and in turn nightside GMDs. However, as IMF B_z is most southward during the second storm, it is not an indicator of the GMD response, although the Sym-H index may be.

The nightside and ring current play greater roles during the final storm in driving the system, for the other storms the correlations are in general very poor. As mentioned, we see the influence of tail reconnection and substorms on the nightside GMD magnitudes, however, during the final storm alone the nightside FAC magnetic latitudes and GMD magnitudes both correlate with the Sym-H index, suggestive of the increasing presence of Region 2 FACs and the influence of the ring current on FACs and GMDs. The largest GMDs occur in the nightside sector and peak during the final storm, despite southward IMF B_z peaking in magnitude during the second storm. This may be an indicator of preconditioning in this system enhancing the mechanisms in place during the final storm to induce a larger GMD response, or instead shows these Sym-H index correlations (and lack of IMF B_z correlations) are only valid for storms of higher intensities, also implied

by the tighter correlations with the Dst index observed by Wang et al. (2006) studying storms of higher intensities. We note a statistical analysis of many storms is needed to verify this. This case study has provided the groundwork and methodology for such a study.

3.7 Further Work

The next stage of this research is to extend the study to a statistical analysis of many storms of similar intensity, preconditioning and peak GMD strength using the methodology established in this chapter. Due to the time span of SuperMAG magnetometers, there is an abundance of GMD data. FAC measurements are confined to the CHAMP mission life (2000-2010), although with the availability of Swarm magnetic field data (see for example, Ritter et al. (2013)) and the AMPERE FAC dataset (Milan et al. 2018) we can include FACs from 2010 onwards (2013 in the case of Swarm). Increasing the datasets of both FACs and GMDs will aid in the assessment of their correlation to each other, which is lacking in these case studies. It should also be noted that as a constellation mission Swarm uses a two-satellite FAC derivation method (Ritter et al. 2013), which does not need to assume stationary FAC sheets (like CHAMP), improving the precision of the FAC measurements.

Moreover, the presence of several FAC sheets and varieties, namely the poleward Region 1 FACs and equatorward Region 2 FACs (and even more poleward Region 0 FACs), may contaminate correlations. These relationships may be improved by separating FAC populations by region before correlating. This involves retaining the polarity of the FAC when transforming to the FA frame, and can also be aided by more advanced regression analysis that is less sensitive to outliers[5].

We are currently preparing a paper to focus on the statistical relationship between solar wind driving and FACs over many storms (Hood et al. 2018), and another focusing on the statistical relationship between FACs and GMDs, identifying extreme FACs and observing GMDs at nearby stations. We have identified 16 storms during 2000-2006 where CHAMP orbits ±2 hours within the magnetic noon-midnight meridian (see for example, Figure 3.4), with sufficient storm intensities to allow for comparison. We have amalgamated data from these storms to produce a single multi-dimensional 1-second resolution dataset, including:

[5]See for example: RANSAC and Huber regression.

date, time, magnetic latitude, MLT, FAC current density, Sym-H index, IMF B_z and solar wind pressure. The analysis and methodology discussed in this chapter is currently being applied to these storms to verify the findings of this study. Due to the null finding between FAC and GMD correlations in this chapter, the second study will focus on the importance of distance in their correlations and how this depends on their location and intensity.

Chapter 4

A neutral wind disparity in measuring Joule Heating

In the previous chapter we probed one electrodynamic aspect of FACs in the transfer of energy and circulation between the solar wind and magnetosphere-ionosphere system, namely their association with ground GMDs. However, the electromagnetic energy FACs convey to the ionosphere via Pedersen currents is also significant locally as it dissipates as Joule heating, and transfers momentum (mechanical energy) to the neutrals via ion-neutral collisions (see for example: St.-Maurice & Hanson (1982); Thayer (2000); Iijima (2013); Cowley (2000) and references therein). Indeed, Joule heating is a significant energy dissipation mechanism in the magnetosphere-ionosphere-thermosphere system (Akasofu 1981; Cierpka et al. 2000) affecting, amongst other properties, the density profile and composition of the upper atmosphere, the knowledge of which is vital to satellite orbit determination (see for example, Vallado (2001); Lühr et al. (2004); Storz et al. (2005)), and general circulation models (see for example: Deng & Ridley (2007); Huang et al. (2012)). In this chapter we therefore move away from FACs and turn our focus to Joule heating and the neutral thermospheric wind it affects.

A generalised view of ionospheric Joule heating is its equivalence to frictional heating, where the local temperature increase due to ion-neutral collisions can be approximated from the relative flow between ions and neutrals. However, there is a disparity between the UCL ground-based SCANDI and CHAMP accelerometer-derived neutral winds measured

at ∼250 km and 300-450 km respectively, directly affecting this calculation and necessitating a statistical comparison study. We first discuss this disparity by modelling viscosity as a possible source of error using CMAT2, concluding the two datasets should be equivalent unless molecular viscosity is greatly overestimated in the upper atmosphere. We then present averaged flow-derived Joule heating patterns in the northern polar region during the winter periods of the 2005-9 solar minimum, comparing SCANDI (ground-based instrument), CHAMP (satellite) and CMAT2 (model) neutral winds, with SuperDARN providing the necessary ion velocities. We find similar distributions but a magnitude difference between ground, satellite and model-calculated Joule heating, again highlighting the extremity of the neutral wind disparity. We suggest the disparity is either due to an outdated coefficient of molecular viscosity or an instrumental error. We rule out FPIs as the cause of the neutral wind bias by using CMAT2 to simulate ground-based FPI height-integrated winds, finding their measuring technique introduces a small error (8%). Due to other known biases from the aerodynamic modelling of satellites (Emmert et al. 2006*a*,*b*; Förster et al. 2008; Dhadly et al. 2017*a*,*b*), we suggest the uncertainty lies with CHAMP. Crucially, this implies a bias to models assimilating CHAMP data. Finally, we utilise the frictional heating assumption in conjunction with SCANDI neutral temperatures, EISCAT ion temperatures and CMAT2 to probe the disparity independently of winds. We find agreement between wind-derived and temperature-derived Joule heating between 0-12 MLT and within the same order of magnitude between 12-24 MLT.

4.1 Introduction

In this section we first introduce the neutral wind disparity between UCL FPI observations and CHAMP drag-derived measurements. We then discuss why they should be equivalent due to the viscosity of the upper atmosphere, despite their different measuring altitudes, and how CMAT2 calculates this respective viscosity. Finally, we describe how Joule heating can be viewed mechanically as frictional heating, and how under this assumption the ion-energy equation can be simplified to a relationship between net flow of neutral winds and ion drifts and resultant temperature changes between ions and neutrals as they collide.

4.1.1 A neutral wind disparity between UCL FPIs and CHAMP

There is a disparity between neutral winds measured by satellites and ground-based FPIs, with satellite magnitudes reaching up to twice that of FPIs despite being in phase. This is shown in Figure 4.1 (also see Förster et al. (2008) and Aruliah et al. (2018) in preparation; data were obtained from Aruliah et al. (2018)), which shows the average CHAMP cross-track winds during 2000-2003 compared to the average Svalbard FPI zonal winds during 1980 and the same period. Model winds for two versions (1987 and 1990) of the semi-empirical HWM (see for example, Drob et al. (2008) and references therein) are also included. On average Figure 4.1 shows CHAMP overestimating the FPI by a factor of 1.73. These data were collected during solar maximum and at the beginning of the CHAMP mission when the drag-derived winds are most precise. Emmert et al. (2006*a*) and Emmert et al. (2006*b*) saw a magnitude difference factor of 2-3 between CHAMP and FPIs. Dhadly et al. (2017*b*) found a similar discrepancy with the Gravity Field and Steady-State Ocean Circulation Explorer (GOCE) (Drinkwater et al. 2003) winds, which also uses accelerometer data and the same aerodynamical model to determine horizontal wind components (see Doornbos et al. (2010) as mentioned in Chapter 2).

Due to limited thermospheric measurements and the inability of one instrument alone to provide high spatial resolution and temporal coverage (see for example, Dhadly et al. (2017*a*) and references therein), each dataset able to measure the high-latitude upper atmosphere is important and needs to be accurate and unbiased. This particularly applies to satellite data, which can provide global coverage and are often assimilated into models such as the semi-empirical HWM (Drob et al. 2008), which in turn can be used in GCMs to provide initial wind conditions (in CMAT2 this occurs in the spinup, see Chapter 2).

When comparing SCANDI to CHAMP an obvious difference is the altitude the instruments sample – ground-based FPIs measure the red atomic oxygen emission line at ∼250 km, whilst during the period studied in this chapter, CHAMP sampled altitudes between 325-363 km. Due to the large viscosity of the upper atmosphere (see for example: Rishbeth & Garriott (1969); Kohl & King (1967)), a common assumption is minimal altitude variation of winds over this height range, as in Dhadly et al. (2017*a*) and Dhadly et al. (2017*b*) which assume the equivalence of satellite and FPI winds between 210-320 km. Satellite data also support equivalent winds across the FPI-CHAMP altitude range: Wharton et al. (1984) analysed Dynamics Explorer 2 (DE-2) zonal wind measurements

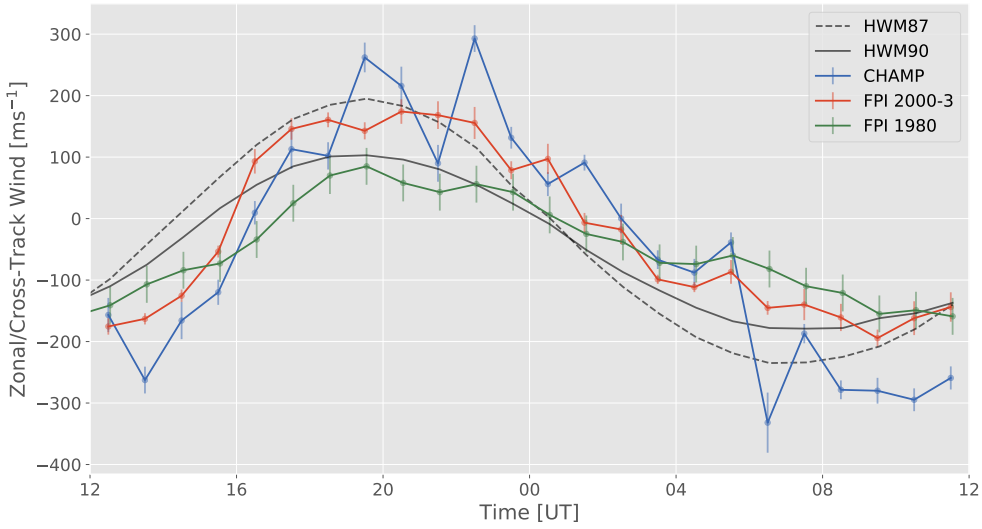

Figure 4.1. Averaged CHAMP (blue) cross-track winds during 2000-2003, averaged Svalbard FPI zonal winds during 2000-2003 (red) and averaged Svalbard FPI zonal winds during 1980 (green) from 12-12 UT. HWM87 (black dash) and HWM90 (black solid) model wind data are also included. Data were obtained from Aruliah et al. (2018).

at all local times to find no significant altitude dependence between 200-700 km; Killeen et al. (1982) saw little variation in the meridional and zonal winds sampled by the DE-2 satellite between 200-400 km; and Emmert et al. (2002) found this above 150 km using WINDII-derived daytime disturbance winds.

Focusing on ion drag as a contributor of neutral motion acceleration, Rishbeth & Garriott (1969) describe (hypothetically, i.e. without the other terms of Equation 1.27) the acceleration of horizontally-flowing neutral air as a sum of the ion-neutral collisions (or ion drag) and the viscous drag of air, respectively:

$$\frac{\partial V_n}{\partial t} = \nu_{ni}\,(V_i - V_n) + \frac{\mu}{\rho}\frac{\partial^2 V_n}{\partial h^2} \tag{4.1}$$

where ν_{ni} is the collision frequency between neutrals and ions, V_n is the neutral velocity, V_i is the ion drift, μ is the coefficient of viscosity, ρ is the density of air, t is time and h is height. Ignoring viscosity, the time constant associated with Equation 4.1 ($1/\nu_{ni}$) is of order hours in the F region (Rishbeth & Garriott 1969), detailing the delay of the acceleration of neutrals by collisions with ions. Rishbeth & Garriott (1969) continue to show the significance of viscosity by assuming a steady state system where Equation 4.1

equates to zero; thus, rearranging Equation 4.1 gives:

$$H_\nu^2 \frac{\partial^2 V_n}{\partial h^2} - V_n = -V_i \tag{4.2}$$

where H_ν is the 'scale distance':

$$H_\nu = (\frac{\mu}{\rho \nu_{ni}})^{\frac{1}{2}} \tag{4.3}$$

If we make the simple assumption of only V_n varying with height this can be solved as a second order differential, where V_n depends exponentially with the ratio of the height and scale distance. H_ν is equivalent to the distance where ion drag can affect the neutral motion despite viscous drag. Rishbeth & Garriott (1969) use this scale distance and the time constant above to assess the effects of viscosity in the F region (150-300 km). Below 150 km the length of the time constant (many hours) reduces the likelihood of ion drag influence on the neutrals (and is instead linked to tides and gravity waves), and above 300 km the scale distance extends greatly (∼100 km). However, between 150-300 km $1/\nu_{ni}$ and H_ν vary between day and night; during the day ion drag dominates as ions accelerate the neutrals ($1/\nu_{ni}$ ∼1 hour, H_ν ∼30 km), during the night viscosity becomes more significant as the ion composition of the region reduces ($1/\nu_{ni}$ ∼5 hour, H_ν ∼100 km).

Kohl & King (1967) also show viscosity as less influential during the daytime by calculating the ratio of the viscous and driving (pressure gradient) forces modulating horizontal wind with respect to altitude for daytime ion concentrations (3×10^5 cm^{-3} or above). This ratio reduces by over a factor of four between 220 and 350 km (near the F2 layer peak) where the ion drag force is greater than the Coriolis and inertial forces (Kohl & King 1967), and only starts to dominate above 500 km. As the observational studies mentioned above include both daytime and nighttime measurements, we find a discrepancy between observation and theory, further warranting an investigation. Part of this study is therefore an investigation into viscosity as a possible source of the discrepancy between these two neutral wind datasets using the CMAT2 model.

CMAT2 uses two coefficients of viscosity: molecular, μ_m, and turbulent, μ_t. Within CMAT2 the two coefficients are combined, with the weighted mean calculated and divided by the scale height. This viscosity term is then used in the main program of CMAT2 to calculate the vertical viscosity, the zonal and meridional momentum vertical diffusion through vertical viscous drag terms, the horizontal transfer of momentum equivalent and the vertical viscous energy density drag term in the energy equation for vertical diffusion.

The weighted viscosity is also used to calculate the diffusion equation for a varying diffusion coefficient. μ_t is calculated from the coefficient of thermal conductivity, K_t, and specific heat capacity at constant pressure, c_p:

$$\mu_t = \frac{P_r K_t}{c_p} \tag{4.4}$$

where P_r is a constant termed the Prandtl number, that is, the ratio of the total turbulent momentum to its respective heat diffusivity (Huang & Smith 1991). The Prandtl number has been previously estimated experimentally, and is taken as 2 in CMAT2 (see for example: Hickey (1988); Huang & Smith (1991); Liu et al. (2013*b*)). μ_m is given for atomic oxygen, which has the largest concentration in our altitude range during solar minimum, and is dependent on temperature, T (Banks & Kockarts 1973):

$$\mu_m = 4.5 \times 10^{-5} (\frac{T}{1000})^{0.71} \quad [\text{kg m}^{-1} \text{ s}^{-1}] \tag{4.5}$$

and thus will begin to dominate in the thermosphere (>100 km). This is theoretically derived, and in agreement with experiment-based values (see Banks & Kockarts (1973)). It should also be noted that N_2, He and O_2, as the next largest constituent populations, have similar molecular viscosity coefficients to Equation 4.5, and have also been shown to have little effect if included in the calculation of viscosity (Vadas & Crowley 2017).

Using CMAT2 we are first able to assess whether zonal winds measured by FPIs at ∼250 km and cross-track winds measured by CHAMP at >320 km are equivalent in our model atmosphere. We are then able to adapt molecular and turbulent viscosity within CMAT2 to probe whether their miscalculation affects the winds being equivalent between this altitude range. As molecular diffusion dominates the transport processes in the thermosphere, changes due to turbulent diffusion above the turbopause should be unlikely. Conversely, at altitudes below 100 km the density is so high that the molecular viscosity should be negligible (Marshall & Plumb 1972). To confirm the altitude range at which turbulence dominates we increase the Prandtl number in Equation 4.4 by a factor of 50; high enough to see trends but low enough to maintain model stability and equilibrium (extreme values can trigger CMAT2 safeguards). Physically, this raises the height at which gravity waves break as the thermal diffusivity is inversely proportional to Prandtl number (Liu et al. 2013*b*).

Turning to molecular viscosity, Vadas & Crowley (2017) used the TIDDBIT ionospheric

sounding rocket horizontal wind measurements to show that molecular viscosity could be severely overestimated. This was a campaign launched from Wallops Island (U.S.A.), a mid-latitude location, on the 30th October 2007 during 04-07 UT, which showed wind instead varying with altitude between 320-385 km and peaking at 325 km. Vadas & Crowley (2017) found that gravity waves breaking at higher altitudes were able to force non-equivalent winds despite the predicted high molecular viscosity in the region. A major assumption of Equation 4.5 is that the average separation between molecules is tens of atomic units, instead Vadas & Crowley (2017) found this to be a gross underestimation, computing a value at 250 km of hundreds of thousands of atomic units. With increasing altitude this distance will increase still further, tending to a collision-less and non-viscous atmosphere. We therefore decrease Equation 4.5 by two orders of magnitude (i.e. a multiplication factor of 1/100) to test the effects of an extreme case of reduced molecular viscosity on wind equivalence in the upper atmosphere. Finally, we can also model these changes for both daytime and nighttime conditions, to probe the dissimilarity suggested by Rishbeth & Garriott (1969) and Kohl & King (1967).

4.1.2 Joule heating as frictional heating

The primary mechanism of Joule heating has been previously discussed in Chapter 1, where Poynting flux dissipates in the ionospheric E region as FACs close via Pedersen currents, which are parallel to the electric field (see Equation 1.31). However, ion-neutral collisions can also be considered thermodynamically as dissipating energy as frictional heating (see Equation 1.32), extending to the F region (St.-Maurice & Hanson 1982; Thayer & Semeter 2004; Strangeway 2012). In the F region ion drag modulates the neutral circulation in the thermosphere (see for example: Rishbeth & Garriott (1969); Iijima (2013); Cowley (2000)), which is otherwise primarily driven by EUV solar heating generating pressure gradients (see for example: Kohl & King (1967); Cierpka et al. (2000)). This exchange of momentum during ion-neutral collisions increases the ion temperatures in the ionosphere relative to the neutrals, which increase at a slower rate (Strangeway 2012).

Focusing on the F region, St.-Maurice & Hanson (1982) use the frictional heating assumption, assuming that this exchange of thermal energy can be approximated by the relative flow of ions and neutrals (also adopted by Bjoland et al. (2015)), such that Equation 1.33 in Chapter 1 equals zero to give (St.-Maurice & Hanson 1982; Thayer & Semeter

2004):

$$m_n(\mathbf{V}_i - \mathbf{V}_n)^2 \approx 3k_b(T_i - T_n) \tag{4.6}$$

where m_n is the averaged neutral particle mass assumed as atomic oxygen, $\mathbf{V}_i$ and $\mathbf{V}_n$ are the respective ion and neutral flow vectors, k_b is Boltzmann's constant and T_i and T_n are the respective ion and neutral temperatures. This reduces the ion-energy equation in Chapter 1 to a first order approximation and can be used as an estimate of the frictional heating given in Equation 1.32, valid at F region heights between 250-500 km. This also assumes that ion motion is incompressible (ignoring the divergence of ion drifts), the spatial scale lengths are greater than $|\mathbf{V}_i - \mathbf{V}_n|/\nu_{in}$ preventing viscous heating and that heat advection and conduction are negligible up to 500 km (for further details on these assumptions see St.-Maurice & Hanson (1982)). It should also be noted that we only study ion-neutral collisions, as electron-neutral collisions have a negligible effect on neutral motion (Rishbeth & Garriott 1969). There is much debate about the equivalence of frictional and Joule heating (see for example, Strangeway (2012) and references therein); the latter is often associated at E region altitudes where Pedersen currents are present and incoherent scatter radars are available to measure electric field profiles, the former relies on thermospheric wind measurements and is associated with satellite and FPI data and is therefore used in this study.

Assuming the equivalence of frictional heating and Joule heating, we use the relationship proposed by St.-Maurice & Hanson (1982) in Equation 4.6 to present approximate statistical wind-derived Joule heating maps for the northern hemisphere polar region during the 2005-9 solar minimum winter periods, as determined using CMAT2, SCANDI and CHAMP neutral winds in conjunction with SuperDARN ion drifts. We also include their respective high-latitude northern hemisphere neutral wind vector and ion drift patterns. SCANDI and CHAMP overlapped during the solar minimum period only (2005-2011), therefore we do not compare solar maximum in this study. It should also be noted that we do not compare the two solar maxima of solar cycles 23 and 24, which CHAMP and SCANDI encompassed respectively, as the latter was unusually quiet (with the F10.7 index equal to 129.8 sfu compared to its predecessor, 178.6 sfu). Again utilising Equation 4.6, we present temperature-derived Joule heating maps using CMAT2 and SCANDI neutral temperatures with CMAT2 and EISCAT ion temperatures respectively. This allows us to probe the consistency of CMAT2 and SCANDI wind-derived Joule heating after compar-

ing to CHAMP (as well as the validity of Equation 4.6). The CMAT2 model also provides a base comparison, predicts general features and allows us to see bias or inaccuracy in our datasets.

4.2 Data and Methodology

In this section we expand on the descriptions provided in Chapter 2 of the datasets used in this study, including CMAT2, SCANDI and CHAMP providing neutral winds and (in the case of the former two) temperatures, and SuperDARN and EISCAT measuring the ion drifts and temperatures respectively. Table 4.1 outlines how the datasets are used to calculate the wind-derived and temperature-derived Joule heating using Equation 4.6.

Table 4.1. Description of data sources used to calculate each side of Equation 4.6, that is, wind-derived and temperature-derived approximated Joule heating. Each row corresponds to the instrument or model we are comparing, namely CMAT2 (model), SCANDI (ground-based instrument) and CHAMP (satellite). Each column gives the data source of the given variable and its respective subplot in Figure 4.15.

	$m_n(\mathbf{V}_i - \mathbf{V}_n)^2$			$3k_b(T_i - T_n)$		
	$\mathbf{V}_n$	$\mathbf{V}_i$	Fig 4.15	T_n	T_i	Fig 4.15
Model	CMAT2	SuperDARN	(a)	CMAT2	CMAT2	(b)
Ground	SCANDI	SuperDARN	(c)	SCANDI	EISCAT	(d)
Satellite	CHAMP	SuperDARN	(e)	-	-	-

4.2.1 CHAMP

CHAMP neutral winds, as derived from accelerometer drag measurements (Doornbos et al. 2010), are discussed in Chapter 2 along with their transformation from geographic to solar magnetic coordinates. As ions are organised by the geomagnetic field and as ion drag modulates the neutrals both populations are best viewed in magnetic coordinates (see for example: Emmert et al. (2002, 2010*b*); Laundal & Richmond (2017)). CHAMP had a 131-day precession for 24-hour local time coverage (Förster et al. 2008; Häusler & Lühr 2009), this is the minimum sample amount to extract the global horizontal wind vectors (particularly at the polar cap). In this study CHAMP data were from the November-January winter periods during the 2005-9 solar minimum for direct comparison to SCANDI. As we used data for each 3-month November-January winter period this amounted to a full 12 months of data (368 days).

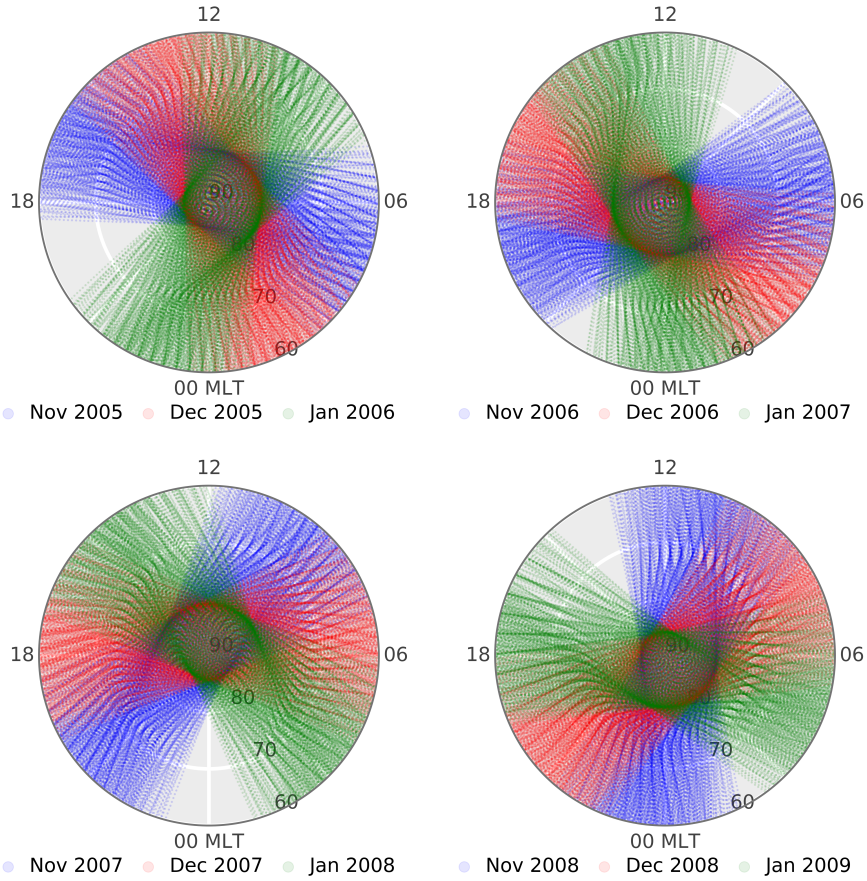

Figure 4.2. CHAMP orbits in solar magnetic coordinates for each November (blue), December (red) and January (green) period from 2005-9.

Figure 4.2 shows the CHAMP orbit in solar magnetic coordinates during these periods. Data were restricted to low geomagnetic activity conditions (Kp < 3) to reduce effects from substorms. We used both daytime and nighttime measurements to increase the data sample, consistent with other statistical studies (see for example: Wharton et al. (1984); Killeen et al. (1982); Dhadly et al. (2017*a*)). Data were binned by concentric rings with a width of 2° magnetic latitude and 15° magnetic longitude (or 1 hour MLT). Figure 4.3 details the number of data points per bin for SCANDI and CHAMP in this frame. This is a compromise between observing small-scale structure and having distributions that are statistically significant. We have not limited the data to conjunctions with CHAMP and the magnetic longitude of SCANDI as this reduces the coverage of the former.

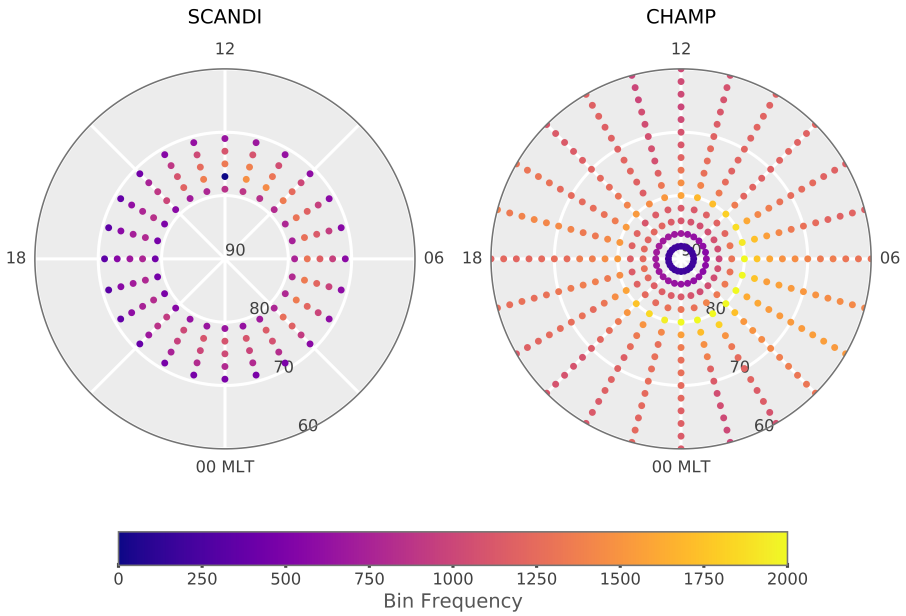

Figure 4.3. SCANDI and CHAMP bin frequency of neutral wind available data in solar magnetic coordinates for the combined November-January winter period during the years 2005-9.

4.2.2 SCANDI

SCANDI is described fully in Chapter 2, again we include further detail relevant to this study here. SCANDI's FOV overlaps with both the ESR and SuperDARN radars, with data provided in solar magnetic coordinates. From operation, the imager has recorded data primarily in solar cycle 24, encompassing one solar minimum (2007-2011). Its latitude location provides 24-hour observations in December and January, and almost 24-hour observations during November. We used data from this November-January winter period, removing data during cloudy nights; this totalled 48 nights and provided sufficient coverage (see Figure 4.4) and data sample size (see Figure 4.3). Figure 4.4 shows the SCANDI location and FOV on a solar magnetic grid with the available data during each solar minimum winter. During 2008-2009 the data sample was reduced as SCANDI redirected observation from the red to green emission line, which is too low in altitude to be considered in this study.

We include the following data limitations of this study: ESR data were not available during January 2010, SuperDARN data were not available during November 2009 and

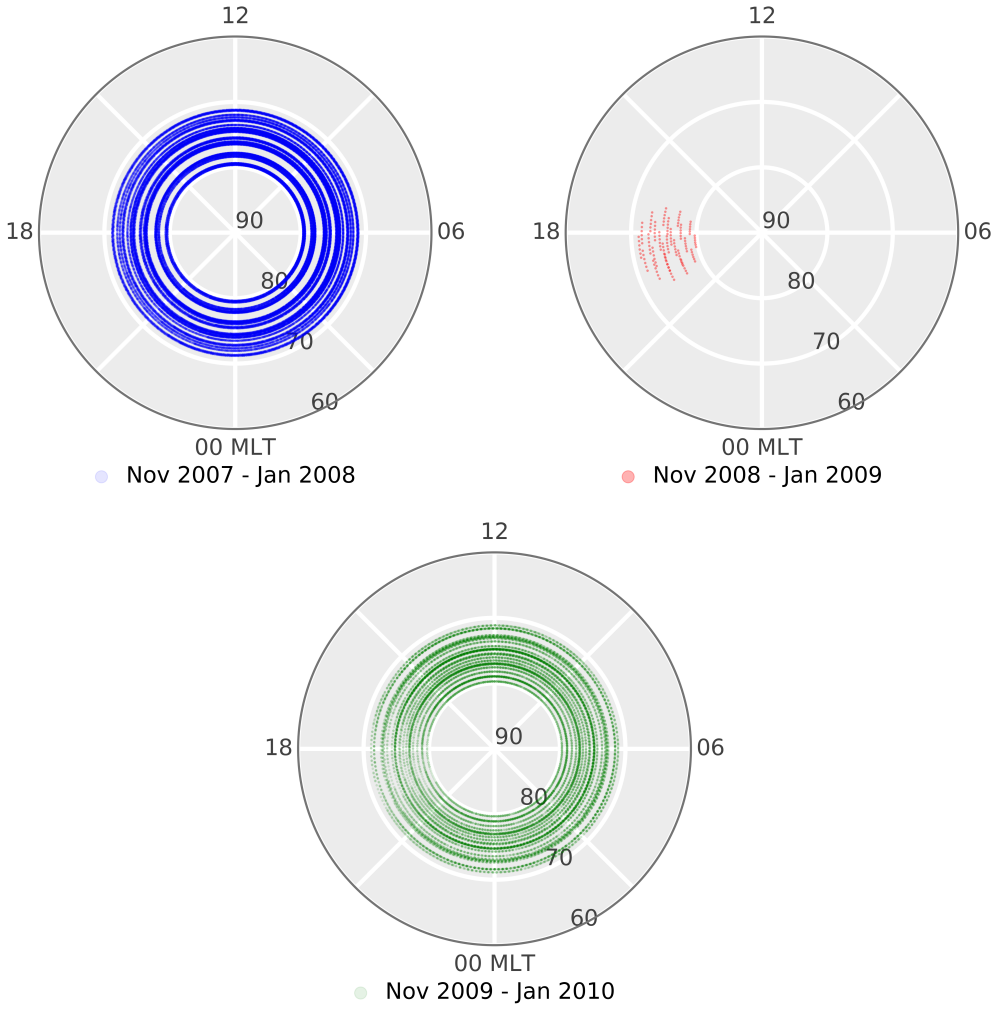

Figure 4.4. SCANDI locations in solar magnetic coordinates for each November (blue), December (red) and January (green) period from 2005-9.

SCANDI data were not available during November 2007, December 2008 and January 2009. We have not restricted by Kp due to limited data, however the average Kp during the nights available was representative of low geomagnetic activity (Kp < 3). Figure 4.3 shows the number of data points per bin for SCANDI is comparable to CHAMP.

4.2.3 EISCAT and SuperDARN

Both EISCAT and SuperDARN have also been discussed previously in Chapter 2, and have been provided in solar magnetic coordinates. The ESR provides altitude profiles at the zenith zone (which lies in the centre of the SCANDI FOV and is equivalent to 75°N magnetic latitude with a 5° FOV, see Figure 2.5) of, amongst others, ion temperature. In

conjunction with SCANDI neutral temperature data, this allows the temperature-derived Joule heating for ground-based data to be calculated at 75°N magnetic latitude. Due to the high variability of the ionosphere (Aruliah et al. 2004) and the 7-minute resolution of SCANDI, we averaged EISCAT data over a 7-minute period and only consider the zenith zone rather than extrapolating over the full SCANDI FOV (1000 km). The ion temperatures used in this study have a standard deviation of 332 K. SuperDARN provides one altitude measurement at ∼250 km of electrostatic potential and ion flow vectors. The ion x and y drift components used in this study have a respective standard deviation of 156 m s^{-1} and 180 m s^{-1} across the entire grid. The SuperDARN ion drifts are used in all wind-derived Joule heating maps, that is, with CMAT2, SCANDI and CHAMP neutral winds.

4.2.4 CMAT2

CMAT2 has been discussed in detail in Chapter 2. In this section we discuss the two types of CMAT2 simulations used in the Joule heating and viscosity studies.

Joule heating simulation

We used the Barnes (2017) version of the CMAT2 model for the Joule heating study, which uses SuperDARN to provide the electrostatic potential (rather than Foster electric fields), in turn providing more realistic ion drift values. We also transformed the geographic CMAT2 grid into solar magnetic coordinates, as detailed in Chapter 2. As we are not focusing on conjunctions with CHAMP and SCANDI, we therefore used the full CMAT2 global grid rather than precessing the magnetic longitude of SCANDI with time, though this will remove longitudinal dependence. CMAT2 has quite a low resolution for longitude, thus extracting the magnetic longitude (which intersects non-adjacent geographic grid points) is another benefit of using the entire grid at a specific UT. We used the 12 UT time slice as UT dependence of polar neutral winds reduces significantly when in magnetic coordinates (Emmert et al. 2010*b*; Dhadly et al. 2017*a*), although it should be noted that some UT dependence in the winds is still present (Billett et al. 2018). We also interpolated to 250 km altitude for comparison with instrument data. The solar minimum period is represented by an average simulation on the 14th December 2007, which had a maximum Kp of 1+ on the day and a F10.7 index close to the average (76.6 sfu) for the period (note that CMAT2 has a minimum Kp of 1+). This was achieved with a 30-day spinup using

GIP. This used an averaged SuperDARN potential map, as observations were unavailable; although this is preferable as we are concerned with an average representation of the solar minimum.

We used the following model outputs: height, neutral temperature, ion temperature and the three components of the neutral wind vector (meridional, zonal and vertical). The horizontal ion flow vector was obtained from the SuperDARN average of the solar minimum winter periods. As CMAT2 provides all necessary parameters for the calculation of wind-derived and temperature-derived Joule heating in Equation 4.6, the model can also be used as a base comparison for ground-based and satellite measurements. CMAT2 also outputs Joule heating as a data product, as derived from the electric field strength, Earth's magnetic field dipole, conductivities and neutral horizontal wind and density (see Equation 1.32 in Chapter 1). The distribution of Joule heating in this data product can also be used as a guide when comparing our derived Joule heating.

Viscosity simulation

We used the standard Foster electric fields (see Chapter 2) for the viscosity study, as we are solely interested in the neutral atmosphere during quiet geomagnetic activity. A 10-day quiet period was chosen from the 9-19th December 2008, with Kp $<$ 3- throughout and the F10.7 index practically constant, remaining between 66.2-68.8 sfu. During this period the CHAMP orbit averaged $\sim$325 km, close to the upper boundary altitude of CMAT2 for low activity. We ran a 30-day spinup for the 9th December 2008, which was used as an input for the day-step runs for each change of viscosity, where the molecular or turbulent coefficient of viscosity was altered by adapting the temperature relationship in Equation 4.5[1] in the case of the former, or Prandtl number in Equation 4.4[2] in the case of the latter. The model was then recompiled and run in day-stepping mode for 10 days.

In this study we present the zonal mean zonal wind plots for the 18th December 2008 (day 9 of run) for lowering the molecular viscosity coefficient by two orders of magnitude, and increasing the turbulent viscosity coefficient by a factor of 50. We present midday and midnight profiles to test the dayside/nightside relation in Equation 4.2. Kohl & King (1967) show the zonal wind component is more variable with height than the meridional, which saturates at $\sim$250 km contrasted to $>$500 km for the zonal wind. As the wind

[1]See Planet.f90 in the CMAT2 code.
[2]See InputParamsPlanet.f90 in the CMAT2 code.

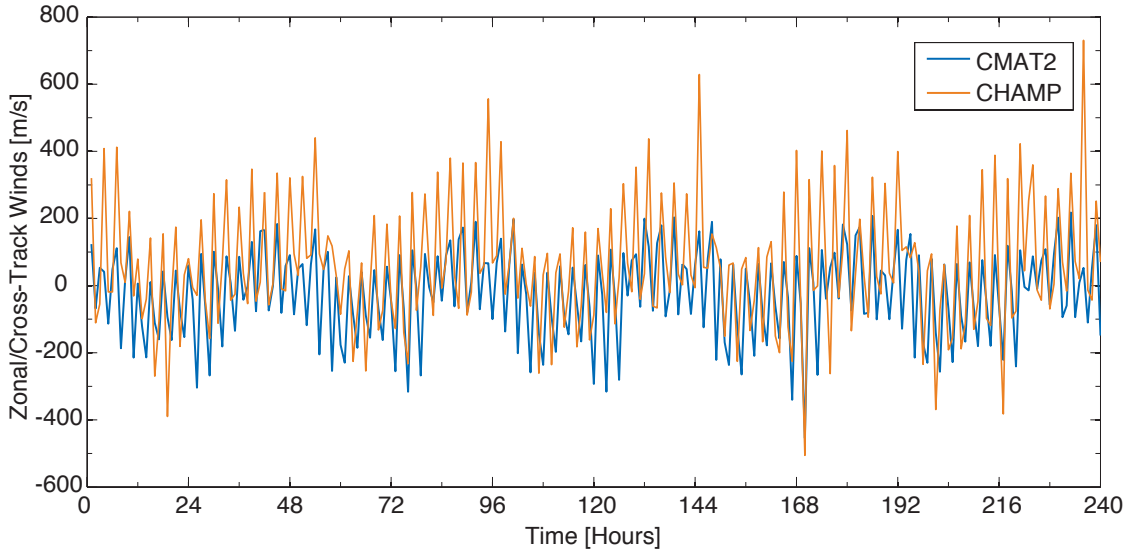

Figure 4.5. CHAMP cross-track and CMAT2 zonal winds during 9-19th December 2008 (in hours from the 9th December 2008 0 UT).

varies least zonally, the zonal mean zonal wind is a useful (and commonly used) method to simplify the view of global circulation whilst still observing large-scale trends (see for example, James (1995)). As CHAMP measured cross-track winds, which are analogous to zonal winds, this allows for a direct comparison without introducing error from the horizontal wind analysis required in the Joule heating study. Thus, we used the zonal wind and height CMAT2 outputs to observe zonal mean zonal wind profiles and the location of their vertical contours at high altitudes. Figure 4.5 shows the CHAMP cross-track and corresponding CMAT2 zonal winds at that CHAMP location during the simulation period. Importantly, CHAMP and CMAT2 are in phase, which means the wind distribution of CMAT2 should be indicative of the wind that CHAMP samples. However, it should be noted that CHAMP wind magnitudes are on average 1.4 times higher than CMAT2, but CMAT2 persistently favours a (more negative) westward wind direction. This bias is discussed in further detail in Chapter 5.

4.3 Results and Discussion

Here we present the results of the viscosity study using CMAT2. We then present the statistical analysis of solar minimum neutral wind for CMAT2, SCANDI and CHAMP in the northern polar region, their analogous averaged flow-derived Joule heating patterns, the CMAT2 and SCANDI temperature-derived Joule heating patterns and the validation

of the simplified ion energy equation (Equation 4.6) presented in St.-Maurice & Hanson (1982).

4.3.1 Viscosity in the Upper Atmosphere

Figure 4.6 shows a contour plot of the zonal mean zonal wind with respect to altitude (y-axis) and geographic latitude (x-axis) for midday and midnight on the 18th December 2008, with the wind magnitude denoted by the colour bar where positive is eastward. We can see distinct vertical zonal wind contours, with respect to geographic latitude, are produced in CMAT2 from ∼250 km upwards for both midday and midnight; thus it follows their extrapolation to the orbiting altitude of CHAMP dictate similar zonal wind magnitudes to the UCL FPIs or SCANDI measurements.

Figure 4.7 uses the same format as Figure 4.6, where solid contours outline the standard viscosity run from Figure 4.6, and the colour contour fill and dotted contours show the winds when forcing the molecular viscosity to be two orders of magnitude lower than a standard CMAT2 atmosphere. We can see the reduction in viscosity has decreased the scale height in which winds are equivalent, increasing the velocity gradient and shear, which leads to less efficient levelling by the shear stress to smooth the gradients out. This increases the magnitude of the winds and alters the wind structure in the upper atmosphere raising the vertical character of contours to ∼280 km. Focusing on the high-latitude northern hemisphere this wind increase, most clearly shown by Figure 4.8 which details the residual difference between Figures 4.6 and 4.7, peaks at ∼230 km at ∼70°, lower than the peak in Vadas & Crowley (2017). However, the percentage change is still not large enough to explain the difference in our FPIs (in Figure 4.1), indeed at the FPI latitudes there is a very limited change. Figure 4.8 shows the largest increase in wind is centred at 230 km, and implies the FPIs at Kiruna (68°N, 20°E) should measure stronger winds and at Svalbard (78°N, 16°E) are still equivalent. Figure 4.9 shows the zonal wind profile at Svalbard for each simulation, where control is in blue, increased turbulent viscosity is in green and decreased molecular viscosity is in red. We can see that in all simulations the winds at both measuring altitudes are equivalent, and that the sounding rocket profile in Vadas & Crowley (2017) is still not replicable by decreasing the molecular viscosity by two orders of magnitude (see Figure 1 in Vadas & Crowley (2017) for this wind profile). Thus we should find that the magnitude of the winds measured by CHAMP are consistent with our FPIs and SCANDI. At altitudes below 100 km the

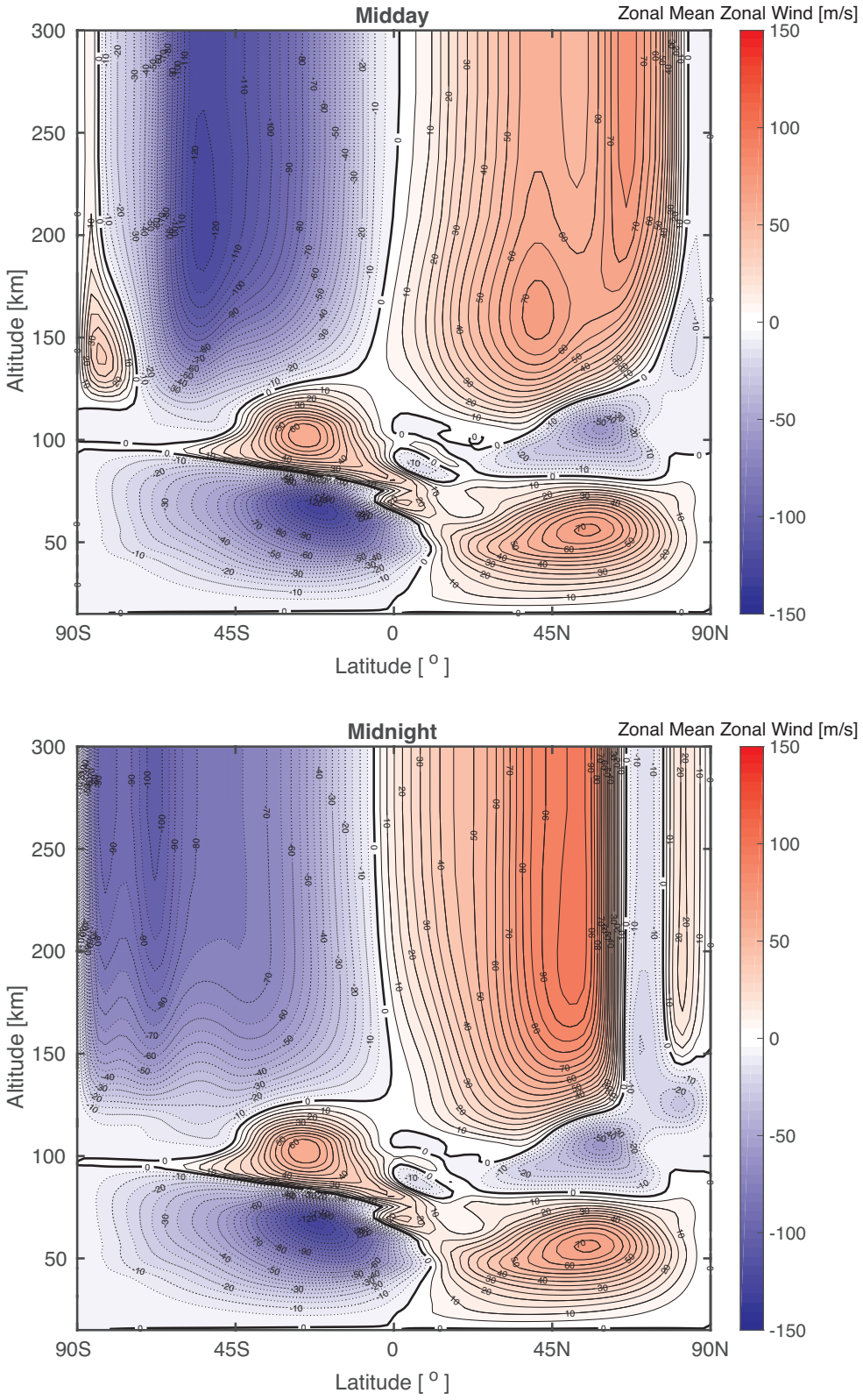

Figure 4.6. Zonal mean zonal wind of the standard CMAT2 run with respect to geographic latitude (x-axis) and altitude (y-axis), where the colour bar denotes the magnitude and direction of wind (+East) for midday and midnight on the 18th December 2008.

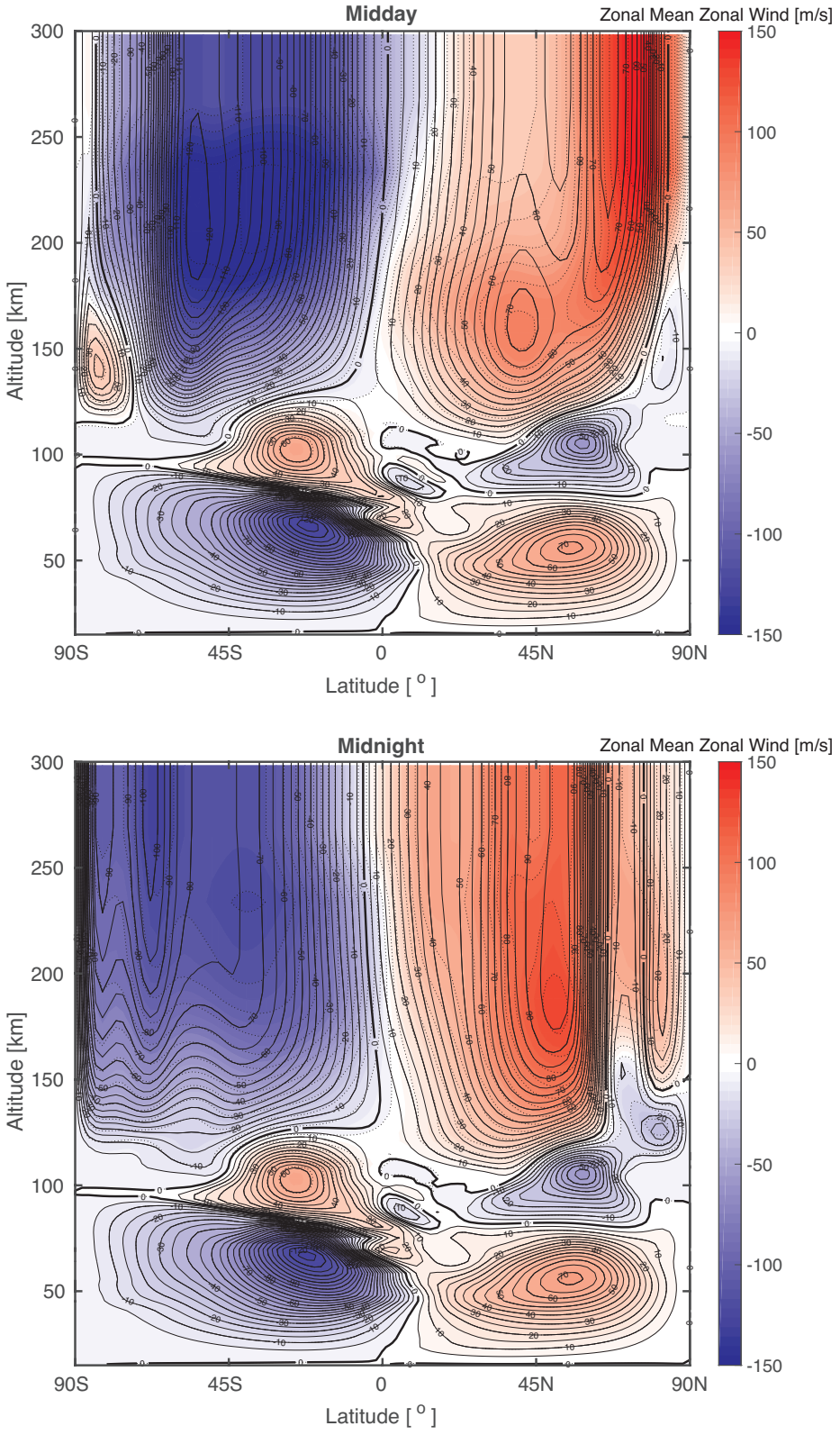

Figure 4.7. Zonal mean zonal wind, where the molecular viscosity has been reduced by two orders of magnitude, with respect to geographic latitude (x-axis) and altitude (y-axis), where the colour bar denotes the magnitude and direction of wind (+East). Solid contours outline the standard viscosity run from Figure 4.6, and the colour contour fill and dotted contours show forcing the molecular viscosity two orders of magnitude lower than a standard CMAT2 atmosphere.

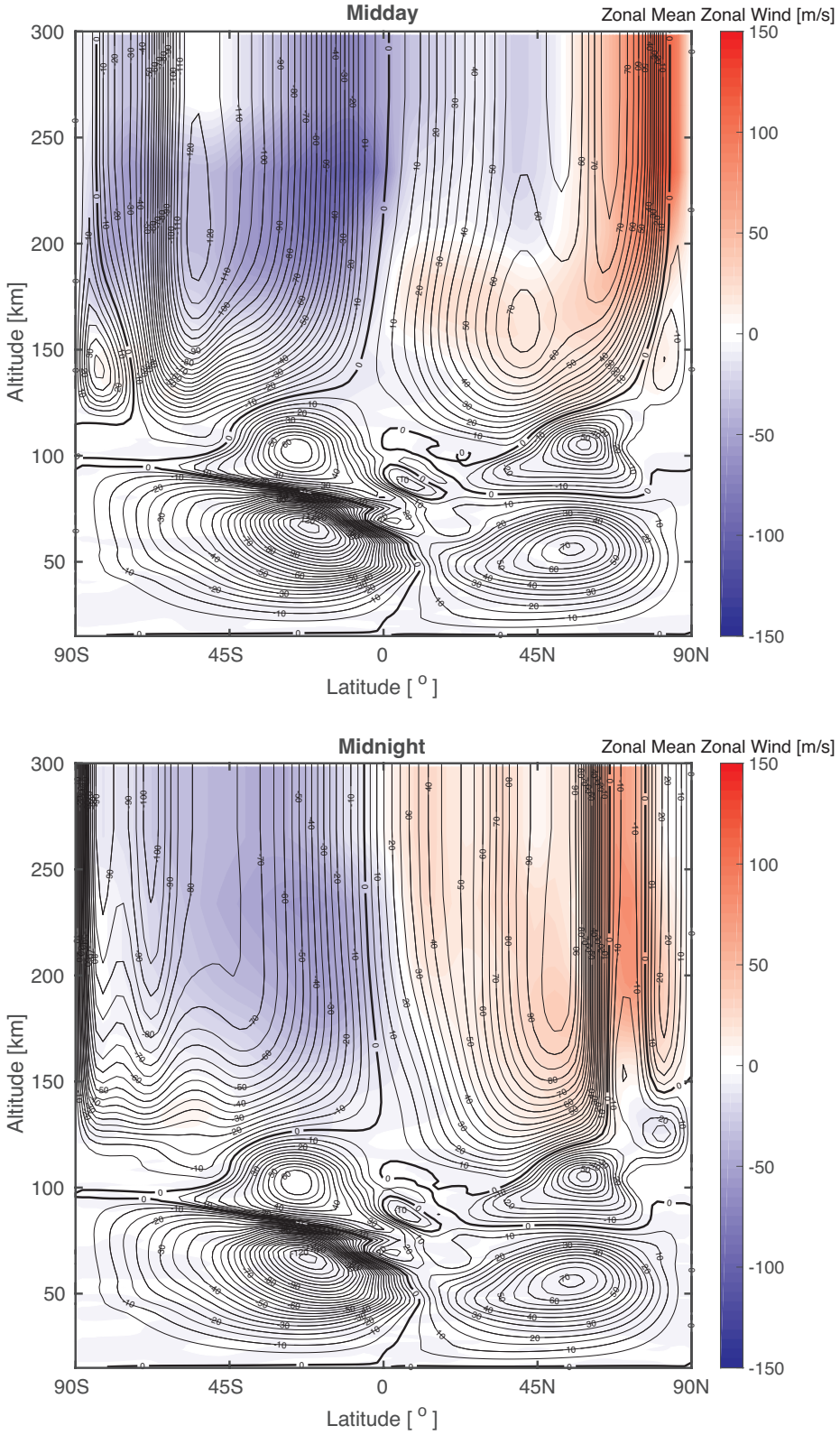

Figure 4.8. The residual difference between the zonal mean zonal wind in Figures 4.7 and 4.6 with respect to geographic latitude (x-axis) and altitude (y-axis), where the colour bar denotes the magnitude of the wind difference. Solid contours outline the standard viscosity run from Figure 4.6, and the colour contour fill shows the residual zonal mean zonal wind.

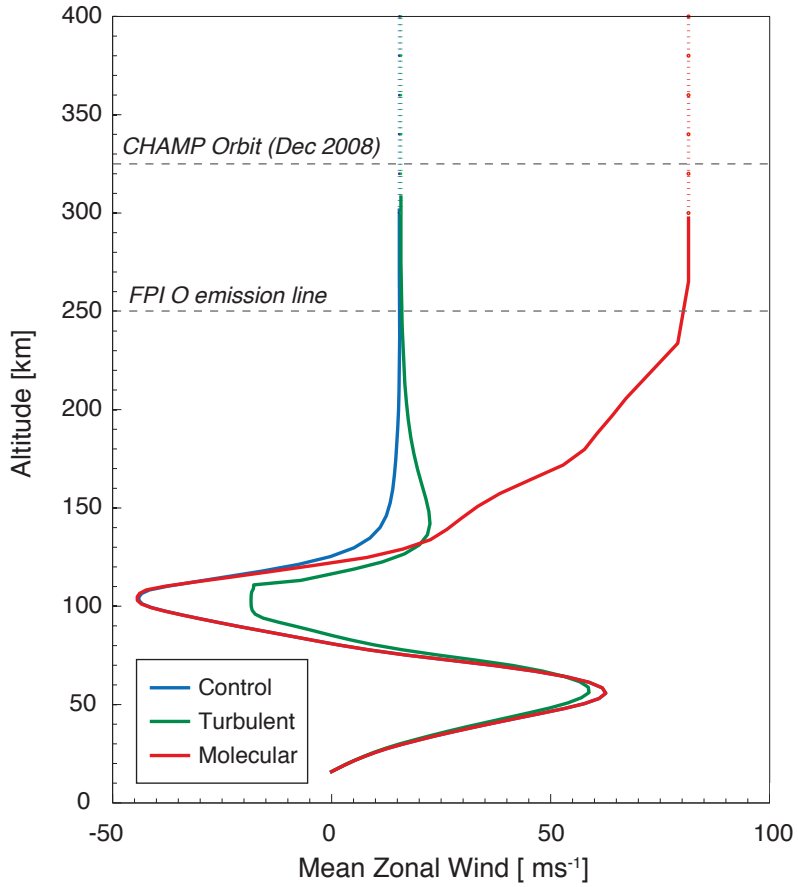

Figure 4.9. Zonal wind profile at Svalbard for the control simulation (blue), increased turbulent viscosity (green) and decreased molecular viscosity (red). Dashed lines indicate an interpolation of the data.

density is so high that the molecular viscosity is negligible (Marshall & Plumb 1972), and we see little change below this altitude in Figure 4.8. Any low magnitude anomalies are from computational noise (i.e. $< \pm 5$ m s^{-1}, calculable by re-running CMAT2 for the same conditions).

Alternatively, Figures 4.7 and 4.8 may indicate that a two order magnitude reduction of the molecular viscosity coefficient is still not enough. A decrease in molecular viscosity is also suggested by Vadas & Crowley (2017), where the coefficient of molecular viscosity (see Equation 4.5) reduces proportionally to $\rho^{-0.67}$ with height, which reproduced their sounding rocket horizontal wind profile. Solomon et al. (2011) showed the thermosphere in 2007-8 was at its lowest in density for the past five decades. This low density would in turn cause a decrease in thermospheric temperature, which, would reduce the molecular viscosity.

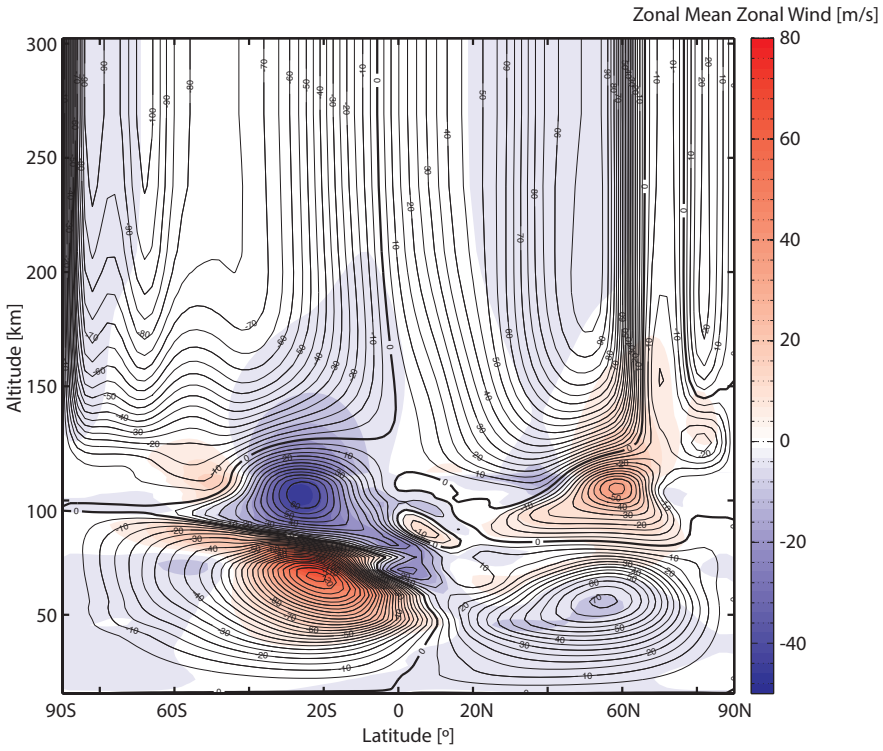

Figure 4.10. The residual difference between the zonal mean zonal wind where the turbulent viscosity has been increased by a factor of 50 and the standard CMAT2 atmosphere in Figure 4.6, with respect to geographic latitude (x-axis) and altitude (y-axis), where the colour bar denotes the magnitude of the wind difference.

Figure 4.10 uses the same format as Figure 4.8, where the contour plot instead shows the residual difference between an atmosphere where turbulent viscosity is a factor of 50 greater than a standard CMAT2 atmosphere and the control simulation. We can clearly see the modulation of wind is restricted to the lower atmosphere with the most significant changes around the height of the turbopause (∼100 km) and under where gravity waves break, an area of significant insertion of momentum and energy (Liu et al. 2013*b*). This is consistent with established theory (see for example, Marshall & Plumb (1972)). However, Liu et al. (2013*b*) found that higher Prandtl numbers (and therefore greater turbulent viscosity) raised the height at which the gravity wave dissipated (such as those seen by Vadas & Crowley (2017)), as the thermal diffusivity is inversely proportional to the Prandtl number. This should result in an energy source at higher altitudes, in turn increasing the thermal speed of molecules and affecting the thermospheric wind pattern. On further inspection of the model CMAT2 forces the gravity waves to break at the turbopause and the range over which each viscosity coefficient is effective (Yiğit 2008), which may have an

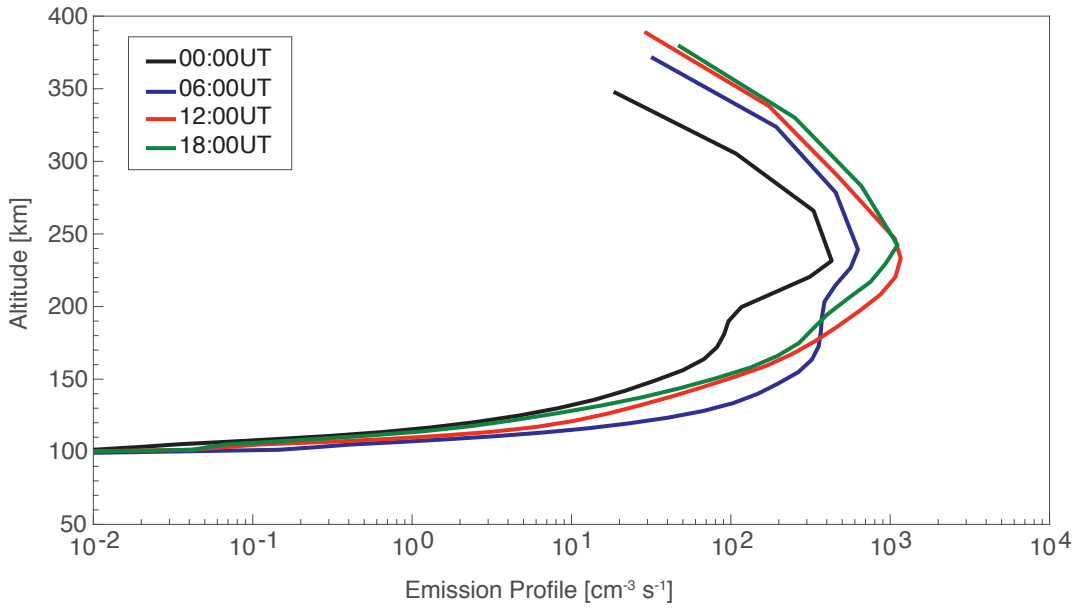

Figure 4.11. The emission profile calculated with the Vlasov et al. (2005) model at 0, 06, 12 and 18 UT and applied to the zonal winds as a 'weighting'.

impact on wind equivalence as well as coupling between the mesosphere and thermosphere as both viscosity and gravity waves determine the transport within the atmosphere along with its respective diffusion. This is outside the scope of this thesis but is left as future work. For the purposes of the Joule heating study we accept the height restriction imposed by CMAT2 on viscosity and use the CMAT2 standard viscosity outputs. The CHAMP-FPI neutral wind disparity is currently the subject of a paper in preparation (Aruliah et al. 2018), which includes this work on using CMAT2 to probe viscosity, and is also discussed further in Chapter 5.

So far we have seen that ground-based FPIs and CHAMP measurements should agree, which suggests a problem with bias or accuracy with at least one of the datasets. The drag parameter is a possible source of error with the CHAMP accelerometer-derived neutral winds (see for example: Dhadly et al. (2017*a*,*b*); Aruliah et al. (2018)), which is discussed in Chapter 5. In this chapter we can use CMAT2 to recreate the FPI measuring technique, that is, model height-integrated winds, a significant source of uncertainty in FPI measurements (Aruliah et al. 2005, 2018) previously mentioned in Chapter 2.

FPIs measure the line-of-sight Doppler shifts of the neutral atmosphere from the ground upwards within their FOV, which translates to a column of air. The red line emission height weights this column, peaking between 220-250 km (Link & Cogger 1988;

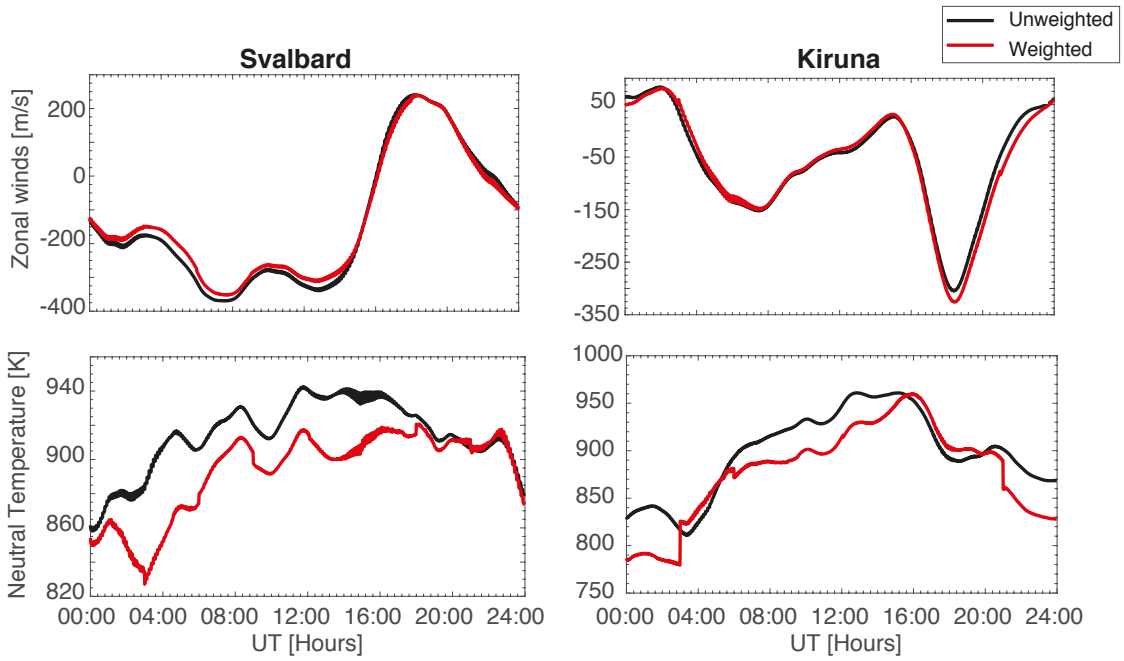

Figure 4.12. The weighted (red) FPI-simulated winds and neutral temperatures using CMAT2 and the emission profile in Figure 4.11 compared to the un-weighted winds and neutral temperatures (black) of CMAT2 interpolated to 250 km for the Kiruna and Svalbard locations with respect to UT.

Vlasov et al. 2005). Figure 4.11 shows this emission profile at 0, 06, 12 and 18 UT using the Vlasov et al. (2005) model with constants provided by Yiu (2014), detailing the altitudes FPIs sample. Here we can see the emission profile reduces substantially below 200 km where increasing densities cause alternative and more favourable collisional de-excitation pathways so that atomic oxygen recombines, and above as the separation of source from the FPI increases. We use this emission profile to weight the CMAT2 winds every 10 km at Svalbard and Kiruna, two locations of the UCL FPI network, for each UT of the standard CMAT2 simulation. This produces simulated height-integrated FPI winds. We then compare these height integration winds to standard simulated winds interpolated at 250 km.

Figure 4.12 shows the CMAT2 zonal winds and neutral temperatures at the Kiruna and Svalbard locations interpolated to 250 km ('un-weighted') and height-integrated ('weighted') using the emission profile in Figure 4.11. Figure 4.12 shows that the data remain in phase, the method of height integration ('weighted') causes FPIs to on average underestimate the neutral wind and temperature by at most ∼8%; though a noticeable exception occurs at ∼18 UT at Kiruna, where both the weighted neutral wind and temperature overestimate.

However, this is still not comparable with CHAMP.

4.3.2 Comparison of $\mathbf{V}_n$

In the previous section we used CMAT2 to probe viscosity as a possible source of the neutral wind disparity between FPIs and CHAMP, supporting their similarity; this focused on zonal winds. This section instead analyses the northern hemisphere polar region neutral horizontal winds as part of the Joule heating study, producing statistical maps of the 2005-9 solar minimum winter periods using CMAT2, SCANDI and CHAMP. This section focuses on distinctive polar wind features common in each of the datasets, describes where the data differ, including magnitude, and concludes with an assessment of the reliability of CHAMP data. Figure 4.13 shows polar projection plots of the neutral wind directions and magnitudes measured by (a) CMAT2, (b) SCANDI, (c) CHAMP and the ion drifts of (d) SuperDARN in the northern hemisphere F region in solar magnetic coordinates from 60-90° and 0-24 hour MLT, for the November-January winter periods during the 2005-9 solar minimum. To reduce overlap of vectors the scales vary where stated. SCANDI and CHAMP data are binned by concentric rings with a width of 2° magnetic latitude and 15° magnetic longitude (or 1 hour MLT). To avoid overlap at the pole, we restrict plots to a maximum of 88° magnetic latitude. CMAT2 data is shown with its 2° × 18° grid resolution maintained after transforming into magnetic coordinates (see Chapter 2). SuperDARN is shown as a 40 × 40 grid as described in Section 4.2.

We now discuss the well-known neutral wind features (see for example: Killeen et al. (1982); Lühr et al. (2007); Förster et al. (2008); Emmert et al. (2006*b*); Dhadly et al. (2017*a*,*b*) and references therein; and as discussed in Chapter 1) as seen in the CMAT2, SCANDI and CHAMP neutral wind patterns in Figure 4.13, as well as their distinct differences. All neutral wind plots indicate solar heating as a primary driver of neutral wind circulation, with a lag of order hours (Strangeway 2012) and predominantly anti-sunward wind consistent with theory (see for example: Kohl & King (1967); Cierpka et al. (2000)). Other heating sources include Joule heating and precipitation in the cusp and auroral regions (Cierpka et al. 2000; Förster et al. 2008; Dhadly et al. 2017*a*). Pressure gradient forces from these heating sources cause the neutrals to flow anti-sunward over the polar cap, aligning with the ion drifts as the ions couple via collisions with the neutrals (Thayer et al. 1995). Consequently the polar cap shows the strongest winds in the region from the momentum exchange between ions and neutrals (Killeen et al. 1991; Lühr et al.

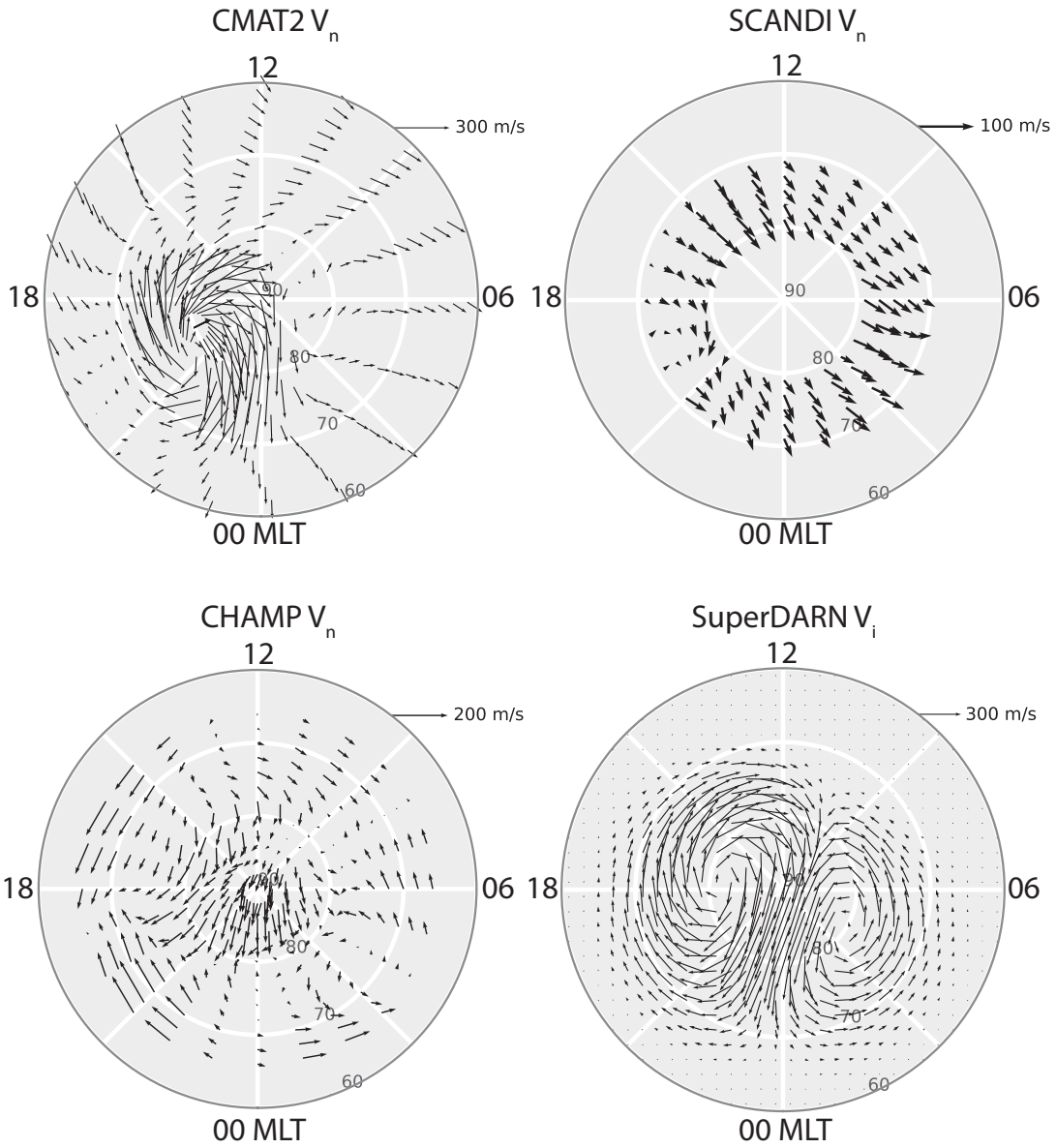

Figure 4.13. Averaged polar projection plots of the neutral wind directions and magnitudes measured by (a) CMAT2, (b) SCANDI, (c) CHAMP and the ion drifts of (d) SuperDARN in the northern hemisphere in solar magnetic coordinates from 60-90° and 0-24 hour MLT, for the November-January winter periods during the 2005-9 solar minimum. It should be noted that to reduce overlap of vectors the scales are not equal.

2007). The strong neutral wind then flows duskward in the dusk-midnight sector, and is dependent on IMF clock angle (Förster et al. 2008). Indeed, the pressure gradient driven winds are modulated in most regions by the ion drift convection pattern through ion-neutral coupling (see for example, Lühr et al. (2007); Förster et al. (2008) and references therein); although the effects are less prominent in winter (Lühr et al. 2007; Dhadly et al. 2017*a*). Evidence of coupling can remain long after increased geomagnetic activity due to the inertia of the neutral atmosphere, known as the flywheel effect (Lyons et al. 1985; Odom et al. 1997); this may therefore be the case also in low geomagnetic activity. Indeed, the movement of ions generated by solar ionisation on the dayside to the nightside and precipitation both aid to maintain ion-neutral coupling (Kwak & Richmond 2007). However, low geomagnetic conditions do reduce the dominance of ion drag due to the reduced electric field (see Equation 1.28), and contribute to the low magnitude of the ion drifts measured by SuperDARN in Figure 4.13.

Focusing on the plasma circulation (as discussed in Chapter 1), a typical twin cell convection controls the ions (Cowley & Lockwood 1992; Lockwood & Cowley 1999; Lockwood & Morley 2004) flowing as an $\mathbf{E} \times \mathbf{B}$ drift with anti-sunward flow across the polar cap and sunward flow at lower latitudes, larger in magnitude than the neutral wind due to magnetospheric electric field forcing. The twin cell convection can also be seen to influence the neutral circulation sunward via ion drag (Kwak & Richmond 2007) with help from inertial forces, with a strong clockwise vortex at the dusk cell near 80° between 17-19 MLT with westward wind at auroral latitudes, and a weaker anti-clockwise vortex at the dawn cell near 80° between 3-7 MLT with eastward wind at auroral latitudes. The dusk vortex winds are very strong, similar in magnitude to the polar cap winds, and rotate with the Coriolis force (Fuller-Rowell & Rees 1984) and ion drag, particularly at auroral latitudes (see for example: Kwak & Richmond (2007); Dhadly et al. (2017*a*) and references therein). The centrifugal and Coriolis force also add here to strengthen winds (Fuller-Rowell & Rees 1984). The duskside vortex also leads to large wind shears as two flow channels, sunward from ion drag and anti-sunward from solar heating, are anti-parallel at $\sim$70°(see for example, Dhadly et al. (2017*a*) and references therein). This dawn-dusk asymmetry is also seen in the plasma circulation. Indeed, the inertia of the neutral atmosphere also causes the ion convection pattern to be prolonged even if the magnetosphere driver is reduced (Banks 1972). In the dawnside vortex the Coriolis and centrifugal forces balance (Fuller-Rowell & Rees 1984), however in winter the vortex is stronger (Dhadly et al. 2017*a*), and

is pronounced in the neutral wind patterns of CMAT2 and CHAMP, and to some extent SCANDI. The CMAT2 and SCANDI wind patterns are most consistent with other studies (Lühr et al. 2007; Förster et al. 2008; Dhadly et al. 2017*a*).

A final wind feature to note is the stagnation near the cusp region seen in Lühr et al. (2007); Förster et al. (2008) and references therein. This occurs at 12 MLT at ∼65° and can be see only in CHAMP in Figure 4.13. It should be noted that although SCANDI cannot measure at this latitude there is reduced wind at 12 MLT at 70°. This is due to a significant upwelling of wind from particle precipitation and Joule heating (see for example: Lühr et al. (2004); Förster et al. (2008)) and is discussed in detail in Chapter 5.

Concerning differences between the data sources in Figure 4.13, magnitude is the most apparent. Typical winds for solar minimum measured by satellites are ∼200 m s^{-1} (see for example, St.-Maurice & Hanson (1982); Förster et al. (2008) and references therein). In general, the neutral winds are particularly low in magnitude in Figure 4.13 due to the solar minimum, the low Kp restriction implied on the data and the time of year (surrounding winter solstice). This quiet activity is also reflected in the ion drifts, although consistent with respect to the neutral wind magnitudes of CHAMP and SCANDI, being double their magnitude in the F region (Aruliah et al. 2005). CMAT2 shows the strongest winds, peaking at ∼300 m s^{-1} and comparable to the ion drift magnitudes. CMAT2 also follows the SuperDARN duskside cell exactly, showing the dominance of ion drag on the neutral wind direction in this region, and this is where the wind peaks. CMAT2 may be overestimating here due to the abnormally quiet solar minimum (see for example, Solomon et al. (2011)). Models, such as CMAT2, are unable to replicate such a low solar minimum when they have been calibrated with higher F10.7 index values of other solar minima. This bias is discussed in depth in Chapter 5.

CMAT2 is known to overestimate the FPI wind measurements (see for example, Griffin et al. (2004)). This is most likely due to the modelling of the electric field forcing, which is currently based on climatologies and not representative of temporal variability. CMAT2 and other GCMs were calibrated with the DE-2 satellites from the early 1980s (Aruliah et al. 2018), see for example Killeen et al. (1982, 1984). Although models benefited from data obtained using a spectrometer to directly measure wind as opposed to inferring from accelerometer data, DE-2 sampled winds when solar flux was abnormally large for the period (due to the grand solar maximum), which introduces a bias. This may also explain the large model winds, and suggests the model may need re-calibrating for a new era

of grand solar minimum. CMAT2 winds are also more westward than both SCANDI and CHAMP, particularly at dusk and near 12 MLT. This is also evident in Figure 4.5, which shows CMAT2 winds systematically westward of CHAMP winds. As a result of this CMAT2 bias, the general wind patterns should be compared in favour of the magnitudes themselves.

SCANDI has the lowest magnitude winds, however with known biases in both CMAT2 (Griffin et al. 2004; Aruliah et al. 2018) and satellite data (Emmert et al. 2006*a*,*b*; Förster et al. 2008; Dhadly et al. 2017*a*,*b*; Aruliah et al. 2018), these are not necessarily incorrect. SCANDI has the added benefit of very few assumptions using Doppler shifts and the FPI dimensions (Aruliah et al. 2005) to derive the neutral winds compared to satellites, which assume satellite cross-sections and surface reflection behaviour (Doornbos et al. 2010). However, in the previous section we saw that the height integration method of FPIs may lead to an underestimation, although relatively small. Moreover, during solar minimum and low geomagnetic activity the intensities of FPI measurements can be low reducing the signal-to-noise ratio (Aruliah et al. 2005, 2018). This study would also benefit from more SCANDI data to improve the averaging.

CHAMP, in contrast, shows larger winds with a more eastward bias, particularly at dawn and dusk compared to both SCANDI and CMAT2. The outflow from the polar cap as measured by CHAMP is more duskward than CMAT2, with the duskward vortex similar to SCANDI, although the magnitude discrepancy is largest here (also seen in GOCE data (Dhadly et al. 2017*a*)). This divergence is also seen in Bjoland et al. (2015), indeed their 12-18 MLT sector is very similar to this study. However, CHAMP also shows a strong dawnside vortex, comparable in scale to the duskside vortex. This may be related to the winter season which produces lower magnitude winds (Dhadly et al. 2017*a*), although this is not seen in SCANDI as prominently, which instead agrees better with CMAT2. Contrary to other CHAMP accelerometer-derived wind studies, namely Lühr et al. (2007), Förster et al. (2008) and Bjoland et al. (2015), which averaged over all seasons and did not restrict Kp, we average over the winter periods and restrict Kp to represent quiet geomagnetic activity. We therefore see a distinct decrease in CHAMP wind magnitudes compared to these studies. However, noting the scales in Figure 4.13, CHAMP winds are still on average double the SCANDI winds. It should be noted that we may be adding to the errors introduced by CHAMP by not including enough data to reduce the statistical error and by using poorer quality data from later in the mission.

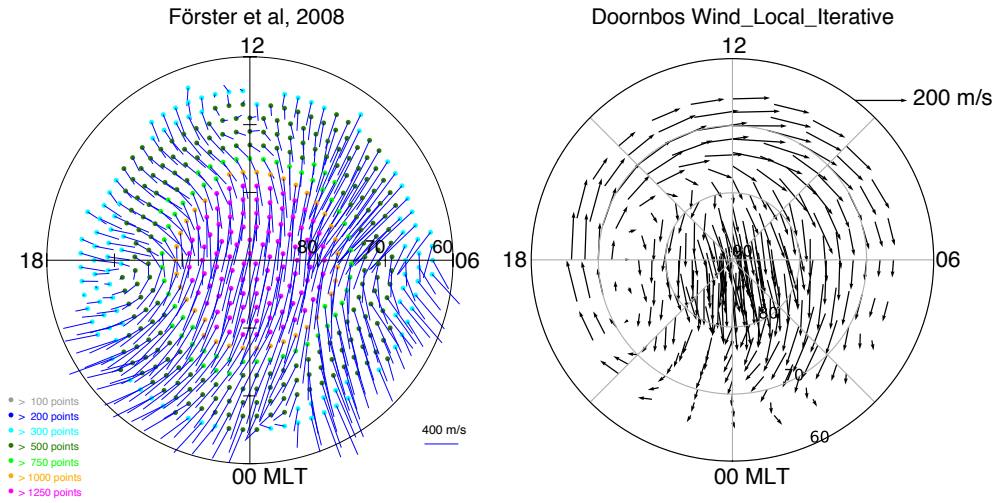

Figure 4.14. Averaged polar plots of the neutral wind direction and magnitude in 2003 as presented in Förster et al. (2008) (left) and calculated using the Doornbos et al. (2010) aerodynamical model (described in Chapter 2, right). Winds are shown in the same coordinate system as Figure 4.13.

We can also compare our CHAMP wind directions loosely (due to the different conditions) to these studies, also noting that though their data are derived from the same CHAMP accelerometer measurements, their derivation of winds preceded the methodology outlined in Chapter 2, adopting statistical approaches to extract the horizontal wind components. There is most agreement along the noon-midnight line (the straight line drawn from 12 to 0 MLT); the lack of agreement in the dawn-dusk line (similarly, for 6-18 MLT) may be due to season. We investigate this further by replicating the northern hemisphere wind plot in Figure 1 of Förster et al. (2008), as shown in Figure 4.14, which uses the entire 2003 wind dataset again plotting on a magnetic northern hemisphere polar grid. This comparison shows similarity across the polar cap, however there is clearly a co-rotation at lower latitudes in our data, which is more typical at mid-latitudes. At latitudes below the auroral oval, the direction of the Coriolis and centrifugal forces can reverse as winds become more sunward-directed (Förster et al. 2008), this may explain some of the behaviour we see in CHAMP in Figures 4.13 and 4.14, though not all. Förster et al. (2008) uses legacy data (as described by Liu et al. (2006)) no longer available on the DEOS Thermosphere web server for satellite drag observations (see Chapter 2); instead in this study we use the local iterative wind data product which uses the aerodynamical model described by Doornbos et al. (2010). Förster et al. (2008) also notes their dissimilarity with FPI measurements, suggesting the wind derivation may need to be reinvestigated.

This may be contributing to the discrepancy seen in Figure 4.13 as the datasets are not comparable, however at the latitudes we are examining they should be near-equivalent. More recent wind data products available on the DEOS Thermosphere web server have also undergone rigorous error reduction and filtering to improve the data quality, including an assessment of the large wind magnitudes seen in Förster et al. (2008)[3].

4.3.3 Comparison of Joule Heating

Having established the climatologies of $\mathbf{V}_n$ from the independent sources of CMAT2, SCANDI and CHAMP, we may investigate the consequences for calculating Joule heating. Figure 4.15 uses the same coordinate system as Figure 4.13, detailing the (a) CMAT2, (c) SCANDI and (e) CHAMP wind-derived and (b) CMAT2 and (d) SCANDI temperature-derived Joule heating patterns as outlined in Table 4.1. (f) shows the predicted (non-mechanical) Joule heating output of CMAT2, calculated using Equations 1.31 and 1.13 in Chapter 1. All data are binned by concentric rings with a width of 2° magnetic latitude and 15° magnetic longitude (or 1 hour MLT). The same scale has been used to allow for easier comparison of magnitude and phase. In the calculation of wind-derived Joule heating (in Equation 4.6), the squaring is applied to all drifts and then the binned average taken to reduce the standard deviation error (Codrescu et al. 2000). We expect Joule heating to peak where the neutral winds and ion drift vectors are anti-parallel, such that there is a shear reversal and the relative ion-neutral motion is largest (St.-Maurice & Hanson 1982); we see this in Figure 4.13. The latitude locations of the heating spots, centred on ∼75°, are therefore related to the expansion of the convection pattern shown by SuperDARN in Figure 4.13, which increases the friction between neutrals and ions (Goodwin et al. 2014).

The following is a description of the Joule heating hot spots seen in Figure 4.15 (a)-(e): (a) CMAT2 wind-derived Joule heating with CMAT2 $\mathbf{V}_n$ and SuperDARN $\mathbf{V}_i$. We see a faint post-midnight heating spot centred on 75° and spanning 2-11 MLT, peaking between 5-7 MLT. There is a larger post-noon heating spot centred also on 75° and spanning 13-24 MLT, peaking between 17-22 MLT and reaching $\sim 0.6 \times 10^{-20}$ kg m^2 s^{-2}. (b) CMAT2 temperature-derived Joule heating with CMAT2 T_i and CMAT2 T_n. This has less spread in MLT than (a), and is shifted from dusk towards midnight. There is a peak between 18-24 MLT similar in magnitude to (a), with spread reaching the latitudes of the heating spots in (a). (c) SCANDI wind-derived Joule heating with SCANDI $\mathbf{V}_n$ and SuperDARN $\mathbf{V}_i$.

[3]At the time of writing we are currently in contact with Eelco Doornbos to resolve this issue.

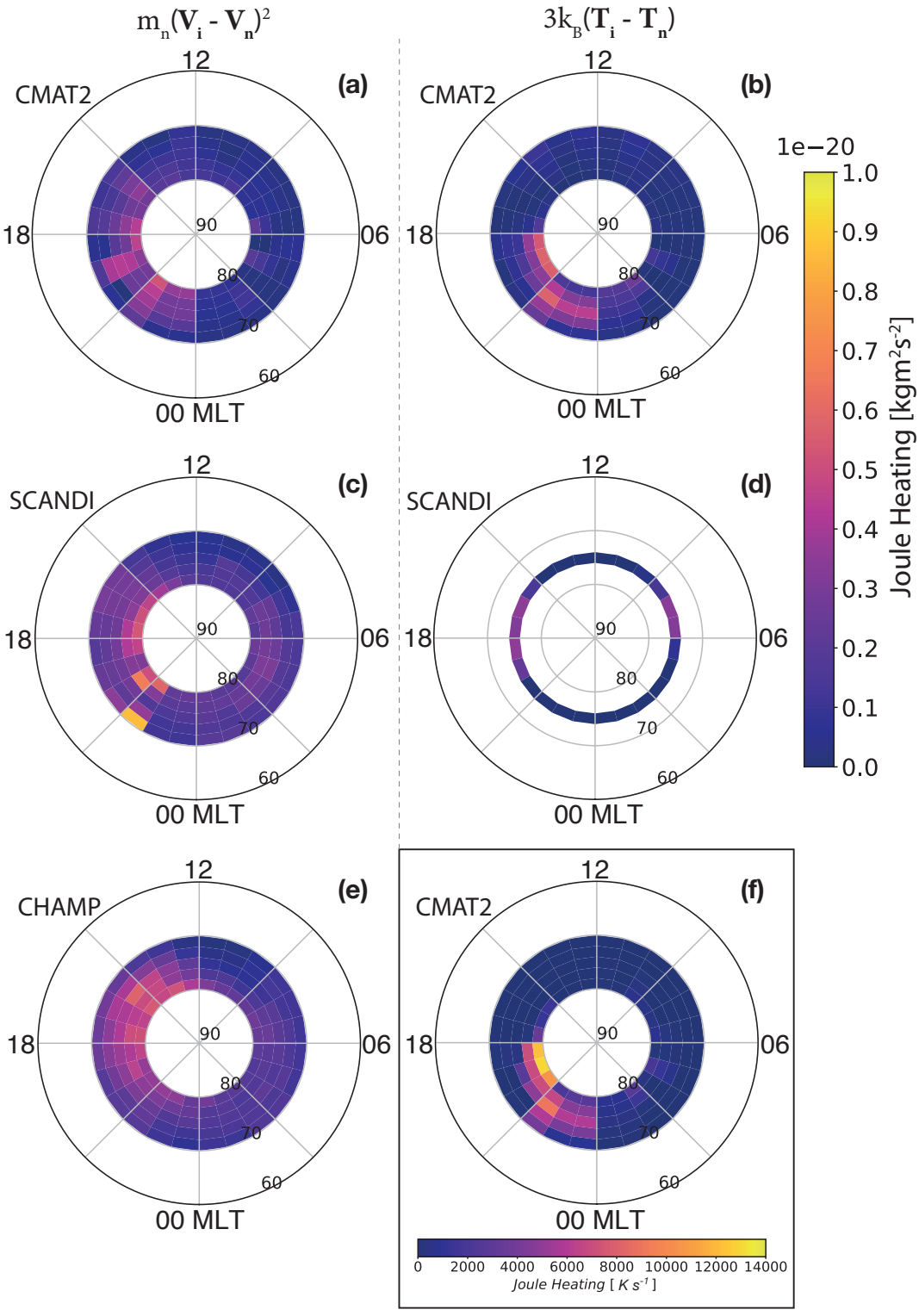

Figure 4.15. Northern hemisphere polar plots of the wind-derived Joule heating using (a) CMAT2, (c) SCANDI and (e) CHAMP neutral winds and SuperDARN ion drifts, and temperature-derived Joule heating using (b) CMAT2 and (d) SCANDI neutral temperatures and CMAT2 and EISCAT ion temperatures respectively, in magnetic coordinates from 60-90° and 0-24 hour MLT, for the November-January winter periods during the 2005-9 solar minimum. This is further outlined in Table 4.1. (f) shows the CMAT2 Joule heating output.

We can identify a faint ($\sim 0.3\times10^{-20}$ kg m^2 s^{-2}) post-midnight heating spot, although there is much spread, centred on 74° and spanning 2-11 MLT, peaking near 5 MLT. There is a larger, more obvious heating spot centred also on 75° and spanning 13-20 MLT, peaking sharply at 21 MLT and reaching $\sim 0.9\times10^{-20}$ kg m^2 s^{-2}. (d) SCANDI temperature-derived Joule heating with SCANDI T_i at the zenith zone and EISCAT T_n. We see a post-midnight heating spot spanning 6-7 MLT, peaking at 6 MLT. There is a larger heating spot spanning 16-19 MLT, peaking between 17-18 MLT. The magnitude of both heating spots is the lowest of all plots, peaking at $\sim 0.3\times10^{-20}$ kg m^2 s^{-2}. (e) CHAMP wind-derived Joule heating with CHAMP $\mathbf{V}_n$ and SuperDARN $\mathbf{V}_i$, we see a faint post-midnight heating spot centred above 75° spanning 3-11 MLT (like CMAT2 and SCANDI), peaking at ∼6 MLT. There is a larger heating spot centred above 75° spanning 12-23 MLT (again like CMAT2), peaking between 14-16 MLT at $\sim 0.6\times10^{-20}$ kg m^2 s^{-2}.

(f) shows the Joule heating output of CMAT2 in units of K s^{-1}, in thermal energy 14,000 K s^{-1} $\approx 0.3\times10^{-20}$ kg m^2 s^{-2}. This is similar to (b) in size and location, although half the magnitude. This shows CMAT2 may be underestimating its Joule heating output. Indeed, models typically underestimate Joule heating due to the oversimplification of the electric field, failing to include the large temporal variability of ionospheric flows, which can have an equal amplitude contribution compared to the average field-calculated Joule heating (Codrescu et al. 1995; Deng & Ridley 2007). This is mitigated to some extent by assimilating the 2-minute resolution SuperDARN potentials into CMAT2, however there is still smoothing due to the lower temporal resolution bins of CMAT2. There is also no frictional heating component included in the CMAT2 model, though between 90-500 km frictional heating should be equivalent to Joule heating (St.-Maurice & Hanson 1982; Thayer & Semeter 2004). It should be noted that the poor resolution of global models in general means they underestimate Joule heating and reduce local heating features (Deng & Ridley 2007).

Reviewing Figure 4.15 in its entirety, we can discern two heating spots both lying at ∼75° magnetic latitude, a weaker post-midnight heating spot centred around 6±1 MLT and a post-noon heating spot centred just before 18±2 MLT, in agreement with other studies (see for example: St.-Maurice & Hanson (1982); Deng & Ridley (2007); Bjoland et al. (2015) and references therein), and also seen in ion drift and temperature data (Baron & Wand 1983). The post-noon heating spot covers a larger spatial scale, and is also the larger in magnitude of the two heating spots in agreement with Bjoland et al.

(2015) which found this to be a trait of solar minimum. During CHAMP's solar maximum the post-midnight heating spot was larger, also seen in Deng & Ridley (2007) which used the Global Ionosphere Thermosphere Model (GITM) with a F10.7 index value of 150 sfu, more typical for solar maximum, to map Joule heating. However, it should be noted that the two heating spots in the CHAMP Joule heating pattern tend more towards dawn and dusk than those in Bjoland et al. (2015), which may be due to the focus on winter-only data or the CHAMP data product used. This offset, however, does agree with GITM-predicted $\mathbf{V}_i - \mathbf{V}_n$ (Deng & Ridley 2007). Post-noon heating is in part driven by solar heating (see for example, Cierpka et al. (2000)), as the latter drives the neutral wind flow which opposes the flow (anti-parallel at dusk) of the ion drifts (see Figure 4.13). The wind-derived post-midnight heating spot (in Figure 4.15 (a), (c) and (e)) is lesser in magnitude as the ion drifts in that region are slightly diminished compared to post-noon. We also see this in the temperature-derived Joule heating pattern (in Figure 4.15 (b) and (d)), as the ion temperature is affected by a change in ion drift which arises from collisions with neutrals (St.-Maurice & Hanson 1982).

Comparing Figure 4.15 (a), (c) and (e) wind-derived Joule heating, (c) SCANDI has the highest peak magnitude, followed by (e) CHAMP and then (a) CMAT2. As all use SuperDARN $\mathbf{V}_i$ drifts, the wind-derived Joule heating differences tie back to the magnitude and direction of their respective neutral winds in Figure 4.13. The heating patterns, such as the locations of the two heating spots and magnitude, agree with the location of most shear and (in general) with each other. Indeed, the two heating spots CHAMP samples are very similar in size to the CMAT2 and SCANDI wind-derived Joule heating. It should be noted that CHAMP neutral winds exceed SuperDARN ion drifts in some locations not included in the 70-80° latitude range of Figure 4.15 (e), which will be masked by squaring the velocity difference in Equation 4.6.

On closer inspection there are further dissimilarities between the patterns that can be explained. Referring to the wind-derived SCANDI Joule heating pattern (see Figure 4.15 (c)), the post-noon heating spot is less continuous than its CMAT2 and CHAMP counterparts. This is likely due to the lack of data during this period as SCANDI was operational from November 2007, and we are also reliant on the availability of EISCAT data. In contrast, CHAMP uses 12 months of data. However, the magnitude and location of the post-noon heating spot can still be determined. There is also a clear offset between the post-noon heating spot of the CMAT2 temperature-derived Joule heating (see Figure

4.15 (b)) and the other patterns. This is linked to the Joule heating output of CMAT2 in Figure 4.15 (f). The CMAT2 temperature-derived Joule heating also overestimates when compared to the SCANDI temperature-derived Joule heating. This may be related to overestimation of densities in GCMs, which is linked to temperature and wind in the model (see for example: Cierpka et al. (2000); Murray et al. (2015)). This is discussed further in Chapter 5.

4.3.4 St.-Maurice Equation Validation

The temperature-derived Joule heating patterns in Figure 4.15 (b) and (d) can be used to validate the wind-derived Joule heating in (a) and (c) respectively and therefore CHAMP in (e), as well as Equation 4.6 itself. The Joule heating CMAT2 output in (f) is also an indication of the predicted heating distribution as a physics-based and self-consistent GCM. As the neutral atmosphere (which is orders of magnitude denser than the ionosphere) introduces inertia into the ionosphere, frictional heating from collisions between the ions and neutrals causes an ion temperature increase (Strangeway 2012), responsible for 96% of the increase in local ion temperature (Cierpka et al. 2000). We expect the ion temperatures to increase where there are shears in circulation (St.-Maurice & Hanson 1982; Dhadly et al. 2017*a*). Goodwin et al. (2014) also found T_i enhancements to be strongly linked to $(\mathbf{V}_i - \mathbf{V}_n)^2$ using Poker Flat Incoherent Scatter Radar (PFISR) data (also seen in Cierpka et al. (2000)), and recent studies have used Equation 4.6 to derive unknown variables in the relation (see for example: Bjoland et al. (2015); Kiene et al. (2017)).

CMAT2 and SCANDI temperature-derived Joule heating in Figure 4.15 support the location of the wind-derived heating spots, suggesting the magnitude discrepancy does not drastically affect the spatial distribution of the heating pattern. However, SCANDI temperature-derived Joule heating peaks at almost half the magnitude of its wind-derived counterpart. Figure 4.16 provides a more transparent comparison, and is the Joule heating values of Figure 4.15 at the zenith zone of SCANDI (75° magnetic latitude) with respect to its MLT for CMAT2 temperature-derived (dashed blue), CMAT2 wind-derived (solid blue), SCANDI temperature-derived (dashed green), SCANDI wind-derived (solid green) and CHAMP wind-derived Joule heating (solid red). Figure 4.16 better highlights the magnitude difference between the datasets, whilst still showing they are predominantly in phase.

The CHAMP-SCANDI magnitude discrepancy is most extreme post-noon with CHAMP

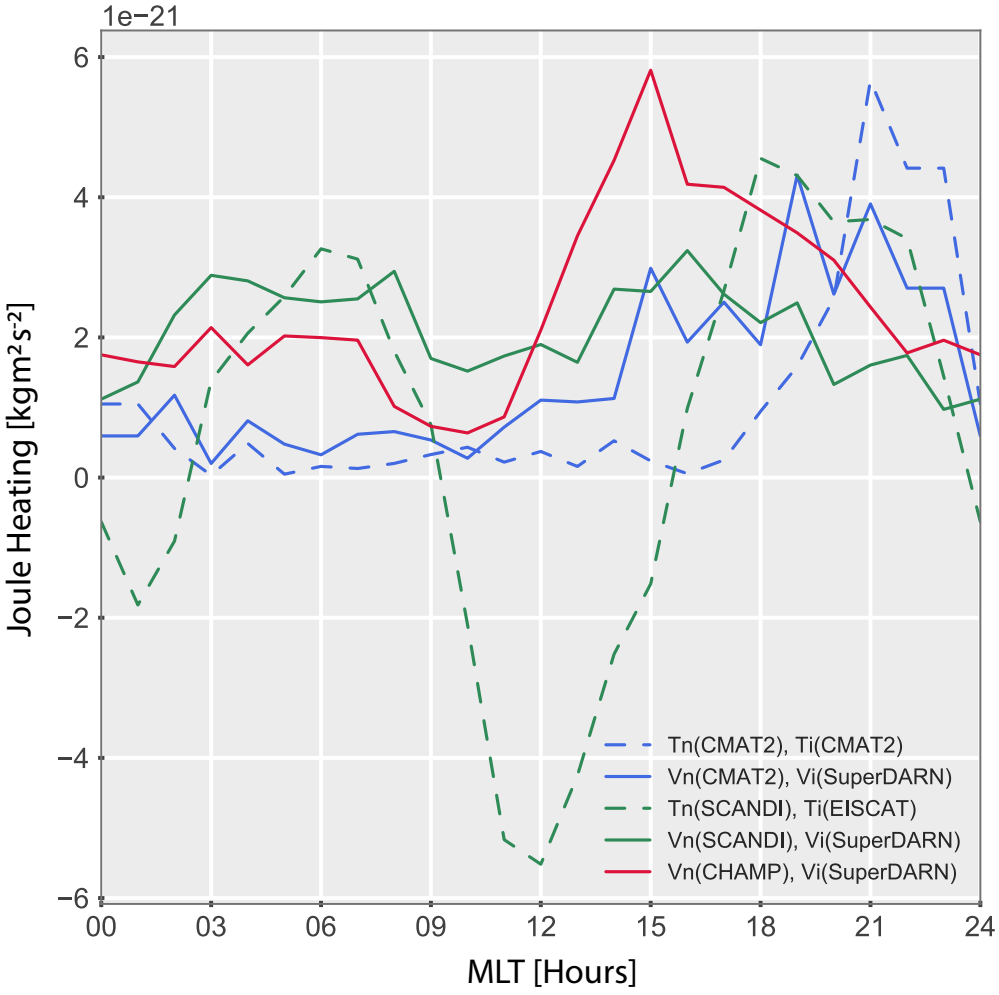

Figure 4.16. Wind-derived and temperature-derived Joule heating values of Figure 4.15 at the zenith zone of SCANDI (75° magnetic latitude) with respect to MLT. The legend indicates the type of Joule heating (temperature-derived or wind-derived) and the dataset used. CMAT2 is in blue, SCANDI is in green and CHAMP is in red. Temperature-derived Joule heating is shown by a dashed line and wind-derived Joule heating is shown by a solid line.

(solid red) reaching over a factor of 2 above SCANDI wind-derived (solid green) Joule heating at ∼15 MLT, but otherwise CHAMP compares well with SCANDI. This large peak in CHAMP-derived Joule heating at 15 MLT is also seen later in CMAT2 temperature-derived (dashed blue) Joule heating at 21 MLT. Both CMAT2 wind-derived (solid blue) and temperature-derived (dashed blue) Joule heating perform poorly in representing the post-midnight region between 3-9 MLT, and are very low in comparison to both the SCANDI (green) datasets and CHAMP (solid red) despite being in agreement with each other. The MSISE-90 neutral atmosphere model (Hedin 1991), which CMAT2 uses, can overestimate the neutral temperatures by 100 K over the ion temperatures during quiet conditions (Cierpka et al. 2000), which may explain the reduced temperature-derived Joule heating in this region. SCANDI temperature-derived (dashed green) Joule heating shows some agreement with SCANDI wind-derived (solid green) Joule heating, particularly during the post-midnight heating spot, however, at 12 MLT there is a significant discrepancy in magnitude, and during the post-noon heating there is a slight lag in temperature-derived compared to wind-derived Joule heating. Indeed, we expect the ion drifts to be near-instantaneous with a ∼20-minute delay (Heelis et al. 2002), and the neutral wind and temperature changes to have a lag of order hours in the F region (see for example: Rishbeth & Garriott (1969); Cierpka et al. (2000); Heelis et al. (2002); Strangeway (2012)).

Figure 4.15 (d) shows the SCANDI-EISCAT temperature-derived Joule heating pattern. This has been limited where the Joule heating value dropped below zero as an assumption of frictional heating is that ion temperatures surpass the neutrals by 100-200 K (St.-Maurice & Hanson 1982). Figure 4.16 instead has not been limited and shows 'cooling', where we can identify significant reductions in heating centred on 12 MLT and, to a lesser extent, 0 MLT where the ion temperatures can be decreased by as much as 100 K at 0 MLT compared to the neutrals. The latter cooling region at 0 MLT is also seen in observations by Kiene et al. (2017) in the last few hours of their all-sky FPI and (few minutes of their) rocket campaign at the Poker Flat Research Range in Alaska, where they saw $T_i < T_n$ near 12 UT (∼0 MLT at this location). The neutral temperatures measured by FPIs at 0 MLT are likely higher due to the poor signal-to-noise ratio, which is particularly low at midnight and worsened during solar minimum and quiet geomagnetic activity (Aruliah et al. 2005), however this does not explain the same behaviour at 12 MLT. Interestingly, both cooling regions are also present in Deng & Ridley (2007) when using GITM to calculate similar $\mathbf{V}_i - \mathbf{V}_n$ distributions (in their Figure 5), though not

in CMAT2. We suggest the cooling at 12 MLT is not a real effect, and that we may not be satisfying the assumptions of the simplified ion energy equation in Equation 4.6. This assumes that below 400 km the rate of heat exchange equals the frictional heating rate, and Thayer & Semeter (2004) showed this ion frictional rate is not always equal to the Joule heating rate. The variability of the electric field may also break the assumption (see for example, Thayer & Semeter (2004) and references therein). Perhaps in time scales of a few minutes thermodynamic equilibrium is not balanced, however the FOV of an all-sky camera implies a large-scale effect. Equation 4.6 is valid on $>\sim$seconds temporal scales and >15 km (St.-Maurice & Hanson 1982); these scales may need to be re-investigated in the 12 MLT region. This is part of a current on-going statistical study by the UCL group (paper in preparation). Moreover, a 7-minute averaging of EISCAT data may be masking larger ion temperatures as the ionosphere has a higher variability than the neutral atmosphere (Aruliah et al. 2004).

In order to compare the wind-derived Joule heating of CMAT2, SCANDI and CHAMP in Figure 4.15 (a), (c) and (e) respectively, we can also use the CMAT2 temperature-derived Joule heating in (b) as a base to subtract. Figure 4.17 shows these CMAT2, SCANDI and CHAMP residual difference plots. Figure 4.17 suggests more significant differences than a magnitude discrepancy, as there is no net systematic error between CMAT2, SCANDI and CHAMP. We expect the CMAT2 residual in Figure 4.17 (a) to be near-zero if Equation 4.6 is valid, as CMAT2 is a self-consistent and physics-based GCM; we see in general this is the case. There is, however, a systematic trend in Figure 4.17 (a, b, c) where the wind-derived Joule heating underestimates the temperature-derived Joule heating to produce a negative residual between 18-24 MLT. This shows the two are not equivalent in this region, and therefore Equation 4.6 is invalid in this region, irrespective of the dataset used. It can also be argued that CMAT2, SCANDI and CHAMP all show a systematic overestimation of wind-derived Joule heating compared to temperature-derived Joule heating between 12-18 MLT. This may suggest Equation 4.6 is only truly applicable between 0-12 MLT where the CMAT2 residual is near-zero. This non-equivalence may also explain why Figure 4.15 (f) agrees more with both wind-derived heating in (a) and temperature-derived heating in (b) between 0-12 MLT, where it is almost identical, than wind-derived heating in (a) between 12-24 MLT. The calculation of Joule heating in CMAT2 is therefore more dependent on temperature changes during ion-neutral collisions between 12-24 MLT rather than their net flow.

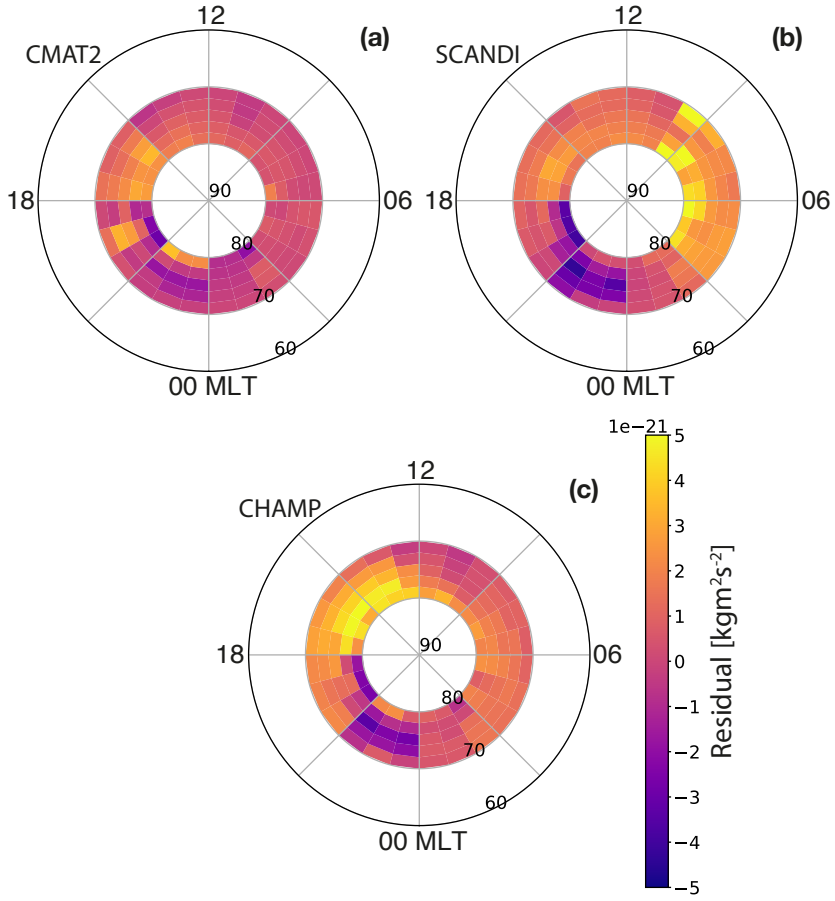

Figure 4.17. Polar projection of the wind-derived Joule heating of CMAT2, SCANDI and CHAMP (see Figure 4.15 (a), (c) and (e)) with the CMAT2 temperature-derived Joule heating (see Figure 4.15 (b)) subtracted to produce residual difference plots. All plots are of the northern hemisphere in magnetic coordinates from 60-90° and 0-24 hour MLT, for the November-January winter periods during the 2005-9 solar minimum. The same scale has been used to allow for easier comparison of magnitude and phase.

If we assume Figure 4.17 (a) validates the assumption in all other regions, it is evident that SCANDI and CHAMP do not; CHAMP has a similar distribution to CMAT2 but is over twice the magnitude, and SCANDI shows a displacement of the peak residual by ∼9 hours. These residuals are expected when referring to Figure 4.15, SCANDI has the stronger post-midnight heating spot compared to CMAT2 and CHAMP, whilst CHAMP has a post-noon heating spot closer to noon than both CMAT2 and SCANDI. However, this distinct offset in the peak residual between SCANDI and CHAMP implies substantially different errors in the two datasets.

4.4 Conclusions

This chapter moved away from FACs and set out to investigate the high-latitude thermospheric system they affect through Joule heating and the modulation of the neutral wind. Joule heating is one of the most significant energy dissipation mechanisms of FAC electromagnetic energy (Akasofu 1981; Cierpka et al. 2000), and, crucially, affects the density profile and composition of the upper atmosphere, both major components of satellite orbit dynamics and general circulation models (see for example: Vallado (2001); Lühr et al. (2004); Storz et al. (2005); Deng & Ridley (2007); Huang et al. (2012)).

We probed the neutral wind disparity between SCANDI and CHAMP, and tested whether they should be equivalent measurements at altitudes of ∼250 km and >300 km respectively by changing viscosity in CMAT2. We showed with CMAT2 that the datasets should sample similar magnitude winds unless the molecular viscosity coefficient of the upper atmosphere is grossly overestimated. We also acknowledged the disadvantages of using the model for solar minimum: the calibration with the DE-2 satellites (Aruliah et al. 2018) when solar flux was abnormally large for the period; the inability to model densities in a grand solar minimum; the overestimation of FPI measurements (see for example, Griffin et al. (2004)) due to the modelling of the electric field forcing; and the restriction on the breaking altitude of gravity waves preventing resultant coupling between the mesosphere and thermosphere (Yiğit 2008).

We then presented neutral wind patterns and averaged flow-derived Joule heating patterns in the northern polar region during the winter periods of the 2005-9 solar minimum comparing SCANDI, CHAMP and CMAT2 neutral winds, with SuperDARN providing the ion velocities. In all datasets we found post-noon and post-midnight heating spots, the former largest, consistent with other studies (see for example: St.-Maurice & Hanson (1982); Baron & Wand (1983); Deng & Ridley (2007); Bjoland et al. (2015) and references therein). We found a magnitude difference between ground, satellite and model-calculated Joule heating over the 70-80° latitude range (see Figure 4.15), but when focusing on the zenith zone at the centre of the SCANDI FOV (75°, see Figure 4.16) this dissimilarity was more apparent, with CHAMP-calculated Joule heating overestimating the magnitude of SCANDI wind-derived Joule heating in the post-noon region (peaking at a factor of 2 at ∼15 MLT), with the reverse occurring in the post-midnight region, though not as extreme. Until the cause of this dissimilarity is known, models assimilating CHAMP data may be

introducing a magnitude bias (also see Chapter 5) where the winds, and therefore Joule heating, are overestimated.

We used the frictional heating assumption to calculate temperature-derived Joule heating with the aim of supporting the wind-derived Joule heating distributions, using CMAT2 ion and neutral temperatures and SCANDI neutral temperatures with EISCAT ion temperatures. We found agreement between wind-derived and temperature-derived Joule heating within less than an order of magnitude, but with temperature lagging behind the drifts in the post-noon region (see Figure 4.16). This region also has a systematic error where wind-derived Joule heating underestimates the temperature-derived Joule heating between 18-24 MLT, and overestimates between 12-18 MLT, regardless of the dataset used. This implies the assumption is not valid in the dusk-midnight region, however we can conclude in general the simplified ion energy equation is a reasonable approximation, particularly between 0-12 MLT. However, the approximation does not allow us to resolve the cause of the wind disparity.

We therefore conclude that the cause of the wind disparity between SCANDI and CHAMP is either due to an outdated model of molecular viscosity of the upper atmosphere or an instrumental error. Assuming an instrumental error as the cause, we found that the FPI height-integration technique, a main source of uncertainty, produced a very small error ($\sim$8%). Based on the bias of satellite winds seen by Emmert et al. (2006*a*,*b*); Förster et al. (2008); Dhadly et al. (2017*a*), we suggest the bulk of the disparity therefore lies with CHAMP overestimating the neutral winds. This may be explained by the drag modelling discussed in the following chapter, which assumes absolute cross-sections and surface reflection behaviour (Doornbos et al. 2010) (also see Chapter 2). In the case of GOCE, Dhadly et al. (2017*a*) found these parameters to be the most probable errors and is currently investigating them. Other potential errors may arise in the calibration of the accelerometer data and from the models used, such as the radiation pressure model (also see Chapter 2), used to convert accelerometer measurements to drag data (Dhadly et al. 2017*a*).

4.5 Further work

Throughout this chapter we have discussed several lines of further work, here we summarise and expand on them further. Firstly, an obvious extension to the Joule heating study

would be to repeat the methodology for solar maximum (or even to investigate seasonal dependence as in Dhadly et al. (2017*a*) and Dhadly et al. (2017*b*)). As the CHAMP and SCANDI data encompassed different solar maxima (solar cycles 23 and 24 respectively), they are difficult to compare due to the low maxima of solar cycle 24. Any comparison would no doubt be biased, however this is still an important comparison to make and could be used in correcting model wind overestimations of solar maxima conditions.

Indeed, CMAT2 improvements are the focus of much future work. Firstly, to aid comparisons with satellites, the model should be extrapolated above its current upper boundary, ∼300 km for quiet conditions. Secondly, CMAT2 produced disproportionally large neutral winds, compared to SCANDI and CHAMP. CMAT2 and other GCMs were calibrated with the DE-2 satellites (Aruliah et al. 2018), see for example Killeen et al. (1982, 1984). Although models benefited from data obtained using a spectrometer to directly measure wind as opposed to inferring from accelerometer drag data, the DE-2 satellite sampled winds when solar flux was abnormally large for the period, which introduced a bias in CMAT2. This leads to the large model winds we see, and suggests the model needs re-calibrating for quiet solar activity conditions. Thirdly, the height restriction imposed on turbulent viscosity and the breaking of gravity waves needs to be updated considering new findings (see for example, Yiğit (2008); Vadas & Crowley (2017)). In particular the changes recommended by Yiğit (2008) should be implemented to allow gravity waves to break at higher altitudes, as they are a significant coupling mechanism in the atmosphere. This is particularly important for the neutral winds as it may be forcing the equivalence over the SCANDI-CHAMP altitude range. Moreover, investigations into molecular viscosity in this chapter and by Vadas & Crowley (2017), suggest the molecular viscosity coefficient may be too large. An interesting study using CMAT2 would be to implement the findings of Vadas & Crowley (2017). Here, the molecular viscosity coefficient reduces proportionally to $\rho^{-0.67}$, which reproduced their sounding rocket horizontal wind pattern.

Finally, if SCANDI and CHAMP are equivalent datasets, there may be an instrumental error we have not accounted for in either dataset. FPIs are highly calibrated and have been functional for decades, whereas a bias has already been realised in satellite data (Emmert et al. 2006*a*,*b*; Förster et al. 2008; Dhadly et al. 2017*a*,*b*; Aruliah et al. 2018). This potential CHAMP bias is described in further detail in Chapter 5. The CHAMP-FPI neutral wind disparity is currently the subject of a paper in preparation (Aruliah et al. 2018), which includes the work presented in this chapter on using CMAT2

to probe viscosity. This may lead to FPIs as a calibrating tool for satellites (and GCMs) (Aruliah et al. 2018), desirable due to the global and high-temporal coverage of the latter dataset and accuracy of the former. Moreover, missions such as QB50 (Muylaert et al. 2009), an E.U. FP-7 project using data from 50 CubeSats, are currently probing the lower thermosphere, providing data in a poorly sampled region and facilitating re-entry studies. The QB50 CubeSats orbit between 100-500 km, and may contribute to determining the necessary update to density datasets and aid in testing the altitude range where neutral temperatures and horizontal winds are constant.

Chapter 5

Modelling the Cusp Neutral Density Enhancement

In the previous chapters we studied two direct effects of FACs, namely ground GMDs and Joule heating in the ionosphere, the latter in turn responsible for modulating the neutral winds in the thermosphere. We briefly touched on a small localised feature of the wind pattern, the stagnation near the cusp, and this is where we now move our attention. This region is of particular interest because a consistent neutral density enhancement has been observed by the CHAMP on-board accelerometer, reaching twice the magnitude of the surrounding measured density (Bruinsma et al. 2004; Lühr et al. 2004; Liu et al. 2005). This increases the drag experienced by a satellite, and left un-modelled has significant implications on orbit determination (see for example: Vallado (2001); Storz et al. (2005)). Though a neutral wind disparity has been identified between CHAMP and polar region ground-based instruments (see Chapter 4), this newly sampled feature is unique in its localised nature and consistency, suggestive of a cusp density anomaly. However, we also review the reliability of CHAMP density measurements, as both CHAMP wind and density measurements are derived from the same accelerometer data (Doornbos et al. 2010).

The near-polar nature of the CHAMP orbit has allowed this fixed region to be probed over several passes. In each pass an increase in air density was observed along with small-scale FACs (Lühr et al. 2004). From this we infer the occurrence of FAC- and precipitation-driven Joule heating, as studied in Chapter 4, where soft electron precipi-

tation and fast plasma flows are typical of the cusp region, resulting in an upwelling in the thermosphere (see for example: Lühr et al. (2004); Carlson et al. (2012)), the latter inferred from the stagnation observed in CHAMP horizontal wind measurements and detected by FPI vertical wind measurements. Indeed, UCL ran two campaigns in 2012 and 2013 (SP-UK-CUSP and SP-UK-CUSPN respectively) as Svalbard passed through the cusp region to detect this upwelling.[1] UCL also ran a FPI-EISCAT experiment in February 2015 detecting another large upwelling at Kiruna near magnetic midnight in the nightside auroral oval, suggestive of a similar mechanism.

We use an adapted version of CMAT2[2] to simulate an empirical heating source representative of Joule heating as Svalbard passes through the cusp and Kiruna passes through magnetic midnight in the auroral oval. We individually inject heat in the F (∼150-200 km) and E (∼100-120 km) regions, characteristic of soft (∼100s eV) and hard (∼keV) electron precipitation respectively, to assess the cause and effects of the heating, and probe the significance of its location on the neutral densities, winds and temperatures of the two regions. We then compare the CMAT2-simulated neutral density at CHAMP's altitude (∼450 km) to that measured by CHAMP, and the CMAT2-simulated upwellings to FPI upwelling measurements during the UCL CUSP and FPI-EISCAT campaigns at Svalbard and Kiruna.

We find that CMAT2 reproduces the near-doubling of density at CHAMP's altitude when soft precipitation is applied to the cusp region, supporting a mechanism of increased conductivity and Joule heating in the F region, and in agreement with Carlson et al. (2012). CMAT2 successfully models a neutral fountain upwelling with vertical winds peaking at 46 m s^{-1} during the heating, though underestimates FPIs, which reach magnitudes of ∼200 m s^{-1}. This is due to the assumption of hydrostatic equilibrium in the model, which restricts vertical transport. Modelling hard precipitation in the cusp region produced a non-negligible density increase, a factor of 1.30 above the control. We suggest soft electrons are responsible for the largest enhancements, but that energies from ∼1 keV and below contribute to the average observed density enhancement. Neither soft or hard precipitation energies were able to mimic the magnitude of the upwelling measured by FPIs in the nightside auroral oval region, with the vertical winds, temperature, and density highly

[1] A third ran during the 20th March 2015 eclipse where SCANDI carried out high-time resolution measurements over a 2.5 minute period, detecting a strong upwelling in the cusp during daylight hours - this has never previously been possible using FPIs.

[2] This adapted version of CMAT2 was developed by Tim Spain when at UCL and used by Carlson et al. (2012).

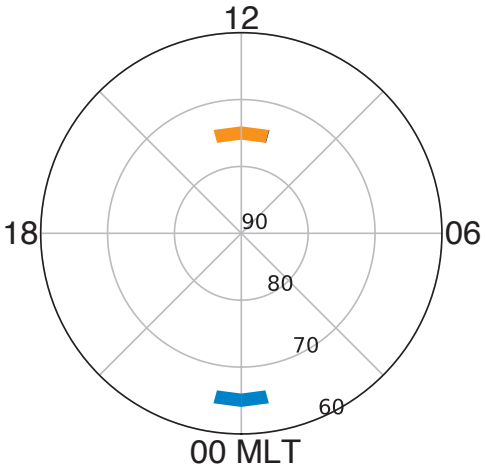

Figure 5.1. Illustration of cusp (orange) and magnetic midnight auroral oval (blue) locations in solar magnetic coordinates using a polar projection.

modulated by the cross-polar cap winds seen in Chapter 4. We instead suggest this is a storm-related anomaly.

5.1 Introduction

The cusps are characterised by sites of entry where the solar wind interacts with the atmosphere along recently opened geomagnetic field lines following magnetic reconnection (see for example, Russell (2000)). They are fixed with respect to solar magnetic coordinates (non-Earth fixed), and are on average located at 12±1-1.5 MLT with a magnetic latitudinal width of ∼1° and spread between 72-76° (see for example, Newell et al. (1989) and references therein). This is also detailed in Chapter 1 and demonstrated by a polar projection in Figure 5.1.

The near-polar LEO of CHAMP allows the satellite to observe the entire globe, including the cusp region. CHAMP uses an onboard triaxial accelerometer, as discussed in Chapter 2, to measure the local air drag (Bruinsma et al. 2004). Doornbos et al. (2010) uses an aerodynamical model with CHAMP drag measurements to extract cross-track neutral winds (used in Chapter 4) and neutral mass density. In the case of the latter, Liu et al. (2005) calculated the global thermospheric total mass density using CHAMP accelerometer data. However, Lühr et al. (2004) first noticed a significant density enhancement in the cusps, spanning a width of 350±150 km (see Moe & Moe (2008) for a historical review of the anomaly). Figure 5.2 shows the CHAMP drag-derived density measurements during

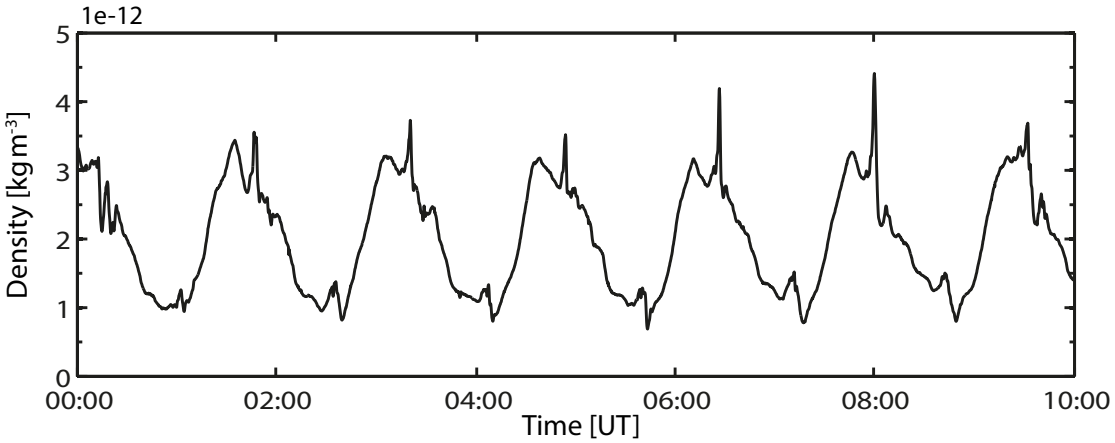

Figure 5.2. CHAMP accelerometer-derived densities over several passes during the period studied by Lühr et al. (2004), at an altitude of ∼450 km on 25th September 2000. The northern hemisphere cusp region is coincident with the spikes after the density maxima.

several passes at an altitude of ∼450 km on the 25th September 2000, three days after autumnal equinox and the period studied by Lühr et al. (2004). This is also seen in the unprocessed accelerometer data (see Lühr et al. (2004)). At around 06:30 UT the density in the northern cusp region is a factor of 1.8 higher than the surrounding areas. A more extensive survey during 2002-5 showed CHAMP observed enhanced drag at the northern hemisphere cusp for >50% of passes, averaging a factor of 1.33 above the relative density (Kervalishvili & Lühr 2013). On average, this translates to a few percent of the total drag experienced by the satellite, and is therefore a comparatively small, but persistent, effect. The southern hemisphere has a weaker cusp signature and is on average ∼25% smaller than the northern hemisphere enhancement, in part due to the larger separation between its respective geographic and geomagnetic poles (Rentz & Lühr 2008).

Lühr et al. (2004) also found the density enhancement persisted during quiet geomagnetic activity, as did the small-scale FACs (Kervalishvili & Lühr 2013). The anomaly is therefore not just a storm-time effect. Kervalishvili & Lühr (2013) further showed that the occurrence and magnitude of the enhancement are not season dependent. The persistence of the enhancement, though small, will therefore result in an additional systematic drag on a satellite in LEO precessing through the cusp for several passes, which in turn has implications for the satellite's respective orbit determination and degradation, leading to earlier re-entry or possible collisions (see for example, Royal Academy of Engineering (2013)).

If included in orbit prediction models, this effect can be accounted for and corrected. However, Lechtenberg et al. (2013) found that popular density models, such as the Orbit Determination Took Kit (ODTK) which uses the precision orbit ephermerides of the satellite, the High-Accuracy Satellite Drag Model (HASDM) which assimilates satellite density measurements including CHAMP (see also, Storz et al. (2005)) and the empirical Jacchia 1971 model (Jacchia 1970), all currently fail to reproduce the cusp anomaly due to their poor time resolution. This is also the case for the commonly used MSIS neutral atmosphere model (Hedin 1991; Picone et al. 2002), including MSISE-90 (Liu et al. 2005) and NRLMSISE-00 (Crowley et al. 2010). In the case of the former, Liu et al. (2005) compared MSISE-90 and CHAMP to show the model underestimated by 20-30% in the cusp and midnight regions, and most in the cusp; otherwise they agree within 5%. Moreover, empirical models that use spherical harmonics, including MSIS and Jacchia, lack enough data to support more harmonics, thus the data appear smoother (Crowley et al. 2010).

5.2 The Cusp Neutral Density Enhancement Mechanism

The open geomagnetic field lines in the cusp region extend to the IMF, which results in deposits of energy and plasma in the atmosphere as particles precipitate from the magnetosheath into the low altitude ionosphere, and Poynting flux travels along FACs (see for example, Russell (2000) and Chapter 1). In the cusp region intense ($\sim$ hundreds of μA m^{-2}) small-scale ($\sim$1 km) FAC filaments have been measured at the time of any density enhancement (Lühr et al. 2004). Neubert & Christiansen (2003) investigated small-scale FACs further, using Ørsted magnetic field data to derive small-scale FACs over 25,000 orbits. They found the majority of small-scale FACs are located in the cusp, and are up to two orders larger in magnitude than Region 1 and 2 FACs (seen in Chapter 3), with typical current densities of 10-100 μA m^{-2} and peaks of 1,000 μA m^{-2}. Like the density enhancement, these small-scale FACs persist in all geomagnetic activity (Lühr et al. 2004). Their 'filament' nature refers to the quick reversal of their polarity (Kervalishvili & Lühr 2013). Their closure and associated small-scale electric fields in the ionosphere can lead to Joule heating in the cusp region (Lühr et al. 2004). Indeed, strong local Poynting flux has been observed near the cusp, as well as strong electric fields and a peak in Joule heating (Crowley et al. 2010; Knipp et al. 2011). This local Poynting flux is particularly significant because the high-latitude dayside ionosphere-thermosphere will be experiencing

geomagnetically active conditions not represented by the Kp index, which measures the disturbed horizontal component of the magnetic field (Knipp et al. 2011).

Particle precipitation has also been observed in the cusp (see for example, Newell et al. (1989)), with the flux of soft 100 eV electron precipitation reaching up to two orders of magnitude greater in the cusp region than its surroundings (see for example: Newell et al. (1989); Clemmons et al. (2008); Deng et al. (2013) and references therein). Lühr & Marker (2013) used DMSP particle measurements to show that precipitation in the cusp is usually simultaneous with small-scale FACs. Lühr & Marker (2013) also showed that precipitation determines the location of the enhancement, whilst the magnitude is related to the merging electric field, which is itself tied to reconnection and the cross-polar cap potential (Rentz & Lühr 2008; Lühr & Marker 2013). Rentz & Lühr (2008) studied four years of CHAMP cusp density observations between 2002-5 to find the enhancement followed a 1-hour increased merging electric field, supporting Joule heating as the energy source, with small-scale FACs and particle precipitation as drivers (Kervalishvili & Lühr 2013). Events showing significant increases in EISCAT-measured electron temperatures from soft electron precipitation in the F region, have also been linked to Joule heating and high intensity small-scale FACs (see for example, Neubert & Christiansen (2003) and references therein).

The simultaneous presence of small-scale FACs and soft electron precipitation may therefore be key to such a significant density enhancement at the cusp. The soft electron precipitation can ionise the F region and increase conductivity, in turn increasing the altitude of peak Joule heating from the E to F region (see for example: Carlson et al. (2012); Deng et al. (2013) and references therein), being proportional to the Pedersen conductivity. This raises the current closures of small-scale FACs so that Poynting flux dissipates in the less dense F region, where the heating contributes more to the density enhancement as the energy is distributed between fewer particles. Soft proton precipitation and ions, with for example 2 keV energies and an energy flux of 0.3 mW m^{-2} in active conditions (see for example, Newell et al. (1989)), reach the E region and produce little significant Joule heating that can contribute to the density enhancement, actually causing a 4% depletion (Deng et al. 2013); this may be related to the depletion seen in Clemmons et al. (2008) and discussed in Section 5.2.1.

Rentz & Lühr (2008) also found the enhancement increased in magnitude with increased solar wind input and EUV radiation, suggesting the strong influence of the solar

wind and IMF on the enhancement (Kervalishvili & Lühr 2013). This may in part be due to the change in density from EUV (Lühr et al. 2004). Similarly, Neubert & Christiansen (2003) found that the amplitude of small-scale FACs related to the amount of solar wind turbulence. A further feature of the mechanism is ion upflow as a potential driver of (or at least contributor to) the upwelling, where the electric field from precipitating electrons relates to the respective ion upflow (see for example, Kervalishvili & Lühr (2013) and references therein, and Pollock et al. (1990) for an extensive survey of upwelling ion events and their characteristics). Though both the upwelling seen in neutrals and ions is simultaneous, the ion upflow may either be related to the pull of neutrals upwelling from heating or from the electron gas being heated and expanding, lifting the ions (Kervalishvili & Lühr 2013). The latter occurs along the geomagnetic field lines, increasing the plasma scale height (analogous to the change in the neutral density scale height), and is slowed down at lower altitudes by electron cooling, dependent itself on ion density (Kervalishvili & Lühr 2013). This mechanism is supported by the reduced electron temperatures and upflow drifts observed in the summer when the ion density is greater (Kervalishvili & Lühr 2013). Liu et al. (2010) studied similar enhancements with respective upwellings in the polar cap region during geomagnetic storms, and found small-scale FACs were not always present, but FACs did coincide with upflows measured by DMSP and the CHAMP-observed density enhancement in the polar cap, suggesting a possible mechanism of ion upflow. This effect has also been modelled by Sadler et al. (2012) using FAST satellite particle measurements that overlapped with CHAMP as an input into a model to simulate the thermosphere during an enhancement. Ion upflows were found to cause the neutral upwelling due to the increase in electron temperature, themselves driven by soft electron precipitation.

Both Poynting flux and soft electron precipitation are therefore significant drivers of the enhancement (the extent of the former dependent on the latter) through direct deposition of energy and indirectly through increased ionisation. The soft electron precipitation and rapid bursts of plasma flow due to the Poynting flux from these FACs, dissipate in the ionosphere via collisions in the form of Joule heating, predominantly at $\sim$150 km and under (see for example: Deng & Ridley (2007); Huang et al. (2012) and references therein), as described in Chapter 1 and studied in Chapter 4. This injection of energy heats the surrounding atmosphere, which expands, causing an upwelling and increased density at higher altitudes. This changes the composition of the atmosphere, in turn

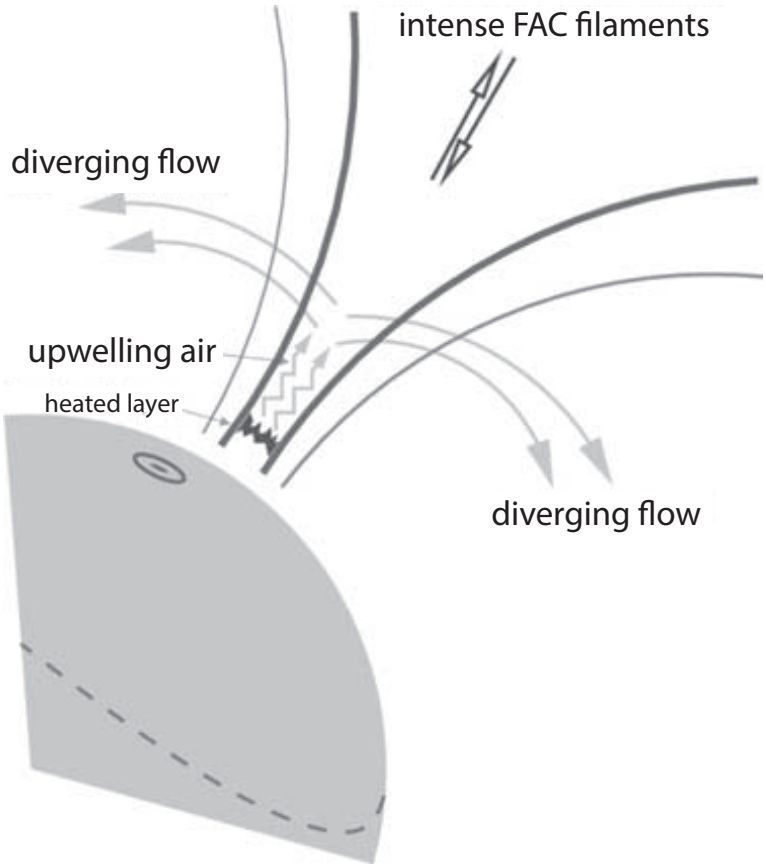

Figure 5.3. Illustration adapted from Lühr et al. (2004) demonstrating the upwelling of air from FAC-driven Joule heating. To be applicable to the Carlson et al. (2012) mechanism, the heating layer shown is in the F region due to increased ionisation and therefore conductivity.

increasing the density above the heating site, where CHAMP orbits. This mechanism is illustrated in Figure 5.3 (Lühr et al. 2004). Carlson et al. (2012) suggest a slight modification to the Lühr et al. (2004) mechanism, that the Joule heating is not driven by FACs directly, but indirectly through the increased ionisation in the region due to soft precipitation and therefore increased conductivity at F region altitudes (150-200 km). This also assumes coincident fast ion drifts, up to 2-3 km s^{-1}, that lead to strong frictional heating (Carlson et al. 2012). Slower but more typical flows of 1-2 km s^{-1} would drive the averaged observed density enhancement (Lühr et al. 2004). Based on our understanding from previous chapters and current observations we focus on the Lühr et al. (2004) and Carlson et al. (2012) mechanisms.

5.2.1 Further Effects of the Driving Mechanism

With the driving mechanisms established, we are now concerned with further effects of the resultant heating. Joule heating will lead to an increase in neutral and ion temperature at the height of the heating and below 200 km (Lühr & Marker 2013), with a further temperature increase at higher altitudes due to the resultant density enhancement and upwelling of the atmosphere, raising the scale height as detailed in Equation 1.22 in Chapter 1. This in turn affects the composition and chemistry of the atmosphere, and therefore surroundings of the satellite. The drag experienced by the satellite depends on the mass density of the atmosphere it passes through (see Chapter 2, and specifically Equation 2.2), and the drag coefficient (used in Equation 2.2) is dependent on the composition of the atmosphere and its temperature. Thus, we can see the cumulative effect this additional drag will have on a satellite trajectory, and the importance of modelling more than density by using a physical-based model such as CMAT2. It should also be noted that an error in the drag coefficient may also serve to reduce or amplify the enhancement.

The increase in scale height also implies a density depletion where the heat is injected, which we can test using CMAT2 or observe with lower altitude satellites such as the Streak mission (Clemmons et al. 2008), which measured altitudes between 123-325 km. Clemmons et al. (2008) used ten months of observations made by an ionisation-gauge sensor detecting gas pressure on the front surface of Streak during 2005-6. Streak measured a density depletion in the southern hemisphere cusp at an altitude 150 km below CHAMP, depleted by 1-2% compared to adjacent regions. Clemmons et al. (2008) infer soft precipitation as the cause; as most energy is lost at higher altitudes during collisions this would mean no detectable upwelling at the altitude of Streak. In the adjacent regions, harder precipitation occurs, with heating injected at a lower altitude, hence the respective depletion in the cusp region (see Clemmons et al. (2008) and references therein). When modelling soft precipitation as the main driver, Deng et al. (2013) also saw a depletion below the heating region. However, it should be noted that when Streak sampled above 260 km, still no enhancement was observed; Clemmons et al. (2008) suggest that the CHAMP accelerometer is more sensitive to mass density (not number density) thus the change in composition at higher altitudes from the upwelling may affect the comparison as CHAMP will sample heavier constituents. Depletions were also measured by the DE-2 satellite at 350 km, explained by the divergence of winds away from the heating decreasing the atomic

oxygen density (Prölss 2008). Prölss (2008) proposed a 'transition region' where above the 300-400 km temperature and density increase due to soft electron precipitation.

As noted in Chapter 4 there is a considerable lack of datasets in this region, and we cannot rely on density observations from so few satellites. We can use CMAT2 to simulate temperature, density, winds and other parameters, but comparisons to real data are also needed. Carlson et al. (2012) describe four key aspects of their mechanism: velocity shears near the cusp region; frictional heating; an upwelling; and a reliance on the electron density. In Chapter 4 we discussed frictional heating in depth, and briefly referred to the stagnation near the cusp region. In the case of the latter, at CHAMP's altitude the enhancement has increased mass, therefore due to momentum conservation the neutral wind must react accordingly (see Equation 1.27). Indeed, wind shears are known to lead to changes in neutral density, which have been observed (St.-Maurice & Hanson 1982). Recently, Conde et al. (2017) proposed a study to identify neutral wind perturbations at the site of the density enhancement using rocket campaign, FPI and satellite data. In the meantime, the stagnation seen in the CHAMP wind data (see Chapter 4, Lühr et al. (2007), Förster et al. (2008) and references therein) is suggestive of a localised wind effect, and we can use high time and spatial resolution UCL FPI measurements to improve this picture. The UCL CUSP campaigns (and FPI-EISCAT campaign for the nightside auroral oval) provide vertical wind and EISCAT electron density measurements to identify any resultant upwelling, the role of electron density and the presence of increased horizontal plasma flows (see Section 5.5). Vertical winds are a significant response to the heating as they control thermal transport, as well as mass transport affecting the composition. Moreover, the vertical winds themselves may result in frictional heating (Deng & Ridley 2007), further complicating this mechanism.

5.2.2 Applying the Cusp Mechanism to the Nightside Auroral Oval

With a density enhancement (Liu et al. 2005) and small-scale FACs (Neubert & Christiansen 2003) also observed in the nightside auroral oval, we probe the same mechanism in the magnetic midnight region where particles precipitate as a result from magnetic reconnection in the tail (see for example, Cowley (2000)). Though an enhancement and Joule heating are observed by CHAMP in the nightside auroral oval, the enhancement is much weaker than the respective cusp anomaly (see for example: Clemmons et al. (2008); Carlson et al. (2012) and references therein). Liu et al. (2005) measured a broad den-

sity enhancement between 50-72°N in the pre-midnight region in both hemispheres (near the Harang discontinuity). Its presence can also be inferred noting that MSISE-90 underestimated by 20-30% in the cusp and midnight regions (Liu et al. 2005), as well as using UCL FPI measurements to detect upwellings in the region (see Section 5.5). The enhancement is more evident in active conditions and expands equatorward, thus it may be tied to substorms and active geomagnetic conditions (Liu et al. 2005) – this may imply a storm-driven mechanism unlike the cusp.

Moreover, the cusp and nightside auroral oval have different precipitating populations due to dayside and nightside reconnection respectively. As the populations precipitating on the dayside are from magnetic reconnection at the magnetopause, the cusp experiences the less energetic soft precipitation, which deposits energy at less dense altitudes (150-200 km) producing a larger and faster response. Nightside precipitating electrons have a larger total energy flux (∼keV) and reach the denser E region (100-120 km), which has more inertia due to its higher mass density, and gives rise to non-dissipative Hall currents (Carlson et al. 2012), thus Joule heating is not as effective here and the distribution of Joule heating with respect to height is unchanged (see for example, Deng et al. (2013)). Knowing the presence of both soft and hard precipitation in the cusp and nightside auroral oval, it is important to simulate both energy sources when testing the Lühr et al. (2004) and Carlson et al. (2012) mechanisms.

5.3 Global Neutral Mass Density in Models

As we identified a discrepancy in the CHAMP neutral winds in Chapter 4 (see also: Emmert et al. (2006*a*,*b*); Förster et al. (2008); Dhadly et al. (2017*a*,*b*); Aruliah et al. (2018)), a similar effect in neutral density data may be implied as they too are derived using accelerometer data (Doornbos et al. 2010). Any uncertainty in density measurements will have significant implications for orbit determination (Vallado 2001; Storz et al. 2005), such as when calculating the in-track error and forecasted orbit (Emmert et al. 2017). Atmospheric drag is also the largest source of error in force models used in orbit prediction of LEO satellites (Storz et al. 2005).

Density models, such as the semi-empirical Drag Temperature Model (DTM) (Bruinsma 2015), assimilate satellite data (including CHAMP) to output temperature, density, composition and neutral winds (Bruinsma et al. 2004); thus the accuracy of the assimi-

lated density data are crucial. However, the drag-derived CHAMP densities also depend on accurate density models, as detailed in Chapter 2. Indeed, the largest error in density measurements is from model uncertainties introduced in Equation 2.1 (Bruinsma et al. 2004). In this section we focus on any known discrepancy between CHAMP and density models, as well as any known biases in CMAT2. This will also aid in the validation of CMAT2 simulations. We also discuss previous modelling of the cusp by Schlegel et al. (2005), Demars & Schunk (2007), Clemmons et al. (2008), Crowley et al. (2010), Yiğit & Ridley (2011), Carlson et al. (2012) and Deng et al. (2013).

5.3.1 Comparing Global Neutral Density in Models to CHAMP

Most recently, Murray et al. (2015) studied two 60-day periods around vernal equinox during solar minimum and maximum, comparing densities simulated using the Thermosphere Ionosphere Electrodynamic General Circulation Model (TIEGCM) (Richmond et al. 1992), similar to CMAT2, and the semi-empirical DTM (Bruinsma 2015), which assimilates satellite data including CHAMP, to densities derived using CHAMP and the Gravity Recovery And Climate Experiment (GRACE) satellites (Tapley et al. 2004), the latter similar to CHAMP in mission objectives but comprising two satellites inserted at the higher altitude of 500 km in 2002. Both TIEGCM and DTM underestimated the satellites during solar maximum and overestimated at solar minimum. Similarly, Bruinsma et al. (2014) compared GOCE densities to the HASDM model during 2009-2012, suggesting a scale factor of 1.29 be applied to GOCE densities; also showing the model overestimating satellite data during this solar minimum. In 2007-8 the thermosphere was at its lowest density for the past five decades (Emmert et al. 2010*a*; Solomon et al. 2011), which would particularly affect GCM models which rely on historic data. Indeed, Murray et al. (2015) found TIEGCM under-performed compared to DTM when comparing to CHAMP- and GRACE-derived densities.

Liu et al. (2014) compared CHAMP- and GRACE- derived density data to the semi-empirical NRLMSISE-00 model (Picone et al. 2002), noting the deep solar minimum led to higher He concentrations at lower altitudes, with NRLMSISE-00 underestimating by 30-70% in 2008. Higher He concentrations at this altitude are known to increase the drag coefficient, and therefore the density would be underestimated by NRLMSISE-00 (Thayer et al. 2012). The drag parameter is used to calculate density and is dependent on accurate density models (which rely on accurate density data). Dhadly et al. (2017*a*)

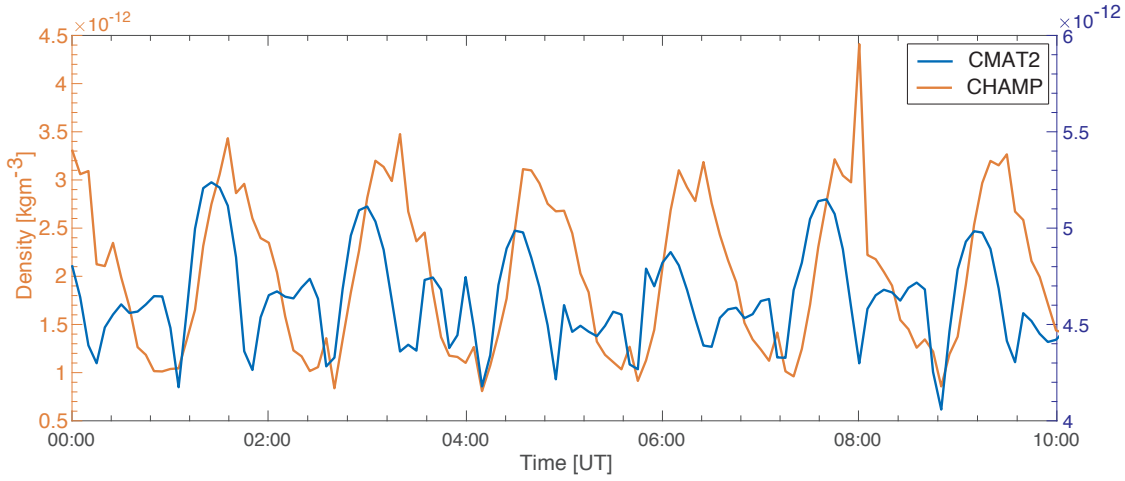

Figure 5.4. CHAMP (left y-axis, orange) and CMAT2 (right y-axis, blue) neutral densities at CHAMP locations on 25th September 2000.

also state the drag parameter as the most likely source of error in GOCE winds due to the uncertainty in geometry modelling of the spacecraft and variables calculated for gas-to-surface interactions. As this is a systematic effect, by comparing CMAT2 and CHAMP densities we can assess our own scaling factor by running several typical simulations for the period, as with GOCE in Bruinsma et al. (2014) and the neutral wind bias in Figure 4.5 in the previous chapter. We produce an equivalent density plot in Figure 5.4. Again, we can see CMAT2 and CHAMP are in phase, but CMAT2 overestimates CHAMP, as also seen with TIEGCM (Murray et al. 2015). This requires only a scale factor (as suggested by the use of two y axes) to CMAT2 or CHAMP to reach agreement between the densities. In Figure 5.4 CMAT2 densities are on average a factor of 2.7 greater than CHAMP densities.

It is important to note that even when correcting for this scaling error the cusp density enhancement will still be present (Liu et al. 2005). Though empirical models agree with each other, for example NRLMSISE-00, Jacchia-Bowman 2008 and DTM agree within 10% of GOCE (Bruinsma et al. 2014), most models seem to have too poor a temporal resolution to compare with CHAMP (see for example: Storz et al. (2005); Bruinsma et al. (2014); Murray et al. (2015)). In the case of CMAT2 the low temporal resolution can lead to noise and its coarse grid can often average out smaller features. HASDM, Jacchia 1971, MSISE-90 and NRLMSISE-00 all currently fail to reproduce the cusp anomaly due to their poor time resolution or lack of data to support more harmonics (Liu et al. 2005; Crowley et al. 2010; Lechtenberg et al. 2013).

5.3.2 Previous Modelling of the Cusp Density Enhancement

Other models have simulated the density anomaly, we briefly summarise them in this section. Firstly, Demars & Schunk (2007) used a global 3-D model similar to TIEGCM (Richmond et al. 1992) but with improved resolution and no hydrostatic equilibrium, allowing vertical transport and the full wind vector to be simulated. They used ion-neutral frictional heating to insert an additional artificial heating, ignoring precipitation. To ensure a 1.8 factor increase in density at CHAMP's altitude, heating was increased by an unrealistic factor of 110 (Demars & Schunk 2007). Demars & Schunk (2007) also produced a double peak in density in the cusp region, which is not present in the CHAMP data (see for example, Lühr et al. (2004)), and was also simulated in the modelled temperatures of the same region (Demars & Schunk 2007).

Schlegel et al. (2005) used Hall currents sampled by CHAMP and electric fields determined with EISCAT to estimate Joule heating, which was then used as an input to the Thermosphere-Ionosphere-Mesosphere-Electrodynamics general circulation model (TIMEGCM) (Roble & Ridley 1994). However, the density enhancement could not be produced as the modelled electric field, and therefore Joule heating, was too low in magnitude. Schlegel et al. (2005) suggest E region Joule heating from FACs may not be the main driver of the density enhancement, and propose other energy sources such as small-scale FACs, soft precipitation and F region Joule heating from electric fields and neutral winds. However, by using averaged electric fields, Schlegel et al. (2005) may have underestimated the resultant heating (Codrescu et al. 2000). Yiğit & Ridley (2011) used GITM to assess the effects of resolution on Joule heating, finding better resolution can increase heating by 40%, particularly as it allowed the inclusion of electric field peaks.

Clemmons et al. (2008) used an electron transport model to simulate precipitating particles, using a 100 eV Gaussian energy distribution with an energy flux of 1.6 mW m^{-2} in the cusp region and a 300 eV population with a flux of 2.3 mW m^{-2} in the adjacent regions. Depletions were seen by the Streak satellite, as mentioned above and also seen by Deng et al. (2013) for lower altitudes, although this may be linked to model limitations. Using CHAMP density measurements, Schlegel et al. (2005) saw both density enhancements and higher-latitude depletions in the cusp region.

Carlson et al. (2012), however, found a realistic doubling of density in the cusp was obtained by using electron densities and flow shears appropriate for reconnection in the

cusp region. Carlson et al. (2012) were able to reproduce 10-100% increases in density for plasma flow shears of 1-3 km s^{-1}, claiming the doubling was reasonable considering large magnitude IMF B_y components, also suggested by Crowley et al. (2010) due to the strong resultant ion drifts in the cusp region. Conversely, Cosgrove et al. (2014) found that very northward B_z produced a strong cusp signature of Poynting flux, where reconnection occurs at the cusp and the field line foot-points are pulled equatorward, resulting in frictional heating.

Crowley et al. (2010) used TIMEGCM in conjunction with high-latitude input from the Assimilative Mapping of Ionospheric Electrodynamics (AMIE) algorithm, which uses ground magnetometer and satellite current data, to also successfully reproduce the doubling of density during a period of strong positive B_y. Zhang et al. (2012) used the Coupled Magnetosphere Ionosphere Thermosphere (CMIT) model, comprising a magnetosphere model coupled to TIEGCM, to model both soft electron precipitation and increased conductivity as drivers of the density enhancement. They produced a 25% enhancement in the cusp and a 15% enhancement in the pre-midnight auroral oval region at 400 km.

Deng et al. (2013) instead used GITM, which has no hydrostatic equilibrium assumption (similar to Demars & Schunk (2007)). Deng et al. (2013) quantified the density enhancement due to Joule heating, soft electron precipitation and soft proton precipitation after a 3-hour period. They introduced a Poynting flux of 75 mW m^{-2} which was distributed using the Pedersen conductivity within the model, producing a 34% density increase. They also tested soft electron precipitation from 100 eV with a flux of 2 mW m^{-2}, using this to model a Maxwellian particle spectrum and to calculate the necessary particle ionisation rate and heating rate. This caused a 5% increase from the direct particle heating and 24% increase from the following ionisation and change in Pedersen conductivity in the F region, which controls the distribution of Joule heating, combining to a net effect of 29% (Deng et al. 2013). When combined further with the Poynting flux, the net effect is 50%. However, Knipp et al. (2011) found evidence of strong Poynting flux in the cusp region, reaching 170 mW m^{-2}, significantly greater than that modelled by Deng et al. (2013).

5.4 Modelling the Cusp Neutral Density Enhancement using CMAT2

An adapted version[3] of CMAT2 is used to model the density enhancement with the inclusion of an additional heating source, used by Carlson et al. (2012) to model soft precipitation and fast plasma flows as the source of the cusp anomaly. Several modifications were made to CMAT2: reading in the F10.7 index as a function of time rather than one value for a given day; outputting any number of times per hour to monitor short-term effects of the heating; and the optional inclusion of an empirical-based heating region to the neutral atmosphere[4]. This is in accordance with the Carlson et al. (2012) mechanism, however, its empirical nature means that it can be used to represent bulk heating from other mechanisms by changing the location, magnitude and altitude of injected heat.

Carlson et al. (2012) suggest that by simulating realistic electron densities and flow shears a density doubling can be explained with this modified version of CMAT2, as Joule heating correlates with electron density and the square of the plasma flow (see Equation 1.32). Increased electron density details the altitude the electrons precipitate for a given incident flux as well as the height at which Poynting flux will deposit its electromagnetic energy. Carlson et al. (2012) used ESR electron density profiles during reconnection events to calculate the height of the heat injection by comparing ion production rates of electrons with various characteristic energies. The energy deposition rate is then inputted into the model by fitting a Chapman function, which describes the ionising effect of radiation in the atmosphere (Chapman 1931). This details the vertical component of the heating, and in CMAT2 has the functional form, C_F:

$$C_F(P) = \frac{P}{P_c} \exp(1 - \frac{P}{P_c}) \tag{5.1}$$

where P is the respective pressure level in the model and P_c is the pressure level at the centre of the heating. The mechanism described in Carlson et al. (2012) injects heating at an altitude of 150 km ($P_c = 4{\times}10^{-4}$ Pa), which is the peak altitude of soft electron precipitation penetration; this function fits enhanced electron density profiles within ∼15% over the 145-300 km region.

Figure 5.5 details this function for two insertion heights representative of soft (red)

[3]Developed by Tim Spain when at UCL and used by Carlson et al. (2012).
[4]The heating is introduced in the ExternalTerms.f90 subroutine.

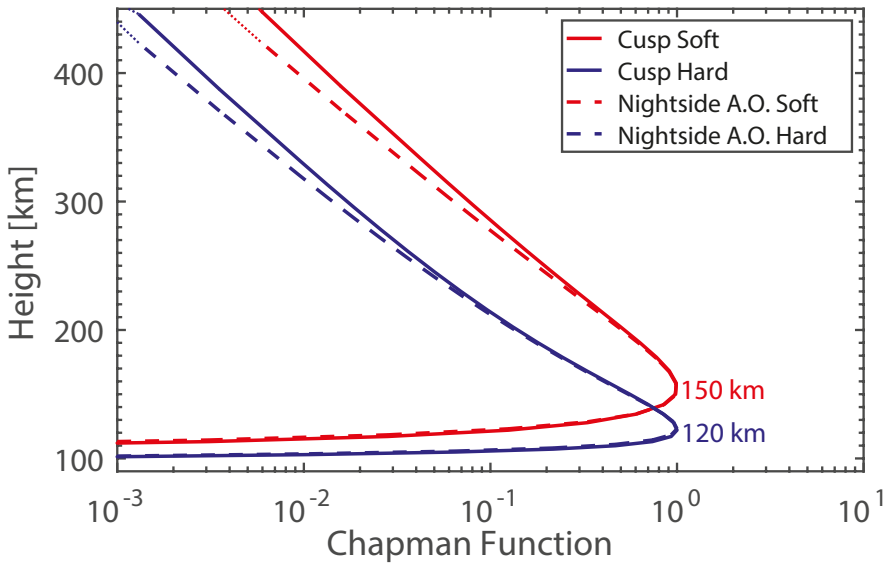

Figure 5.5. Chapman function profile representing Joule heating, used in this study to introduce ∼30 nW m^{-3} heating power for 1 hour as Svalbard passes under the cusp (solid lines) and Kiruna passes through the nightside auroral oval (dashed lines). Soft precipitation (red) indicates energy deposition of ∼100s eV peaking at 150 km in altitude, and hard precipitation (blue) of ∼keV at 120 km. The x-axis is unit-less and is scaled such that its peak is equivalent to the maximum heating power.

and hard (blue) precipitation at the cusp (solid lines, where solid red was used in Carlson et al. (2012)) and nightside auroral oval (dashed lines). Referring to Figure 5.5, we can see that for a given flux with increasing characteristic energy of the precipitating electrons the peak deposition altitude decreases, the ion production rate decreases for a given altitude above the peak deposition altitude (represented by the unit-less Chapman function x-axis) and the range of altitudes at which electrons are effective at ion production reduces. The Chapman function also has useful properties to model precipitation such as its sharp lower cut off of altitude for a given energy. The horizontal component of the heating region is modelled as a 2-D Gaussian function with a standard deviation latitudinal width of 4° (∼400 km) and longitudinal width of 1.5 hour LT (∼600 km). This is similar to other GCMs, for example Deng et al. (2013) use a 5° latitudinal width and 2 hour LT, and is mainly related to model resolution. Moreover, assuming a uniform distribution is a common simplification (see for example, Deng et al. (2013)).

The modelled heating provides functionality to control the following: (i) the altitude the heat is inserted; (ii) the magnitude of the heating; (iii) the constancy of the heating, that is, stochastic or constant magnitudes; (iv) the duration of the heating; and (v) the

Table 5.1. List of simulations showing the heating site with chosen geographical location, and precipitation mechanism, an injection of heat at a given height. The diagram illustrates the locations of the dayside cusp and nightside auroral oval (A.O.).

	Heating Site	Heating Mechanism and Height
Control	No heating	-
1	Svalbard at Cusp (78°N, 12 MLT)	Soft, 150 km
2	Svalbard at Cusp (78°N, 12 MLT)	Hard, 120 km
3	Kiruna at Nightside A.O. (68°N, 0 MLT)	Soft, 150 km
4	Kiruna at Nightside A.O. (68°N, 0 MLT)	Hard, 120 km

magnitude and period of the ramping up and down of the heating (for an example of ramping see Figure 5.6). We build upon Carlson et al. (2012), introducing a heating source characteristic of soft precipitation at 150 km, as well as investigating another energy source, that is, the lower altitude hard precipitation injected at 120 km, also demonstrated in Figure 5.5. We introduce heat characteristic of soft and hard precipitation as Svalbard (78°N, 16°E geographic coordinates) passes through the cusp at 12 MLT to probe the cusp density enhancement. We also repeat this for Kiruna (68°N, 21°E geographic coordinates) passing through 0 MLT in the nightside auroral oval to probe its respective observed density enhancement. Svalbard and Kiruna are chosen as opposed to arbitrary locations to coincide with the two UCL FPI sites, allowing for comparison of model and FPI-measured vertical winds. The locations of these sites at the cusp (orange) and magnetic midnight auroral oval (blue) are demonstrated in Figure 5.1 (in magnetic coordinates).

5.4.1 Summary of CMAT2 simulations

A summary of the CMAT2 simulations used in this study is outlined in Table 5.1. All simulations modelled the 25th September 2000 period in accordance with Lühr et al. (2004), Demars & Schunk (2007) and Deng et al. (2013), which either modelled this exact date or another equivalent autumnal equinox. The amplitude of the heating injected was 30 nW m^{-3} to produce an approximate density doubling at CHAMP's orbiting altitude, and lasted 1 hour in accordance with the length of typically observed heating events (more extreme events can last 3 hours (Deng et al. 2013)), with a 10-minute ramping up and down characteristic of small-scale FACs seen in Lühr et al. (2004). This ramping also

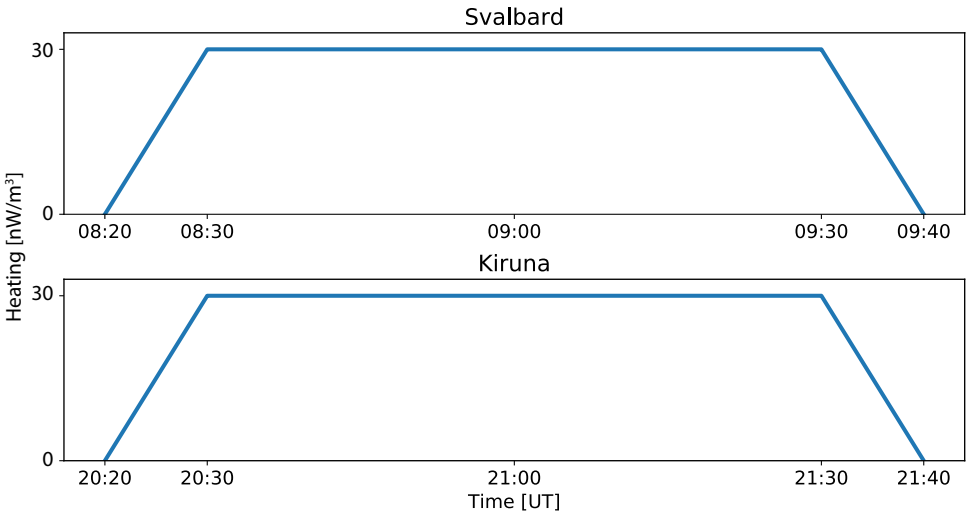

Figure 5.6. Illustration demonstrating time-dependence of heating for the Svalbard site at the cusp, and Kiruna site at magnetic midnight in the auroral oval.

ensures no artificial disturbances were introduced into the model (such as a gravity wave). We injected heat in the E (120 km) and F (150 km) regions, as both Svalbard passes under the cusp and Kiruna passes through magnetic midnight. The 1-hour heating with ramping was centred on the FPIs sites, that is, 09 UT for Svalbard and 21 UT for Kiruna. This is demonstrated schematically in Figure 5.6. We also simulated no cusp heating in a control run.

For simplicity the heating magnitude was fixed and not stochastic. If we integrate over the area the heating is applied we can calculate an approximate heating power applied to the cusp region. This translated to $\lesssim$10 GW, which is equivalent to Kp $<$ 2 and therefore low geomagnetic activity (Foster et al. 1986). This supports the anomaly in the cusp as a non-storm related phenomenon. CMAT2 tends to underestimate Kp as a driver, thus we used Kp representative of low to moderate geomagnetic activity. All simulations had a F10.7 index of 180 sfu, Kp = 3- and outputted data 12 times an hour. The composition[5] calculated major constituents self-consistently using reaction equations, and minor constituents from climatologies. A 30-day spinup of the previous day was used as input to the heating run; like the control this contained no additional heating.

[5]Composition switch = 3, see Chapter 2.

5.5 Using FPIs to measure the upwelling

As well as modelling the cusp and nightside auroral oval neutral density enhancements to compare with CHAMP measurements, we can also compare the resultant modelled upwelling to ground-based FPI vertical wind measurements. Strong upwellings in the auroral zone have been previously detected by the DE-2 satellite (Innis & Conde 2001), the UCL FPIs (Aruliah & Rees 1995; Aruliah et al. 2005) and other FPIs and Fabry-Pèrot spectrometers (FPSs) (Price et al. 1995; Larsen & Meriwether 2012). More recently, UCL[6] has run several cusp campaigns including SP-UK-CUSP on the 22nd January 2012 and SP-UK-CUSPN on the 12th and 14th January 2013, and one nightside auroral oval campaign, that is, the UCL FPI-EISCAT February 2015 campaign. These campaigns utilised the UCL FPIs in Kiruna and Svalbard to sample the thermosphere (as described in Chapter 2) to detect upwellings in the cusp and nightside auroral oval regions, with nearby EISCAT radars to measure the ionosphere. Svalbard is located in the polar cap and is able to sample the cusp at ∼09 UT, which during November-January has 24-hour darkness allowing the use of FPIs, whilst Kiruna is located in the auroral oval and samples magnetic midnight at 21 UT, with up to 18-hour darkness during November-December. EISCAT provides profiles of electron density, electron temperature, ion temperature and ion drift velocity away from the radar; this allows us to investigate soft and hard electron precipitation, Joule heating and ion upflow as drivers of upwellings.

5.5.1 The SP-UK-CUSP and SP-UK-CUSPN Campaigns

Figure 5.7 shows the vertical winds (upward is positive) and respective errors measured by the Svalbard FPI during the SP-UK-CUSP (22nd January 2012, in blue) and SP-UK-CUSPN (12th January 2013 in red and 14th January 2013 in green) campaigns in the top three panels, with a histogram of the vertical winds for each night in the fourth panel. Gaps in the data are due to cloud removal or low 630 nm intensities. The error bar is proportional to the 630 nm intensities measured by the FPI, and reduces to ∼10 m s^{-1} during the upwellings. Svalbard passes through the cusp around 09 UT, where we can see an upwelling in Figure 5.7 on the 22nd January 2012 peaking at ∼200 m s^{-1} around 08:50 UT and on the 14th January 2013 peaking at ∼100 m s^{-1} around 10 UT. On the 12th January 2013 there is no signature at the cusp, but a strong upwelling at ∼0 UT where

[6]Data provided by Anasuya Aruliah from the SP-UK-CUSP, SP-UK-CUSPN and UCL FPI-EISCAT February 2015 campaigns.

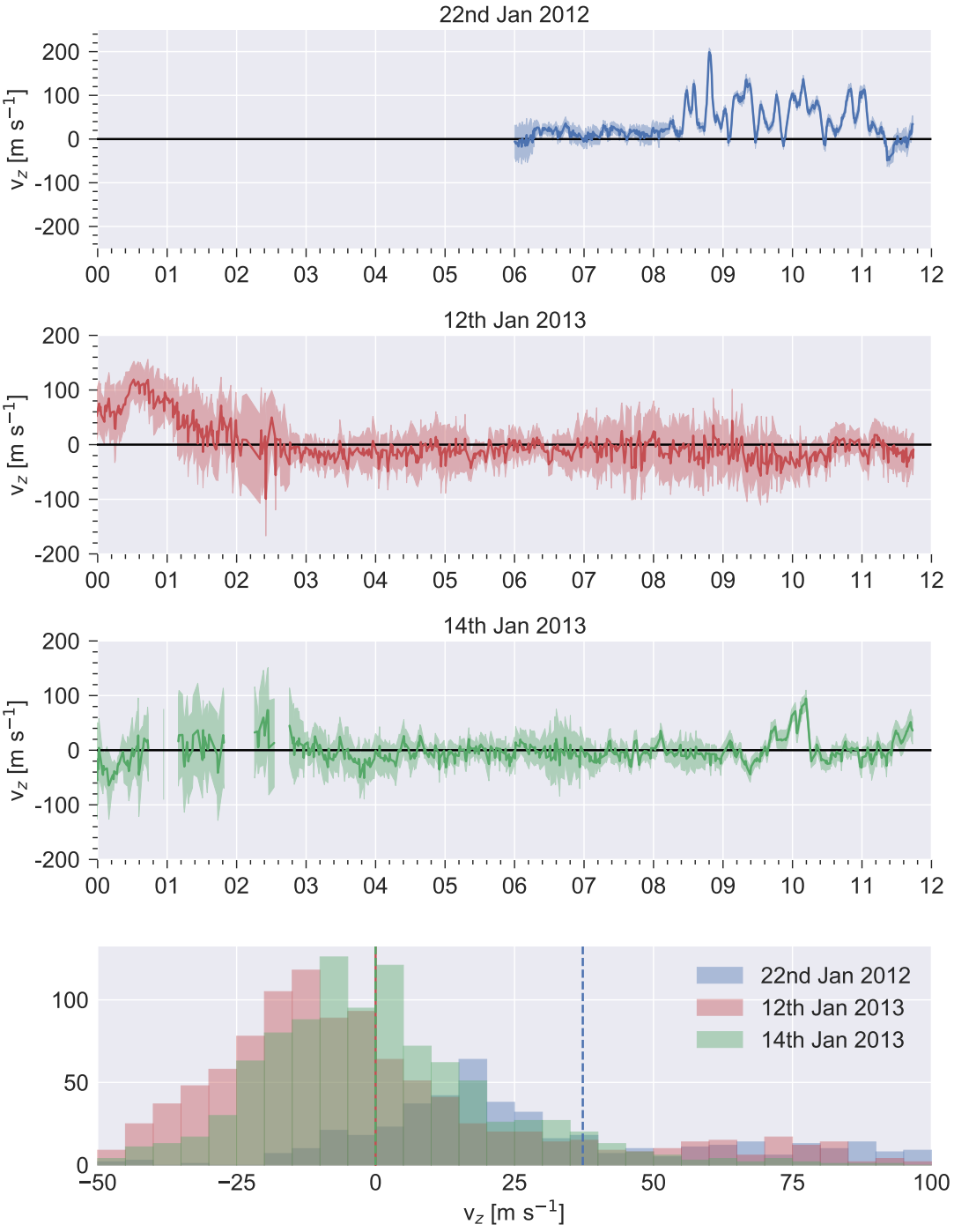

Figure 5.7. Vertical winds measured by the Svalbard FPI during the SP-UK-CUSP and SP-UK-CUSPN campaigns. The bottom panel is a histogram of the vertical winds for each of the nights, with their respective means shown by the dashed vertical lines. Positive winds describe an upward motion.

Svalbard is near magnetic midnight (nightside upwellings are discussed in the following section). FPIs measure the vertical winds at 30-second intervals, thus we can see the thermosphere responds quite rapidly in this region; referring to Figure 5.7 this is on the minute scale. Outside of the cusp and magnetic midnight regions the vertical winds are predominantly $\sim$0 m s^{-1} due to hydrostatic equilibrium. The histograms provide an aid to view the skew of the winds, as no upwelling would follow an approximate Gaussian centred on 0 m s^{-1}. The respective standard deviation of the vertical winds for each night are: 40, 34 and 21 m s^{-1}. The respective means of the vertical winds for each night are: 37, 1 and -1 m s^{-1} (see the histograms in Figure 5.7). The mean of the FPI winds on the 12th and 14th January 2013 (in red and green, Figure 5.7) are $\sim$0 m s^{-1}, despite upwellings in the nightside and cusp respectively, due to an average downwelling outside of these regions. This is best shown by their histograms in Figure 5.7 (red and green), which are skewed to downward (negative) wind with elongated upward (positive) wind tails. Due to cloud contamination the FPI data on the 22nd January 2012 is restricted to near the time of the upwelling; the wind distribution is therefore centred on a positive mean in Figure 5.7 (blue, histogram).

It should also be noted that FPIs are likely observing a very spatially localised upwelling; one statistical study confined this scale to 540 km cross-correlating vertical winds measured by two SCANDI-type instruments in Alaska (see Anderson et al. (2012) and references therein). Though we have noted the possible FPI contamination sources in Chapter 2, such as scattered light, aerosols and others, the low errors and multiple measurements of the cusp suggest that, like the density enhancement, this is a true anomaly.

During the 2012 campaign two EISCAT radars were operational, we include the results from the 42 m ESR. Figure 5.8 shows the profiles of electron density, electron temperature, ion temperature and ion drift velocity away from the radar measured by the EISCAT ESR 42 m radar on the 22nd January 2012. The ESR 42 m radar was in 'ipy' mode, used for lower thermosphere studies, the specifications of which are detailed in Figure 2.7 in Chapter 2. Referring to the electron density in Figure 5.8, there is a prolonged burst of electrons between $\sim$08-11 UT as Svalbard passes through the cusp, spanning 200-450+ km and peaking at $\sim 10^{12}$ m^{-3}, with spikes reaching down to $\sim$150 km between 09-12 UT. This correlates temporally well with the vertical winds seen by the FPI in Figure 5.7 (blue), particularly the spikes seen at heights characteristic of soft precipitation. Noticeably there is no peak in the E region and a depletion in the lower E and D regions ($<$100 km).

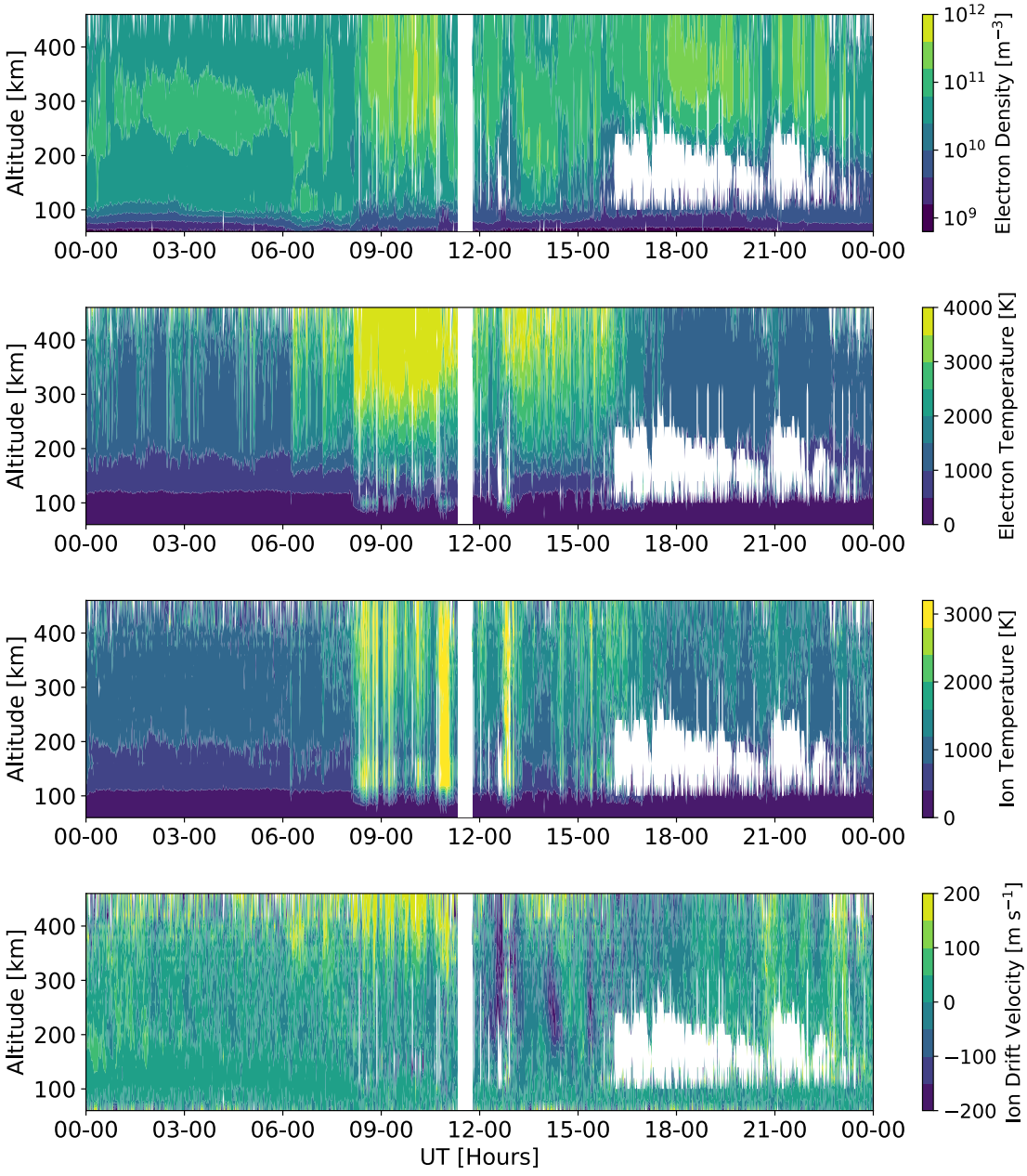

Figure 5.8. Electron density, electron temperature, ion temperature and ion drift velocity profiles measured by the EISCAT ESR 42 m radar during the SP-UK-CUSP campaign on 22nd January 2012.

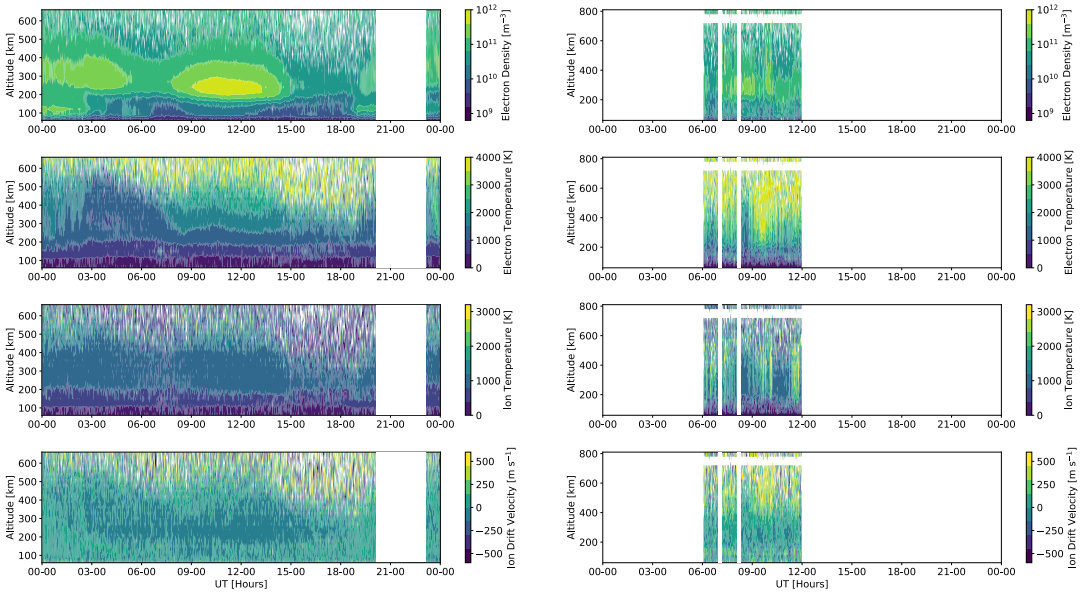

Figure 5.9. Electron density, electron temperature, ion temperature and ion drift velocity profiles measured by the EISCAT UHF radar and ESR 42 m radar during the SP-UK-CUSPN campaign on 12th (left) and 14th (right) January 2013 respectively.

There is strong ion upflow, reaching up to 200 m s^{-1} in the cusp region, which coincides with increased electron temperature, supportive of hot electron gas as as the cause of the upflow. We can also infer strong frictional heating from the increase in ion temperature (see Chapter 4) reaching ∼3,000 K in the E and F regions. Moreover, there are two electron density signatures from two CMEs hitting Earth on the 22nd January 2012 just after 06 UT in Figure 5.8 indicating soft precipitation, but no upwelling is observed by the FPIs or strong ion temperatures to indicate Joule heating. This shows the mechanism is unique to the cusp and nightside auroral oval regions. This may also suggest that small-scale FACs, present mainly in the cusp, are an important part of the cusp mechanism.

Figure 5.9 uses the same format as Figure 5.8, as measured by the EISCAT UHF and ESR 42 m radars during the SP-UK-CUSP campaign on 12th and 14th January 2013 respectively (see Figure 5.7 in red and green). The UHF radar was in 'beata' mode and the ESR 42 m radar was in 'taro' mode, both used for lower and upper thermospheric studies (again, see Figure 2.7 for the specifications). Referring to Figure 5.9, there is a large increase in electron density (10^{12} m^{-3}) in the cusp F region on the 12th January 2013 (left) between ∼08-15 UT, and a depletion in the upper E region (10^{10} m^{-3}) between ∼03-19 UT, the latter likely due to high-frequency radio blackout from an enhanced lower

E region hindering EISCAT measurements. Significantly, there are no accompanying increases in ion temperature to indicate Joule heating, and no signatures of ion upflow. The corresponding FPI vertical wind measurements in Figure 5.7 (red) are near ∼0 m s^{-1}, showing no upwelling, although intensities during this period were low, increasing the size of the error bars. For an upwelling to occur there must therefore be both precipitation and strong plasma drifts signifying strong frictional heating, as proposed by Carlson et al. (2012).

Conversely, on the 14th January 2013, also shown in Figure 5.9 (right), there is less precipitation but in the form of bursts (between 07-12 UT). There are clear signatures of ion upflow (∼200 m s^{-1} between 10:00-10:30 UT) and increases in electron temperature (∼4,000 K at ∼10 UT) and ion temperature (>2,000 K at ∼10 UT), and therefore increased electron precipitation and Joule heating, which also correspond to strong vertical winds measured by the FPIs (see Figure 5.7 in green at 10 UT). Unlike the upwelling on the 22nd January 2012 (Figure 5.7 in blue), which contained several peaks over a 3-hour period, there is only one peak in upwelling lasting ∼40 minutes. The duration of the upwelling may be related to the enhancement from electron precipitation that can remain after reconnection events, despite the electrons drifting due to the drag on the ions from the neutrals (see for example, Deng et al. (2013) and references therein). A clear difference between upwelling and non-upwelling events is the nature of the precipitation, namely short pulses. This may be tied to small-scale FACs which operate under short time scales or the initial drivers of cusp reconnection. Unfortunately CHAMP de-orbited in 2010 so we do not have FAC density measurements to compare (as discussed in Chapter 3). We can however use the Average Magnetic field and Polar current System (AMPS), a climatological model based on CHAMP and Swarm magnetic field measurements (Laundal et al. 2018), to produce typical FAC values for given inputs of solar wind speed, IMF B_y and B_z components, dipole tilt angle and the F10.7 index. We use this in conjunction with OMNI data representative of these solar wind conditions to simulate broadly how the FACs were distributed and their respective magnitudes. During winter in the northern hemisphere the dipole tilt angle is ∼-25° (Laundal et al. 2018), whilst the F10.7 index values on the 12th and 14th January 2013 are 163 and 149.1 sfu respectively.

Figure 5.10 shows high-resolution OMNI data of the IMF B_y and B_z components and the solar wind speed during the 12th (left) and 14th (right) January 2013. The solar wind conditions of each night are vastly different from each other. When the upwelling

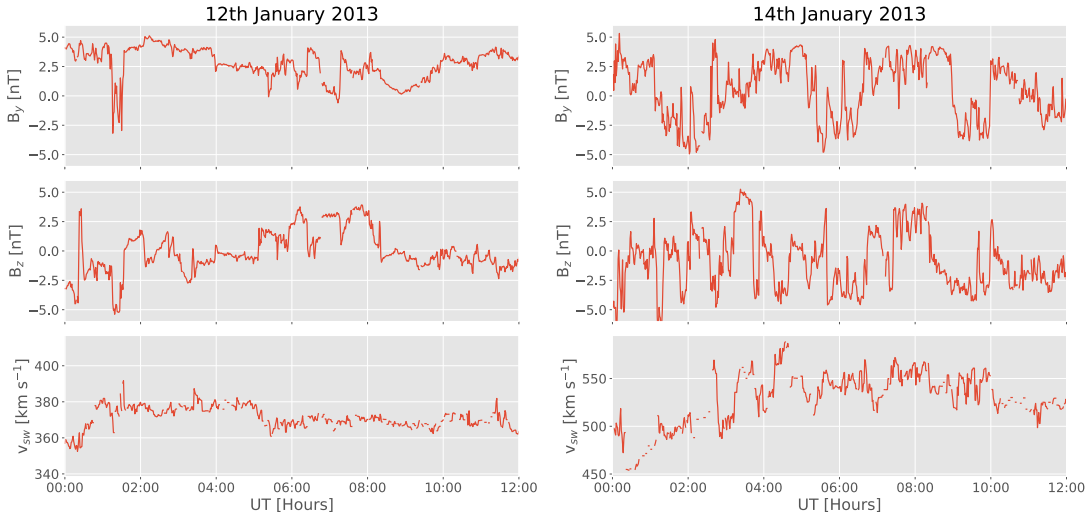

Figure 5.10. High-resolution OMNI data of the IMF B_y and B_z components and solar wind speed during the 12th (left) and 14th (right) January 2013.

is observed on the 14th January 2013, B_y is positive before 09 UT and B_z is southward, implying dayside reconnection and large ion drifts in the cusp. Two days before the solar wind is very calm as Svalbard passes under the cusp. The average Kp on the 12th and 14th January 2013 was 1- and 2 respectively; though the Kp on the 14th is higher than the Kp on the 12th, both values are still indicative of non-storm time conditions. This suggests that though the cusp anomaly is non-storm related, it is very tied to solar wind conditions. Figure 5.11 shows the AMPS-calculated FACs for the solar wind conditions presented in Figure 5.10 at 09 UT on the 12th (left) and 14th (right) January 2013. We can see that modelled FACs on the 14th January 2013 are approximately twice the magnitude of those on the 12th January 2013. Crucially, FACs are only present in the cusp region (72-76° at ∼12 MLT) on the 14th January 2013. Though we may be ignoring preconditioning of the ionosphere, by using the AMPS climatological model we can infer that solar wind conditions on the 14th January 2013 were more likely to produce FACs in the cusp region, which were shown to be coincident with upwellings (Lühr et al. 2004). Moreover, Carlson et al. (2012) and Crowley et al. (2010) suggest that large IMF B_y results in large ion drifts in the cusp, which cause density enhancements. Kervalishvili & Lühr (2013) and Neubert & Christiansen (2003) also suggest IMF and turbulence respectively as drivers. This is complementary to our findings in Chapter 3, which showed IMF B_z as a strong driver of Region 1 and 2 FACs on the dayside.

One feature to note on the 22nd January 2012 is the sustained ∼10 m s^{-1} positive ver-

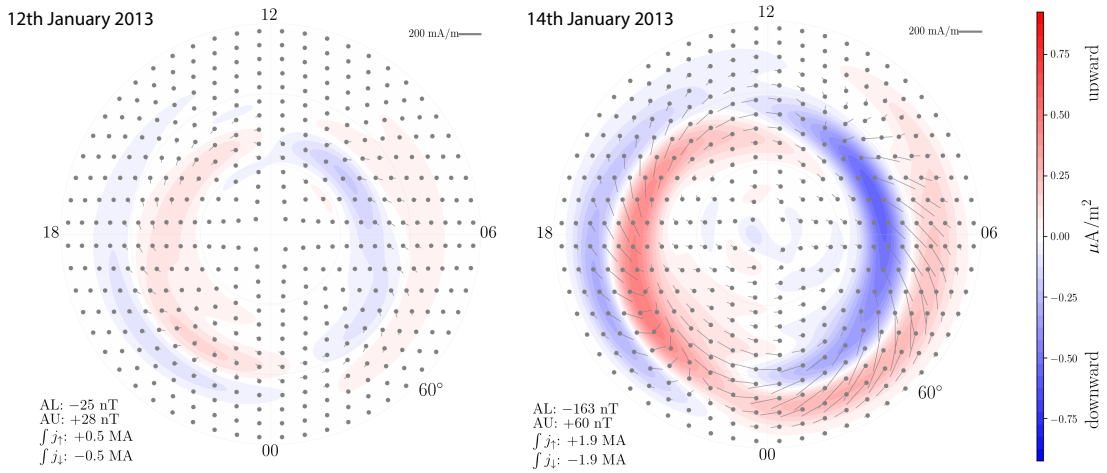

Figure 5.11. AMPS-calculated FACs in the northern hemisphere for solar wind conditions shown in Figure 5.10 at 09 UT on the 12th (left) and 14th (right) January 2013. Data are shown in magnetic coordinates from 60° to the northern geomagnetic pole. The colour bar indicates the magnitude and direction of FACs. This figure was produced using AMPS (Laundal et al. 2018).

tical winds between ∼06-08 UT leading up to the upwelling, not seen before the upwelling on the 14th January 2013. Figure 5.8 shows this sustained but small upwelling coincides with increases in E and F region electrons, translating to hard and soft precipitation respectively. Electron density is related to conductivity (see Chapter 1), thus the low level of soft precipitation may not be enough to ionise the thermosphere to raise the Pedersen conductivity peak to the F region. The Joule heating in the E region cannot contribute enough energy to cause a large upwelling, but may be producing a ∼10 m s^{-1} upward flow. Another feature is the large upwelling on the 22nd January 2012 being followed by a downward wind after 11 UT, whilst the upwelling on the 14th January 2013 is preceded and succeeded by downwellings at 09:30 and 10:30 UT respectively. This suggests a process of wind divergence creating a neutral fountain effect.

5.5.2 The FPI-EISCAT February 2015 Campaign

The purpose of the FPI-EISCAT campaign was to investigate the Carlson et al. (2012) mechanism in the auroral oval, where upwellings have also been detected (see for example: Aruliah & Rees (1995); Price et al. (1995); Innis & Conde (2001); Aruliah et al. (2005); Larsen & Meriwether (2012)), and the nightside polar cap where Svalbard is located (see Figure 5.7). During the campaign, EISCAT radars and the Kilpisjärvi Atmospheric

Imaging Receiver Array (KAIRA) (McKay-Bukowski et al. 2015), a VHF array along EISCAT's VHF Tromsø radar line-of-sight, measured the same region of atmosphere in a tristatic mode above the Kiruna FPI, which allowed the ion drift horizontal and vertical velocity components to be derived between 150-200 km, and therefore Joule heating. The radar also scanned with respect to height, allowing Joule heating profiles to be inferred. This was arranged during two 6-hour observations on the 15th (unfortunately cloudy) and 17th February centred on 21 UT as Kiruna passes through magnetic midnight. This involved a schedule of look directions every ∼8 minutes, and quick exposures during an upwelling. Low intensity and cloudy FPI data have been removed.

Figure 5.12 shows the vertical winds measured by the Kiruna FPI on the 14th (in blue) and the 17th (in red) February 2015, again with their respective histograms shown in the bottom panel. We can see in Figure 5.12 that there appears to be no sustained upwelling at magnetic midnight (21 UT) on the 14th February 2015 (in blue), coinciding with weak northward IMF B_z. This may also be tied to the location of the auroral oval during quiet geomagnetic conditions, which may not reach the magnetic latitude of Kiruna due to due to a more contracted polar cap. Spikes in the neutral wind between 18-19 UT are related to negative IMF B_y, which increases the intensity of FACs in the pre-midnight region (with positive B_y having the same effect in the post-midnight region near 0 UT) (Tenfjord et al. 2015). There is a strong sustained upwelling of 100 m s^{-1} as Kiruna (in red) passes through magnetic midnight on the 17th February 2015, with smaller downwellings at 20 and 23 UT of ∼40 m s^{-1}. Between 21-24 UT the AE index has peaks of ∼600 and 800 nT, IMF B_y is intermittently positive and B_z is ∼-10 nT, indicating an active magnetosphere driven by dayside reconnection with intensified FACs in the post-midnight region (Tenfjord et al. 2015). The standard deviation of the vertical winds on the 15th and 17th February 2015 at Kiruna are 24 and 19 m s^{-1} respectively, whilst their means are both 0 m s^{-1} (see the histogram panel in Figure 5.12); again any observed upwelling has been averaged out due to downwellings occurring elsewhere during the period. The distribution of the histogram in Figure 5.12 (red) is skewed to downward (negative) wind with an elongated upward (positive) wind tail indicative of a sustained upwelling, similar to the histograms in Figure 5.7.

At Kiruna on the 17th February 2015 (Figure 5.12 in red) the upwellings between 21-23 UT are near-simultaneous with Kiruna passing through the 0-2 MLT region, which lies within the location of the post-midnight heating spot seen in Figure 4.15 in Chapter

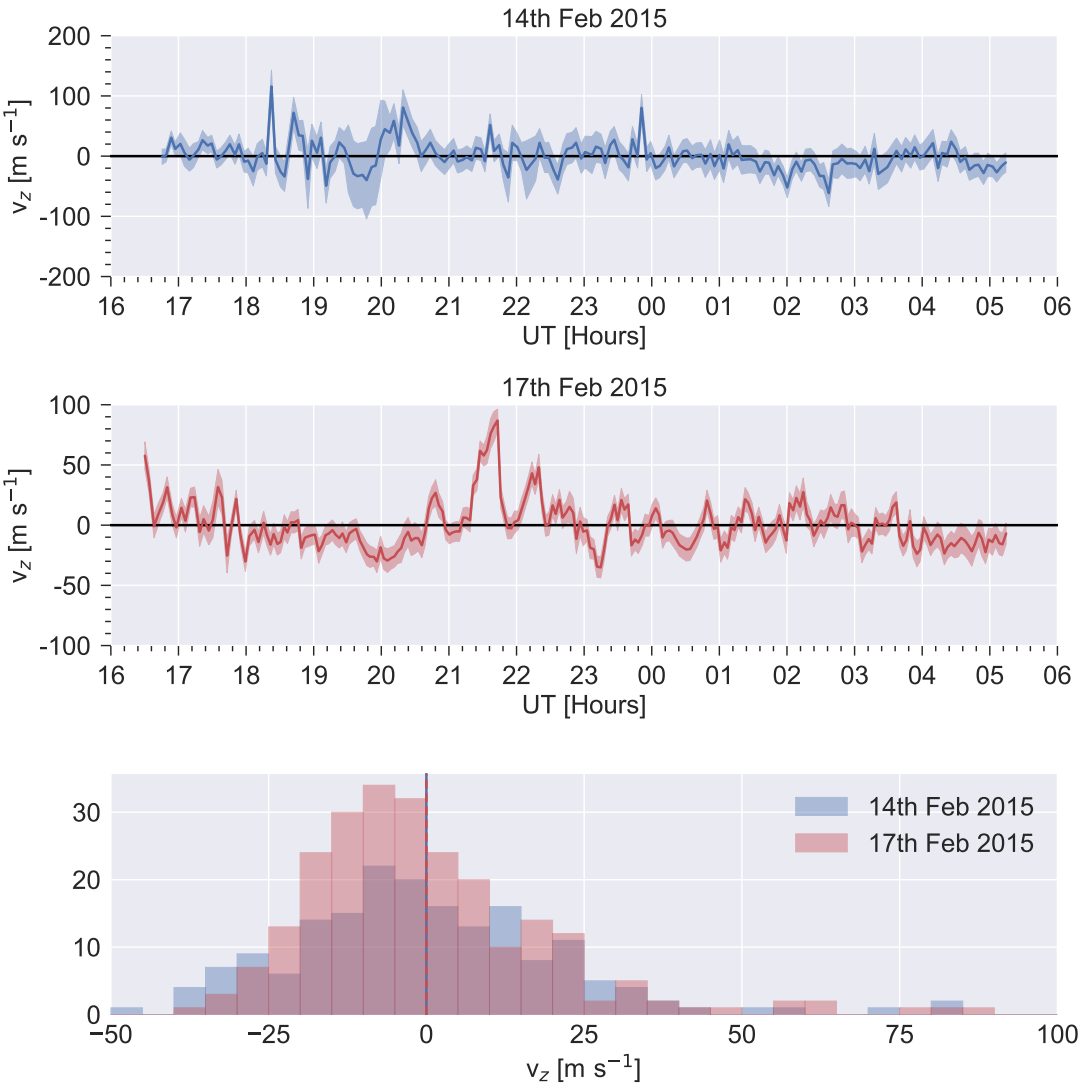

Figure 5.12. Vertical winds detected by the Kiruna FPI on the 14th (blue) and 17th (red) February 2015 during the FPI-EISCAT campaign. The bottom panel is a histogram of the vertical winds for both nights, with their respective means shown by the dashed vertical lines. Positive winds describe an upward motion. Both nights also show the first few hours of the succeeding day (the 15th and 18th February 2015 respectively).

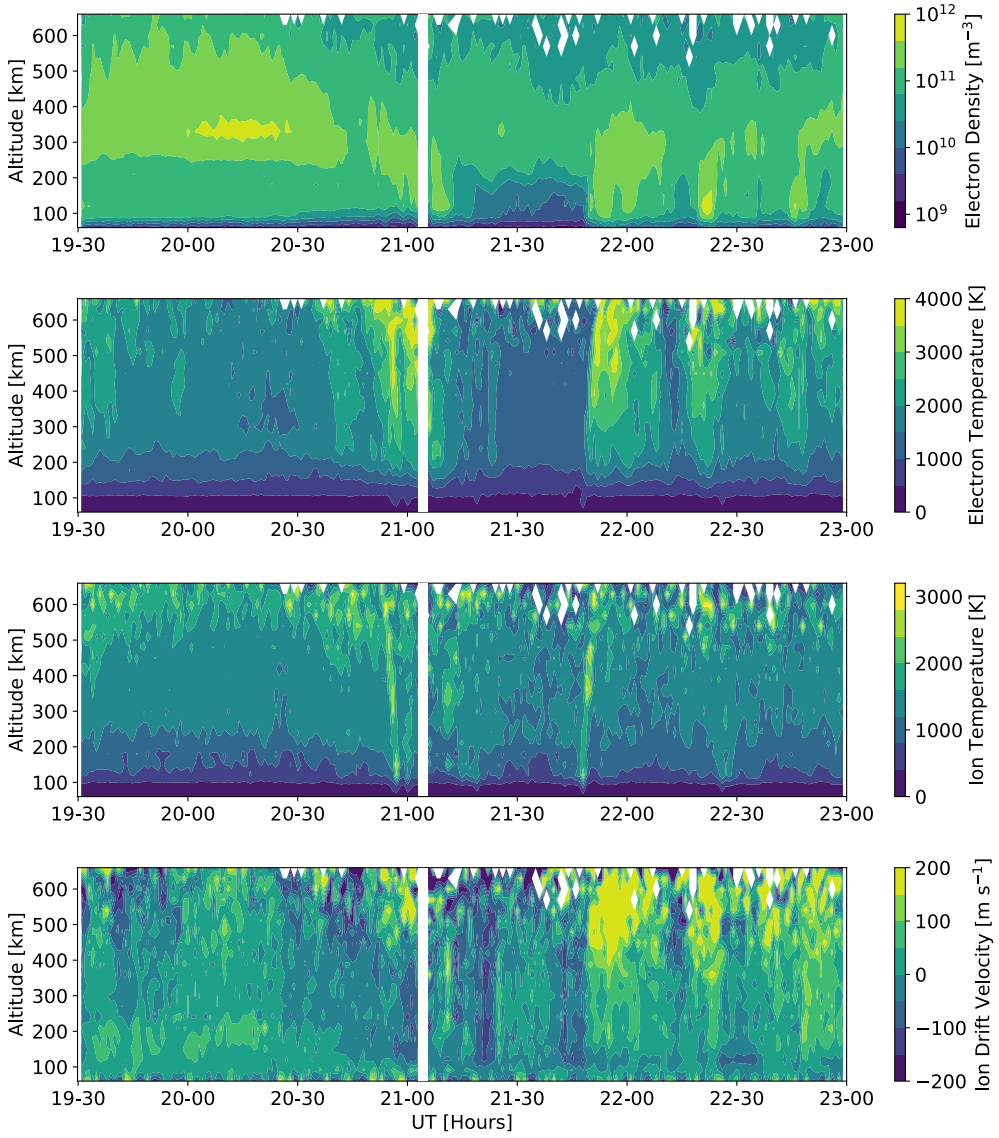

Figure 5.13. Electron density, electron temperature, ion temperature, ion drift velocity profiles and radar parameters measured by the EISCAT VHF radar during the FPI-EISCAT campaign on 17th February 2015.

4. This suggests that upwellings (and density enhancements) may be due to Region 1 and 2 FAC-driven Joule heating. Indeed, Prölss (1981) used the polar-orbiting ESRO 4 satellite's gas analyser to show large density increases in the auroral oval at 260 km in the high-latitude morning sector and evening sector. This may also explain why the upwelling is so prolonged at the cusp on the 22nd January 2012 in Figure 5.7 (in blue), as Svalbard moves into the post-noon region. Moreover, the 17th February 2015 upwelling coincides with more active geomagnetic conditions. The respective averaged Kp index values for the 14th and 17th February 2015 are 0+ and 4-, the latter peaking at 5∘ at 21 UT. As upwellings are solely present during the second night and are simultaneous with strong southward IMF B_z, this is suggestive of a storm-related upwelling mechanism.

Figure 5.13 shows the electron density, electron temperature, ion temperature and ion drift velocity profiles measured by the EISCAT VHF radar during the FPI-EISCAT campaign on 17th February 2015. The specifications of the radars used in Figure 5.13 are detailed in Figure 2.7. We use the 'beata' experiment mode, which allows measurements of the E and F regions simultaneously. Focusing on 21 UT in Figure 5.13, we observe a spike in electron density in the E and lower F regions indicating the presence of hard and soft electrons, penetrating to 150 km and still lower to 100 km. There is also a simultaneous spike in ion temperature in the lower F region with increased F region soft electrons, peaking at ∼3,000 K, suggestive of fast plasma flows heating the ions via Joule heating. In the auroral oval, these plasma flows are likely to be from the electrojets. Ion upflow is not as apparent, with signatures of ion downflow present at 21 UT, though there is increased electron temperature.

Assuming a constant electric field, we can compare the KAIRA plasma velocity vectors measuring at 150 km with FPI-measured neutral winds at 250 km, where over this range ion-neutral collisions are so few that ion and electron drifts are approximately equal. Figure 5.14 shows the profiles of geomagnetic East, geomagnetic North and along the geomagnetic field line ion drifts with respect to time as measured by KAIRA on the 17th February 2015, when a sustained upwelling was observed. The colour bar indicates the magnitude of the drift and direction, being positive eastwards, northwards and upwards. Figure 5.14 shows strong horizontal plasma flows, indicative of strong Joule heating, reaching ∼4,000 m s^{-1} in the East, West, North and South directions between 21:15-21:45 and 150-200 km, as Kiruna passes through magnetic midnight (yellow streaks in v_{ix} and v_{iy} in Figure 5.14). We can also see ion upflow, peaking at ∼2,000 m s^{-1} briefly at ∼21:50 UT

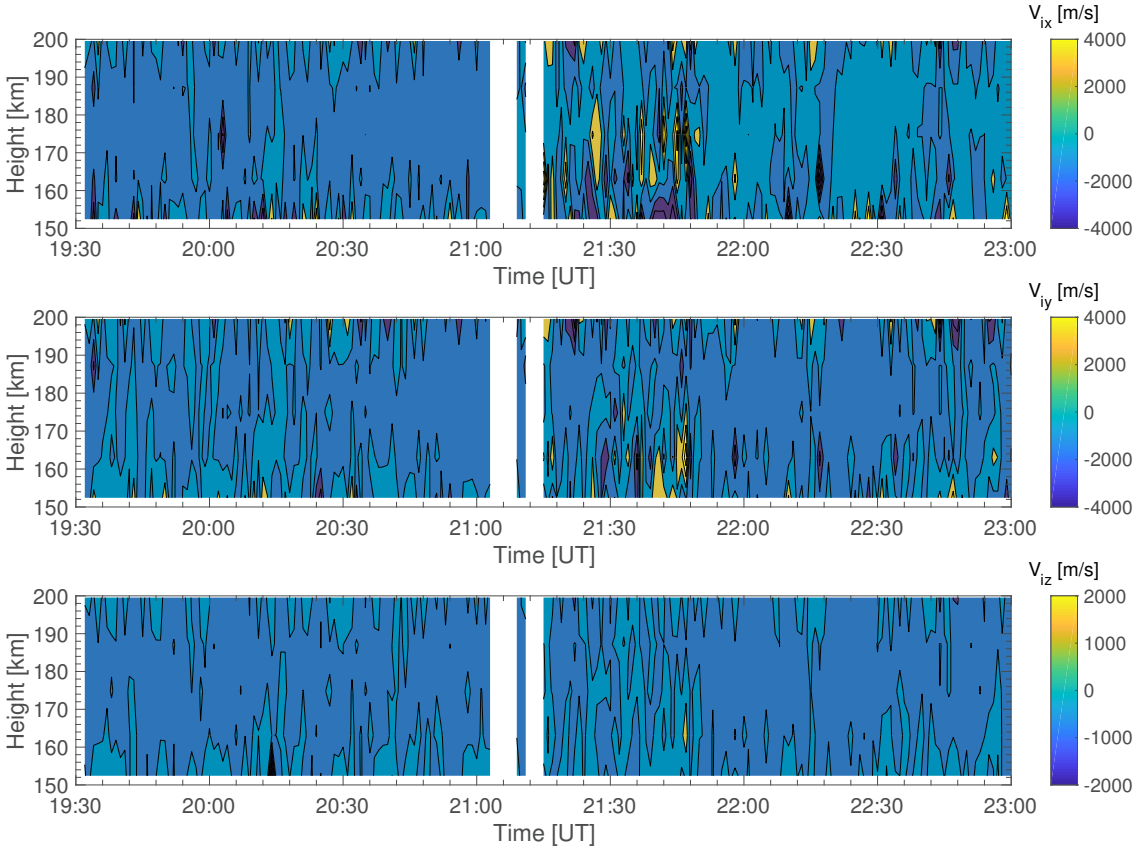

Figure 5.14. KAIRA ion drift profiles in the geomagnetic East (x), North (y) and along the field line (z) with respect to time on the 17th February 2015. The colour bar indicates the magnitude of the drift and direction, being positive eastwards, northwards and upwards.

at ∼165 km (yellow streak in v_{iz} in Figure 5.14). These fast plasma flows are all consistent with Carlson et al. (2012) proposed flows, in conjunction with soft precipitation, to drive Joule heating to produce a strong upwelling. Figure 5.13 shows substantial F region precipitation before 21 UT, which later penetrates to the lower F region. There are then intervals of depletion and weak F region precipitation ($<10^{11}$ m^{-3}) between 21:15-21:40 UT. This is a relatively small response for such a large upwelling observed by the Kiruna FPI.

5.6 Results and Discussion of the CMAT2 simulations

Figure 5.15 shows the temperature increase due to soft cusp precipitation at Svalbard with respect to the control run from 100-550 km for high geographic northern latitudes during 08-11 UT, with overlaid wind vectors. The wind scale is shown in the top left of the figure

and the colour bar indicates the temperature difference. At 08 UT, before the heating event, the runs are equivalent. At 09 UT, during the heating, a significant temperature increase of ∼400 K occurs where the heating is added, that is, centred on the latitude of Svalbard at the cusp. An upwelling also occurs at this location, with winds reaching 46 m s^{-1} and with divergence either side of the peak temperature rise. This divergence increases with height and is largest at the top of the model atmosphere. Divergence is a key signature of an upwelling due to heating, where pressure levels rise creating a heating-induced gradient between the levels, which the winds aim to restore (see for example, Dhadly et al. (2017*a*) and references therein). This produces the stagnation observed by CHAMP near the cusp region in Chapter 4. There is also an inward flow towards Svalbard's latitude at lower altitudes in Figure 5.15, where the heat is injected at 150 km.

The heating has increased temperatures across all altitudes above its insertion, with the largest temperature rise seen from 400 km upwards. The temperature reaches an isotherm near the top of the model (see the vertical contours from >450 km in Figure 5.15), which is likely linked to the Chapman profile (see Figure 5.5) correlating exponentially with density at high altitudes (see Equation 5.1). At this height, the strong divergence of the winds is aiding the redistribution of the heating, thus cooling the atmosphere. There is both equatorward and poleward redistribution of heating, with temperature increases spanning ∼67° up to the pole. After the heating has finished at 10 UT, the spread spans to below 60°. CMAT2 quickly reacts to reverse the changes by creating a downwelling larger in magnitude than the upwelling, due to its dependence on hydrostatic equilibrium and mass continuity (see Chapter 2), both commonly applied to GCMs (see for example: Richmond et al. (1992); Roble & Ridley (1994)). However, a downwelling is expected as the raised atmosphere loses energy to nearby colder regions. This downwelling is observed by the Svalbard FPI in Figure 5.7 (blue and green) on the 22nd January 2012 and 14th January 2013 after ∼11 UT, though lesser in magnitude than the upwelling. The latter night also saw a downwelling preceding the upwelling at ∼09:20 UT, supporting the presence of divergent winds and the creation of a neutral fountain effect. By 11 UT the atmosphere in Figure 5.15 closely resembles pre-heating at 08 UT.

Figure 5.16 shows the density increase due to soft cusp precipitation at Svalbard with respect to the control run over all latitudes and longitudes at 450 km at 08:30, 09, 09:30 and 10 UT. The colour bar indicates the density increase, peaking at 150 × 10^{-14} kg m^{-3}. At 08:30 UT we begin to see the density anomaly forming near Svalbard with a ∼5°

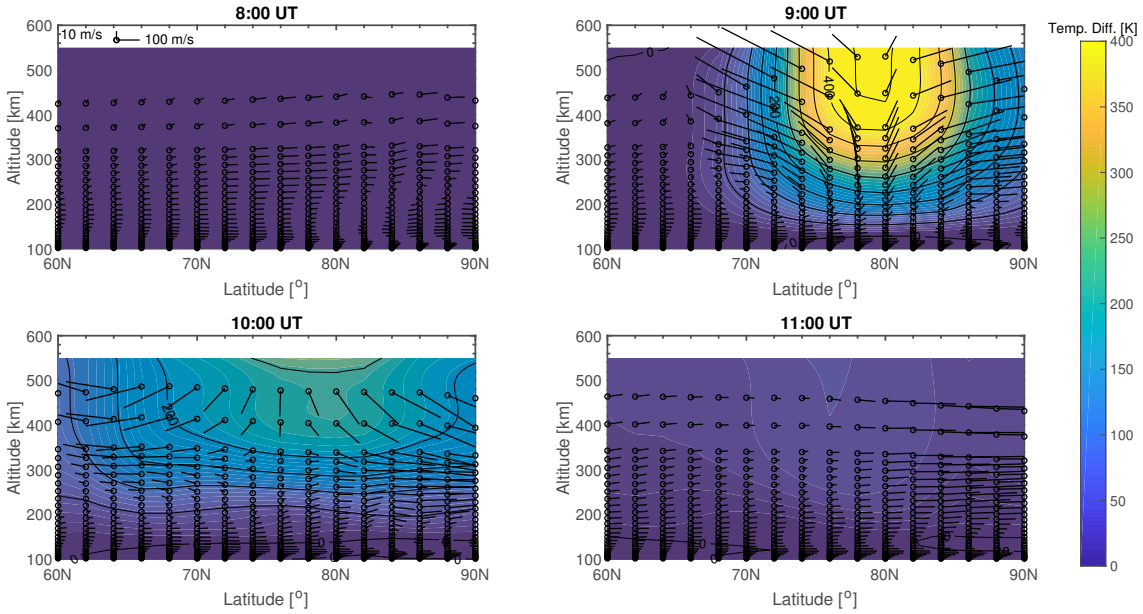

Figure 5.15. Difference in temperature with respect to altitude and latitude between the soft precipitation mechanism, with an injection of 30 nW m^{-3} heat for 1 hour as Svalbard passes through the cusp at 09 UT, and the control. Overlaid wind vectors are shown for the former, with magnitudes given by the wind scale in the top left of the figure. The colour bar indicates the temperature difference.

latitudinal width and ∼70° longitudinal length. By 09 UT the anomaly peaks at Svalbard with the majority of increased density still confined near this region, but the heating has also affected the surrounding area. At 09:30 UT the heating has been active for 1 hour and the density increase at Svalbard peaks. There is again some increase in density in the surrounding regions, showing the redistribution of mass due to the divergent winds in Figure 5.15. At 10 UT the heating has ceased and the increased density is redistributed by CMAT2. The anomaly has shifted westward and to lower latitudes, losing its original shape, and has created an asymmetry between the East and West of the heated region. This is due to the wind diffusion at 10 UT in Figure 5.15, also seen in Lühr et al. (2004) and Demars & Schunk (2007).

The other simulations of hard precipitation at the cusp and both soft and hard precipitation at the nightside auroral oval do not produce an increase in density comparable to Figure 5.16 at 450 km. Hard precipitation in the cusp region produced the second largest response, with a mean density difference of 5×10^{-14} kg m^{-3} compared to the control. Both soft and hard precipitation in the nightside auroral oval were unable to produce a significant density increase, suggesting the denser location (compared to the cusp) reduces

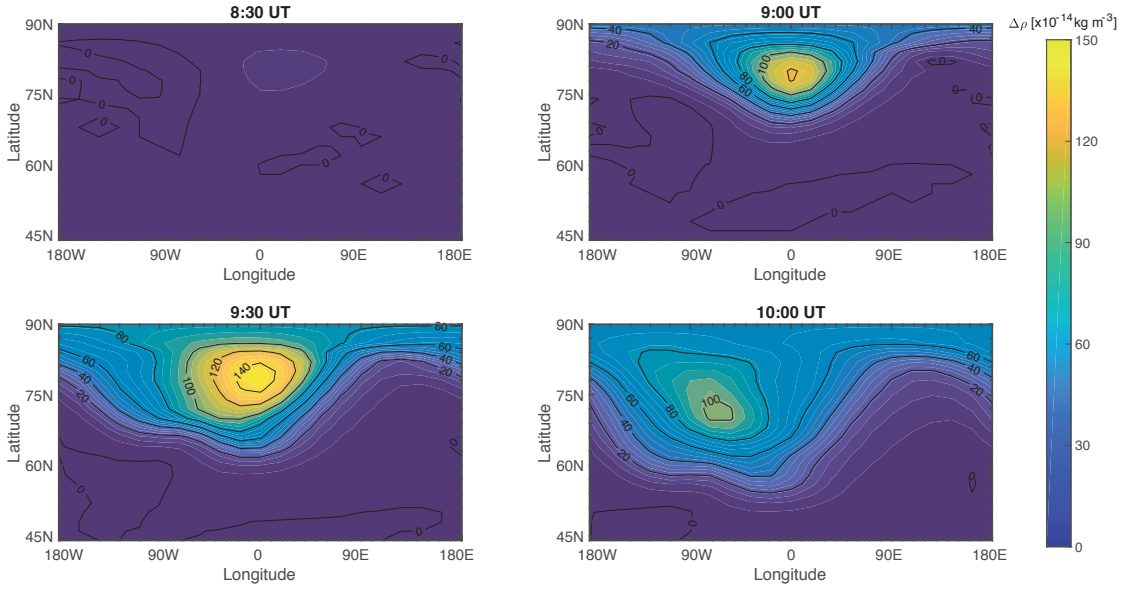

Figure 5.16. Geographic map with respect to latitude and longitude showing the density difference between soft precipitation as Svalbard passes through the cusp at 09 UT and the control at 450 km.

any upwelling, and therefore density increase, in the region. We can infer more by focusing on the Svalbard and Kiruna locations with respect to time for each simulation, and by calculating corresponding density ratios compared to the control run. Figure 5.17 shows both the density and ratio time series at the lower altitude of 400 km at both Svalbard (in red) and Kiruna (in blue) for soft precipitation (solid line) and hard precipitation (dashed line).

Figure 5.17 shows that soft precipitation in the cusp at Svalbard produces an increase in density by a factor of ∼1.66, close to the 1.8 factor seen in Figure 5.2 and Lühr et al. (2004), and to the doubling shown by Carlson et al. (2012). Soft precipitation at the nightside auroral oval produces a density increase by a factor of ∼1.30, which is in fact higher than hard precipitation at the cusp at ∼1.14. Hard precipitation at the nightside auroral oval produces the smallest density increase of ∼1.08. The effect of precipitating electrons on producing a large density enhancement therefore decreases with increased energy of the electrons (also seen by Deng et al. (2013) and references therein). Indeed, hard precipitation penetrating below 120 km in the cusp region will not produce any significant heating to affect densities at CHAMP's (and other LEO satellites) orbiting altitude.

Both soft and hard precipitation in the magnetic midnight region produce weaker

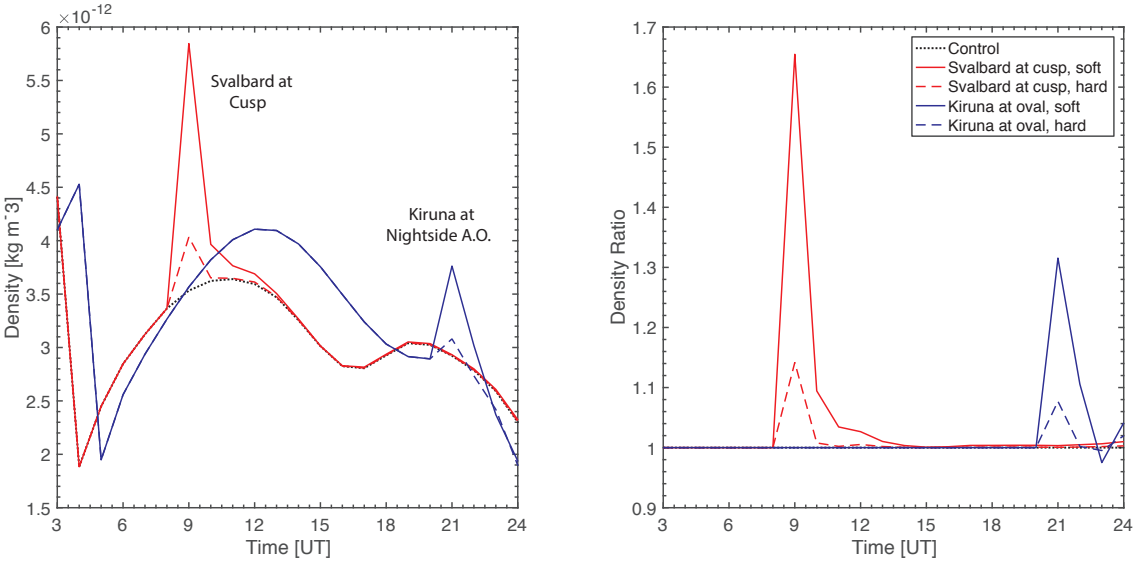

Figure 5.17. Modelled densities of the simulations (left) and their ratios compared to the control (right) with respect to time and at 400 km. Initial heating starts 30 minutes before Svalbard passes through the cusp at 09 UT and Kiruna passes through magnetic midnight in the nightside auroral oval at 21 UT, with an additional 10-minute ramping up and down (see Figure 5.6).

upwelling, temperature and density responses compared to their counterparts in the cusp region. This is due to the larger nominal density of the nightside auroral oval compared to the cusp region. However, soft precipitation in the nightside auroral oval produces greater responses than hard precipitation in the cusp region. Indeed, soft precipitation is most effective at increasing density in both the nightside auroral oval and cusp regions. As all simulations caused an increase in density, we suggest both soft and hard precipitation are contributing to the upwellings observed by the FPIs in the cusp and magnetic midnight regions, and the density bulge measured by CHAMP in the cusp region. The average density increase in the cusp by a factor of 1.33 above the relative density, calculated by Kervalishvili & Lühr (2013), may be explained by heat injected between the ranges of characteristic energies chosen in this study to represent soft and hard precipitation. Moreover, all enhancements in Figure 5.17 quickly reach steady state and return to control conditions within ∼3-4 hours, consistent with our FPI measurements. The decays in Figure 5.17 (right) scale with magnitude, and appear to be dependent on location as the Svalbard and Kiruna simulations produced different decays. The decays may be related to the inertia of the atmosphere, or alternatively the hydrostatic equilibrium enforced in the model. Referring to Equation 1.23 in Chapter 2, the change in pressure over height

is dependent on density, which varies exponentially with height; this may explain the exponential-like decay times and why they correlate with magnitude.

Liu et al. (2005) compared MSISE-90 and CHAMP densities to show the model underestimated by 20-30% in the cusp and midnight regions, implying a density enhancement of that percentage. Focusing on the midnight region, this 20-30% density deficit can be explained by soft precipitation in the nightside auroral oval which produced a factor of ∼1.30 increase in our simulation (see Figure 5.17). However, this region is associated with hard precipitation due to tail reconnection (Carlson et al. 2012). Hard precipitation (factor of ∼1.08) cannot account for this deficit or produce an upwelling comparable to that observed in the midnight region by FPIs (see Figure 5.12). We therefore suggest a different upwelling mechanism in the nightside region to that of the cusp. Liu et al. (2005) noted that the enhancement is more evident in active conditions and expands equatorward. This suggests the anomaly is linked to intense Region 2 FACs expanding with the auroral oval as seen in Chapter 3, in turn tied to substorms and the ring current. This would also explain why the upwelling is not always observed in the midnight region by FPIs, as it is storm related or at least IMF related. Indeed, we have previously seen in Section 5.5 that strong southward B_z and positive B_y between 21-24 UT during the 17th, and not the 14th February 2015, increased the intensity of FACs in the post-midnight region and led to active geomagnetic conditions and a sustained nightside upwelling (see Figure 5.11 and also Tenfjord et al. (2015)).

Moreover, the density time series for Svalbard and Kiruna (see Figure 5.17, left) are typical of that altitude, with Kiruna slightly lagging Svalbard and the greatest nominal density of both at ∼09 UT. The cusp density spike at ∼09 UT is very similar to that measured by CHAMP in Figure 5.4, however, a noticeable difference is the relative density either side of the anomaly. CMAT2 densities are larger after exiting the cusp than when entering the cusp, whilst in the CHAMP data the opposite occurs. This is likely due to the model redistributing mass to achieve a steady state, as seen in Figure 5.15 after the heating has stopped.

Figure 5.18 shows the density and temperature profiles of the cusp and nightside auroral oval for the control run with no heating (black), soft precipitation (red) and hard precipitation (blue). This outlines the initial heating as the site enters the heating region (solid line), and after 1 hour of heating as the site has exited the heating region (dashed line). At Svalbard and Kiruna, temperature and density increase with time for both soft

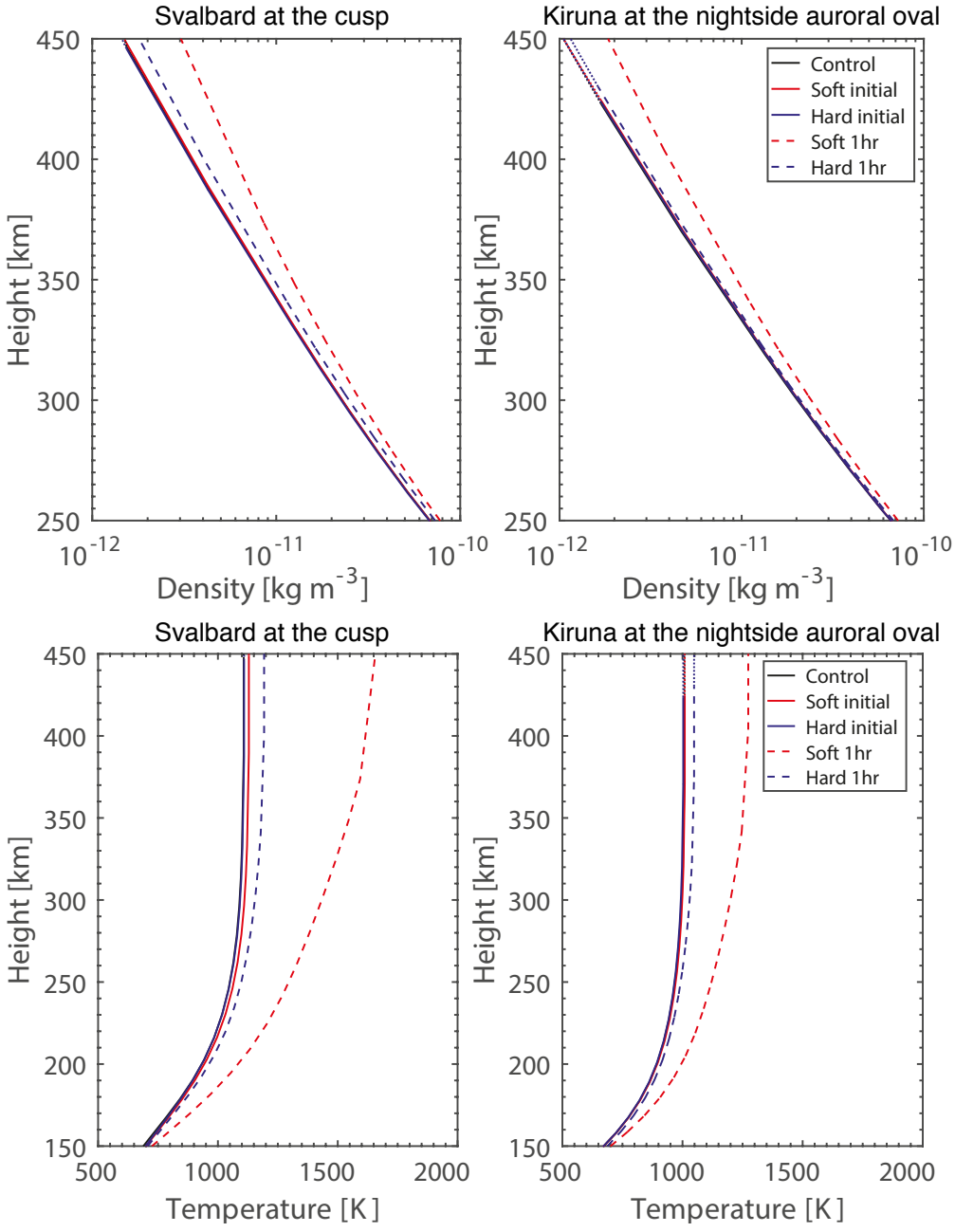

Figure 5.18. Density (top) and temperature (bottom) profiles at the cusp (left) and nightside auroral oval (right) for the control run with no heating (black), soft precipitation (red) and hard precipitation (blue). This outlines the initial heating as the site enters the heating region (solid line), and after 1 hour of heating as the site has exited the heating region (dashed line).

and hard precipitation. Soft precipitation produces the greatest density and temperature increase compared to hard precipitation, and has most effect at the cusp (as in Figure 5.17). In all simulations the rise in temperature and density from heating increases with altitude and produces a positive increase in temperature and density above the heating region, ruling out the 'transition region' where above 300-400 km the temperature and density increase due to soft electron precipitation as proposed by Prölss (2008). Moreover, the 1-2% depletion seen by the Streak satellite at low altitudes in Clemmons et al. (2008) and predicted when modelling soft precipitation by Deng et al. (2013), is seen as a $\sim$1% depletion at the altitude of the inserted heating and below. As this percentage is within computational noise (i.e. the percentage difference between two CMAT2 simulations produced using the same conditions) we cannot draw any conclusions. Referring to Figure 5.17 (right) in the nightside auroral oval both soft and hard precipitation produce a density depletion after the heating has stopped between 0.97 and 0.99 for soft and hard precipitation respectively, though most noticeable in the soft precipitation simulation at 23 UT. This may support a depletion occurring in the adjacent regions of the heating site in the nightside auroral oval as observed by Clemmons et al. (2008) at the cusp, although it may also be linked to the model reaching steady state.

Figure 5.19 shows Figure 5.15 with a higher time resolution from halfway through the heating at 09 UT and onwards at 09:15, 09:30 and 09:45 UT. This shows that while heating is supplied (constant between 08:30-09:30 UT) the temperature continues to increase across the region. The wind vectors indicate a continuous upwelling throughout the heating, also suggested by Lühr et al. (2004), though there are some slight variations during the heating. In Figure 5.19 at 09:15 UT a very weak downwelling can be observed during the heating at 66° below 300 km, which supports a fountain-like structure in the wind. When the heating has ramped down by 09:45 UT the downwelling begins instantly, producing stronger downward winds at high altitudes than the previous upwelling, peaking at 81 m s^{-1} at 09:45 UT. At 09:30 UT, when the ramp down begins, there is an immediate reduction in the magnitude of the upwelling compared to 09:15 UT. As mentioned, this is due to hydrostatic equilibrium in CMAT2, which suppresses vertical motion in the model. This is also leading to an underestimation of the magnitude, and possibly duration, of the vertical winds observed by our UCL FPIs in Section 5.5. Firstly, in the cusp region FPI winds can reach 100-200 m s^{-1} (see Figure 5.7 in blue and green) compared to a peak vertical wind of 46 m s^{-1} at 09 UT in Figure 5.15. Other models using hydrostatic

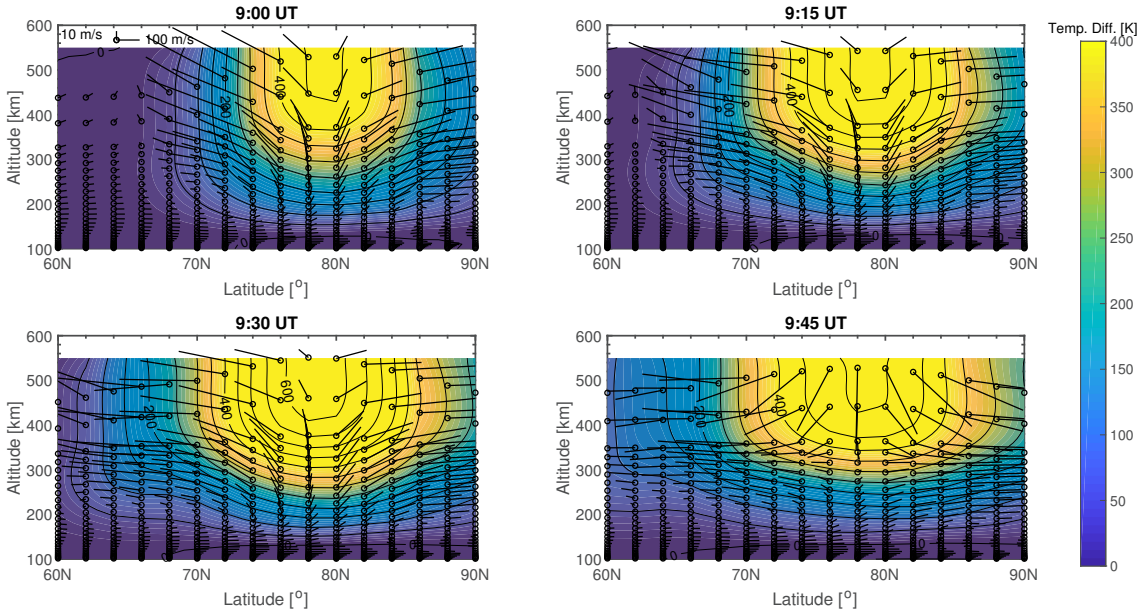

Figure 5.19. High-time resolution difference in temperature with respect to altitude and latitude between the soft precipitation mechanism, with an injection of 30 nW m^{-3} heat for 1 hour as Svalbard passes through the cusp at 09 UT, and the control. Overlaid wind vectors are shown for the former, with magnitudes given by the wind scale in the top left of the figure. The colour bar indicates the temperature difference.

equilibrium as a constraint produced either weaker or comparable vertical winds to CMAT2 (see for example: Demars & Schunk (2007); Clemmons et al. (2008); Sadler et al. (2012)). However, as mentioned previously, GITM does not assume hydrostatic equilibrium, thus their modelling of the enhancement with soft precipitation and Poynting flux as drivers produced stable vertical winds of ∼100 m s^{-1} (Deng et al. 2013), in agreement with FPI observations (see Figure 5.7 in green). Secondly, CMAT2 vertical winds are not as persistent as the FPI-measured upwellings, which are maintained over a period of several hours. Besides hydrostatic equilibrium, their short-lived nature may also be tied to thermal wind balance in the model, which relates the winds to the temperature gradient. Here, vertical winds create a horizontal divergence that differs from the temperature gradient, thus again any vertical winds will be quickly suppressed.

Despite this underestimation of the magnitude and duration of winds by CMAT2, the FPI winds observed at the cusp and corresponding CHAMP-measured density enhancement are consistent with our CMAT2 soft precipitation simulation. The FPI-measured upwellings in the cusp region also occur near-simultaneously with EISCAT-measured increases in electron densities at altitudes representative of soft precipitation and spikes in

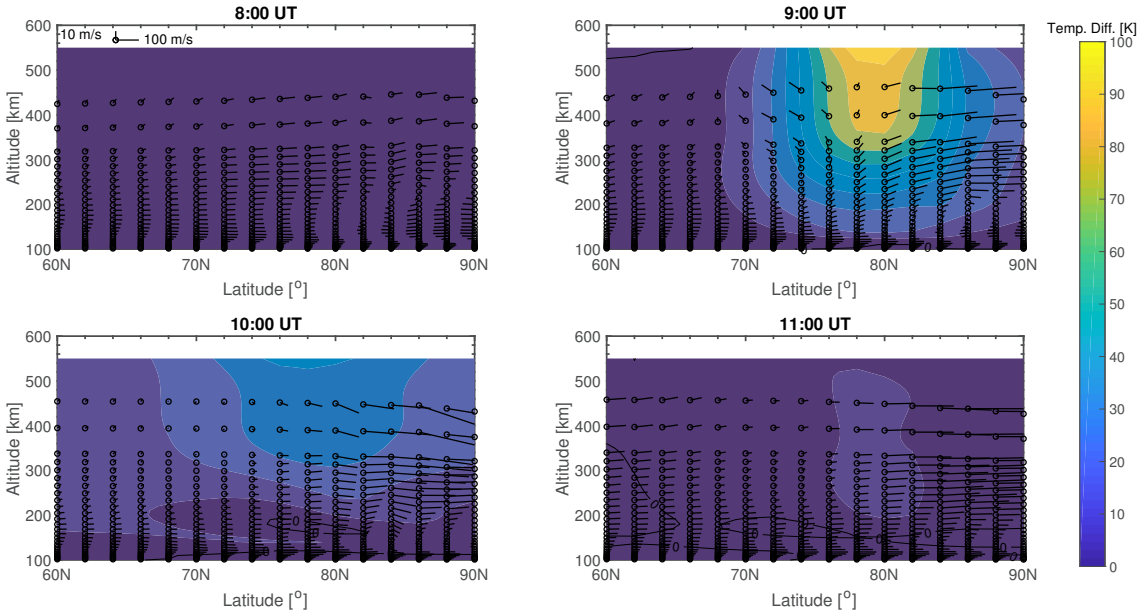

Figure 5.20. Difference in temperature with respect to altitude and latitude between the hard precipitation mechanism, with an injection of 30 nW m^{-3} heat for 1 hour as Svalbard passes through the cusp at 09 UT, and the control. Overlaid wind vectors are shown for the former, with magnitudes given by the wind scale in the top left of the figure. The colour bar indicates the temperature difference.

ion drifts, ion temperatures and electron temperatures, indicative of Joule heating and ion upflow in the region (see Section 5.5). This shows that CMAT2, EISCAT and our FPIs are all in agreement with a cusp upwelling and enhancement produced by a mechanism of soft precipitation and Joule heating, supporting the Carlson et al. (2012) mechanism.

Figure 5.20 again uses the same format as Figure 5.15, with a reduced colour bar scale (capped at 100 K rather than 400 K), for hard cusp precipitation at Svalbard. Comparing to Figure 5.15, hard precipitation in the cusp region produces a similar sized response, within 2° equatorward, but with significantly reduced magnitude. At 09 UT soft precipitation produces a temperature increase over four times greater than that of hard precipitation. This shows that the heating is less effective at increasing the local temperature, that is, the injected heat is dissipated more slowly for hard precipitation due to the higher density at the lower 120 km altitude. The upwelling is therefore significantly reduced in magnitude at 09 UT in Figure 5.20 compared to Figure 5.15, peaking at 10 m s^{-1} near the enhancement, as is the downwelling at 10 UT, peaking at 21 m s^{-1} near the enhancement. The downwelling also has a bias, producing a northward wind, which is strongest at high latitudes. By 10 UT the winds are comparable in magnitude and

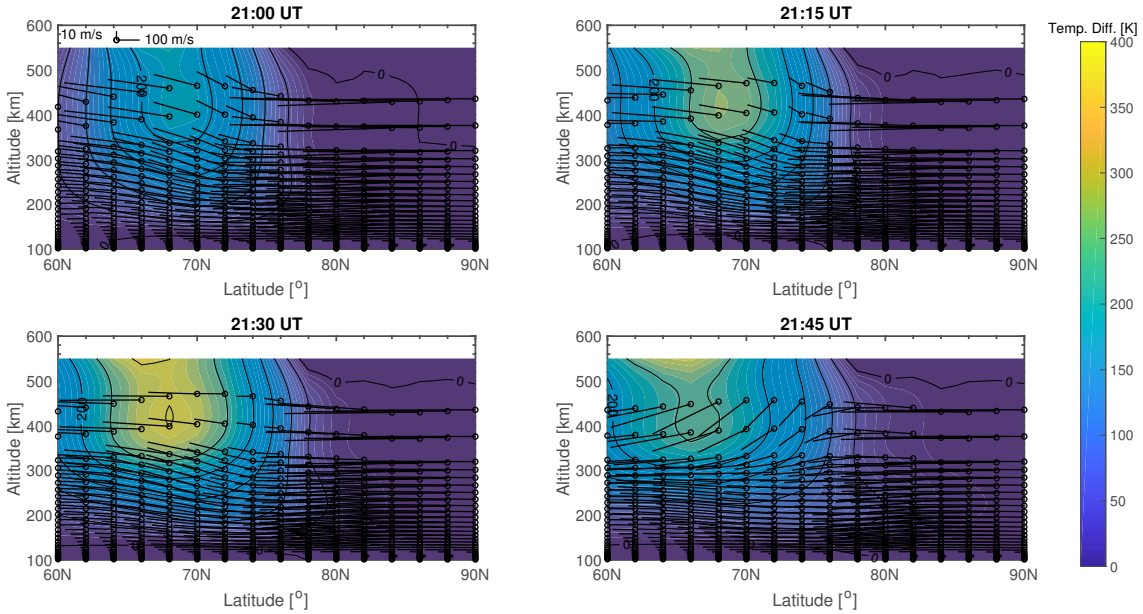

Figure 5.21. Difference in temperature with respect to altitude and latitude between the soft precipitation mechanism, with an injection of 30 nW m^{-3} heat for 1 hour as Kiruna passes through magnetic midnight at 21 UT, and the control. Overlaid wind vectors are shown for the former, with magnitudes given by the wind scale in the top left of the figure. The colour bar indicates the temperature difference.

direction to those of Figure 5.15 at 11 UT. We can conclude heating at 120 km is unable to sufficiently heat the above gas to produce a density enhancement detectable by CHAMP or an upwelling observable by the Svalbard FPI.

Figure 5.21 uses the same format, temporal resolution and colour bar scale as Figure 5.19 for soft precipitation as Kiruna passes through magnetic midnight at 21 UT. We do not include a corresponding figure for hard precipitation at Kiruna due to the low density and temperature responses and minimal upwelling. Figure 5.21 shows the temperature increase is centred at Kiruna's latitude, with temperature peaking at the end of maximum heating at 21:30 UT. The upwelling (between 21-21:30 UT in Figure 5.21) has an equatorward wind bias due to the strong anti-sunward winds crossing the polar cap (see Figure 4.13 in Chapter 4), which is distorting the shape of the temperature enhancement to be more equatorward at higher altitudes, and is also creating a double temperature peak between 350-550 km. The vertical wind magnitudes are comparably small to those of Svalbard passing through the cusp during soft precipitation in Figure 5.19, peaking at 10 m s^{-1} near the enhancement at 21 UT, midway through the heating. There is also no downwelling during the heating, suggesting the fountain-like wind structure observed in Figure 5.19 is

dependent on the location of the heating. The latitudinal span of increased temperature is also smaller than that of Figure 5.19.

The downwelling in Figure 5.21 occurs when the peak heating has ceased and the ramp down has finished at 21:45 UT reaching 18 m s^{-1}, similar to Figure 5.19 though reduced in magnitude. We can conclude that soft precipitation is not as effective as a driver in the auroral region compared to the cusp firstly due to the increased density, and therefore increased mass to heat, but also the strength of the anti-sunward winds crossing the polar cap, which may be reducing the upwelling. These meridional winds are diverted when reaching the upwelling near ∼76-78°N at 21:45 UT, and therefore produce a small stagnation in the horizontal wind pattern in the post-midnight region (i.e. ∼76-78°N and ∼1-2 MLT), as seen by Lühr et al. (2007) and Förster et al. (2008) (and possibly CHAMP in Figure 4.13). Although, this stagnation is also due in part to the anti-parallel flows of ions and neutrals (Lühr et al. 2007).

In the nightside auroral oval the Kiruna FPI observed vertical winds reaching ∼100 m s^{-1} soon after 21 UT, as shown in Figure 5.12 (red), preceded and succeeded by downwellings of ∼40 m s^{-1}. The reduced magnitudes of the FPI winds compared to those measured in the cusp region by the Svalbard FPI are consistent with CMAT2, which also saw this magnitude difference in winds between the cusp and nightside auroral oval for soft precipitation (see Figures 5.19 and 5.21 respectively). Figure 5.14 in Section 5.5 shows strong horizontal plasma flows indicative of Joule heating near 21 UT between 150-200 km, as well as ion upflow. Though the region is characteristic of hard precipitation, there are clearly signatures of soft precipitation and F region Joule heating. As CMAT2 produced a negligible upwelling for hard precipitation in this region, a mechanism of soft precipitation is implied to cause any observable upwelling. The fast plasma flows in Figure 5.14, in conjunction with soft precipitation EISCAT measurements, are consistent with the Carlson et al. (2012) mechanism. However, upwellings in our FPI-EISCAT campaign are only seen during active geomagnetic conditions. In active geomagnetic conditions significant amounts of energy can be transferred via nightside FACs into the midnight region (see Chapter 3), which dissipate via ion-neutral collisions (see Chapter 4). This energy transfer may be significant enough to counteract the higher density of the region, which we have shown reduces upwellings. We therefore suggest the upwelling is storm-related and may be tied to the intensity of FACs in the post-midnight region.

5.7 Conclusions

The aim of this chapter was to use CMAT2 to simulate the cusp density enhancement measured by CHAMP and resultant upwelling observed by the UCL FPIs, whilst simultaneously probing their drivers. A further aim was to test the same mechanism in the nightside auroral oval, where upwellings and increased density are also observed. We used CMAT2 to simulate an empirical heating source representative of Joule heating in the cusp and nightside auroral oval. By injecting heat in the F (∼150-200 km) and E (∼100-120 km) regions, characteristic of soft (∼100s eV) and hard (∼keV) electron precipitation respectively, we were able to assess the cause and effects of the heating, and probe the significance of its location by reviewing its influence on the density, winds and temperature in the two regions, as well as determining the scale size and temporal span of the heating and upwelling. Crucially, this study was able to draw on data and understanding of several coupled regions, namely, the ionosphere, thermosphere and solar wind, as well as the previous work of Chapters 3 and 4, to compare CMAT2 model simulations with FPI neutral winds, CHAMP density measurements, OMNI IMF observations and KAIRA and EISCAT ionospheric data to support the Carlson et al. (2012) mechanism in the cusp region and also apply it to the nightside auroral oval.

We found that CMAT2 reproduced the near-doubling in density when soft precipitation was applied to the cusp region, supporting a mechanism of increased conductivity and fast plasma flows due to Poynting flux-induced Joule heating in the F region, in agreement with Carlson et al. (2012). Carlson et al. (2012) suggested the doubling was reasonable considering large IMF B_y, also suggested in Crowley et al. (2010) due to the strong resultant ion drifts in the cusp region. The IMF conditions during FPI-measured upwellings are consistent with this. CMAT2 also successfully modelled the upwelling, with vertical winds peaking at 46 m s^{-1} in the cusp region during the heating (at 09 UT), though this underestimates FPIs which have measured magnitudes of up to ∼200 m s^{-1}, as observed by the Svalbard FPI on the 22nd January 2012. This is due to the assumption of hydrostatic equilibrium in the model, which restricts vertical transport. This also led to an extreme downwelling after the heating had stopped, which produced downward winds larger than those observed by FPIs. Despite the magnitude variations, both CMAT2 and FPIs support a neutral fountain wind structure in the cusp region. Indeed, the FPI and EISCAT results both support the Carlson et al. (2012) mechanism. We suggest the inclusion of the

cusp density enhancement in other GCMs as modelled with CMAT2. If the resolution in drag models used in orbit determination is too low to include this enhancement, GCMs, like CMAT2 in this study, may provide a vital aid in this region to accurately monitor and predict satellite orbits as well as monitor the neutral density of the thermosphere.

Upwellings observed during the SP-UK-CUSP and the SP-UK-CUSPN campaigns appear to be reliant on solar wind conditions. Though they are not reliant on active geomagnetic periods, they are not a permanent feature of quiet activity. A relation to the solar wind must be included in the Lühr et al. (2004) and Carlson et al. (2012) proposed mechanisms. Our results support the cusp as responsive to IMF, in particular to negative B_z and positive B_y, and therefore to FACs, which lead to fast plasma flows and therefore large frictional heating.

Hard precipitation in the cusp region produced a non-negligible density increase at CHAMP's orbiting altitude, a factor of 1.14 above the control. The higher density at these lower precipitating altitudes hinder the dissipation of energy. We suggest soft electrons are responsible for the largest enhancements, but that energies from ∼keV and under contribute to the average observed enhancement. Neither soft or hard precipitation energies were able to mimic the upwelling measured by FPIs in the nightside auroral oval region, with the vertical winds, temperature and density highly modulated by increased background density and anti-sunward winds. Fast plasma flows are again observed in conjunction with soft precipitation, suggestive of a similar mechanism to Carlson et al. (2012) in place. However, FPIs only observed significant upwellings in this region during active geomagnetic conditions. We suggest this is a storm-related anomaly, in agreement with Liu et al. (2005), requiring an adjusted mechanism to that of Carlson et al. (2012). Crucially, we have shown that the mechanism in the nightside auroral oval is at least related to that of the cusp, and will also affect the orbit dynamics of a satellite. This chapter has provided several case studies but is clear that a statistical study is necessary to fully understand this mechanism.

5.8 Further Work

Based on the measurements made during the UCL FPI campaigns and the CMAT2 simulations in this chapter, we suggest a statistical survey of FPI, EISCAT and satellite data is necessary to fully understand both the density enhancements and upwellings in the cusp

and nightside auroral oval regions. Indeed, a coordinated effort, in conjunction with our CMAT2 simulations, is required to measure the various components which contribute to these mechanisms. New data from the Swarm and QB50 missions will aid in this endeavour, sampling a range of altitudes in the thermosphere. Aside from statistical studies of the cusp and nightside auroral oval, we now also include further related work, which will improve the understanding of these regions.

Firstly, there are several improvements to CMAT2 that can be made. CMAT2 has systematically larger densities (by a factor of 2.7) than those measured by CHAMP, thus an improvement to CMAT2 may lie in data assimilation, also used in drag models. Murray et al. (2015) found that assimilating CHAMP and GRACE density data into TIEGCM (Richmond et al. 1992) improved values by 4%, predicting the use of GCMs in real-time forecasting. However, with such a density bias present in CMAT2 we predict this improvement would be much greater. Data assimilation within CMAT2 is outside the scope of this thesis but is an active area of research being pursued in the UCL Astrophysics group. Alternatively, the density could be scaled as implemented by Bruinsma et al. (2014) with GOCE satellite data. This requires several seasonal-dependent simulations during solar minima and maxima to assess a reproducible factor/s. If successful, this may be included in the model.

CMAT2 also outputs Joule heating, thus it is feasible to model the heating increase without the use of an empirical heating source. Total electron content, conductivity, ion drifts and ion, electron and neutral temperatures are all modelled within CMAT2, which allow precipitation and FACs to be simulated as drivers. However, the accuracy of Joule heating in the model would first need to be assessed. Joule heating within CMAT2 is derived using temporally and spatially averaged electric fields (see Chapters 2 and 4); including variability can increase the amount of Joule heating by a factor of 2 (Codrescu et al. 2000), whilst improving the spatial resolution of the grid to include high variability of the electric fields can increase the heating by 40% (Yiğit & Ridley 2011). A further limitation of CMAT2 and the majority of GCMs compared to, for example, GITM, is hydrostatic equilibrium reducing the upwelling. Relaxing hydrostatic equilibrium in CMAT2 would require a significant amount of work to stabilise the model. Instead we suggest that it must be acknowledged when drawing conclusions in this chapter.

Moving away from model improvements, we now discuss several useful extensions to the work presented in this chapter. The average density increase in the cusp by a factor of

1.33 above the relative density calculated by Kervalishvili & Lühr (2013) may be explained by heat injected between the energy ranges of soft and hard precipitation. An interesting and useful project would be to assess the energy sources responsible for this average increase and a range of other density enhancements, as well as the effects of including adjacent precipitation regions, as in Clemmons et al. (2008). Moreover, an assessment of the behaviour of small-scale FACs and their durations would improve modelling their energy transfer more accurately. In CMAT2 a stochastic (rather than constant) option exists for the empirical heating magnitude, and the duration of the heating can also be changed, which may improve modelling the variation of these small-scale FACs and their resultant heating with time, as well as simulating realistic IMF conditions. A final complementary study to this chapter would be to repeat the simulations for storm time conditions, modifying the Kp index in CMAT2 and the power of the empirical heating inserted (currently $\sim$30 nW m^{-3}). This would be particularly useful in assessing how geomagnetic activity affects the strength of the upwelling and density enhancement in the nightside auroral oval, which we suggested is storm-related.

This page was intentionally left blank

Chapter 6

Conclusions

Space weather is a disruptive and costly effect of the Sun's interaction with the Earth; whether describing ambient solar wind conditions or severe events, such as solar flares and coronal mass ejections, it poses a great risk to both space and ground infrastructure. FACs are pivotal in enabling the transfer of energy from the solar wind into the ionosphere-thermosphere system. In both quiet and storm conditions they are responsible for some of the most extreme and persistent effects of space weather. In this thesis we studied two main consequences of FACs in the ionosphere-thermosphere system, namely, induced GMDs on the ground, which arise as FACs close in the ionosphere, and the resultant Joule heating and perturbed thermospheric neutral winds as the energy transferred by FACs dissipates via their closure currents.

The study of ground GMDs is essential in safe-guarding the electrical grid network and gas industries, which rely on susceptible long manmade framework able to conduct induced ground currents during geomagnetic storms, causing pipelines to crack and transformers to overload and melt. Joule heating, however, is significant locally as a dissipation mechanism in the ionosphere-thermosphere system, heavily modulating the density profile and composition of the upper atmosphere, a major component of general circulation models, drag models and space weather forecasting. A further localised but noticeable example affecting drag models is the cusp neutral density enhancement, which introduces a systematic increase to the drag experienced by a satellite precessing through the region. This in turn has significant impacts on understanding atmospheric physical processes used in,

for example, satellite orbit determination and prediction, a notable failure being satellite collision. It is therefore vital that these effects of FACs and their role in space weather are well-understood. The aim of this thesis was to probe these related effects, and to see them as components of one FAC-driven mechanism in the polar ionosphere-thermosphere system.

In Chapter 3 we used the CHAMP fluxgate magnetometer to calculate FAC current densities and magnetic latitudes, with SuperMAG ground magnetometers analogously providing GMD magnetic perturbations and latitudes, to probe FAC locations and strengths as predictors of GMD locations and strengths. We chose a storm time interval containing three ICME-driven storms, with particularly large GMDs given their respective storm intensities, to probe these correlations. Indeed, the GMDs studied occurred at latitudes that could affect infrastructure in many populated regions, including mainland Europe and North America. Crucially, we found no strong linear correlation between FAC and GMD magnitudes, contrary to a common assumption. This may in part be due to limitations of the CHAMP and SuperMAG datasets, such as orbit limitations or ground magnetometer coverage, which we acknowledge, however we were able to confirm other relationships with these datasets. This suggests that any magnitude relationship is non-local and non-linear, and that a better understanding of the underlying mechanism is required. This is the first study of its kind to explicitly probe this relationship, and provides a strong groundwork to finally realise how the main facilitator of energy transfer into the ionosphere-thermosphere system is related to one of the most harmful effects of space weather.

We also studied the relationships between solar wind drivers and global magnetospheric activity and both FACs and GMDs using IMF B_z and the Sym-H index. We found solar wind to be a significant dayside driver of the location of FACs and GMDs, whilst on the nightside GMD magnitudes, the largest GMDs recorded, were strongly correlated with IMF B_z and the Sym-H index, supportive of their generation via tail reconnection and substorms. The increased influence of the nightside and ring current during the final storm, when the nightside FAC magnetic latitudes and GMD magnitudes both correlated with the Sym-H index, showed the importance of preconditioning in the system in inducing a larger GMD response. Taking this forward, a statistical analysis of many storms will allow us to find the Sym-H index threshold in which this preconditioning occurs, and to probe the FAC-GMD relationship further. This chapter was vital in highlighting where unverified assumptions concerning the relationships between FACs and GMDs and solar

wind drivers break down.

In Chapter 4 we probed the effect a disparity between UCL ground-based SCANDI and CHAMP accelerometer-derived neutral winds has on the distribution and magnitude of wind-derived Joule (frictional) heating, after using CMAT2 to show the winds at their respective measuring altitudes should be equivalent if the molecular viscosity of the upper atmosphere is not greatly overestimated. We presented neutral wind patterns and averaged flow-derived Joule heating patterns in the northern polar region during the winter periods of the 2005-2009 solar minimum comparing SCANDI, CHAMP and CMAT2 neutral winds, with SuperDARN providing the ion drifts. We identified large post-noon and smaller post-midnight heating spots. We also found the wind disparity translated to a magnitude difference between ground, satellite and model-calculated Joule heating, which implies a bias to models assimilating data. We used the assumption of frictional heating still further to investigate the disparity using a simplified ion-energy equation. We found agreement between wind-derived and temperature-derived Joule heating within less than an order of magnitude, but showed that wind-derived Joule heating did underestimate the temperature-derived Joule heating between 18-24 MLT, and overestimate between 12-18 MLT.

Using CMAT2 we also simulated the FPI height-integration measuring technique, which we found introduced a small error, unable to account for the wind disparity. Based on a similar density bias in the CHAMP and GOCE data seen in Chapter 5, which are derived using the same aerodynamical model, we therefore proposed that the calculation of the drag parameter and other model uncertainties are contributing to CHAMP overestimating UCL FPI measurements. The lack of data in this region necessitates reliable datasets. We have shown that they are not only non-equivalent but that their disparity will harm the derivation of other features in GCMs assimilating their data, such as Joule heating. Indeed, a lack of homogenous data in the ionosphere-thermosphere system is a significant challenge facing the space weather community.

Finally, in Chapter 5 we investigated small-scale FAC-driven Joule heating and electron precipitation as the causes of a satellite-measured cusp density enhancement and FPI-measured cusp and nightside auroral oval upwellings. Significantly, all of the components mentioned in the chapters before, that is, FACs, Joule heating and thermospheric neutral winds, are observed as part of one mechanism in this chapter. This study was able to draw on data and understanding of several coupled regions essential to cross-disciplinary

mechanisms, namely, the ionosphere, thermosphere and solar wind, as well as the previous work of Chapters 3 and 4, to compare CMAT2 model simulations with FPI neutral winds, CHAMP density measurements, OMNI IMF observations and KAIRA and EISCAT ionospheric data to support the Carlson et al. (2012) mechanism in the cusp region and also apply it to the nightside auroral oval.

We modelled an empirical heating source representative of soft and hard precipitation in the cusp and nightside auroral oval regions to simulate the density enhancements and upwellings, whilst simultaneously probing its drivers. We found that CMAT2 reproduces a near-doubling in density when soft precipitation is applied to the cusp region, supporting a mechanism of increased conductivity and fast plasma flows due to Poynting flux-induced Joule heating in the F region. We also found FPI-measured upwellings occurred near-simultaneously with soft electron precipitation and ion upflow measured with EISCAT, and were not dependent on geomagnetic conditions. They did, however, show a relationship with solar wind conditions, which we saw in Chapter 3 was a driver of FAC location, again supporting FACs (with soft precipitation) as a driver. We acknowledge CMAT2 is limited by its assumption of hydrostatic equilibrium, which restricts vertical transport, but we were able to simulate a neutral fountain effect in the winds, similar to those measured by FPIs. We suggest the inclusion of the cusp density enhancement in other GCMs as modelled by CMAT2. If the resolution in drag models is too low to include this enhancement, GCMs like CMAT2 may provide an aid in this region to accurately determine and predict satellite orbits as well as monitor the neutral density of the thermosphere.

In the nightside auroral oval, only soft precipitation produced a notable density enhancement, despite hard precipitation being more typical of the region. Coupled with signatures of soft precipitation detected by EISCAT at the time of FPI-measured upwellings, we suggest soft electrons are also responsible for the largest enhancements on the nightside, but that energies from ∼keV and under contribute to the average observed enhancement. Moreover, FPIs only observed upwellings in this region during active geomagnetic conditions. We therefore suggest that this is a storm-related anomaly, requiring an adjusted mechanism to that of the cusp, so that significant amounts of incoming energy counteract the greater density in the region stifling the upwelling. This chapter provided several case studies but a statistical study is required to fully understand this mechanism. Crucially, we were able to demonstrate the cascading effects of FACs in just two localised areas of the ionosphere-thermosphere system; their distributed effects are far

more complex.

To conclude, this thesis investigated individual effects of FACs as well as components of the same FAC-driven mechanism. This thesis was able to improve our understanding of each of the processes and their coupling, as well as stressing the importance of uniformity across model, ground-based instrument and satellite measurements in probing the complex resultant processes of FACs in the ionosphere-thermosphere system. Several commonly adopted assumptions in the ionosphere-thermosphere system were also questioned, providing clarity and in-depth analysis where it had previously not been. The findings of this thesis have immediate implications for drag models, particularly work on data dissimilarities and cusp modelling, as well as the national grid network industry, which will benefit from our ground geomagnetic disturbance study. Above all, we have shown that FACs are a pivotal facilitator of terrestrial space weather, the knowledge of which is vital if we are to counteract and prevent against its harmful effects.

Appendix A

Appendix A

A.1 List of Publications and Presentations

Hood, R.K.E., Woodroffe J.R., Morley, S., & Aruliah, A.L., 2017, *Correlations between Geomagnetic Disturbances and Field-Aligned Currents during the 22-29 July 2004 Storm Time Interval [SM41A-2683]*, presented at 2017 Fall Meeting, AGU, New Orleans, L.A., U.S.A., 11-15 Dec. **Awarded AGU and RAS grants**.

Aruliah, A.L., Foerster, M., Doornbos, E., **Hood, R.** & Johnson, D., 2017, *Comparing High-Latitude Thermospheric Winds From FPI and CHAMP Accelerometer Measurements [SA41A-2613]*, presented at 2017 Fall Meeting, AGU, New Orleans, L.A., U.S.A., 11-15 Dec.

Hood, R.K.E., Woodroffe J.R., Morley, S., & Aruliah, A.L., 2017, *Correlations between Geomagnetic Disturbances and Field-Aligned Currents during the 22-29 July 2004 Storm Time Interval*, Autumn MIST, RAS, London, U.K., 24 Nov.

Hood, R.K.E., Ronksley, A. & Aruliah, A., 2017, *Using CMAT2 to investigate the consistency of FPI and CHAMP thermospheric wind measurements in terms of Joule heating*, NAM MIST session, Hull, U.K., 4 July.

Aruliah, A., Hall, J., Jairaj-Jacklin, L., **Hood, R.**, Ronksley, A., Johnson, D., Barnes, D.

& Ray, V., 2017, *Cubesats as Space Weather "balloons" for regular in-situ monitoring of the middle/lower thermosphere*, Science with Cubesats, RAS, London, U.K., 7 April.

Hood, R.K.E., Woodroffe, J. & Morley, S, 2016, *The evolution of the magnetospheric response during the 22-29 July 2004 storm time interval*, 2016 Los Alamos Space Weather Summer School Research Reports, LANL.

Hood, R.K.E., Woodroffe, J., Morley, S. & Aruliah, A., 2016, *The evolution of the magnetospheric response during the 22-29 July 2004 storm time interval*, Autumn MIST, RAS, London, U.K., 25 November.

Hood, R.K.E., Aruliah, A., Spain, T. & Aylward, A., 2016, *Investigating soft and hard precipitation as sources of the geomagnetic cusp density enhancement observed by CHAMP using the CMAT2 general circulation model*, CEDAR-GEM, Sante Fe, N.M., U.S.A, 19-24 June.

Hood, R.K.E., Aruliah, A., Spain, T. & Aylward, A., 2016, *Modelling the geomagnetic cusp density enhancement observed by CHAMP using the CMAT2 general circulation model*, Luner MIST, Lancaster, U.K., 5-7 April.

Carlson, H.C., Aruliah, A., McWhirter, I., Ronksley, A. & **Hood, R.K.E.**, 2015, *First high time resolution FPI observations of the daytime thermosphere during the eclipse over Svalbard on 20th March 2015*, AGU, San Francisco, C.A., U.S.A., 14-18 December.

Aruliah, A., McWhirter, I., Ronksley, A., **Hood, R.K.E.** & Johnson, D., 2015, *First high time resolution FPI and SCANDI observations of the day thermosphere during the eclipse over Svalbard on 20th March 2015*, NAM, Llandudno, U.K., 5-9 July.

Hood, R.K.E. & Aruliah, A., 2015, *Differences in satellite to ground-based wind measurements: modelling viscosity as a possible source*, NAM MIST session, Llandudno, U.K., 7 July. **Awarded RAS grant**.

Bibliography

Adhikari, B., Dahal, S. & Chapagain, N. P., 2017, *Study of field-aligned current (FAC), interplanetary electric field component (Ey), interplanetary magnetic field component (Bz), and northward (x) and eastward (y) components of geomagnetic field during supersubstorm*, *Earth and Space Science*, **4**(5), 257, 2017EA000258

AIAA Standards, 1999, *Guide: Guide to Reference and Standard Ionosphere Models (ANSI_AIAA_G-034A-2014)* (American Institute of Aeronautics and Astronautics, Inc., Virginia, USA)

Akasofu, S.-I., 1979, *Interplanetary energy flux associated with magnetospheric substorms*, *Planetary and Space Science*, **27**(4), 425

Akasofu, S.-I., 1981, *Energy coupling between the solar wind and the magnetosphere*, *Space Science Reviews*, **28**(2), 121

Alexander, M. J. & Dunkerton, T. J., 1999, *A Spectral Parameterization of Mean-Flow Forcing due to Breaking Gravity Waves*, *Journal of the Atmospheric Sciences*, **56**(24), 4167

Anderson, C., Conde, M. & McHarg, M. G., 2012, *Neutral thermospheric dynamics observed with two scanning Doppler imagers: 2. Vertical winds*, *Journal of Geophysical Research: Space Physics*, **117**(A3)

Angelopoulos, V., McFadden, J. P., Larson, D., Carlson, C. W., Mende, S. B., Frey, H., Phan, T., Sibeck, D. G., Glassmeier, K.-H., Auster, U., Donovan, E., Mann, I. R., Rae, I. J., Russell, C. T., Runov, A., Zhou, X.-Z. & Kepko, L., 2008, *Tail Reconnection Triggering Substorm Onset*, *Science*, **321**(5891), 931

Aruliah, A. L., Förster, M., Doornbos, E., Hood, R. K. E. & Johnson, D., 2018, *Comparing*

high-latitude thermospheric winds from FPI and CHAMP accelerometer measurements, In submission

Aruliah, A. L. & Griffin, E., 2001, *Evidence of meso-scale structure in the high-latitude thermosphere*, *Annales Geophysicae*, **19**(1), 37

Aruliah, A. L., Griffin, E. M., Aylward, A. D., Ford, E. A. K., Kosch, M. J., Davis, C. J., Howells, V. S. C., Pryse, S. E., Middleton, H. R. & Jussila, J., 2005, *First direct evidence of meso-scale variability on ion-neutral dynamics using co-located tristatic FPIs and EISCAT radar in Northern Scandinavia*, *Annales Geophysicae*, **23**(1), 147

Aruliah, A. L., Griffin, E. M., McWhirter, I., Aylward, A. D., Ford, E. A. K., Charalambous, A., Kosch, M. J., Davis, C. J. & Howells, V. S. C., 2004, *First tristatic studies of meso-scale ion-neutral dynamics and energetics in the high-latitude upper atmosphere using collocated FPIs and EISCAT radar*, *Geophysical Research Letters*, **31**(3), L03802

Aruliah, A. L., Griffin, E. M., Yiu, H.-C. I., McWhirter, I. & Charalambous, A., 2010, *SCANDI – an all-sky Doppler imager for studies of thermospheric spatial structure*, *Annales Geophysicae*, **28**(2), 549

Aruliah, A. L., Müller-Wodarg, I. C. F. & Schoendorf, J., 1999, *Consequences of geomagnetic history on the high-latitude thermosphere and ionosphere: Averages*, *Journal of Geophysical Research: Space Physics*, **104**(A12), 28073

Aruliah, A. L. & Rees, D., 1995, *The trouble with thermospheric vertical winds: geomagnetic, seasonal and solar cycle dependence at high latitudes*, *Journal of Atmospheric and Terrestrial Physics*, **57**(6), 597

Baker, D. N., Pulkkinen, T. I., Angelopoulos, V., Baumjohann, W. & McPherron, R. L., 1996, *Neutral line model of substorms: Past results and present view*, *Journal of Geophysical Research: Space Physics*, **101**(A6), 12975

Banks, P. M., 1972, in S. A. Bowhill, L. D. Jaffe & M. J. Rycroft (eds.), *Magnetospheric processes and the behavior of the neutral atmosphere*, volume 2 of *Space Research Conference*, pp. 1051–1067

Banks, P. M. & Kockarts, G., 1973, *Aeronomy* (Academic Press, Inc., London, UK)

Bargatze, L. F., Baker, D. N., McPherron, R. L. & Hones Jr., E. W., 1985, *Magnetospheric impulse response for many levels of geomagnetic activity*, *Journal of Geophysical Research: Space Physics*, **90**(A7), 6387

Barnes, D., 2017, *Forecasting and Modelling the Terrestrial Effects of Space Weather using STEREO and CMAT2*, Ph.D. thesis, University College London

Baron, M. J. & Wand, R. H., 1983, *F region ion temperature enhancements resulting from Joule heating*, *Journal of Geophysical Research: Space Physics*, **88**(A5), 4114

Benacquista, R., Rochel, S. & Rolland, G., 2017, *Understanding the variability of magnetic storms caused by ICMEs*, *Annales Geophysicae*, **35**(1), 147

Billett, D. D., Grocott, A., Wild, J. A., Walach, M.-T. & Kosch, M. J., 2018, *Diurnal Variations in Global Joule Heating Morphology and Magnitude Due To Neutral Winds*, *Journal of Geophysical Research: Space Physics*, **123**(3), 2398

Bjoland, L. M., Chen, X., Jin, Y., Reimer, A. S., Skjæveland, Å., Wessel, M. R., Burchill, J. K., Clausen, L. B. N., Haaland, S. E. & McWilliams, K. A., 2015, *Interplanetary magnetic field and solar cycle dependence of Northern Hemisphere F region Joule heating*, *Journal of Geophysical Research: Space Physics*, **120**(2), 1478, 2014JA020586

Boscher, D., Bourdarie, S., O'Brien, P. & Guild, T., 2004-2008, *IRBEM library V4.3*, [Online; accessed 2016-10-03]
URL: *https://sourceforge.net/projects/irbem/*

Bruinsma, S., 2015, *The DTM-2013 thermosphere model*, *J. Space Weather Space Clim.*, **5**, A1

Bruinsma, S., Tamagnan, D. & Biancale, R., 2004, *Atmospheric densities derived from CHAMP/STAR accelerometer observations*, *Planetary and Space Science*, **52**(4), 297

Bruinsma, S. L., Doornbos, E. & Bowman, B. R., 2014, *Validation of GOCE densities and evaluation of thermosphere models*, *Advances in Space Research*, **54**(4), 576

Burch, J. L., 1973, *Rate of erosion of dayside magnetic flux based on a quantitative study of the dependence of polar cusp latitude on the interplanetary magnetic field*, *Radio Science*, **8**(11), 955

Burch, J. L., 1979, *Effects of the interplanetary magnetic field on the auroral oval and plasmapause*, *Space Science Reviews*, **23**(3), 449

Cabinet Office, 2015, *National Risk Register of Civil Emergencies 2015 edition* (Crown, Cabinet Office, 70 Whitehall London SW1A 2AS, UK), [Online; accessed 2016-12-10] **URL:** *https://www.gov.uk/government/uploads/system/uploads/attachment_data/file/419549/20150331_2015-NRR-WA_Final.pdf*

Cai, G., Chen, B. M. & Lee, T. H., 2011, *Coordinate Systems and Transformations* (Springer London, London), pp. 23–34

Carlson, H. C., Spain, T., Aruliah, A., Skjæveland, A. & Moen, J., 2012, *First-principles physics of cusp/polar cap thermospheric disturbances*, *Geophysical Research Letters*, **39**(19)

Chapman, S., 1931, *The absorption and dissociative or ionizing effect of monochromatic radiation in an atmosphere on a rotating Earth part II. Grazing incidence*, *Proceedings of the Physical Society*, **43**(5), 483

Cheng, Z. W., Shi, J. K., Dunlop, M. & Liu, Z. X., 2013, *Influences of the interplanetary magnetic field clock angle and cone angle on the field-aligned currents in the magnetotail*, *Geophysical Research Letters*, **40**(20), 5355

Chisham, G., Lester, M., Milan, S. E., Freeman, M. P., Bristow, W. A., Grocott, A., McWilliams, K. A., Ruohoniemi, J. M., Yeoman, T. K., Dyson, P. L., Greenwald, R. A., Kikuchi, T., Pinnock, M., Rash, J. P. S., Sato, N., Sofko, G. J., Villain, J.-P. & Walker, A. D. M., 2007, *A decade of the Super Dual Auroral Radar Network (SuperDARN): scientific achievements, new techniques and future directions*, *Surveys in Geophysics*, **28**(1), 33

Chiu, Y. T., 1975, *An improved phenomenological model of ionospheric density*, *Journal of Atmospheric and Terrestrial Physics*, **37**(12), 1563

Chu, X., Hsu, T.-S., McPherron, R. L., Angelopoulos, V., Pu, Z., Weygand, J. J., Khurana, K., Connors, M., Kissinger, J., Zhang, H. & Amm, O., 2014, *Development and validation of inversion technique for substorm current wedge using ground magnetic field data*, *Journal of Geophysical Research: Space Physics*, **119**(3), 1909, 2013JA019185

Cierpka, K., Kosch, M. J., Rietveld, M., Schlegel, K. & Hagfors, T., 2000, *Ion-neutral coupling in the high-latitude F-layer from incoherent scatter and Fabry-Perot interferometer measurements*, *Annales Geophysicae*, **18**(9), 1145

Clemmons, J. H., Hecht, J. H., Salem, D. R. & Strickland, D. J., 2008, *Thermospheric density in the Earth's magnetic cusp as observed by the Streak mission*, *Geophysical Research Letters*, **35**(24)

Codrescu, M. V., Fuller-Rowell, T. J. & Foster, J. C., 1995, *On the importance of E-field variability for Joule heating in the high-latitude thermosphere*, *Geophysical Research Letters*, **22**(17), 2393

Codrescu, M. V., Fuller-Rowell, T. J., Foster, J. C., Holt, J. M. & Cariglia, S. J., 2000, *Electric field variability associated with the Millstone Hill electric field model*, *Journal of Geophysical Research: Space Physics*, **105**(A3), 5265

Conde, M., Larsen, M. F., Troyer, R., Gillespie, D. & Kosch, M., 2017, *Do Transient Electrodynamic Processes Support Enhanced Neutral Mass Densities in Earth's Cusp-Region Thermosphere via Divergent Upward Winds?*, *American Geophysical Union (AGU)*, [SA52A-05] presented at 2017 Fall Meeting, AGU, New Orleans, L.A., 11-15 Dec.

Cosgrove, R. B., Bahcivan, H., Chen, S., Strangeway, R. J., Ortega, J., Alhassan, M., Xu, Y., Van Welie, M., Rehberger, J., Musielak, S. & Cahill, N., 2014, *Empirical model of Poynting flux derived from FAST data and a cusp signature*, *Journal of Geophysical Research: Space Physics*, **119**(1), 411

Cowley, S. W. H., 2000, *Magnetosphere-Ionosphere Interactions: A Tutorial Review* (American Geophysical Union), pp. 91–106

Cowley, S. W. H., Davies, J. A., Grocott, A., Khan, H., Lester, M., McWilliams, K. A., Milan, S. E., Provan, G., Sandholt, P. E., Wild, J. A. & Yeoman, T. K., 2003, *Solar–wind–magnetosphere–ionosphere interactions in the Earth's plasma environment*, *Philosophical Transactions of the Royal Society of London A: Mathematical, Physical and Engineering Sciences*, **361**(1802), 113

Cowley, S. W. H. & Lockwood, M., 1992, *Excitation and decay of solar wind–driven flows in the magnetosphere–ionosphere system*, *Annales Geophysicae*, **10**(1-2), 103

Cowley, S. W. H., Morelli, J. P. & Lockwood, M., 1991, *Dependence of convective flows and particle precipitation in the high-latitude dayside ionosphere on the X and Y components of the interplanetary magnetic field*, *Journal of Geophysical Research: Space Physics*, **96**(A4), 5557

Crowley, G., Knipp, D. J., Drake, K. A., Lei, J., Sutton, E. & Lühr, H., 2010, *Thermospheric density enhancements in the dayside cusp region during strong By conditions*, *Geophysical Research Letters*, **37**(7)

Daglis, I. A., Thorne, R. M., Baumjohann, W. & Orsini, S., 1999, *The terrestrial ring current: Origin, formation, and decay*, *Reviews of Geophysics*, **37**(4), 407

Daniell, Jr., R. E., Brown, L. D., Anderson, D. N., Fox, M. W., Doherty, P. H., Decker, D. T., Sojka, J. J. & Schunk, R. W., 1995, *Parameterized ionospheric model: A global ionospheric parameterization based on first principles models*, *Radio Sci.*, **30**(5), 1499

Davis, T. N. & Sugiura, M., 1966, *Auroral electrojet activity index AE and its universal time variations*, *Journal of Geophysical Research*, **71**(3), 785

Demars, H. G. & Schunk, R. W., 2007, *Thermospheric response to ion heating in the dayside cusp*, *Journal of Atmospheric and Solar-Terrestrial Physics*, **69**(6), 649

Deng, Y., Fuller-Rowell, T. J., Ridley, A. J., Knipp, D. & Lopez, R. E., 2013, *Theoretical study: Influence of different energy sources on the cusp neutral density enhancement*, *Journal of Geophysical Research: Space Physics*, **118**(5), 2340

Deng, Y. & Ridley, A. J., 2007, *Possible reasons for underestimating Joule heating in global models: E field variability, spatial resolution, and vertical velocity*, *Journal of Geophysical Research: Space Physics*, **112**(9), A09308

Dhadly, M., Emmert, J., Drob, D., Conde, M., Doornbos, E., Shepherd, G., Makela, J., Wu, Q., Niciejewski, R. & Ridley, A., 2017*a*, *Seasonal dependence of northern high-latitude upper thermospheric winds: A quiet time climatological study based on ground-based and space-based measurements*, *Journal of Geophysical Research: Space Physics*, **122**(2), 2619, 2016JA023688

Dhadly, M. S., Emmert, J. T., Drob, D. P., Conde, M. G., Doornbos, E., Shepherd, G. G., Makela, J. J., Wu, Q., Nieciejewski, R. J. & Ridley, A. J., 2017*b*, *Seasonal*

Dependence of Geomagnetic Active-Time Northern High-Latitude Upper Thermospheric Winds, *Journal of Geophysical Research: Space Physics*, **123**(1), 739, 2017JA024715

DHS Office of Risk Management and Analysis, 2011, *The Strategic National Risk Assessment in Support of PPD 8: A Comprehensive Risk–Based Approach toward a Secure and Resilient Nation* (Homeland Security Office, Washington, DC, USA), [Online; accessed 2016-10-03]
URL: *https://www.dhs.gov/xlibrary/assets/rma-strategic-national-risk-assessment-ppd8.pdf*

Doornbos, E., van den Ijssel, J., Lühr, H., Förster, M. & Koppenwallner, G., 2010, *Neutral Density and Crosswind Determination from Arbitrarily Oriented Multiaxis Accelerometers on Satellites*, *Journal of Spacecraft and Rockets*, **47**(4), 580

Drinkwater, M. R., Floberghagen, R., Haagmans, R., Muzi, D. & Popescu, A., 2003, *GOCE: ESA's First Earth Explorer Core Mission* (Springer Netherlands, Dordrecht), pp. 419–432

Drob, D. P., Emmert, J. T., Crowley, G., Picone, J. M., Shepherd, G. G., Skinner, W., Hays, P., Niciejewski, R. J., Larsen, M., She, C. Y., Meriwether, J. W., Hernandez, G., Jarvis, M. J., Sipler, D. P., Tepley, C. A., O'Brien, M. S., Bowman, J. R., Wu, Q., Murayama, Y., Kawamura, S., Reid, I. M. & Vincent, R. A., 2008, *An empirical model of the Earth's horizontal wind fields: HWM07*, *Journal of Geophysical Research: Space Physics*, **113**(A12), A12304

Dungey, J. W., 1961, *Interplanetary Magnetic Field and the Auroral Zones*, *Phys. Rev. Lett.*, **6**, 47

Ebihara, Y., Fok, M.-C., Sazykin, S., Thomsen, M. F., Hairston, M. R., Evans, D. S., Rich, F. J. & Ejiri, M., 2005, *Ring current and the magnetosphere-ionosphere coupling during the superstorm of 20 November 2003*, *Journal of Geophysical Research: Space Physics*, **110**(A9), A09S22

Emmert, J. T., Faivre, M. L., Hernandez, G., Jarvis, M. J., Meriwether, J. W., Niciejewski, R. J., Sipler, D. P. & Tepley, C. A., 2006*a*, *Climatologies of nighttime upper thermospheric winds measured by ground-based Fabry-Perot interferometers during geomagnet-*

ically quiet conditions: 1. Local time, latitudinal, seasonal, and solar cycle dependence, *Journal of Geophysical Research: Space Physics*, **111**(A12), A12302

Emmert, J. T., Fejer, B. G., Shepherd, G. G. & Solheim, B. H., 2002, *Altitude dependence of middle and low-latitude daytime thermospheric disturbance winds measured by WINDII*, *Journal of Geophysical Research: Space Physics*, **107**(A12), SIA 19, 1483

Emmert, J. T., Hernandez, G., Jarvis, M. J., Niciejewski, R. J., Sipler, D. P. & Vennerstrom, S., 2006*b*, *Climatologies of nighttime upper thermospheric winds measured by ground-based Fabry-Perot interferometers during geomagnetically quiet conditions: 2. High-latitude circulation and interplanetary magnetic field dependence*, *Journal of Geophysical Research: Space Physics*, **111**(A12), A12303

Emmert, J. T., Lean, J. L. & Picone, J. M., 2010*a*, *Record-low thermospheric density during the 2008 solar minimum*, *Geophysical Research Letters*, **37**(12), L12102

Emmert, J. T., Richmond, A. D. & Drob, D. P., 2010*b*, *A computationally compact representation of Magnetic-Apex and Quasi-Dipole coordinates with smooth base vectors*, *Journal of Geophysical Research: Space Physics*, **115**(A8), A08322

Emmert, J. T., Warren, H. P., Segerman, A. M., Byers, J. M. & Picone, J. M., 2017, *Propagation of atmospheric density errors to satellite orbits*, *Advances in Space Research*, **59**(1), 147

Förster, M., Rentz, S., Köhler, W., Liu, H. & Haaland, S. E., 2008, *IMF dependence of high-latitude thermospheric wind pattern derived from CHAMP cross-track measurements*, *Annales Geophysicae*, **26**(6), 1581

Forsyth, C., Fazakerley, A. N., Rae, I. J., J. Watt, C. E., Murphy, K., Wild, J. A., Karlsson, T., Mutel, R., Owen, C. J., Ergun, R., Masson, A., Berthomier, M., Donovan, E., Frey, H. U., Matzka, J., Stolle, C. & Zhang, Y., 2014, *In situ spatiotemporal measurements of the detailed azimuthal substructure of the substorm current wedge*, *Journal of Geophysical Research: Space Physics*, **119**(2), 927

Forsyth, C., Rae, I. J., Coxon, J. C., Freeman, M. P., Jackman, C. M., Gjerloev, J. & Fazakerley, A. N., 2015, *A new technique for determining Substorm Onsets and Phases from Indices of the Electrojet (SOPHIE)*, *Journal of Geophysical Research: Space Physics*, **120**(12), 10,592, 2015JA021343

Foster, J. C., Holt, J. M., Musgrove, R. G. & Evans, D. S., 1986, *Ionospheric convection associated with discrete levels of particle precipitation*, *Geophysical Research Letters*, **13**(7), 656

Freeman, M. P., 2003, *A unified model of the response of ionospheric convection to changes in the interplanetary magnetic field*, *Journal of Geophysical Research: Space Physics*, **108**(A1), SMP 14, 1024

Freeman, M. P. & Morley, S. K., 2009, *No evidence for externally triggered substorms based on superposed epoch analysis of IMF Bz*, *Geophysical Research Letters*, **36**(21), L21101

Frey, H. U. & Mende, S. B., 2006, in *Proceedings of the 8th International Conference on Substorms*, pp. 71–76

Frey, H. U., Mende, S. B., Angelopoulos, V. & Donovan, E. F., 2004, *Substorm onset observations by IMAGE–FUV*, *Journal of Geophysical Research: Space Physics*, **109**(A10), A10304

Friis-Christensen, E., Kamide, Y., Richmond, A. D. & Matsushita, S., 1985, *Interplanetary magnetic field control of high-latitude electric fields and currents determined from Greenland Magnetometer Data*, *Journal of Geophysical Research: Space Physics*, **90**(A2), 1325

Fukushima, N., 1976, *Generalized theorem for no ground magnetic effect of vertical currents connected with Pedersen currents in the uniform-conductivity ionosphere*, *Report of Ionosphere and Space Research in Japan*, **30**, 35

Fuller-Rowell, T. J., 1981, *A three-dimensional time-dependant global model of the thermosphere*, Ph.D. thesis, University College London

Fuller-Rowell, T. J. & Evans, D. S., 1987, *Height-integrated Pedersen and Hall conductivity patterns inferred from the TIROS-NOAA satellite data*, *Journal of Geophysical Research: Space Physics*, **92**(A7), 7606

Fuller-Rowell, T. J. & Rees, D., 1984, *Interpretation of an anticipated long-lived vortex in the lower thermosphere following simulation of an isolated substorm*, *Planetary and Space Science*, **32**(1), 69

Gillies, M. D., Knudsen, D., Donovan, E., Jackel, B., Gillies, R. & Spanswick, E., 2017, *Identifying the 630 nm auroral arc emission height: A comparison of the triangulation, FAC profile, and electron density methods*, *Journal of Geophysical Research: Space Physics*, **122**(8), 8181, 2016JA023758

Gjerloev, J. W., 2012, *The SuperMAG data processing technique*, *Journal of Geophysical Research: Space Physics*, **117**(A9), A09213

Gjerloev, J. W., Ohtani, S., Iijima, T., Anderson, B., Slavin, J. & Le, G., 2011, *Characteristics of the terrestrial field-aligned current system*, *Annales Geophysicae*, **29**(10), 1713

Gonzalez, W. D., Joselyn, J. A., Kamide, Y., Kroehl, H. W., Rostoker, G., Tsurutani, B. T. & Vasyliunas, V. M., 1994, *What is a geomagnetic storm?*, *Journal of Geophysical Research: Space Physics*, **99**(A4), 5771

Goodwin, L., St.-Maurice, J.-P., Richards, P., Nicolls, M. & Hairston, M., 2014, *F region dusk ion temperature spikes at the equatorward edge of the high-latitude convection pattern*, *Geophysical Research Letters*, **41**(2), 300

Gopalswamy, N., 2004, in G. Poletto & S. T. Suess (eds.), *The Sun and the Heliosphere as an Integrated System* (Springer Netherlands, Dordrecht), pp. 201–251

Grant, I. S. & Phillips, W. R., 2013, *Electromagnetism*, Manchester Physics Series (Wiley)

Greenwald, R. A., Baker, K. B., Dudeney, J. R., Pinnock, M., Jones, T. B., Thomas, E. C., Villain, J. P., Cerisier, J. C., Senior, C., Hanuise, C., Hunsucker, R. D., Sofko, G., Koehler, J., Nielsen, E., Pellinen, R., Walker, A. D. M., Sato, N. & Yamagishi, H., 1995, *DARN/SuperDARN*, *Space Science Reviews*, **71**(1), 761

Griffin, E. M., Aruliah, A., Müller-Wodarg, I. C. F. & Aylward, A., 2004, *Comparison of high-latitude thermospheric meridional winds II: combined FPI, radar and model Climatologies*, *Annales Geophysicae*, **22**(3), 863

Harris, M., 2001, *A new coupled middle atmosphere and thermosphere general circulation model: studies of dynamic, energetic, and photochemical coupling in the middle and upper atmosphere*, Ph.D. thesis, University College London

Harris, M. J., Arnold, N. F. & Aylward, A. D., 2002, *A study into the effect of the diurnal tide on the structure of the background mesosphere and thermosphere using the new coupled middle atmosphere and thermosphere (CMAT) general circulation model*, *Annales Geophysicae*, **20**(2), 225

Häusler, K. & Lühr, H., 2009, *Nonmigrating tidal signals in the upper thermospheric zonal wind at equatorial latitudes as observed by CHAMP*, *Annales Geophysicae*, **27**(7), 2643

Hedin, A. E., 1991, *Extension of the MSIS Thermosphere Model into the middle and lower atmosphere*, *Journal of Geophysical Research: Space Physics*, **96**(A2), 1159

Heelis, R. A., McEwen, D. & Guo, W., 2002, *Ion and neutral motions observed in the winter polar upper atmosphere*, *Journal of Geophysical Research: Space Physics*, **107**(A12), SIA 17, 1476

Hickey, M. P., 1988, *Effects of eddy viscosity and thermal conduction and Coriolis force in the dynamics of gravity wave driven fluctuations in the OH nightglow*, *Journal of Geophysical Research: Space Physics*, **93**(A5), 4077

Hood, R. K. E., Morley, S. K., Woodroffe, J. R. & Aruliah, A. L., 2018, *Behaviour and Correlation of Storm Time Field-Aligned Currents and Ground Geomagnetic Disturbances*, In submission

Hood, R. K. E., Woodroffe, J. R. & Morley, S. K., 2016, *Understanding and Assessing the Effects of Geomagnetic Preconditioning on the Severity of Ground-Level Geomagnetic Disturbances during the 22-29 July 2004 Geomagnetic Storm* (LANL)

Huang, T. Y. W. & Smith, A. K., 1991, *The Mesospheric Diabatic Circulation and the Parameterized Thermal Effect of Gravity Wave Breaking on the Circulation*, *Journal of the Atmospheric Sciences*, **48**(8), 1093

Huang, Y., Richmond, A. D., Deng, Y. & Roble, R., 2012, *Height distribution of Joule heating and its influence on the thermosphere*, *Journal of Geophysical Research: Space Physics*, **117**(A8), A08334

Hughes, W. J., 1995, in M. G. Kivelson & C. T. Russell (eds.), *Introduction to Space Physics* (Cambridge University Press, Cambridge, UK)

Iijima, T., 2013, *Field-Aligned Currents in Geospace: Substance and Significance* (American Geophysical Union), pp. 107–129

Iijima, T. & Potemra, T. A., 1976, *Field-aligned currents in the dayside cusp observed by Triad*, *Journal of Geophysical Research*, **81**(34), 5971

Innis, J. L. & Conde, M., 2001, *Thermospheric vertical wind activity maps derived from Dynamics Explorer 2 WATS observations*, *Geophysical Research Letters*, **28**(20), 3847

Jacchia, L. G., 1970, *New static models of the thermosphere and exosphere with empirical temperature profiles*, *SAO special report*, **313**

James, I. N., 1995, *Introduction to Circulating Atmospheres* (Cambridge University Press, UK)

Johnson, C. Y., 1969, *Ion and neutral composition of the ionosphere.*, *Annals of the IQSY*, **5**, 197

Jonas, S. & McCarron, E. D., 2016, *White House Releases National Space Weather Strategy and Action Plan*, *Space Weather*, **14**(2), 54, 2015SW001357

Juusola, L., Kauristie, K., Amm, O. & Ritter, P., 2009, *Statistical dependence of auroral ionospheric currents on solar wind and geomagnetic parameters from 5 years of CHAMP satellite data*, *Annales Geophysicae*, **27**(3), 1005

Juusola, L., Milan, S. E., Lester, M., Grocott, A. & Imber, S. M., 2014, *Interplanetary magnetic field control of the ionospheric field-aligned current and convection distributions*, *Journal of Geophysical Research: Space Physics*, **119**(4), 3130

Kamide, Y., 1982, *The relationship between field-aligned currents and the auroral electrojets: A review*, *Space Science Reviews*, **31**(2), 127

Kepko, L., McPherron, R. L., Amm, O., Apatenkov, S., Baumjohann, W., Birn, J., Lester, M., Nakamura, R., Pulkkinen, T. I. & Sergeev, V., 2015, *Substorm Current Wedge Revisited*, *Space Science Reviews*, **190**(1), 1

Kervalishvili, G. N. & Lühr, H., 2013, *The relationship of thermospheric density anomaly with electron temperature, small-scale FAC, and ion up-flow in the cusp region, as observed by CHAMP and DMSP satellites*, *Annales Geophysicae*, **31**(3), 541

Kiene, A., Bristow, W., Conde, M. & Hampton, D., 2017, *Measurements of Ion-Neutral Coupling in the Auroral F-Region in Response to Increases in Particle Precipitation*, *American Geophysical Union (AGU)*, [SA33B-06] presented at 2017 Fall Meeting, AGU, New Orleans, L.A., 11-15 Dec.

Killeen, T. L., Hays, P. B., Carignan, G. R., Heelis, R. A., Hanson, W. B., Spencer, N. W. & Brace, L. H., 1984, *Ion-neutral coupling in the high-latitude F region: Evaluation of ion heating terms from Dynamics Explorer 2*, *Journal of Geophysical Research: Space Physics*, **89**(A9), 7495

Killeen, T. L., Hays, P. B., Spencer, N. W. & Wharton, L. E., 1982, *Neutral winds in the polar thermosphere as measured from Dynamics Explorer*, *Geophysical Research Letters*, **9**(9), 957

Killeen, T. L., McCormac, F. G., Burns, A. G., Thayer, J. P., Johnson, R. M. & Niciejewski, R. J., 1991, *On the dynamics and composition of the high-latitude thermosphere*, *Journal of Atmospheric and Terrestrial Physics*, **53**(9), 797

King, J. H. & Papitashvili, N. E., 2005, *Solar wind spatial scales in and comparisons of hourly Wind and ACE plasma and magnetic field data*, *Journal of Geophysical Research: Space Physics*, **110**(A2)

Kivelson, M. G. & Russell, C. T., 1995, in M. G. Kivelson & C. T. Russell (eds.), *Introduction to Space Physics* (Cambridge University Press, Cambridge, UK), p. 586

Knipp, D., Eriksson, S., Kilcommons, L., Crowley, G., Lei, J., Hairston, M. & Drake, K., 2011, *Extreme Poynting flux in the dayside thermosphere: Examples and statistics*, *Geophysical Research Letters*, **38**(16)

Kohl, H. & King, J. W., 1967, *Atmospheric winds between 100 and 700 km and their effects on the ionosphere*, *Journal of Atmospheric and Terrestrial Physics*, **29**(9), 1045

Kozyra, J. U., Liemohn, M. W., Clauer, C. R., Ridley, A. J., Thomsen, M. F., Borovsky, J. E., Roeder, J. L., Jordanova, V. K. & Gonzalez, W. D., 2002, *Multistep Dst development and ring current composition changes during the 4–6 June 1991 magnetic storm*, *Journal of Geophysical Research: Space Physics*, **107**(A8), SMP 33

Krausmann, E. & Bothmer, V., 2012, *Meeting Report: European Commission's Space-Weather Awareness Dialogue*, *Space Weather*, **10**(4), S04006

Kwak, Y.-S. & Richmond, A. D., 2007, *An analysis of the momentum forcing in the high-latitude lower thermosphere*, *Journal of Geophysical Research: Space Physics*, **112**(A1), A01306

Larsen, M. F. & Meriwether, J. W., 2012, *Vertical winds in the thermosphere*, *Journal of Geophysical Research: Space Physics*, **117**(A9)

Laundal, K. M., Finlay, C. C., Olsen, N. & Reistad, J. P., 2018, *Solar Wind and Seasonal Influence on Ionospheric Currents From Swarm and CHAMP Measurements*, *Journal of Geophysical Research: Space Physics*, **123**(5), 4402

Laundal, K. M., Haaland, S. E., Lehtinen, N., Gjerloev, J. W., Østgaard, N., Tenfjord, P., Reistad, J. P., Snekvik, K., Milan, S. E., Ohtani, S. & Anderson, B. J., 2015, *Birkeland current effects on high-latitude ground magnetic field perturbations*, *Geophysical Research Letters*, **42**(18), 7248, 2015GL065776

Laundal, K. M. & Richmond, A. D., 2017, *Magnetic Coordinate Systems*, *Space Science Reviews*, **206**(1), 27

Lavraud, B., Thomsen, M. F., Lefebvre, B., Schwartz, S. J., Seki, K., Phan, T. D., Wang, Y. L., Fazakerley, A., Rme, H. & Balogh, A., 2006, *Evidence for newly closed magnetosheath field lines at the dayside magnetopause under northward IMF*, *Journal of Geophysical Research: Space Physics*, **111**(A5), A05211

Lechtenberg, T., McLaughlin, C. A., Locke, T. & Krishna, D. M., 2013, *Thermospheric density variations: Observability using precision satellite orbits and effects on orbit propagation*, *Space Weather*, **11**(1), 34

Lester, M., Hughes, W. J. & Singer, H. J., 1984, *Longitudinal structure in Pi 2 pulsations and the substorm current wedge*, *Journal of Geophysical Research: Space Physics*, **89**(A7), 5489

Li, H., Wang, C. & Kan, J. R., 2011, *Contribution of the partial ring current to the SYMH index during magnetic storms*, *Journal of Geophysical Research: Space Physics*, **116**(A11), A11222

Li, H., Wang, C. & Peng, Z., 2013, *Solar wind impacts on growth phase duration and substorm intensity: A statistical approach*, *Journal of Geophysical Research: Space Physics*, **118**(7), 4270

Link, R. & Cogger, L. L., 1988, *A reexamination of the O I 6300-Å nightglow*, *Journal of Geophysical Research: Space Physics*, **93**(A9), 9883

Liu, H., Lühr, H., Henize, V. & Köhler, W., 2005, *Global distribution of the thermospheric total mass density derived from CHAMP*, *Journal of Geophysical Research: Space Physics*, **110**(A4), A04301

Liu, H., Lühr, H., Watanabe, S., Köhler, W., Henize, V. & Visser, P., 2006, *Zonal winds in the equatorial upper thermosphere: Decomposing the solar flux, geomagnetic activity, and seasonal dependencies*, *Journal of Geophysical Research: Space Physics*, **111**(A7), A07307

Liu, J., Angelopoulos, V., Runov, A. & Zhou, X.-Z., 2013*a*, *On the current sheets surrounding dipolarizing flux bundles in the magnetotail: The case for wedgelets*, *Journal of Geophysical Research: Space Physics*, **118**(5), 2000

Liu, R., Lühr, H. & Ma, S.-Y., 2010, *Storm-time related mass density anomalies in the polar cap as observed by CHAMP*, *Annales Geophysicae*, **28**(1), 165

Liu, X., Thayer, J. P., Burns, A., Wang, W. & Sutton, E., 2014, *Altitude variations in the thermosphere mass density response to geomagnetic activity during the recent solar minimum*, *Journal of Geophysical Research: Space Physics*, **119**(3), 2160

Liu, X., Xu, J., Yue, J. & Vadas, S. L., 2013*b*, *Numerical modeling study of the momentum deposition of small amplitude gravity waves in the thermosphere*, *Annales Geophysicae*, **31**(1), 1

Lloyds, 2013, *Solar Storm Risk to the North American Electric Grid* (Lloyds), [Online; accessed 2016-10-27]
URL: *http://www.aer.com//sites/default/files/Solar_Storm_Risk_to_the_North_American_Electric_Grid_0.pdf*

Lockwood, M., 2002, *An evaluation of the correlation between open solar flux and total solar irradiance*, *Astronomy and Astrophysics*, **382**, 678

Lockwood, M. & Cowley, S. W. H., 1999, *Comment on "A statistical study of the ionospheric convection response to changing interplanetary magnetic field conditions using the assimilative mapping of ionospheric electrodynamics technique" by AJ Ridley et al.*, *Journal of Geophysical Research: Space Physics*, **104**(A3), 4387

Lockwood, M. & Morley, S. K., 2004, *A numerical model of the ionospheric signatures of time-varying magnetic reconnection: I. Ionospheric convection*, *Annales Geophysicae*, **22**(1), 73

Lühr, H., Grunwaldt, L. & Förste, Ch., 2002, *CHAMP Reference Systems, Transformations and Standards*, Technical report, GFZ Potsdam, [Online; accessed 2016-10-03]
URL: *http://www-app2.gfz-potsdam.de/pb1/op/champ/docs_CHAMP/CH-GFZ-RS-002.PDF*

Lühr, H. & Marker, S., 2013, in F.-J. Lübken (ed.), *Climate and Weather of the Sun-Earth System (CAWSES): Highlights from a Priority Program* (Springer Netherlands, Dordrecht), pp. 189–205

Lühr, H., Rentz, S., Ritter, P., Liu, H. & Häusler, K., 2007, *Average thermospheric wind patterns over the polar regions, as observed by CHAMP*, *Annales Geophysicae*, **25**(5), 1093

Lühr, H., Rother, M., Köhler, W., Ritter, P. & Grunwaldt, L., 2004, *Thermospheric upwelling in the cusp region: Evidence from CHAMP observations*, *Geophysical Research Letters*, **31**(6), L06805

Lühr, H., Warnecke & Rother, M. K. A., 1996, *An algorithm for estimating field-aligned currents from single spacecraft magnetic field measurements: A diagnostic tool applied to Freja satellite data*, *Geosci. Remote Sens.*, **34**, 1369

Lühr, H., Warnecke, J., Zanetti, L. J., Lindqvist, P. A. & Hughes, T. J., 1994, *Fine structure of field-aligned current sheets deduced from spacecraft and ground-based observations: Initial Freja results*, *Geophysical Research Letters*, **21**(17), 1883

Lyons, L. R., Killeen, T. L. & Walterscheid, R. L., 1985, *The neutral wind 'flywheel' as a source of quiet-time, polar-cap currents*, *Geophysical Research Letters*, **12**(2), 101

Lysak, R. L. & Yoshikawa, A., 2006, *Resonant Cavities and Waveguides in the Ionosphere and Atmosphere* (American Geophysical Union), pp. 289–306

Marshall, J. & Plumb, A., 1972, *Atmosphere, Ocean and Climate Dynamics: An Introductory Text* (Academic Press, Inc, London, UK)

Mauk, B. H. & Zanetti, L. J., 1987, *Magnetospheric electric fields and currents*, *Reviews of Geophysics*, **25**(3), 541

McKay-Bukowski, D., Vierinen, J., Virtanen, I. I., Fallows, R., Postila, M., Ulich, T., Wucknitz, O., Brentjens, M., Ebbendorf, N., Enell, C.-F. et al., 2015, *Kaira: The Kilpisjärvi atmospheric imaging receiver array – System overview and first results*, *IEEE Transactions on Geoscience and Remote Sensing*, **53**(3), 1440

McPherron, R. L., Russell, C. T. & Aubry, M. P., 1973, *Satellite studies of magnetospheric substorms on August 15, 1968: 9. Phenomenological model for substorms*, *Journal of Geophysical Research*, **78**(16), 3131

Menvielle, M. & Berthelier, A., 1991, *The K-derived planetary indices: Description and availability*, *Reviews of Geophysics*, **29**(3), 415

Milan, S., Imber, S. & Lester, M., 2013, *ECLAT SuperDARN User Guide*, [Online; accessed 2018-02-16]
URL: *http://web.archive.org/web/20080207010024/http://www.808multimedia.com/winnt/kernel.htm*

Milan, S. E., 2009, *Both solar wind-magnetosphere coupling and ring current intensity control of the size of the auroral oval*, *Geophysical Research Letters*, **36**(18)

Milan, S. E., 2013, *Modeling Birkeland currents in the expanding/contracting polar cap paradigm*, *Journal of Geophysical Research: Space Physics*, **118**(9), 5532

Milan, S. E., Carter, J. A., Sangha, H., Laundal, K. M., Østgaard, N., Tenfjord, P., Reistad, J. P., Snekvik, K., Coxon, J. C., Korth, H. & Anderson, B. J., 2018, *Timescales of Dayside and Nightside Field-Aligned Current Response to Changes in Solar Wind-Magnetosphere Coupling*, *Journal of Geophysical Research: Space Physics*, **123**(9), 7307

Milan, S. E., Hutchinson, J., Boakes, P. D. & Hubert, B., 2009, *Influences on the radius of the auroral oval*, *Annales Geophysicae*, **27**(7), 2913

Milan, S. E., Lester, M., Cowley, S. W. H., Oksavik, K., Brittnacher, M., Greenwald, R. A., Sofko, G. & Villain, J.-P., 2003, *Variations in the polar cap area during two substorm cycles*, *Annales Geophysicae*, **21**(5), 1121

Milan, S. E., Provan, G. & Hubert, B., 2007, *Magnetic flux transport in the Dungey cycle: A survey of dayside and nightside reconnection rates*, *Journal of Geophysical Research: Space Physics*, **112**(A1)

Millward, G. H., Moffett, R. J., Quegan, S. & Fuller-Rowell, T. J., 1996, in R. W. Schunk (ed.), *Solar-Terrestrial Energy Program: Handbook Of Ionospheric Models* (SCOSTEP, Utah, USA), pp. 239–280

Millward, G. H., Richmond, A. D., Fuller-Rowell, T. J. & Aylward, A. D., 2007, *Modeling the Effect of Changes in the Terrestrial Magnetic Field on the Climatology of the Mid- and Low-Latitude Ionosphere*, *Eos. Trans. AGU, Fall Meet. Suppl.*, **88**(52), Abstract SA21B-08

Moe, K. & Moe, M. M., 2008, *The high-latitude thermospheric mass density anomaly: A historical review and a semi-empirical model*, *Journal of Atmospheric and Solar-Terrestrial Physics*, **70**(5), 794

Morley, S. K. & Freeman, M. P., 2007, *On the association between northward turnings of the interplanetary magnetic field and substorm onsets*, *Geophysical Research Letters*, **34**(8)

Morley, S. K., Freeman, M. P. & Tanskanen, E. I., 2007, *A comparison of the probability distribution of observed substorm magnitude with that predicted by a minimal substorm model*, *Annales Geophysicae*, **25**(11), 2427

Morley, S. K. & Lockwood, M., 2006, *A numerical model of the ionospheric signatures of time-varying magnetic reconnection: III. Quasi-instantaneous convection responses in the Cowley-Lockwood paradigm*, *Annales Geophysicae*, **24**(3), 961

Morley, S. K., Welling, D. T., Koller, J., Larsen, B. A., Henderson, M. G. & Niehof, J., 2010, in *Proceedings of the 9th Python in Science Conference (SciPy 2010)*, presented in Austin, TX, June 30 – July 1, 2010

Murray, S. A., Henley, E. M., Jackson, D. R. & Bruinsma, S. L., 2015, *Assessing the performance of thermospheric modeling with data assimilation throughout solar cycles 23 and 24*, *Space Weather*, **13**(4), 220, 2015SW001163

Muylaert, J., Reinhard, R., Asma, C., Buchlin, J., Rambaud, P. & Vetrano, M., 2009, in *ESA Atmospheric Science Conference, Barcelona, Spain*, pp. 7–11

Nakamura, M., Yoneda, A., Oda, M. & Tsubouchi, K., 2015, *Statistical analysis of extreme auroral electrojet indices*, *Earth, Planets and Space*, **67**(1), 153

Nakano, S., Ueno, G., Ohtani, S. & Higuchi, T., 2009, *Impact of the solar wind dynamic pressure on the Region 2 field-aligned currents*, *Journal of Geophysical Research: Space Physics*, **114**(A2), A02221

National Research Council, 2008, *Severe Space Weather Events–Understanding Societal and Economic Impacts: A Workshop Report* (The National Academies Press, Washington, DC, USA), [Online; accessed 2016-10-27]
URL: *https://www.nap.edu/catalog/12507/severe-space-weather-events-understanding-societal-and-economic-impacts-a*

Neubert, T. & Christiansen, F., 2003, *Small-scale, field-aligned currents at the top-side ionosphere*, *Geophysical Research Letters*, **30**(19)

Newell, P. T., Meng, C.-I., Sibeck, D. G. & Lepping, R., 1989, *Some low-altitude cusp dependencies on the interplanetary magnetic field*, *Journal of Geophysical Research: Space Physics*, **94**(A7), 8921

Ngwira, C. M., McKinnell, L.-A., Cilliers, P. J. & Coster, A. J., 2012, *Ionospheric observations during the geomagnetic storm events on 24-27 July 2004: Long-duration positive storm effects*, *Journal of Geophysical Research: Space Physics*, **117**(A9), A00L02

Ngwira, C. M., Pulkkinen, A., Wilder, F. D. & Crowley, G., 2013, *Extended study of extreme geoelectric field event scenarios for geomagnetically induced current applications*, *Space Weather*, **11**(3), 121

Nishida, A., 1964, *Ionospheric screening effect and storm sudden commencement*, *Journal of Geophysical Research*, **69**(9), 1861

Odom, C. D., Larsen, M. F., Christensen, A. B., Anderson, P. C., Hecht, J. H., Brinkman, D. G., Walterscheid, R. L., Lyons, L. R., Pfaff, R. & Emery, B. A., 1997, *ARIA II neutral flywheel-driven field-aligned currents in the postmidnight sector of the auroral oval: A case study*, *Journal of Geophysical Research: Space Physics*, **102**(A5), 9749

Ohtani, S., Ueno, G., Higuchi, T. & Kawano, H., 2005, *Annual and semiannual variations of the location and intensity of large-scale field-aligned currents*, *Journal of Geophysical Research: Space Physics*, **110**(A1), A01216

Ohtani, S., Wing, S., Ueno, G. & Higuchi, T., 2009, *Dependence of premidnight field-aligned currents and particle precipitation on solar illumination*, *Journal of Geophysical Research: Space Physics*, **114**(A12)

Oughton, E. J., Skelton, A., Horne, R. B., Thomson, A. W. P. & Gaunt, C. T., 2017, *Quantifying the daily economic impact of extreme space weather due to failure in electricity transmission infrastructure*, *Space Weather*, **15**(1), 65, 2016SW001491

Pant, T. K., Vineeth, C., Sumod, S. G. & Jose, L., 2011, *Evidence for the lowering of the centroid of daytime thermospheric O(1D) 630.0 nm emission over the magnetic equator: First results*, *Advances in Space Research*, **47**(4), 729

Parker, E. N., 1963, *Interplanetary dynamical processes* (Interscience Publishers, New York, USA)

Pedatella, N. M., Forbes, J. M., Lei, J., Thayer, J. P. & Larson, K. M., 2008, *Changes in the longitudinal structure of the low-latitude ionosphere during the July 2004 sequence of geomagnetic storms*, *Journal of Geophysical Research: Space Physics*, **113**(A11), A11315

Peria, W. J., Carlson, C. W., Ergun, R. E., McFadden, J. P., Bonnell, J., Elphic, R. C. & Strangeway, R. J., 2013, *Characteristics of Field-Aligned Currents Near the Auroral Acceleration Region: Fast Observations* (American Geophysical Union), pp. 181–189

Picone, J. M., Hedin, A. E., Drob, D. P. & Aikin, A. C., 2002, *NRLMSISE-00 empirical model of the atmosphere: Statistical comparisons and scientific issues*, *Journal of Geophysical Research: Space Physics*, **107**(A12), SIA 15

Pollock, C. J., Chandler, M. O., Moore, T. E., Waite, J. H., Chappell, C. R. & Gurnett, D. A., 1990, *A survey of upwelling ion event characteristics*, *Journal of Geophysical Research: Space Physics*, **95**(A11), 18969

Press, W. H., Teukolsky, S. A., Vetterling, W. T. & Flannery, B. P., 1992, *Numerical recipes in FORTRAN 77: The art of scientific computing* (Cambridge Univ. Press, Cambridge, UK)

Price, G. D., Smith, R. W. & Hernandez, G., 1995, *Simultaneous measurements of large vertical winds in the upper and lower thermosphere*, *Journal of Atmospheric and Terrestrial Physics*, **57**(6), 631

Prölss, G. W., 1981, *Latitudinal structure and extension of the polar atmospheric disturbance*, *Journal of Geophysical Research: Space Physics*, **86**(A4), 2385

Prölss, G. W., 2008, *Perturbations of the upper atmosphere in the cleft region*, *Journal of Atmospheric and Solar-Terrestrial Physics*, **70**(18), 2374

Reay, S. J., Allen, W., Baillie, O., Bowe, J., Clarke, E., Lesur, V. & Macmillan, S., 2005, *Space weather effects on drilling accuracy in the North Sea*, *Annales Geophysicae*, **23**(9), 3081

Reigber, Ch., Lühr, H. & Schwintzer, P., 2001, *Announcement of opportunity for CHAMP*, *GeoForschungZentrum Potsdam, GFZ Potsdam*

Reigber, Ch., Lühr, H. & Schwintzer, P., 2002, *CHAMP mission status*, *Advances in Space Research*, **30**(2), 129

Rentz, S. & Lühr, H., 2008, *Climatology of the cusp-related thermospheric mass density anomaly, as derived from CHAMP observations*, *Annales Geophysicae*, **26**(9), 2807

Richmond, A. D., Ridley, E. C. & Roble, R. G., 1992, *A thermosphere/ionosphere general circulation model with coupled electrodynamics*, *Geophysical Research Letters*, **19**(6), 601

Rishbeth, H. & Garriott, O. K., 1969, *Introduction to ionospheric physics* (Academic Press, Inc., London, UK)

Rishbeth, H. & Williams, P. J. S., 1985, *The EISCAT ionospheric radar - The system and its early results*, *Quarterly Journal of the Royal Astronomical Society*, **26**, 478

Riswadkar, A. V. & Dobbins, B., 2010, *Solar Storms: Protecting Your Operations Against the Sun's"Dark Side"* (Zurich Services Corporation), [Online; accessed 2016-10-03]
URL: *http://www.zurich.com/NR/rdonlyres/E7A8BC6C-86D9-4C1A-ABFC-F6213EB23D73/0/SolarStorms.pdf*

Ritter, P., Lühr, H. & Rauberg, J., 2013, *Determining field-aligned currents with the Swarm constellation mission*, *Earth, Planets and Space*, **65**(11), 9

Roble, R. G. & Ridley, E. C., 1994, *A thermosphere-ionosphere-mesosphere-electrodynamics general circulation model (time-GCM): Equinox solar cycle minimum simulations (30-500 km)*, *Geophysical Research Letters*, **21**(6), 417

Ronksley, A. M., 2016, *Optical remote sensing of mesoscale thermospheric dynamics above Svalbard and Kiruna*, Ph.D. thesis, University College London

Royal Academy of Engineering, 2013, *Extreme space weather: Impacts on engineered systems and infrastructure* (Royal Academy of Engineering, London, UK), [Online; accessed 2016-10-03]

URL: *http://www.raeng.org.uk/publications/reports/space-weather-full-report*

Ruohoniemi, J. M. & Baker, K. B., 1998, *Large-scale imaging of high-latitude convection with Super Dual Auroral Radar Network HF radar observations*, *Journal of Geophysical Research: Space Physics*, **103**(A9), 20797

Russell, C. T., 2000, *The polar cusp*, *Advances in Space Research*, **25**(7), 1413 , Proceedings of the DO.1 Symposium of COSPAR Scientific Commission D

Russell, C. T., 2000, *The solar wind interaction with the Earth's magnetosphere: a tutorial*, *IEEE Transactions on Plasma Science*, **28**, 1818

Sadler, F. B., Lessard, M., Lund, E., Otto, A. & Lühr, H., 2012, *Auroral precipitation/ion upwelling as a driver of neutral density enhancement in the cusp*, *Journal of Atmospheric and Solar-Terrestrial Physics*, **87-88**, 82

Schlegel, K., Lühr, H., St.-Maurice, J.-P., Crowley, G. & Hackert, C., 2005, *Thermospheric density structures over the polar regions observed with CHAMP*, *Annales Geophysicae*, **23**(5), 1659

Schrijver, C. J., Kauristie, K., Aylward, A. D., Denardini, C. M., Gibson, S. E., Glover, A., Gopalswamy, N., Grande, M., Hapgood, M., Heynderickx, D., Jakowski, N., Kalegaev, V. V., Lapenta, G., Linker, J. A., Liu, S., Mandrini, C. H., Mann, I. R., Nagatsuma, T., Nandy, D., Obara, T., O'Brien, T. P., Onsager, T., Opgenoorth, H. J., Terkildsen, M., Valladares, C. E. & Vilmer, N., 2015, *Understanding space weather to shield society: A global road map for 2015–2025 commissioned by COSPAR and ILWS*, *Advances in Space Research*, **55**(12), 2745

Sergeev, V. A., Angelopoulos, V. & Nakamura, R., 2012, *Recent advances in understanding substorm dynamics*, *Geophysical Research Letters*, **39**(5)

Shepherd, S. G., 2014, *Altitude-adjusted corrected geomagnetic coordinates: Definition and functional approximations*, *Journal of Geophysical Research: Space Physics*, **119**(9), 7501

Sheskin, D. J., 2003, *Handbook of parametric and nonparametric statistical procedures* (Chapman and Hall/CRC, USA)

Sica, R. J., Rees, M. H., Roble, R. G., Hernandez, G. & Romick, G. J., 1986, *The altitude region sampled by ground-based Doppler temperature measurements of the OI 15867 K emission line in aurorae*, *Planetary and Space Science*, **34**(5), 483

Snekvik, K., Tanskanen, E., Østgaard, N., Juusola, L., Laundal, K., Gordeev, E. I. & Borg, A. L., 2012, *Changes in the magnetotail configuration before near-Earth reconnection*, *Journal of Geophysical Research: Space Physics*, **117**(A2), A02219

Solomon, S. C., Qian, L., Didkovsky, L. V., Viereck, R. A. & Woods, T. N., 2011, *Causes of low thermospheric density during the 2007-2009 solar minimum*, *Journal of Geophysical Research: Space Physics*, **116**(A2), A00H07

St.-Maurice, J.-P. & Hanson, W. B., 1982, *Ion frictional heating at high latitudes and its possible use for an in situ determination of neutral thermospheric winds and temperatures*, *Journal of Geophysical Research: Space Physics*, **87**(A9), 7580

Stauning, P., 2013, *Power grid disturbances and polar cap index during geomagnetic storms*, *Journal of Space Weather and Space Climate*, **3**(27), A22

Storz, M. F., Bowman, B. R., Branson, M. J. I., Casali, S. J. & Tobiska, W. K., 2005, *High accuracy satellite drag model (HASDM)*, *Advances in Space Research*, **36**(12), 2497

Strangeway, R. J., 2012, *The equivalence of Joule dissipation and frictional heating in the collisional ionosphere*, *Journal of Geophysical Research: Space Physics*, **117**(A2), A02310

Tamao, T., 1986, *Direct contribution of oblique field-aligned currents to ground magnetic fields*, *Journal of Geophysical Research: Space Physics*, **91**(A1), 183

Tanskanen, E. I., Slavin, J. A., Tanskanen, A. J., Viljanen, A., Pulkkinen, T. I., Koskinen, H. E. J., Pulkkinen, A. & Eastwood, J., 2005, *Magnetospheric substorms are strongly*

modulated by interplanetary high-speed streams, *Geophysical Research Letters*, **32**(16), L16104

Tapley, B. D., Bettadpur, S., Watkins, M. & Reigber, Ch., 2004, *The gravity recovery and climate experiment: Mission overview and early results*, *Geophysical Research Letters*, **31**(9)

Tapping, K. F., 2013, *The 10.7-cm solar radio flux (F10.7)*, *Space Weather*, **11**(7), 394

Tenfjord, P., Østgaard, N., Snekvik, K., Laundal, K. M., Reistad, J. P., Haaland, S. & Milan, S. E., 2015, *How the IMF By induces a By component in the closed magnetosphere and how it leads to asymmetric currents and convection patterns in the two hemispheres*, *Journal of Geophysical Research: Space Physics*, **120**(11), 9368

Thayer, J. P., 2000, *High-latitude currents and their energy exchange with the ionosphere-thermosphere system*, *Journal of Geophysical Research: Space Physics*, **105**(A10), 23015

Thayer, J. P., Crowley, G., Niciejewski, R. J., Killeen, T. L., Buchau, J. & Reinisch, B. W., 1995, *Ground-based observations of ion/neutral coupling at Thule and Qânâq, Greenland*, *Journal of Geophysical Research: Space Physics*, **100**(A7), 12189

Thayer, J. P., Liu, X., Lei, J., Pilinski, M. & Burns, A. G., 2012, *The impact of helium on thermosphere mass density response to geomagnetic activity during the recent solar minimum*, *Journal of Geophysical Research: Space Physics*, **117**(A7)

Thayer, J. P. & Semeter, J., 2004, *The convergence of magnetospheric energy flux in the polar atmosphere*, *Journal of Atmospheric and Solar-Terrestrial Physics*, **66**(10), 807 , Upper Atmosphere Tutorials from the 2001 Joint CEDAR SCOSTEP Meeting

Thébault, E., Finlay, C. C., Beggan, C. D., Alken, P., Aubert, J., Barrois, O., Bertrand, F., Bondar, T., Boness, A., Brocco, L., Canet, E., Chambodut, A., Chulliat, A., Coïsson, P., Civet, F., Du, A., Fournier, A., Fratter, I., Gillet, N., Hamilton, B., Hamoudi, M., Hulot, G., Jager, T., Korte, M., Kuang, W., Lalanne, X., Langlais, B., Léger, J.-M., Lesur, V., Lowes, F. J., Macmillan, S., Mandea, M., Manoj, C., Maus, S., Olsen, N., Petrov, V., Ridley, V., Rother, M., Sabaka, T. J., Saturnino, D., Schachtschneider, R., Sirol, O., Tangborn, A., Thomson, A., Tøffner-Clausen, L., Vigneron, P., Wardinski, I. & Zvereva, T., 2015, *International Geomagnetic Reference Field: the 12th generation*, *Earth, Planets and Space*, **67**(1), 79

Tjulin, A., 2017, *EISCAT Experiments*, [Online; accessed: 2018-04-05]
URL: *https://www.eiscat.se/wp-content/uploads/2017/04/Experiments.pdf*

Tsyganenko, N. A. & Stern, D. P., 1996, *Modeling the global magnetic field of the large-scale Birkeland current systems*, *Journal of Geophysical Research: Space Physics*, **101**(A12), 27187

Vadas, S. L. & Crowley, G., 2017, *Neutral wind and density perturbations in the thermosphere created by gravity waves observed by the TIDDBIT sounder*, *Journal of Geophysical Research: Space Physics*, **122**(6), 6652, 2016JA023828

Vagina, L. I. & Sergeev, V. A., 1996, in E. J. Rolfe & B. Kaldeich (eds.), *International Conference on Substorms*, volume 389 of *ESA Special Publication*, p. 609

Vallado, D. A., 2001, *Fundamentals of Astrodynamics and Applications* (Microcosm Press, El Segundo, CA, USA)

Vallée, M. A., Newitt, L., Mann, I. R., Moussaoui, M., Dumont, R. & Keating, P., 2007, *The spatial and temporal characteristics of Pc3 geomagnetic activity over Canada in 2000, as a guide to planning the times of aeromagnetic surveys*, *Pure and Applied Geophysics*, **164**(1), 161

Vasyliunas, V. M., Kan, J. R., Siscoe, G. L. & Akasofu, S.-I., 1982, *Scaling relations governing magnetospheric energy transfer*, *Planetary and Space Science*, **30**(4), 359

Vennerstrøm, S., Moretto, T., Olsen, N., Friis-Christensen, E., Stampe, A. M. & Watermann, J. F., 2002, *Field-aligned currents in the dayside cusp and polar cap region during northward IMF*, *Journal of Geophysical Research: Space Physics*, **107**(A8), SMP 18

Viljanen, A., Pirjola, R., Prácser, E., Katkalov, J. & Wik, M., 2014, *Geomagnetically induced currents in Europe*, *J. Space Weather Space Clim.*, **4**, A09

Viljanen, A., Tanskanen, E. I. & Pulkkinen, A., 2006, *Relation between substorm characteristics and rapid temporal variations of the ground magnetic field*, *Annales Geophysicae*, **24**(2), 725

Vlasov, M. N., Nicolls, M. J., Kelley, M. C., Smith, S. M., Aponte, N. & González, S. A., 2005, *Modeling of airglow and ionospheric parameters at Arecibo during quiet*

and disturbed periods in October 2002, *Journal of Geophysical Research: Space Physics*, **110**(A7), A07303

Wang, H., Lühr, H. & Ma, S. Y., 2005, *Solar zenith angle and merging electric field control of field-aligned currents: A statistical study of the Southern Hemisphere*, *Journal of Geophysical Research: Space Physics*, **110**(A3), A03306

Wang, H., Lühr, H., Ma, S. Y., Weygand, J., Skoug, R. M. & Yin, F., 2006, *Field-aligned currents observed by CHAMP during the intense 2003 geomagnetic storm events*, *Annales Geophysicae*, **24**(1), 311

Wanliss, J. A. & Showalter, K. M., 2006, *High-resolution global storm index: Dst versus SYM-H*, *Journal of Geophysical Research: Space Physics*, **111**(A2), A02202

Watermann, J., Christiansen, F., Popov, V., Stauning, P. & Rasmussen, O., 2003, in Ch. Reigber, H. Lühr & P. Schwintzer (eds.), *First CHAMP Mission Results for Gravity, Magnetic and Atmospheric Studies* (Springer Berlin Heidelberg, Berlin, Heidelberg), pp. 361–368

Watermann, J. & Gleisner, H., 2009, *Geomagnetic variations and their time derivatives during geomagnetic storms at different levels of intensity*, *Acta Geophysica*, **57**(1), 197

Weimer, D. R., Ober, D. M., Maynard, N. C., Collier, M. R., McComas, D. J., Ness, N. F., Smith, C. W. & Watermann, J., 2003, *Predicting interplanetary magnetic field (IMF) propagation delay times using the minimum variance technique*, *Journal of Geophysical Research: Space Physics*, **108**(A1)

Wharton, L. E., Spencer, N. W. & Mayr, H. G., 1984, *The Earth's thermospheric super-rotation from Dynamics Explorer 2*, *Geophysical Research Letters*, **11**(5), 531

Woodroffe, J. R., Morley, S. K., Jordanova, V. K., Henderson, M. G., Cowee, M. M. & Gjerloev, J. G., 2016, *The latitudinal variation of geoelectromagnetic disturbances during large ($Dst \leq 100$ nT) geomagnetic storms*, *Space Weather*, **14**(9), 668, 2016SW001376

Wu, J. & Stening, R. J., 1991, *Field-aligned currents observed in the inner magnetosphere and their magnetic signature on the ground*, *Journal of Geophysical Research: Space Physics*, **96**(A5), 7721

Xiong, C., Lühr, H., Wang, H. & Johnsen, M. G., 2014, *Determining the boundaries of the auroral oval from CHAMP field-aligned current signatures – Part 1*, *Annales Geophysicae*, **32**(6), 609

Yiu, H. C. I., 2014, *High latitude thermosphere meso-scale studies and long-term database investigations with the new Scanning Doppler Imager and Fabry-Perot Interferometers*, Ph.D. thesis, University College London

Yiğit, E., 2008, *Modelling Atmospheric Vertical Coupling: Role of Gravity Wave Dissipation in the Upper Atmosphere*, Ph.D. thesis, University College London

Yiğit, E. & Ridley, A. J., 2011, *Effects of high-latitude thermosphere heating at various scale sizes simulated by a nonhydrostatic global thermosphere-ionosphere model*, *Journal of Atmospheric and Solar-Terrestrial Physics*, **73**(5), 592

Zanetti, L. J., 2013, *Review of North American Electric Reliability Corporation (NERC) Interim Report: Effects of Geomagnetic Disturbances on the Bulk Power System – February 2012*, *Space Weather*, **11**(6), 335

Zanetti, L. J., Potemra, T. A., Anderson, B. J., Erlandson, R. E., Holland, D. B., Acuña, M. H., Kappenman, J., Lesher, R. & Feero, B., 1994, *Ionospheric currents correlated with geomagnetic induced currents; Freja magnetic field measurements and the Sunburst Monitor System*, *Geophysical Research Letters*, **21**(17), 1867

Zhang, B., Lotko, W., Brambles, O., Wiltberger, M., Wang, W., Schmitt, P. & Lyon, J., 2012, *Enhancement of thermospheric mass density by soft electron precipitation*, *Geophysical Research Letters*, **39**(20)

Zhang, J., Richardson, I. G., Webb, D. F., Gopalswamy, N., Huttunen, E., Kasper, J. C., Nitta, N. V., Poomvises, W., Thompson, B. J., Wu, C.-C., Yashiro, S. & Zhukov, A. N., 2007, *Solar and interplanetary sources of major geomagnetic storms (Dst $\leq$100 nT) during 1996–2005*, *Journal of Geophysical Research: Space Physics*, **112**(A10), A10102

Zheng, Y., Lui, A. T. Y., Fok, M.-C., Anderson, B. J., Brandt, P. C. & Mitchell, D. G., 2008, *Controlling factors of Region 2 field-aligned current and its relationship to the ring current: Model results*, *Advances in Space Research*, **41**(8), 1234